Excitons in van der Waals Heterostructures: A theoretical study

Latini, Simone

Publication date:
2016

Document Version
Publisher's PDF, also known as Version of record

Ph.D. Thesis
Doctor of Philosophy

DTU Physics
Department of Physics

Excitons in van der Waals Heterostructures

A theoretical study

Simone Latini

Kongens Lyngby 2016

DTU

DTU Physics
Department of Physics
Technical University of Denmark

Fysikvej
Building 307
2800 Kongens Lyngby, Denmark
Phone +45 4525 3344
info@fysik.dtu.dk
www.fysik.dtu.dk

Preface

This thesis is submitted in candidacy for the Ph.D. degree in physics from the Technical University of Denmark. The work presented in the thesis has been carried out at the Department of Physics from September 2013 to September 2016 under the supervision of Professor Kristian S. Thygesen. The projected has been funded by the Center of Nanostructured Graphene which has been sponsored by the Danish National Research Council.

My profound gratitude goes to my supervisor Kristian S. Thygesen, not only because he made this life-changing danish experience possible, but also because of his guidance and the countless constructive discussions during these three years. His enthusiasm, his care for details and his physical intuition have inspired me and made my passion for physics constantly grow. Thank you Kristian for all this!

I would also like to thank Professor Thomas Olsen for the fruitful discussions and the technical guidance in the intricate world of excitons. A special thank goes to Kirsten T. Winther for the close collaboration on the van der Waals heterostructure modeling and to Steen Haastrup and Thomas G. Pedersen for making the calculations on the exciton dissociation possible. Thanks also to Jens Jørgen Mortensen for all the support with GPAW. A huge thank goes to Per S. Schmidt (in particular), Marta Majkut, Nicki F. Hinsche, Mohnish Pandey, Korina Kuhar and Sten Haastrup for proofreading my thesis. Thanks also to Ole and Marcin for the technical help with Niflheim and to Marianne for her administrative support.

Next I have to thank the people I have shared the 'frat house' (commonly known as 'my office') with: Per, Filip, Kirsten and Ivano. You have made my office days much better and you have managed to stand me for such along, which, as people that know me would say, is a remarkable achievement. Per, Filip and Ivano I also thank you for being part of my private life and for introducing me to the Danish drinking culture (maybe I should not thank you for that). I would also like to thank all the colleagues at CAMD which made the working environment, and not only, much more pleasant and much less serious: Morten, Korina, Steen, Mohnish, Nicky, Mikkel, Alexander, Chris, Chengjun, Manuel, Martin and Falco. Of course, I cannot forget all the others at the Physics department: Marta, Alberto, Elisa, Elisa and Rasmus. A special thank to you Marta for the nice vacation together and for the nice friendship.

Moving to Denmark has been an awesome experience, it did not take much for me to like the country, the people, the habits and the weather (ok maybe the weather not). In particular there is one person that I got to like a lot (actually more than that) and it is you Karinna. I am grateful to you for everything, even for our endless fights, but you know what? I cannot be without you. You made me grow and taught me that the world is not only made of logic and formulas.

On the other hand, by moving to Denmark, it has been tough to be away from the friends I had grown up with. Despite the distance, the ones that mattered a lot to me are still there: thank you Enrico and Giordano, now I know I can really count on you.

Grazie mamma e papá! Nonostante non mi sia impegnato cosí tanto a tornare a casa regolarmente, voi siete sempre stati lí, incondizionatamente, vi siete sempre fatti bastare una semplice chiamata su skype una volta a settimana e non me lo avete mai fatto pesare. Avete sempre creduto in me e in tutte le mie scelte e so che per voi ció che conta é che sia felice. Grazie anche a te, sorellina, stai crescendo in fretta e purtroppo non sono lí con te ma nonostante ció sei sempre pronta a regalarmi un sorriso.

Infine grazie a tutta la mia famiglia e le mie nonne che hanno sempre dimostrato il loro orgoglio nei mie confronti.

Kongens Lyngby, October 7, 2016

Simone Latini

Summary

Van der Waals heterostructures (vdWHs) represent a novel and largely unexplored class of materials. Since 2013, when Geim and Grigorieva first conceived the stacking of 2D (two-dimensional) materials to create artificial layered structures with tailored properties, a number of promising (opto)electronics devices, e.g. light emitting diodes, solar cells, ultra-fast photodetectors, transistors etc., have been successfully fabricated. It is well established that for isolated 2D semiconductors and vdWHs the optical response is governed by excitonic effects. While it is understood that the reduced amount of electronic screening in freestanding 2D materials is the main origin of extraordinarily strongly bound excitons, a theoretical understanding of excitonic effects and of how the electronic screening is affected for the more complex case of multi-layer structures is still lacking due to the computational limitations of standard ab-initio methods.

In this thesis first-principles models that overcome the limitations of standard ab-initio techniques are developed for the description of dielectric, electronic and excitonic properties in isolated 2D materials and vdWHs. The main contribution is a multi-scale method that seemingly connects the excitonic effects in the monolayer limit to the more challenging case of multi-layered structures. The method is based on the analogy between vdWHs and the popular construction toy Lego. This analogy is much deeper than one would first expect: it is possible to predict the dielectric properties of a vdWH from the dielectric functions of the individual 2D layers, which represent the dielectric genome of the heterostructure. From the vdWH dielectric properties one evaluates the screened interaction between the electron and hole forming the exciton which can then be used in a generalized hydrogenic model to compute exciton binding energies in isolated, supported, or encapsulated 2D semiconductors. The non-locality of the dielectric screening is inherently included in our method and we can successfully describe the non-hydrogenic Rydberg series of low-dimensional systems. This multi-scale method also proves successful when combined with many-body perturbation techniques for accurate prediction of electronic band structure or with complex scaling techniques for exciton dissociation rates in vdWHs. The validity of our techniques is demonstrated through numerous comparison to experimental results.

Ultimately this thesis puts forth a first-principles methodology that allows us to address scientific questions that are beyond the capability of existing state of the art techniques and enables 2D materials researcher to predict and design dielectric, electronic and excitonic properties of general vdWHs.

Resume

Van der Waals heterostrukturer (vdWHs) representerer en ny og uudforsket klasse af materialer. Siden 2013, da Geim og Grigorieva for første gang forestillede sig at stable 2D (to-dimensionelle) materialer for at skabe kunstigt lagdelte strukturer med skræddersyede egenskaber, er det lykkedes at fabrikere lovende (opto)-elektroniske enheder som f.eks. lysdioder, solceller, ultra-hurtige photodetektorer og transistorer. Det er velkendt at for isolerede 2D halvledere og vdWHs, er det optiske respons domineret af excitoner, og at grunden til de særligt stærkt bundne excitoner skal findes i den reducerede elektroniske skærmning. En teoretisk forståelse for de excitonske effekter, og for hvordan den elektroniske skærmning er påvirket i de mere komplekse tilfælde med multi-lags strukturer mangler stadig grundet computationelle begrænsninger af standard ab-initio metoder.

I denne afhandling er ab-initio modeller, som overkommer begrænsningerne på standard teknikker, udviklet til beskrivelse af dielektriske, elektroniske og excitonske egenskaber i isolerede 2D materialer og vdWHs. Hovedbidraget er en metode, som forbinder excitonske effekter i et enkelt lag med det mere udfordrende tilfælde af strukturer bestående af flere lag. Metoden er baseret på analogien mellem vdWHs og det populære konstruktionslegetøj Lego. Denne analogi stikker dybere, end man umiddelbart skulle tro: det er muligt at forudsige de dielektriske egenskaber af en vdWH fra den dielektriske function af de individuelle 2D lag, som således kan siges at repræsentere heterostrukturens dielektriske genom.

Med de dielektriske egenskaber af vdWHs kan man evaluere den skærmede vekselvirkning mellem elektronen og hullet, som danner excitonen, og som dernæst kan blive brugt i en generaliseret hydrogen-model til beregning af bindingsenergier af excitoner i isolerede, understøttede eller indkapslede 2D halvledere. Ikke-lokaliteten af den dielektriske screening er i sagens natur inkluderet i vores metode, og vi kan beskrive den ikke-hydrogenske Rydberg serie af lav-dimensionelle systemer succesfuldt. Denne multi-skala metode har vist sig at fungere, når den kombineres med mange-legeme perturbationsteknikker til præcis bestemmelse af elektroniske båndstrukturer eller med komplex skaleringsteknikker til beregning af excitonske dissocieringsrater i vdWHs. Gyldigheden af vores fremgangsmåder er demonstreret igennem talrige sammenligninger med resultater fra experimenter.

Denne afhandling presenterer ab-initio metoder, som tillader os at takle videnskabelige spørgsmål, som tidligere var uden for rækkevidde med eksisterende teknikker, og gør det muligt for forskere at forudsige og designe dielektriske, elektroniske og excitonske egenskaber af generelle vdWHs.

List of Papers

Paper I
Dielectric Genome of van der Waals Heterostructures
Kirsten Andersen, Simone Latini and Kristian S. Thygesen, *Nano Lett.*, **15** (7), pp 4616–4621 (2015).

Paper II
Excitons in van der Waals heterostructures: The important role of dielectric screening
Simone Latini, Thomas Olsen and Kristian S. Thygesen, *PRB*, **92**, pp 245123 (2015). Editor's suggestion.

Paper III
Simple Screened Hydrogen Model of Excitons in Two-Dimensional Materials
Thomas Olsen, Simone Latini, Filip A. Rasmussen and Kristian S. Thygesen, *PRL*, **116**, pp 056401 (2016).

Paper IV
Interlayer excitons and Band Alignment in MoS_2/hBN/WSe_2 van der Waals Heterostructures
Simone Latini, Kirsten T. Winther, Thomas Olsen and Kristian S. Thygesen, to be submitted.

Paper V
Stark shift and electric-field-induced dissociation of excitons in monolayer MoS_2 and hBN/MoS_2 heterostructures
Sten Haastrup, Simone Latini, Kirill Bolotin and Kristian S. Thygesen, *PRB*, **94**, pp 041401(R) (2016). Rapid Communication

Paper VI
Exciton ionization in multilayer transition-metal dichalcogenides
Thomas G. Pedersen, Simone Latini, Kristian S. Thygesen, Héctor Mera, Branislav K. Nikolić, *New Journal of Physics*, **18** (7), pp 073043 (2016).

Contents

CHAPTER 1

Introduction

During the Second World War, when detectors for radar were based on silicon and germanium and their reliability was a necessity, a lot of effort was put into improving the device performance. At that time very little was known about the physics of the two semiconductors [1]. Scientists soon realized that the fabrication of better detectors could be achieved only through a deeper understanding of the materials they were made of. It was not long until materials research led to the greatest invention of the past century: the transistor, developed by Bardeen and Brattainin in 1948 [2]. Since then, condensed matter physics and materials science have been source of many scientific and technological breakthroughs that have had a tremendous impact on our lives. Think, for example, of how the advance of materials science transformed the computer from an exotic scientific "toy" to an ubiquitous tool in our everyday lives. Inventions such as LEDs, lasers, optical fibers, solar cells and superconductors would have not been possible without an intimate knowledge of materials properties. Nowadays, most technology relies on silicon and related oxides microelectronics. While the popularity of silicon over other equivalent semiconductors is due to its abundance and ease of processability, the key to the success of microelectronics has been the possibility to integrate electronic components in microchips. Integration has been crucial as it has led to low manufacturing cost and great device reliability. The quest for integration on an even smaller scale and the development of nanoelectronics, has motivated the process of miniaturization of silicon transistors, which have now reached sub-micrometer minimum feature size. However silicon technology can no longer keep up with Moore's law [3] due to manufacturing and material properties limitations [4]. Reasearch in nanoelectronics should therefore be directed towards new materials and methods to build electronic devices at the nanoscale.

It was 2004 when Geim and Novoselov succeeded in isolating graphene, a single layer of carbon atoms, from graphite, the material used in our pencils [5]. Graphene is one of a kind material, characterized by exceptionally high electrical and thermal conductivity [6] and high carrier mobility [7]. Graphene is also a playground for fundamental physics showing e.g., the Quantum Hall effect at room temperature [8] or the Klein tunneling [9]. Graphene has allowed researchers to reconsider technological concepts such as spintronics [10], where spin rather than charge is controlled to transfer information, and even gave rise to new fields such as valleytronics [11], which exploits the peculiar valley degrees of freedom to operate the devices. Unfortunately, graphene based field-effect transistors (FETs), the base of modern technology, can-

not be effectively switched on and off because pristine graphene lacks an electronic bandgap. One approach to the development of graphene transistors is engineering a bandgap using methods like nanostructuring [12], chemical functionalization [13] or nanopatterning [14], however these methods are particularly complex and often lead to degradation of the intrinsic graphene properties.

Graphene is not the only material in the class of 2D crystals. The next in line is monolayer hexagonal Boron Nitride (hBN). The interest in hBN began when it proved to be an exceptional substrate for graphene, increasing the quality of graphene's electronic properties as compared to standard SiO_2 substrates [15]. Being a large gap insulator, hBN was used as a gate dielectric [16] and tunnel barrier [17] in transistors. Another key material in the 2D family is monolayer MoS_2, a direct gap semiconductor, which has been successfully used in field effect transistors, achieving high on/off switching ratios with mobilities lower than in graphene but still remarkably higher than standard thin-film semiconductors [18]. MoS_2 belongs to the class of materials with chemical formula MX_2 called transition metal dichalcogenides (TMDs). TMDs appear in two different hexagonal phases depending on whether the chalcogen atoms are aligned (2H) or displaced (1T) in the out-of-plane direction [19]. Atomic layers of TMDs can be isolated via mechanical or liquid-phase exfoliation [20] starting from the bulk counterpart. TMDs span a large space of material properties, ranging from metals VS_2, $TaSe_2$ and TaS_2, semiconductors as WS_2, WSe_2, TaS_2, $RhTe_2$ and even superconductors such as $NbSe_2$, NbS_2 and TaS_2 [21, 22]. Many of the semiconducting bulk TMDs undergo an indirect to direct band gap transition accompanied by a large increase in photoconductivity, absorption and photoluminescence [23, 24] when thinned down to monolayer size. For this reason, monolayer semiconducting TMDs attracted a lot of attention for applications in optoelectronic devices, i.e. electronic devices that can detect, control or generate light. Additionally, the fact that they are atomically thin and mechanically strong makes them appealing for flexible and transparent optoelectronics. Another important characteristic, general to 2D materials, is the reduced dielectric screening due to the reduced dimensionality, which results in strong excitonic effects setting the onset of photoluminescence and absorption well below the electronic band gap [25,26,27,28,29]. TMDs are probably the most investigated among the 2D crystals, but the family of 2D materials is continuously growing. Just to name a few transition metal oxides and halides, phosphorene, silicene, germanene, silicane, GaSe are currently of great interest to the field [30].

Apart from the extraordinary properties of 2D crystals as stand-alone materials, the great promise resides in the possibility of stacking 2D layers together to form hybrid multilayer heterostructures. Because such heterostructures are held together by weak van der Waals forces, they are referred to as van der Waals heterostructures (vdWHs). 2D materials with different properties can be assembled with atomic precision into designer vdWHs with novel and integrated properties, offering a great opportunity for the realization of ultra-thin (opto)electronic devices with embedded multi-functionality [30]. The ultimate goal is to complement or even replace Silicon technology by creating a comprehensive vdWHs platform for building different com-

ponents, such as transistors, batteries, (photo)detectors, photovoltaic cells, lasers and bio- and chemical sensors. First proof of principle devices are already available, such as vertical tunnelling transistors with promising electrical characteristics [31], light emitting diodes with high electroluminescence [32], photodetectors with ultrafast response [33] or high-efficiency ultra-thin photovoltaic devices [34].

Despite the great promises offered by 2D materials and their vdWHs, the main limitation is the current fabrication process, which relies on direct stacking of the 2D layers [30]. In the so called pick-and-lift technique one starts by exfoliating the first 2D layer from its bulk crystal using Scoth-tape and subsequently deposit it on a membrane. The membrane is then brought into contact with a second layer, also isolated using the Scotch-tape technique. Due to van der Waals forces, the second layer sticks to the first when the membrane is lifted. This process is repeated for all required layers. Although this procedure may seem simple, in practice it is extremely slow and poor in terms of device reproducibility. Therefore more controlled and efficient methods, such as direct growth through chemical vapor deposition (CVD) or physical epitaxy [30], need to be developed to achieve mass production and offer long-term prospects.

In any case, there is still very little known about van der Waals heterostructures and, even though their future might be uncertain, we as scientists need to deepen the knowledge of these promising materials. A theoretical understanding of the optical and electronic behavior of these atomically structured materials is crucial. Computer simulation and modeling based on quantum mechanical methods provide direct access to these properties without the need of performing actual experiments. Theoretical simulations have two advantages over experimental measurements. First, they allow us to simplify the investigation by isolating specific physical phenomena otherwise entangled in the actual measurement, as e.g. excitonic and electronic excitations. Second, they are much more efficient for materials screening projects aimed at finding good candidate for a given application, especially considering the enormous phase space of physical properties spanned by the family of 2D materials and their vdWHs. On the other hand computational methods rely on approximation whose validity needs to be critically assessed, often by comparing with experiments.

In this thesis I investigate the excitonic and electronic properties of 2D semiconductors and van der Waals heterostructure with the main focus given to the development of first-principles simplified models. While standard ab-initio methods such as density functional theory (DFT) and many-body perturbation theory (MBPT) have already been successfully applied to freestanding 2D crystals to calculate, e.g., electronic band gaps and exciton binding energy [27, 28], they are computational unfeasible for vdWHs, except for lattice matched heterostructures consisting of a few layers [28,35,36]. This is when our simplified models, that build upon DFT and MBPT, are the most relevant. The main contribution of this thesis is a multi-scale method, the quantum electrostatic heterostructure (QEH) model, which allows us to calculate the dielectric function of general vdWHs by electrostatically coupling the dielectric response of the individual layers without having to perform calculations for the full heterostructure. The dielectric function of the heterostructure can be used to calculate the screened

electron-hole interaction entering a generalized hydrogenic equation for the exciton, which in turn is used to calculate the exciton binding energy. The exciton binding energy is a measure of how strongly the electron and the hole forming the excitons are bound and is of technological relevance in photovoltaic devices or photodectors that rely on exciton dissociation [33,37,38,39,40]. Along these lines, by complex scaling of the hydrogenic equation, we are able to calculate the exciton dissociation rate under the application of an electric field. Ultimately, the QEH model can be combined with MBPT methods, such as GW, for calculating accurate electronic band alignment in vdWHs, relevant for charge transfer mechanisms at the interfaces of the constituent layers. In conclusion, in this thesis I present a comprehensive platform for calculating excitonic and electronic properties of vdWHs.

The structure of the thesis is the following:

- **Chapter 2** provides an introduction to the theoretical foundation of the ab-initio methods to calculate ground- and excited state properties of materials. Specifically, it presents density functional theory and many-body perturbation theory as viable routes for the solution of the many-body problem.
- **Chapter 3** explains the concept of microscopic and macroscopic dielectric and optical response of a crystal and elaborates on the difference between 2D and 3D materials. Additionally, it discusses the importance of excitonic effects for the optical properties of 2D semiconductors and how to account for them through the Bethe-Salpeter equation.
- **Chapter 4** gives a critical assessment of the Mott-Wannier model for excitons in freestanding 2D materials, with emphasis on the role of the screened electron-hole interaction. It also shows how a very simple analytic model can be found for the calculation of exciton binding energies in 2D.
- **Chapter 5** addresses the challenge of modelling vdWHs by presenting the quantum electrostatic heterostructure (QEH) model. Combining the QEH with the Mott-Wannier model it reports a number of calculations on intra and interlayer excitons in vdWHs. Furthermore, combining the QEH with GW it presents the method for calculating band structures and band alignment in vdWHs starting from the isolated layers.
- **Chapter 6** explains the concept of resonance and complex scaling techniques useful for the calculation of exciton dissociation rates in electric fields. It reports the calculation of dissociation rates for ultra-thin vdWHs.
- **Chapter 7** presents a brief summary of the results and an outlook.

CHAPTER 2

The Many-Body Problem

This chapter is devoted to the introduction of the fundamental formalism and methods to calculate the quantum mechanical properties of materials. The behavior of a quantum system is exactly determined by the solution of its Schrödinger equation. Unfortunately for most of the physical problems and in particular the ones relevant for this thesis, a direct solution of the Schrödinger equation cannot be determined. One, then, has to recast to alternative methods in order to calculate physical quantities such as ground state energy, dielectric response, electronic and excitonic excitation energies and so on. Two of such methods are density functional theory and many-body perturbation theory. While the first is in principle an exact ground state theory the second provides a systematic way to achieve increasing accuracy on excited states properties. In the following the basics of the two theories and their connection is provided.

2.1 The Many-Body Hamiltonian

The starting point for the description of the atomic scale physical and chemical properties of a material is the time dependent Schrödinger equation[1]

$$\mathrm{i}\frac{\partial}{\partial t}|\Phi(t)\rangle = \hat{H}(t)|\Phi(t)\rangle, \tag{2.1}$$

with $\hat{H}$ the many-body Hamiltonian of the system and $|\Phi\rangle$ the many-body wave function solution to the Schrödinger equation. For systems at equilibrium, the time independent wave function can be obtained from the stationary version of the Schrödinger equation:

$$\hat{H}|\Phi\rangle = E|\Phi\rangle, \tag{2.2}$$

[1] throughout the thesis atomic units are employed.

where E is many-body energy associated to $|\Phi\rangle$. The many-body Hamiltonian of an unperturbed condensed matter system consisting of interacting electrons and nuclei in motion can be written as:

$$\hat{H} = \sum_{i}^{N_{\text{el}}} \frac{\hat{p}_i^2}{2} + \sum_{I}^{N_{\text{nuc}}} \frac{\hat{P}_i^2}{2M_I} + \sum_{iI} \frac{Z_I}{|\hat{r}_i - \hat{R}_I|} + \frac{1}{2}\sum_{i\neq j} \frac{1}{|\hat{r}_i - \hat{r}_j|} + \frac{1}{2}\sum_{I\neq J} \frac{Z_I Z_J}{|\hat{R}_i - \hat{R}_J|}, \quad (2.3)$$

where the first two terms on the RHS are the kinetic energy of the electrons and nuclei respectively and the last three represent, in order, the nucleus-electron, electron-electron and nucleus-nucleus Coulomb interaction.

Solving the Schrödinger equation with the Hamiltonian above, which contains both electronic and nuclei degrees of freedom, is a daunting task. A great simplification arises by separating the electronic problem from the nuclei one by means of the Born-Oppenheimer approximation [41]. Within this approximation it is assumed that the electrons, because of their light mass, move much faster than the nuclei and therefore from an electron point of view the nuclei can be considered still. This entails that the eq. (2.1) reduces to two separate Schrödinger equations, one for the electronic many-body wave function $|\Psi\rangle$ and the other for the nuclei wave function $|\chi\rangle$, so that $|\Phi\rangle = |\Psi\rangle \otimes |\chi\rangle$. The Born-Oppenheimer approximation is extremely handy when one is mainly interested in the electronic properties, as in the case of this thesis. Indeed the information about the nuclei would appear in electronic problem only parametrically through stationary nuclei positions, and the electronic Hamiltonian would read:

$$\hat{H}_{\text{el}} = \sum_{i}^{N_{\text{el}}} \frac{\hat{p}_i^2}{2} + \sum_{iI} \frac{Z_I}{|\hat{r}_i - \mathbf{R}_I|} + \frac{1}{2}\sum_{i\neq j} \frac{1}{|\hat{r}_i - \hat{r}_j|}. \quad (2.4)$$

Despite the simplification, though, the electron-electron interaction makes the electronic problem unsolvable exactly. Before moving to the next section and see how to tackle the solution of the Schrödinger equation, it is convenient to express the electronic Hamiltonian in second quantization in terms of field operators, $\hat{\psi}^\dagger(x)\hat{\psi}(x)$ (for more details see Ref. [42, 43]):

$$\hat{H}(t) = \int dx dx' \hat{\psi}^\dagger(x)\langle x|\hat{h}(t)|x'\rangle\hat{\psi}(x') + \frac{1}{2}\int dx dx' v(x,x')\hat{\psi}^\dagger(x)\hat{\psi}^\dagger(x')\hat{\psi}(x')\hat{\psi}(x), \quad (2.5)$$

with $x = \mathbf{r}\sigma$ representing a generalized spatial/spin coordinate and $\hat{h}$ the single electron Hamiltonian[2]. As in eq. (2.5), from now on I will drop the subscript "el" when referring to the electronic hamiltonian.

[2] For a condensed matter system subjected to an external electromagnetic perturbation the single particle Hamiltonian is:

$$\hat{h} = \frac{(\hat{p} - \frac{1}{c}A_{\text{ext}}(\hat{r},t))^2}{2} + \sum_{I} \frac{Z_I}{|\hat{r} - \hat{R}_I|} + V_{\text{ext}}(\hat{r},t), \quad (2.6)$$

where $A_{\text{ext}}(\hat{r},t)$ and $V_{\text{ext}}(\hat{r},t)$ are the vector and scalar potentials respectively. Finally $v(x,x') = \frac{1}{|\mathbf{r}-\mathbf{r}'|}$ is the Coulomb interaction

2.2 Density Functional Theory

Inspired by the Thomas-Fermi conjecture on the possibility of expressing the ground state energy of a many-body system as a functional of the ground state electronic density [44, 45], in 1964 Hohenberg and Kohn formally proved that the ground state energy is indeed a unique functional of the ground state density [46]. In particular they showed that there exists a bijective mapping between the external potential, i.e. the system specific part of the Hamiltonian, and the ground state density. In the following I will illustrate the main results of the Hohenberg and Kohn proof and show how such a theorem can be utilized in practice by means of the Kohn and Sham equation [47], in order to avoid the direct solution of the Schrödinger equation.

2.2.1 Hohenberg and Kohn Theorem

Take a N-particle system described by a Hamiltonian of the kind:

$$\hat{H} = \hat{T} + \hat{V}^{\text{el-el}} + \hat{V}^{\text{ext}}, \tag{2.7}$$

where $\hat{T}$ represents the electronic kinetic energy, $\hat{V}^{\text{el-el}}$ the electron-electron interaction and $\hat{V}^{\text{ext}} = \int d\mathbf{r} v^{\text{ext}}(\mathbf{r})\hat{n}(\mathbf{r})$ the system specific part of the Hamiltonian, i.e. Coulomb interaction with the nuclei, external perturbation etc.

The starting point of the Hohenberg and Kohn derivation follows from two assumptions: to each unique (up to a constant) external potential there exists a mapping $C : v^{\text{ext}} \rightarrow \Psi^{\text{GS}}$ that maps into a unique ground state (GS) wave function[3]. At the same time there exists a mapping $D : \Psi^{\text{GS}} \rightarrow n^{\text{GS}}$ that associates a single electronic density to the ground state wave function (see fig. 2.1). This follows directly from the definition of the ground state density in terms of ground state wave function:

$$n^{\text{GS}}(\mathbf{r}) = N \int d\mathbf{r}_1 \cdots \cancel{d\mathbf{r}} \cdots d\mathbf{r}_N \Psi^{\text{GS}*}(\mathbf{r}_1, ..., \mathbf{r}, ..., d\mathbf{r}_N)\Psi^{\text{GS}}(\mathbf{r}_1, ..., \mathbf{r}, ..., d\mathbf{r}_N). \tag{2.8}$$

Next Hohenberg and Kohn derive two main results:

(I) The mappings $D^{-1} : n^{\text{GS}} \rightarrow \Psi^{\text{GS}}$ and $C^{-1} : \Psi^{\text{GS}} \rightarrow v^{\text{ext}}$ exist and are unique and therefore the ground state energy can be expressed as a unique functional of the ground state density:

$$E\left[n^{\text{GS}}\right] = T\left[n^{\text{GS}}\right] + V^{\text{el-el}}\left[n^{\text{GS}}\right] + \int d\mathbf{r} v^{\text{ext}}(\mathbf{r}) n^{\text{GS}}(\mathbf{r}). \tag{2.9}$$

The sum of the first two terms in the RHS is often referred to as universal functional $F\left[n^{\text{GS}}(\mathbf{r})\right]$ since, unlike the last term, its form is the same for any many-body system.

[3] If the ground state is degenerate, the same density can be reproduced by different degenerate ground-state wave functions and therefore a unique functional $\Psi[n]$ does not exist. However, by definition these wave functions all yield the same energy, and the functional $E[n]$ continues to exist and to be minimized by n^{GS} (see Ref. [48])

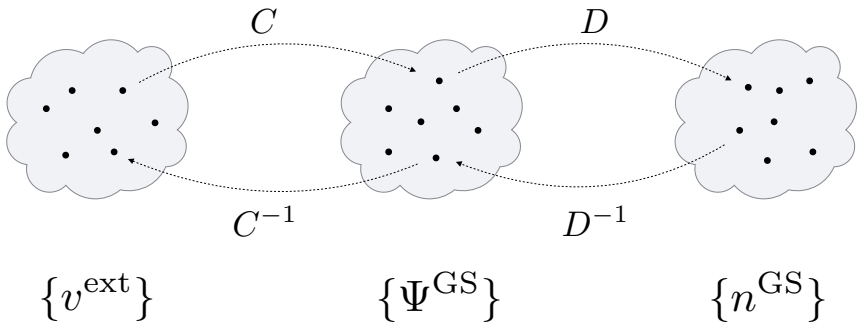

Figure 2.1: Schematic that illustrates the different mappings connecting the sets of external potentials, ground state wave functions and ground state densities. The Hohenberg-Kohn theorem proves the existence of the mapping C^{-1} and D^{-1}.

(II) The energy functional satisfies the variational property with respect to the density:

$$E\left[n^{\mathrm{GS}}\right] \leq E\left[n\right], \tag{2.10}$$

where $n(\mathbf{r})$ is a generic density. This comes really handy for the actual application of DFT. Indeed, even if a one to one mapping from the external potential to the ground state density exists, its explicit form is unknown and the ground state energy cannot be calculated directly. However thanks to the variational principle one can start with a "trial" density and find the the energy extremum:

$$\left.\frac{\delta E\left[n\right]}{\delta n}\right|_{n=n^{\mathrm{GS}}} = 0. \tag{2.11}$$

To conclude, the main points of the Hohenberg and Kohn theory are *invertibility*, *universality* and *variational access*. Finally it is extremely important to emphasize that no approximation has been performed, meaning that DFT is an exact ground state theory.

2.2.2 Kohn-Sham equation

As mentioned in the previous section, a direct minimization of the energy functional is a formidable task since the exact form of its universal part is unknown. In 1965 Kohn and Sham proposed an alternative route for the minimization [47] that determined the success of DFT and opened the possibility for application to real systems. The basic brilliant idea is the construction of a fictitious system of non-interacting electrons for

which energy minimization yields the same ground state density as the real interacting system.

As a starting point, it is customary to rewrite the energy functional in such a way that all the unknowns are contained in the so called *exchange-correlation* energy functional $E^{\mathrm{xc}}[n]$:

$$E[n] = T^{\mathrm{NI}}[n] + V^{\mathrm{H}}[n] + V^{\mathrm{ext}}[n] + E^{\mathrm{xc}}[n], \tag{2.12}$$

where T^{NI} is the kinetic energy of a non-interacting system of density $n(\mathbf{r})$ and $V^{\mathrm{H}}[n(\mathbf{r})] = \int d\mathbf{r}d\mathbf{r}' \frac{n(\mathbf{r})n(\mathbf{r}')}{|\mathbf{r}-\mathbf{r}'|}$ is the Hartree energy, i.e. the classical Coulomb electron-electron repulsion energy. Comparing eq. (2.12) to eq. (2.9), it is clear that $E^{\mathrm{xc}}[n] = T[n] - T^{NI}[n] - V^{\mathrm{H}}[n] + V^{\text{el-el}}[n]$. In the case of the artificial non-interacting system, the energy functional reads:

$$E^{NI}[n] = T^{NI}[n] + V^{\mathrm{KS}}[n], \tag{2.13}$$

with $V^{\mathrm{KS}}[n] = \int d\mathbf{r} v^{\mathrm{KS}}(\mathbf{r}) n(\mathbf{r})$ and v^{KS} the effective potential in which the independent particles are moving. Requiring that both the interacting and non-interacting energy functionals are minimized by the same density, Kohn and Sham found an expression for the effective potential:

$$v^{\mathrm{KS}}(\mathbf{r}) = v^{\mathrm{H}}(\mathbf{r}) + v^{\mathrm{ext}}(\mathbf{r}) + v^{\mathrm{xc}}(\mathbf{r}), \tag{2.14}$$

where each of the potentials is obtained as the functional derivative of their respecting energy functionals with respect to the density, e.g. $v^{\mathrm{xc}}(\mathbf{r}) = \frac{\delta E^{\mathrm{xc}}[n]}{\delta n(\mathbf{r})}$. Since the ground state density of the interacting system is by construction the same as the non-interacting one, it can be readily calculated as:

$$n(\mathbf{r}) \equiv n^{NI}(\mathbf{r}) = \sum_{i}^{occ} |\phi_i(\mathbf{r})|^2, \tag{2.15}$$

with the wave functions $\phi_i(\mathbf{r})$ are obtained from the single-particle Schrödinger equation for the non-interacting system:

$$\left[-\frac{\nabla^2}{2} + v^{\mathrm{KS}}(\mathbf{r}) \right] \phi_i(\mathbf{r}) = \epsilon_i \phi_i(\mathbf{r}). \tag{2.16}$$

Equations (2.14) to (2.16) are usually referred to as Kohn-Sham equations and their solution is much more practical than the minimization of the energy functional. Notice that because v^{H} and v^{xc} depend on n, which in turn depends on ϕ_i, eq. (2.16) is nonlinear and it has to be solved self-consistently until a certain criteria of convergence (usually on the density or on the energy) is satisfied.

One has to be extremely careful when attaching any meaning to the eigenvalues ϵ_i and wave functions ϕ_i obtained from the solution of eq. (2.16). Indeed, they are exclusively designed to give the right ground state density of the interacting system.

However, it is now accepted that Kohn-Sham energies and wave functions give a surprisingly good qualitative picture, especially in the case of solid state systems. For example band structure calculations are often found to agree qualitatively well with photoemission and inverse photoemission experimental data [49].

Despite the simplification brought by the Kohn-Sham approach, the main problem remains the knowledge of the exact expression for the exchange-correlation potential. The simplest, but yet one of the most successful approximations is the local-density approximation (LDA). In LDA one borrows the results for the exchange and correlation functional of the homogeneous electron gas (HEG) and assumes that the system at a given point in space $\mathbf{r}$ can be described as a HEG with density $n(\mathbf{r})$. The exchange-correlation functional then becomes:

$$E_{\mathrm{LDA}}^{\mathrm{xc}}[n] = \int d\mathbf{r} e_{\mathrm{HEG}}^{\mathrm{xc}}(n(\mathbf{r})), \tag{2.17}$$

where $e_{HEG}^{\mathrm{xc}}(n(\mathbf{r}))$ is the exchange-correlation energy per unit volume. The exchange part of the latter is known exactly [48]:

$$e_{HEG}^{x}(n) = -\frac{3}{4}\left(\frac{3}{\pi}\right)^{\frac{1}{3}} n^{\frac{4}{3}}. \tag{2.18}$$

The correlation part is a bit more tricky and an analytic form is not known. However thanks to the numerically exact Quantum Monte Carlo calculations by Ceperley and Alder [50] one can find a parametric expression for $e_{HEG}^{c}(n)$ from their numerical data.

Because of the local homogeneous gas approximation, LDA is expected to perform well for systems with slowly varying density. Surprisingly, LDA has been successfully applied to systems very far from an homogeneous electron gas, yet providing really good results. This is partially due to a systematic underestimation of E^{c} and an overestimation of E^{x} which results in an error cancellation [51]. However LDA is also known to overestimate bond energies and systematicly underestimate the electronic band gap [52]. The jungle of exchange-correlation functionals that try to improve over LDA is extremely vast, but since LDA is going to be the method of choice for practically all the calculations in this thesis, they will not be discussed. I find it important to mention, for later purposes, that a general problem of most of the functionals is the correct description of long range interactions, as in hydrogen or van der Waals bonds. In these cases one should rely on more refined methods based on many body perturbation theory as the GW approximation.

2.2.3 GPAW: Electronic Structure Calculator

One last source of approximation reside in the actual implementation of the Kohn-Sham equation and the choice of an appropriate basis set. The electronic structure calculator used throughout the thesis is GPAW (Grid-based Projector Augmented

Wave) [53, 54]. GPAW offers the possibility to solve the KS equations using three different basis sets, namely real space grid, plane-waves and localized atomic orbitals (LCAO) and all of them support periodic boundary conditions. One of the main challenges for an electronic structure calculator is the ability of describing the rapidly oscillating behavior of the wave functions in the region around the nuclei and the smoother behavior away from them. GPAW does that using the projector augmented wave (PAW) method proposed by Blöchl [55]. In this approach the space is divided up in two different regions: augmentation spheres around each nuclei, where the wave functions are represented in an atomic-like basis set and interstitial region where one can define smooth wave functions which are more conveniently expandable in one of the basis sets mentioned above. In practice one also employs a frozen core approximation where, the core states are assumed to be localized inside the augmentation sphere and not perturbed by the environment. In this way the core states are equivalent to the isolated atoms ones and can be calculated solving the KS equation with a spherically symmetric KS potential once for each element. This approximation is supported by the fact that the valence electrons responsible for most of the physical and chemical properties of the material, whereas the core electrons are mainly unperturbed by the chemical environment. The nice feature of the PAW formalism is that one always has access to the all-electron wave functions, just by means of a linear transformation of the smooth wave functions.

GPAW is not only a DFT calculator, indeed it offers many different features that build upon DFT as for example the linear response modules [56] that allows the users to calculate the dielectric response of a any given material, and many-body perturbation theory methods such as GW approximation [57,58] and the Bethe-Salpeter equation (BSE) [59].

2.3 Many Body Perturbation Theory

In the previous section I mentioned that even though DFT is only meant to describe ground state properties, the KS eigenvalues and eigenfunctions usually give a good qualitative description of the real excitations in the material. However when predicting material properties for application in actual devices, accuracy in quantities such as electronic band gaps, band alignment or optical spectra is strictly necessary and it cannot be achieved via DFT unless one is able to cook up ad hoc exchange-correlation functionals. From an even more fundamental point of view, it is not clear how the single-particle KS framework can be adapted to account for many-body effects such as excitons, which are central in this thesis. A systematic way to overcome the limitations of DFT, and for example achieve better accuracy in the quantities listed above, is provided by many body perturbation theory (MBPT). MBPT can be formulated either by means of Feynman diagrams [42] or by following Schwinger's functional derivatives based approach [42, 60]. Following the latter approach, I will show how it is possible to arrive to a set of equations, the Hedin equations, that provides a unified exact framework for the description of in or out-of-equilibrium quantum sys-

tems. In particular this will lead to the *GW* approximation for accurate calculations of electronic excitations and (in the next chapter) the Bethe-Salpeter equation for the determination of excitonic effects.

2.3.1 One-particle Green's Function

No matter the formulation, the building block of MBPT is the *one-particle* Green's function, defined as the expectation value of time-ordered product of creation and annihilation operators in the following way:

$$G(1;2) \equiv \frac{1}{\mathrm{i}}\langle 0|T\left\{\hat{\psi}_{\mathrm{H}}(1)\hat{\psi}^{\dagger}_{\mathrm{H}}(2)\right\}|0\rangle, \tag{2.19}$$

where $|0\rangle$ is the initial ($t = t_0$) N-particles state, T is the *time-ordering* operator that rearranges the operators in chronological order with later times to the left and we use the short-hand notation $j = \mathbf{x}_j t_j$, with $\mathbf{x}$ a collective space-spin variable. Notice that the subscript H indicates that the field operators are taken in the *Heisenberg picture*. If t_1 is later than t_2, the Green function describes the evolution of a $(N+1)$-particles system, created by adding a particle at 2, until the particle is removed at 1. For the opposite order it describes, instead, a process in which a particle is removed (a hole is created) in 1 and the resulting $(N-1)$-particle system is allowed to evolve till a particle is added back (a hole is destroyed) in 2. In other words the Green function can be interpreted as the probability amplitude for a particle (hole) to go from 1 (2) to 2 (1).

The one-particle Green function is a key quantity in many body perturbation theory because it provides a full access to the expectation value of any one-particle operator. Consider, indeed, an operator $\hat{O}$, diagonal in spin for ease of notation:

$$\hat{O}(t) \equiv \int d\mathbf{x}d\mathbf{x}'\hat{\psi}^{\dagger}(\mathbf{x})\langle\mathbf{x}|\hat{O}(t)|\mathbf{x}'\rangle\hat{\psi}(\mathbf{x}') = \int d\mathbf{x}O(\mathbf{x},t)\hat{\psi}^{\dagger}(\mathbf{x})\hat{\psi}(\mathbf{x}). \tag{2.20}$$

then its expectation value can be expressed using the one-particle Green function as:

$$O(t) = -\mathrm{i}\int d\mathbf{x}\left[O(\mathbf{x},t)G(\mathbf{x},t;\mathbf{x}',t^{+})\right]_{\mathbf{x}=\mathbf{x}'}, \tag{2.21}$$

where with t^{+} we intend a time infinitesimally later than t.

The definition of the Green function in eq. (2.19) is often not convenient for its actual calculation. Another way the Green function can be defined is through its equations of motion. The latter follow directly from the Heisenberg equation[4] for the

[4]Operators in the Heisenberg picture satisfy the well-known Heisenberg equation:

$$\mathrm{i}\frac{d}{dt}\hat{O}_{\mathrm{H}}(t) = \left[\hat{O}_{\mathrm{H}}(t),\hat{H}_{\mathrm{H}}(t)\right]_{-} + \mathrm{i}\frac{\partial}{\partial t}\hat{O}_{\mathrm{H}}(t), \tag{2.22}$$

where the partial derivative is with respect to the explicit t-dependence of the operator $\hat{O}(t)$

field operators, and they read [42]:

$$\mathrm{i}\,\frac{d}{dt_1}G(1;2) - \int d3h(1;3)G(3;2) = \delta(1;2) - \mathrm{i}\int d3v(1;3)G_2(1,3;2,3^+), \tag{2.23}$$

$$-\,\mathrm{i}\,\frac{d}{dt_2}G(1;2) - \int d3G(1;3)h(3;2) = \delta(1;2) - \mathrm{i}\int d3G_2(1,3^-;2,3)v(3;2), \tag{2.24}$$

where I introduced the generalized delta-function $\delta(1;2) = \delta(\mathbf{x}_1 - \mathbf{x}_2)\delta(t_1 - t_2)$ and defined the *two-particles* Green function according to

$$G_2(1,2;1',2') = -\langle 0|T\left[\hat{\psi}_{\mathrm{H}}(1)\hat{\psi}_{\mathrm{H}}(2)\hat{\psi}^{\dagger}_{\mathrm{H}}(2')\hat{\psi}^{\dagger}_{\mathrm{H}}(1')\right]|0\rangle. \tag{2.25}$$

The notation $j^{\pm}$ indicates that the time-argument is taken infinitesimally later $(+)$ or earlier $(-)$ than j, keeping in mind that the limit has to be taken after the application of the time-ordering operator.

The two-particles Green function is composed of four field operators and accounts for the two-particle scattering processes; depending on their order, it can be thought as a quantity describing the propagation of two electrons, two holes or an electron and a hole within an interacting system.

Equations (2.23) and (2.24) are integro-differential equations and their solution has to satisfy Kubo-Martin-Schwinger (KMS) boundary conditions [61, 62]. To solve eqs. (2.23) and (2.24) the two-particle Green function is required. The two-particle Green function, in turn, satisfies its own equations of motion. These, however, involve the three-particle Green function whose equations of motion present the four-particle Green function and so on. Eventually, one generates an infinite hierarchy for the N-particles Green functions

$$G_n(1,...,n;1',...,n') = \frac{1}{\mathrm{i}^n}\langle 0|T\left[\hat{\psi}_{\mathrm{H}}(1)\cdots\hat{\psi}_{\mathrm{H}}(n)\hat{\psi}^{\dagger}_{\mathrm{H}}(n')\cdots\hat{\psi}^{\dagger}_{\mathrm{H}}(1')\right]|0\rangle, \tag{2.26}$$

which is known in the literature as the *Martin-Schwinger Hierarchy* (MSH) [42, 61]. The formal solution to the MSH can be found through Wick's theorem [42, 43, 63], however one way to truncate this hierarchy is to introduce a quantity called *self-energy*:

$$\int d3\Sigma(1;3)G(3;2) = -\mathrm{i}\int d3v(1;3)G_2(1,3;2,3^+). \tag{2.27}$$

The equations of motion for $G(1;2)$ can then be rewritten in the following way:

$$\mathrm{i}\,\frac{d}{dt_1}G(1;2) - \int d3\left[h(1;3) + \Sigma(1;3)\right]G(3;2) = \delta(1;2), \tag{2.28}$$

$$-\,\mathrm{i}\,\frac{d}{dt_2}G(1;2) - \int d3G(1;3)\left[h(3;2) + \Sigma(3;2)\right] = \delta(1;2). \tag{2.29}$$

From these equations we can give to Σ the following physical interpretation: it represents a correction to the single particle Hamiltonian due to the inter-particle interaction. Accordingly, $h + \Sigma$ can be considered as a kind of self-consistent Hamiltonian.

It is worth noting, that in general, $\Sigma(1;3)$ is not local in time and space; this means that corrections to the single particle Hamiltonian in a specific spatial-time coordinate depend also on what happened in another point at a different time.

Equation (2.28) and eq. (2.29) are often expressed in their integral form, the Dyson equation for the Green's function:

$$G(1;2) = G_0(1;2) + \int d3d4 G_0(1;3)\Sigma(3;4)G(4;2), \tag{2.30}$$

where $G_0(1;2)$ is the non interacting particles Green's function that satisfies the Green's function equation of motion with $\Sigma = 0$. The equation above can be readily verified by acting on eq. (2.28) with $[-\mathrm{i}\,(1';1)\frac{\overrightarrow{d}}{dt_1} - h(1';1)]$ from the left and integrating over 1, or by acting on eq. (2.29) from the right with $[-\mathrm{i}\,\frac{\overleftarrow{d}}{dt_2}(2;2') - h(2;2')]$ and integrating over 2.

It is easy to verify that for $G(1;2) = G(\mathbf{x}_1, \mathbf{x}_2, t_1 - t_2)$, i.e. the time-dependence is only on the time difference, eq. (2.28) and eq. (2.29) are equivalent. This is the case for time independent hamiltonians or for steady state regimes. Under this condition it is particularly convenient to use the Lehman representation [64] in frequency space of the Green's function:

$$G(\mathbf{x}_1, \mathbf{x}_2, \omega) = \sum_i \frac{\phi_i^{\mathrm{QP}}(\mathbf{x}_1)\phi_i^{*\ QP}(\mathbf{x}_2)}{\omega - \epsilon_i^{\mathrm{QP}} + \mathrm{i}\eta\,\mathrm{sgn}(\epsilon_i - \mu)}, \tag{2.31}$$

with μ the chemical potential and ϵ_i^{QP}, $\phi_i^{\mathrm{QP}}(\mathbf{x})$ the quasi-particle (QP) eigenvalues and eigenfunctions specified in the following. Such a representation can be directly obtained from eq. (2.19), by inserting the completeness relation in the $N \pm 1$-particles Hilbert space, i.e. $\sum_i |\Psi_i^{N\pm1}\rangle\langle\Psi_i^{N\pm1}|$, Fourier transforming to frequency space and by defining the following quantities:

$$\begin{aligned} \epsilon_i^{\mathrm{QP}} &= \begin{cases} E_i^{N+1} - E_0 & \epsilon_i > \mu \\ E_0 - E_i^{N-1} & \epsilon_i < \mu \end{cases}, \\ \phi_i^{\mathrm{QP}}(\mathbf{x}) &= \begin{cases} \langle 0|\hat{\psi}(\mathbf{x})|\Psi_i^{N+1}\rangle & \epsilon_i > \mu \\ \langle \Psi_i^{N-1}|\hat{\psi}(\mathbf{x})|0\rangle & \epsilon_i < \mu \end{cases}. \end{aligned} \tag{2.32}$$

Inserting Lehman's representation in eq. (2.28) one obtains the quasi-particle equation:

$$h(\mathbf{x})\phi_i^{\mathrm{QP}}(\mathbf{x}) + \int dx' \Sigma(\mathbf{x}, \mathbf{x}', \epsilon_i^{\mathrm{QP}})\phi_i^{\mathrm{QP}}(\mathbf{x}') = \epsilon_i^{\mathrm{QP}}\phi_i^{\mathrm{QP}}(\mathbf{x}). \tag{2.33}$$

This results highlights the meaning of the different quantities in the Lehman representation. Indeed, the equation has the structure of a single-electron Schrödinger problem with a non-local potential, the self-energy. The latter carries information on the correlation to the other electrons in the material and therefore the ϵ_i^{QP} and $\phi_i^{\mathrm{QP}}(\mathbf{x})$ can be thought as eigenvalues and wave functions of a quasi-particle, i.e. an

independent particle dressed with the correlation to other electrons. Notice that since the self-energy is in principle non-hermitian the eigenvalues ϵ_i^{QP} may have an imaginary part, indicating that the quasi-particle has a finite lifetime. This is because a single particle state cannot describe the real excited state of the many-body system.

2.3.2 Hedin's Equations

The next step is to find a way to calculate the self-energy. Without loss of generality one can introduce a perturbing field $\varphi(\hat{r})$ to the single-particle Hamiltonian $\hat{h}$ in eq. (2.5). Such a potential is a mathematical tool that is set to zero at the end of the derivation, but it can be safely interpreted as an external field that polarizes the material. Having this in mind, it is convenient to define the following "classically" inspired quantities:

$$\textbf{Total classical potential}: \qquad \Phi(1) = \varphi(1) + \int d2 v(1,2) n(2), \tag{2.34}$$

$$\textbf{Reducible polarizability}: \qquad \chi(1;2) = \frac{\delta n(1)}{\delta \varphi(2)}, \tag{2.35}$$

$$\textbf{Irreducible polarizability}: \qquad P(1;2) = \frac{\delta n(1)}{\delta \Phi(2)}, \tag{2.36}$$

$$\textbf{Inverse dielectric function}: \qquad \epsilon^{-1}(1;2) = \frac{\delta \Phi(1)}{\delta \varphi(2)}, \tag{2.37}$$

notice that the electron density is directly related to the Green function, indeed $n(1) = -\mathrm{i}G(1:1^+)$[5]. Going in order, Φ represents the classical total potential generated by the perturbation, which is nothing else than the sum of the perturbation itself and the Hartree potential. The irreducible and reducible polarizabilities describe how the electron density varies as a consequence of the external perturbation or the variation of the total potential respectively. These two functions are closely related by a Dyson equation, indeed by applying the functional chain rule and using the definitions above one has:

$$\begin{aligned} \chi(1;2) = \frac{\delta n(1)}{\delta \varphi(2)} &= \int d3 \frac{\delta n(1)}{\delta \Phi(3)} \frac{\delta \Phi(3)}{\delta \varphi(2)} \\ &= \int d3 P(1;3) \left[\delta(3;2) + \int d4 v(3,4) \chi(4;2) \right] \\ &= P(1;2) + \int d3 d4 P(1;3) v(3,4) \chi(4;2). \end{aligned} \tag{2.38}$$

The dielectric function, following the standard definition in electrodynamics, relates the total potential to the perturbation. On the same fashion as for the equation above

[5] This is easy to see, since the expectation value of the density operator is $n(1) = \langle 0 | \hat{\psi}^\dagger_{\mathrm{H}}(1) \hat{\psi}_{\mathrm{H}}(1) | 0 \rangle$

it can be proved that the dielectric function is related to the polarizabilities by the following equations:

$$\epsilon(1;2) = \delta(1;2) - \int d3v(1,3)P(3;2), \tag{2.39}$$

$$\epsilon^{-1}(1;2) = \delta(1;2) + \int d3v(1,3)\chi(3;2). \tag{2.40}$$

As I will emphasize in the next chapter, these quantities are key for understanding the response properties of a material.

Differently from the diagrammatic perturbation theory where the perturbation is the bare Coulomb potential $v(1;2)$, in Hedin's approach [65], the perturbative expansion is over the screened potential defined as:

$$W(1;2) = \int d3v(1;3)\epsilon^{-1}(3;1). \tag{2.41}$$

Such an approach goes along with the idea that the actual interaction between two charges in a material is screened by all the other surrounding charges and therefore $W(1;2)$ is the significant interaction rather than v(1;2).

The last quantity that needs to be introduced is a rather abstract one and it takes the name of *vertex*:

$$\Gamma(1,2;3) = -\frac{\delta G^{-1}(1;2)}{\delta\Phi(3)}, \tag{2.42}$$

where the inverse Green's function $G^{-1}(1;2)$ is defined so that the relation $\int d3G(1;3)G^{-1}(3;2) = \int d3G^{-1}(1;3)G(3;2) = \delta(1;2)$ holds.

Using all the above definitions and playing around with functional differentiation one can arrive to a closed set of integral equations, namely Hedin's equation. Since their derivation can be extensively found elsewhere and it is not a result of this thesis I will spare it to the reader and refer to Ref. [66,67]. Hedin's equations read as follows:

$$\begin{aligned}
G(1;2) &= G_0(1;2) + \int d3d4G_0(1;3)\left(v^{\mathrm{H}}(3)\delta(3,4) + \Sigma^{\mathrm{xc}}(3;4)\right)G(4;2),\\
P(1;2) &= -\mathrm{i}\int d3d4G(1;3)G(4;1)\Gamma(3,4;2),\\
W(1;2) &= v(1,2) + \int d3d4v(1;3)P(3;4)W(4;2),\\
\Sigma^{\mathrm{xc}}(1;2) &= \mathrm{i}\int d3d4G(1;4)W(1^+,3)\Gamma(4,2;3),\\
\Gamma(1,2;3) &= \delta(1;3)\delta(2;3) + \int d4d5d6d7\frac{\delta\Sigma^{\mathrm{xc}}(1;2)}{\delta G(4;5)}G(4;6)G(7;5)\Gamma(6,7;3).
\end{aligned} \tag{2.43}$$

The problem of finding the single-particle is rephrased in terms of these five interdependent equations. Because of the interdependence, the solution has to be found

self-consistently, i.e. starting with an approximation for one or more of the quantities above and then iterate Hedin's equation until a desired level of approximation is reached. To illustrate how this works in practice, I show in the following, how to arrive to probably most known approximation to Hedin's equations: the GW approximation.

2.3.2.1 GW

As mentioned before one has to start with a guess for one of the quantities in eq. (2.43). The simplest approximation for the vertex function is to retain only its trivial part:

$$\Gamma(1,2;3) \simeq \delta(1;2)\delta(2;3), \tag{2.44}$$

which corresponds to neglecting the variation to the self-energy due to the polarization of the material. Plugging this vertex into the expression for the irreducible polarizability one gets:

$$P(1;2) = -\mathrm{i}G(2;1)G(1;2). \tag{2.45}$$

The form of the polarization corresponds to the so called *Random Phase Approximation*. Finally plugging the vertex in the expression of the exchange-correlation self-energy one has:

$$\Sigma^{\mathrm{xc}}(1;2) = \mathrm{i}G(1;2)W(1;2), \tag{2.46}$$

which obviously clarifies the name of GW approximation. Fourier transforming to frequency space gives:

$$\Sigma^{\mathrm{xc}}(\mathbf{x},\mathbf{x}',\omega) = \frac{\mathrm{i}}{2\pi}\int d\omega' G(\mathbf{x},\mathbf{x}',\omega+\omega')W(\mathbf{x},\mathbf{x}',\omega) \tag{2.47}$$

and this expression can then be used directly in the QP eq. (2.33).

In principle the QP equation could be solved self-consistently (scGW method) [67] just as in the case of the KS equation, however in practice this is a formidable computational task and it is preferred to recur to further approximation. To this scope, assuming that the KS equation is already a good description of the system, the exchange and correlation potential $v^{\mathrm{KS}}(\mathbf{x})$ can be added and subtracted to the QP equation as follows:

$$\begin{aligned}\left[h(\mathbf{x}) + v^{\mathrm{KS}}(\mathbf{x})\right]\phi_i^{\mathrm{QP}}(\mathbf{x}) + \int dx' \left[\Sigma(\mathbf{x},\mathbf{x}',\epsilon_i^{\mathrm{QP}}) - v^{\mathrm{KS}}(\mathbf{x})\delta(\mathbf{x}-\mathbf{x}')\right]\phi_i^{\mathrm{QP}}(\mathbf{x}') = \\ = \epsilon_i^{\mathrm{QP}}\phi_i^{\mathrm{QP}}(\mathbf{x}).\end{aligned} \tag{2.48}$$

Now, since $\Sigma - v^{\mathrm{KS}}$ is expected to be small, one can calculate the correction to the KS eigenvalues by means of first order perturbation theory, i.e:

$$\epsilon_i^{\mathrm{QP}} \simeq \epsilon_i^{\mathrm{KS}} - \langle\phi_i^{\mathrm{KS}}|\hat{\Sigma}(\epsilon_i^{\mathrm{QP}}) - \hat{v}^{\mathrm{KS}}|\phi_i^{\mathrm{KS}}\rangle, \tag{2.49}$$

where the self-energy at the QP eigenvalue can be obtained from a first order expansion: $\hat{\Sigma}(\epsilon_i^{\mathrm{QP}}) = \hat{\Sigma}(\epsilon_i^{\mathrm{KS}}) + (\epsilon_i^{\mathrm{QP}} - \epsilon_i^{\mathrm{KS}}) \left.\frac{\partial\hat{\Sigma}(\omega)}{\partial\omega}\right|_{\omega=\epsilon_i^{\mathrm{KS}}}$.

Obviously the self-energy is now meant to be calculated by using KS eigenvalues and wave functions. This method takes the name of G_0W_0 and over the years it has been shown to be extremely successful at describing band gaps and electronic excitation of a large variety of materials ranging from molecules, alkaline and transition metals, semiconductors, 2D materials and so on. The key feature of the GW approximation is the inclusion of the long-range electronic screening effect, which is completely absent in standard KS exchange correlation functionals. This has for example made possible the description of image charge effects for molecules on surfaces [68,69] and the possibility of accounting for long range screening is an important feature for describing van der Waals heterostructures as I will describe later.

2.3.3 Connection to DFT

In the last part of the chapter I would like to briefly illustrate how to link the KS formalism to the results of many-body perturbation theory described above. First of all it is convenient to define the Kohn-Sham Green function as the solution to the following equation:

$$\left[\mathrm{i}\frac{d}{dt_1} - h(\mathbf{x}) - v^{\mathrm{H}}(1) - v^{\mathrm{xc}}(1)\right] G^{\mathrm{KS}}(1;2) = \delta(1;2). \tag{2.50}$$

Adding and subtracting $v^{\mathrm{H}}(1)+v^{\mathrm{xc}}(1)$ to eq. (2.28) and integrating, similarly to what is done to obtain eq. (2.30), a Dyson-like equation can be found, and in frequency space it reads:

$$\begin{aligned} G(\mathbf{x}_1,\mathbf{x}_2,\omega) &= G^{\mathrm{KS}}(\mathbf{x}_1,\mathbf{x}_2,\omega)+ \\ &+ \int d\mathbf{x}_3 d\mathbf{x}_4 G^{\mathrm{KS}}(\mathbf{x}_1,\mathbf{x}_3,\omega)[\Sigma^{\mathrm{xc}}(\mathbf{x}_3,\mathbf{x}_4,\omega) - v^{\mathrm{xc}}(\mathbf{x}_3)\delta(\mathbf{x}_3-\mathbf{x}_4)]G(\mathbf{x}_4,\mathbf{x}_2,\omega). \end{aligned} \tag{2.51}$$

Now, since the full Green function and the KS one are supposed to give the same electron density $n(\mathbf{x})$ by construction of the KS problem, we can write:

$$n(\mathbf{x}) = -\mathrm{i}\int \frac{d\omega}{2\pi} e^{\mathrm{i}\omega\delta} G(\mathbf{x},\mathbf{x},\omega) = -\mathrm{i}\int \frac{d\omega}{2\pi} e^{\mathrm{i}\omega\delta} G^{\mathrm{KS}}(\mathbf{x},\mathbf{x},\omega), \tag{2.52}$$

with $e^{\mathrm{i}\omega\delta}$ to ensure that in the integration the contour has to be closed in the upper half-plane. With this condition in mind, it is clear that integrating eq. (2.51) by $\int \frac{d\omega}{2\pi}$ and setting $\mathbf{x}_1 = \mathbf{x}_2$, the following identity has to hold:

$$\begin{aligned} &\int d\mathbf{x}_3 v^{\mathrm{xc}}(\mathbf{x}_3) \int d\omega e^{\mathrm{i}\omega\delta} G^{\mathrm{KS}}(\mathbf{x}_1,\mathbf{x}_3,\omega) G(\mathbf{x}_3,\mathbf{x}_1,\omega) = \\ &= \int d\omega \int d\mathbf{x}_3 d\mathbf{x}_4 e^{\mathrm{i}\omega\delta} G^{\mathrm{KS}}(\mathbf{x}_1,\mathbf{x}_3,\omega)\Sigma^{\mathrm{xc}}(\mathbf{x}_3,\mathbf{x}_4,\omega)G(\mathbf{x}_4,\mathbf{x}_2,\omega). \end{aligned} \tag{2.53}$$

The last equation takes the name of Sham-Schlüter equation and it formally connects the exchange correlation potential to the many-body self-energy [70]. Combined with Hedin's equation, it provides a systematic way to find approximations for the tedious exchange-correlation potential. Unfortunately the v^{xc} that can be found from MBPT are of high complexity and lead to an unbearable computational cost. Such an approach, indeed, has only been applied to atoms [71] and simple solids [72].

CHAPTER 3

Dielectric Response of a Material

Applying an external perturbation is the way to probe the quantum mechanical properties of a system. That is, for example, what we do in our everyday life whenever we shine light on a material. In that case, the electromagnetic perturbation, by coupling with the electrons, gives us access to the intimate nature of the electronic excitations and provides a solid way to validate the theoretical description of the system. In turn, understanding the way a material responds to an external perturbation from a microscopic point of view allows for rational and clever design of new materials. In this chapter I will describe the concept of dielectric function and its key role in describing the response of a material. A particular focus will be given to the connection between its microscopic and macroscopic definition and how such a connection has to be adapted when dealing with 2D systems. The dielectric function plays a central role also in the description of optical response, however, because of the importance of excitonic effects in 2D materials, a single-particle picture is no longer enough and one has to rely on two-particle based many-body methods, such as the Bethe-Salpeter equation.

3.1 Linear Response Theory: a brief overview

Let us apply a perturbation $\hat{H}'(t)$ to a system described by the Hamiltonian in eq. (2.5). For simplicity, I only consider a perturbation generated by a longitudinal field so that $\hat{H}'(t)$ can be written in terms of the density operator (neglecting spin variables: $\mathbf{x} \to \mathbf{r}$):

$$\hat{H}'(t) = \int d\mathbf{r} \hat{n}(\mathbf{r}) v_{\text{ext}}(\mathbf{r}, t). \tag{3.1}$$

Considering only longitudinal fields might seem like an extreme restriction, but, as I will discuss in section 3.4, it is what it takes to describe the kind of response relevant for the problems within this thesis including the response to electromagnetic radiation in the long wavelength limit.

If the magnitude of the perturbation is small enough, the variation in the expectation value of the density operator can be calculated by applying Kubo's linear response formula[1]:

$$\delta n(\mathbf{r},t) = \int_{t_0}^{t} dt' \int d\mathbf{r} \chi^{\mathrm{R}}(\mathbf{r},t;\mathbf{r}',t') v_{\mathrm{ext}}(\mathbf{r}',t'), \tag{3.2}$$

where the so-called density-density correlator is given by:

$$\chi^{\mathrm{R}}(\mathbf{r},t;\mathbf{r}',t') = -\mathrm{i}\theta(t-t')\langle 0| \left[\hat{n}_{\mathrm{H}}(\mathbf{r},t), \hat{n}_{\mathrm{H}}(\mathbf{r}',t')\right]_{-} |0\rangle. \tag{3.3}$$

The choice of the symbol χ is not random. Indeed one can show that the density-density correlation function is nothing else than the retarded component[2] of the reducible polarizability introduced in section 2.3.2. In general any kind of physical response function is a retarded function as a consequence of the causality principle [42], for which the response of the system has to be non-zero only after the perturbation is applied. Mathematically speaking, causality is guaranteed by the presence of a Heaviside function, exactly as in eq. (3.3).

The actual calculation of χ requires some approximations. As explained in section 2.3.2, χ is related to the irreducible polarizability P by a Dyson equation. As in the GW method, the random-phase approximation (RPA) for P is considered. Furthermore, assuming that the system is well described at the Kohn-Sham level, the dressed Green functions in eq. (2.45) can be replaced with the Kohn-Sham ones. With homogeneity in time, i.e. $\chi^{\mathrm{R}}(\mathbf{r},t;\mathbf{r}',t') = \chi^{\mathrm{R}}(\mathbf{r},\mathbf{r}',t-t')$, an explicit expression for the retarded component of P can be found, and in frequency space it reads [56]

$$\begin{aligned} P^{\mathrm{R}}(\mathbf{r},\mathbf{r}',\omega) &\approx 2\sum_{n,n'}\sum_{\mathbf{kq}}^{\mathrm{BZ}} (f_{n\mathbf{k}} - f_{n'\mathbf{k}+\mathbf{q}}) \frac{\phi^{*\,\mathrm{KS}}_{n\mathbf{k}}(\mathbf{r})\phi^{\mathrm{KS}}_{n'\mathbf{k}+\mathbf{q}}(\mathbf{r})\phi^{\mathrm{KS}}_{n\mathbf{k}}(\mathbf{r}')\phi^{*\,\mathrm{KS}}_{n'\mathbf{k}+\mathbf{q}}(\mathbf{r}')}{\omega + \epsilon^{\mathrm{KS}}_{n\mathbf{k}} - \epsilon^{\mathrm{KS}}_{n'\mathbf{k}+\mathbf{q}} + \mathrm{i}\eta} \\ &\equiv \chi^{0}(\mathbf{r},\mathbf{r}',\omega). \end{aligned} \tag{3.5}$$

with the factor two accounting for the spin, the occupation factors $f_{n\mathbf{k}}$ being either 1 or 0 (at zero Temperature) and $+\mathrm{i}\eta$ an infinitesimal imaginary number guaranteeing the analyticity property of a retarded function. The reason why I have not use the

[1] The variation of the expectation value of an operator $\hat{O}(t)$ in linear response approximation, is given by: $\delta O(t) = -\mathrm{i}\int_{t_0}^{t} dt' \langle 0| \left[\hat{O}_{\mathrm{H}}(t'), \hat{H}'_{\mathrm{H}}(t')\right]_{-} |0\rangle$. This formula takes the name of Kubo's formula [42, 62]

[2] In general the retarded component of a correlator of the form $C(1;2) = \langle 0|T\left[\hat{O}_{\mathrm{H}}(1)\hat{O}_{\mathrm{H}}(2)'\right]|0\rangle$ is defined as:

$$C^{\mathrm{R}}(1;2) = \theta(t_1 - t_2)\left[\langle 0|\hat{O}_{\mathrm{H}}(1)\hat{O}_{\mathrm{H}}(2)'|0\rangle - \hat{O}_{\mathrm{H}}(2)'\hat{O}_{\mathrm{H}}(1)|0\rangle\right]. \tag{3.4}$$

equal sign in the equation above is to stress that using the KS eigenvalues and wave functions is an approximation. The expression above represents the independent-particle approximation for the irreducible polarization and is commonly denoted with χ^0, known as independent-particle polarizability. Notice that, since the materials investigated in this thesis are periodic in at least two dimensions, I specialized the expression above to Bloch type wave functions.

Another fundamental response function is the one that relates the total potential to the external one:

$$v_{\text{tot}}(\mathbf{r},t) = \int_{t_0}^{t} dt' \int d\mathbf{r} \epsilon^{-1\,\text{R}}(\mathbf{r},t;\mathbf{r}',t') v_{\text{ext}}(\mathbf{r}',t'). \tag{3.6}$$

Once again, the choice of the notation $\epsilon^{-1\,\text{R}}$ is not random since one can show that such a response function is the retarded component of the inverse dielectric function introduced in section 2.3.2. This also means that one can apply eqs. (2.39) and (2.40) to calculate $\epsilon^{-1\,\text{R}}$ from P^{R} or χ^{R} respectively. This is usually done within the RPA.

To illustrate the effect of dielectric screening, I show in fig. 3.1 how an external potential of the form $v_{\text{ext}}(\mathbf{r},t) = v_0 e^{i\mathbf{q}_\parallel \cdot \mathbf{r}_\parallel}$ is screened by a monolayer MoS_2 along the out-of-plane direction. As expected the total potential is reduced inside the material, where the external perturbation is screened by the electrons, and it recovers the external potential values only far away from it.

In the rest of the thesis, I will drop the superscript R as it will be clear from the context whether or not it is the retarded component of a given function that is needed.

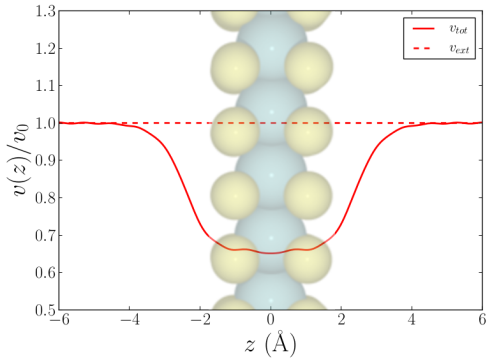

Figure 3.1: Illustration of the dielectric screening in a MoS_2 layer. An external perturbation of the form $v_{\text{ext}}(\mathbf{r},t) = v_0 e^{i\mathbf{q}_\parallel \cdot \mathbf{r}_\parallel}$ with $q_\parallel = 1.5 a.u.$ is applied and because of electronic screening the total microscopic potential inside the material is reduced.

3.2 Response Functions in Periodic Systems

Since all the systems treated in this thesis are periodic either in two or three dimensions, it is convenient to express the quantities introduced in the previous section in a plane-wave basis. This is, indeed, the basis set of choice in GPAW when it comes to the calculation of linear response functions. In general any function associated with a periodic system has to satisfy the translational symmetry of the lattice. In the case of a two spatial variable functions, this means that $f(\mathbf{r},\mathbf{r}') = f(\mathbf{r}+\mathbf{R},\mathbf{r}'+\mathbf{R}')$, with $\mathbf{R}$ and $\mathbf{R}'$ lattice vectors. If such a condition is satisfied, then $f(\mathbf{r},\mathbf{r}')$ can be expressed through its inverse Fourier transform as follows:

$$f(\mathbf{r},\mathbf{r}',\omega) = \frac{1}{\Omega}\sum_{\mathbf{G},\mathbf{G}'}\sum_{\mathbf{q}}^{\mathrm{BZ}} e^{i(\mathbf{G}+\mathbf{q})\mathbf{r}} f_{\mathbf{G},\mathbf{G}'}(\mathbf{q}) e^{-i(\mathbf{q}+\mathbf{G}')\mathbf{r}'}, \tag{3.7}$$

where Ω is the volume of the primitive cell, $\mathbf{G}$ is a reciprocal lattice vector and $\mathbf{q}$ is a vector in the first Brillouin Zone (BZ). Using this result, χ^0 can be expressed in a plane wave representation [73, 74]:

$$\chi^0_{\mathbf{G}\mathbf{G}'}(\mathbf{q},\omega) = \frac{2}{\Omega}\sum_{n,n'}\sum_{\mathbf{k}}^{\mathrm{BZ}}(f_{n\mathbf{k}} - f_{n'\mathbf{k}+\mathbf{q}})\frac{\rho_{n\mathbf{k},n'\mathbf{k}+\mathbf{q}}(\mathbf{G})\rho^*_{n\mathbf{k},n'\mathbf{k}+\mathbf{q}}(\mathbf{G}')}{\omega + \epsilon^{\mathrm{KS}}_{n\mathbf{k}} - \epsilon^{\mathrm{KS}}_{n'\mathbf{k}+\mathbf{q}} + \mathrm{i}\eta}, \tag{3.8}$$

with $\rho_{n\mathbf{k},n'\mathbf{k}+\mathbf{q}}(\mathbf{G}) = \langle\phi^{\mathrm{KS}}_{n\mathbf{k}}|e^{\mathrm{i}(\mathbf{q}+\mathbf{G})\cdot\mathbf{r}}|\phi^{\mathrm{KS}}_{n'\mathbf{k}+\mathbf{q}}\rangle$ the so called charge-density matrix.

The RPA expression in eq. (2.39) for the dielectric matrix can be readily obtained in a plane wave representation as well:

$$\epsilon_{\mathbf{G},\mathbf{G}'}(\mathbf{q},\omega) = \delta_{\mathbf{G},\mathbf{G}'} - v_{\mathrm{C}}(\mathbf{q}+\mathbf{G})\chi^0_{\mathbf{G},\mathbf{G}'}(\mathbf{q},\omega), \tag{3.9}$$

where $v_{\mathrm{C}}(\mathbf{q}+\mathbf{G})$ is the Fourier transform of the Coulomb potential and χ^0 is the independent-particles polarizability introduced in eq. (3.5). The relation between the total and external microscopic potential is conveniently refurmulated as:

$$v^{\mathrm{tot}}_{\mathbf{G}}(\mathbf{q},\omega) = \sum_{\mathbf{G}'}\epsilon^{-1}_{\mathbf{G},\mathbf{G}'}(\mathbf{q},\omega)v^{\mathrm{ext}}_{\mathbf{G}}(\mathbf{q},\omega), \tag{3.10}$$

which is the Fourier space version of eq. (3.6).

It is instructive to analyze the long wavelength limit ($\mathbf{q}\to 0$) of $\chi^0_{0\,0}(\mathbf{q},\omega=0)$, i.e. the "DC" component of the static independent particle polarizability. Using $\mathbf{k}\cdot\mathbf{p}$ theory, it is possible to show [56] that the leading order in the charge-density matrix is:

$$\rho_{n\mathbf{k},n'\mathbf{k}+\mathbf{q}}(\mathbf{G}=0) \approx \mathbf{q}\cdot\frac{\langle\phi^{KS}_{n\mathbf{k}}|\hat{p}|\phi^{KS}_{n'\mathbf{k}}\rangle}{\epsilon_{n\mathbf{k}} - \epsilon_{n'\mathbf{k}}} \qquad \mathbf{q}\to 0. \tag{3.11}$$

For a semiconductor the eigenvalues difference in the denominator is finite and therefore $\rho_{n\mathbf{k},n'\mathbf{k}+\mathbf{q}}(\mathbf{G}=0) \propto q$, which implies $\chi^0_{00}(\mathbf{q}\to 0) = aq^2 + o(q^2)$ with a just a constant that can be determined as the coefficient of the second order term, i.e.

$a = \frac{1}{2} \left. \frac{d^2 \chi^0_{00}(\mathbf{q}\to 0)}{d\mathbf{q}_\parallel^2} \right|_{\mathbf{q}_\parallel = 0}$. Notice that this result does not depend on the dimensionality of the system. Now, let us consider $\epsilon^0_{00}(\mathbf{q} \to 0)$ in the same long wavelength limit. From eq. (3.9) one has $\epsilon^0_{00}(\mathbf{q} \to 0) = 1 + av(q)q^2 + o(q^2)$. Because the Coulomb kernel depends on the dimensionality, namely $v^{3\mathrm{D}}(q) \propto 1/q^2$ and $v^{2\mathrm{D}}(q) \propto 1/q$, the screening behavior of 2D material is different from a 3D one. In particular while in 2D $\epsilon^0_{00}(\mathbf{q} \to 0)$ is has to go to 1 ($\epsilon^0_{00}(\mathbf{q} \to 0) \sim 1 + a\frac{2\pi}{q}q^2 \to 1$), in 3D it can assume any finite value above 1, depending on a. This observation gives a first hint on the fact that dielectric screening is reduced in 2D, a concept that will be central in the next chapters.

To finish this section a few word have to be spent on the Coulomb Kernel in eq. (3.9) in the case of 2D materials. From an ab-initio point of view, even if a 2D material is periodic along only two dimensions, it is more practical to apply 3D periodic boundary conditions. In doing so, one has to make sure that the primitive cell in the out-of-plane direction is large enough to avoid spurious hybridization and/or interaction between the artificial replica of the 2D layers. While avoiding hybridization among replicas does not require a particularly elongated cell, the long range nature of the Coulomb interaction makes the use a very large cell a necessity. If h is a measure of the extension of the out-of-plane electron density around the layer, then it is a good rule of thumb to choose a cell which is larger than $2h$. This is computationally quite unfortunate, as by increasing the cell size the number of basis set functions increases drastically and with that the computational cost. One trick to avoid this is to use a Coulomb interaction which is truncated in the out-of-plane direction in realspace:

$$v_{\mathrm{C}}^{\mathrm{trunc}}(\mathbf{r}, \mathbf{r}') = \frac{\theta(\frac{L}{2} - |r_z - r'_z|)}{\sqrt{(\mathbf{r}_\parallel - \mathbf{r}'_\parallel)^2 + (r_z - r'_z)^2}}, \tag{3.12}$$

with L the out-of-plane dimension of the primitive cell and the truncation length set to $L/2$. A simple analytic form of its Fourier transform can be found [75] and it reads:

$$v_{\mathrm{C}}^{\mathrm{trunc}}(\mathbf{k}) = \frac{4\pi}{|\mathbf{k}|^2}\left[1 + e^{-k_\parallel \frac{L}{2}}\left(\frac{k_z}{k_\parallel}\sin\left(k_z\frac{L}{2}\right) - \cos\left(k_\perp\frac{L}{2}\right)\right)\right]. \tag{3.13}$$

From the expression above it is easy to verify that, for an infinitely large primitive cell $L \to \infty$, the 3D Coulomb potential is recovered, i.e. $v_{\mathrm{C}}^{\mathrm{trunc}}(\mathbf{k}) \to v_{\mathrm{C}}^{3\mathrm{D}}(\mathbf{k}) = \frac{4\pi}{|\mathbf{k}|^2}$, whereas for $q \ll 1/L$ the 2D limit is obtained, namely $v_{\mathrm{C}}^{\mathrm{trunc}}(\mathbf{k}) \to v_{\mathrm{C}}^{2\mathrm{D}}(\mathbf{k}) = \frac{2\pi L}{k}$. Using a truncated Coulomb interaction reduces the computational cost of response calculations considerably, but careful convergence test on the out of plane cell size have to be performed.

3.3 Macroscopic Dielectric Function: the $3D$ and $2D$ case

When applying an external perturbation, such as, e.g. an electric field, to a crystal, the perturbation varies on a spatial scale much larger that the unit cell of the material. The material response, however, induces variation of the total potential on an atomic scale (see fig. 3.2). These variations are usually referred to as *local field effects*. The latter cannot be resolved experimentally, where the fields measured are rather an average over the unit cell than the microscopic total field itself. For this reason, one is interested in a dielectric function that directly relates the *macroscopic* total potential, V_{tot}, to the external one:

$$V_{\text{tot}}(\mathbf{r},\omega)\int d\mathbf{r}'\epsilon_{\text{M}}^{-1}(\mathbf{r}-\mathbf{r}',\omega)v_{\text{ext}}(\mathbf{r}',\omega). \tag{3.14}$$

Notice that because it is a macroscopic response, the spatial dependence of the response function is on $\mathbf{r}-\mathbf{r}'$, which indicates homogeneity in space. In this section I will show how the macroscopic dielectric function ϵ_{M} can be calculated in the case of 3D and 2D periodic systems.

Since we are interested only in variations on a scale larger than the unit cell, the macroscopic total potential can be defined as the average of the microscopic one over the unit cell [73]:

$$V_{\text{tot}}(\mathbf{r},\omega)\equiv\frac{1}{\Omega}\int_{\Omega(\mathbf{r})}d\mathbf{r}'v_{\text{tot}}(\mathbf{r}',\omega), \tag{3.15}$$

where the unit cell is centered at $\mathbf{r}$. The microscopic total potential can be conveniently expanded as:

$$v_{\text{tot}}(\mathbf{r},\omega)=\frac{1}{\Omega}\sum_{\mathbf{G}}\sum_{\mathbf{q}}^{\text{BZ}}v_{\mathbf{G}}^{\text{tot}}(\mathbf{q},\omega)e^{-\text{i}(\mathbf{q}+\mathbf{G})\cdot\mathbf{r}}. \tag{3.16}$$

A similar expression can be written for the external potential v_{ext}, but in that case the only non-zero component is the $\mathbf{G}=0$ one. This is because typical external perturbation are spatially smooth over the unit cell, whereas $\mathbf{G}\neq 0$ components would describe oscillations with a period shorter than the unit cell. In formulas this means:

$$v_{\text{ext}}(\mathbf{r},\omega)=\frac{1}{\Omega}\sum_{\mathbf{q}}^{\text{BZ}}v_{0}^{\text{ext}}(\mathbf{q},\omega)e^{-\text{i}\mathbf{q}\cdot\mathbf{r}}. \tag{3.17}$$

The macroscopic total potential can then be calculated by taking the average of

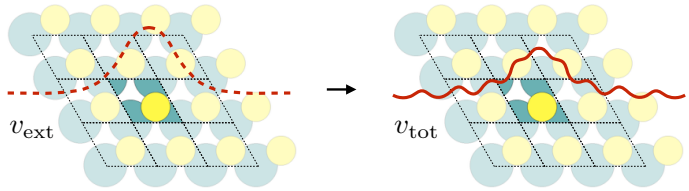

Figure 3.2: Illustration of the local field effects in a periodic system.

eq. (3.16):

$$\begin{aligned} V_{\text{tot}}(\mathbf{r},\omega) &= \frac{1}{\Omega^2}\sum_{\mathbf{G}}\sum_{\mathbf{q}}^{\text{BZ}} v_{\mathbf{G}}^{\text{tot}}(\mathbf{q},\omega)\int_{\Omega(\mathbf{r})} d\mathbf{r}' e^{-\mathrm{i}\mathbf{q}\cdot\mathbf{r}'} e^{-\mathrm{i}\mathbf{G}\cdot\mathbf{r}'} \\ &= \frac{1}{\Omega^2}\sum_{\mathbf{G}}\sum_{\mathbf{q}}^{\text{BZ}} v_{\mathbf{G}}^{\text{tot}}(\mathbf{q},\omega) e^{-\mathrm{i}\mathbf{q}\cdot\mathbf{r}}\int_{\Omega(\mathbf{r})} d\mathbf{r}' e^{-\mathrm{i}\mathbf{G}\cdot\mathbf{r}'} \\ &= \frac{1}{\Omega}\sum_{\mathbf{q}}^{\text{BZ}} v_{0}^{\text{tot}}(\mathbf{q},\omega) e^{-\mathrm{i}\mathbf{q}\cdot\mathbf{r}}, \end{aligned} \tag{3.18}$$

where in the second line I took $e^{-\mathrm{i}\mathbf{q}\cdot\mathbf{r}'}$ out of the integral as it varies slowly on the unit cell scale and in the third line I used the Kronecker delta $\delta_{\mathbf{G}0}$ coming from $\frac{1}{\Omega}\int_{\Omega(\mathbf{r})} d\mathbf{r}' e^{-\mathrm{i}\mathbf{G}\cdot\mathbf{r}'}$. Using eqs. (3.17) and (3.18) and defining $V_{\text{tot}}(\mathbf{q},\omega) = v_0^{\text{tot}}(\mathbf{q},\omega)$ and $v_{\text{ext}}(\mathbf{q},\omega) = v_0^{\text{ext}}(\mathbf{q},\omega)$, eq. (3.14) can be rewritten in reciprocal space as:

$$V_{\text{tot}}(\mathbf{q},\omega) = \epsilon_{\text{M}}^{-1}(\mathbf{q},\omega) v_{\text{ext}}(\mathbf{q},\omega), \tag{3.19}$$

with $\epsilon_{\text{M}}^{-1}(\mathbf{q},\omega) = \int d\mathbf{r} e^{\mathrm{i}\mathbf{q}\cdot\mathbf{r}}\epsilon_{\text{M}}^{-1}(\mathbf{r},\omega)$. Now, from eq. (3.10) the $\mathbf{G} = 0$ component of the total potential is given by $v_0^{\text{tot}}(\mathbf{q},\omega) = \sum_{\mathbf{G}'}\epsilon_{0,\mathbf{G}'}^{-1}(\mathbf{q},\omega) v_{\mathbf{G}'}^{\text{ext}}(\mathbf{q},\omega)$ and since, as explained before, the only contribution from the external potential is for $\mathbf{G}' = 0$, I can write:

$$V_{\text{tot}}(\mathbf{q},\omega) = \epsilon_{00}^{-1}(\mathbf{q},\omega) v_{\text{ext}}(\mathbf{q},\omega). \tag{3.20}$$

Comparing to eq. (3.19), I can relate the macroscopic dielectric function to the microscopic one:

$$\epsilon_{\text{M}}^{\text{3D}}(\mathbf{q},\omega) = \frac{1}{\epsilon_{00}^{-1}(\mathbf{q},\omega)}, \tag{3.21}$$

which is a simple and elegant result. It is important to stress that $\frac{1}{\epsilon_{00}^{-1}(\mathbf{q},\omega)} \neq \epsilon_{00}(\mathbf{q},\omega)$, since the latter does not contain local field effects [73,74]. Indeed picking directly the $\mathbf{G} = \mathbf{G}' = 0$ component of the dielectric matrix corresponds to completely neglect

the response to fields oscillating with a period shorter than the unit cell, i.e. the local field effects. If instead the $\mathbf{G} = \mathbf{G}' = 0$ component is taken after the inversion of the dielectric matrix, unless $\epsilon_{\mathbf{G}\mathbf{G}'}(\mathbf{q},\omega)$ is diagonal, the $\mathbf{G}, \mathbf{G}' \neq 0$ components of $\epsilon_{\mathbf{G}\mathbf{G}'}(\mathbf{q},\omega)$ contribute to $\epsilon^{-1}_{00}(\mathbf{q},\omega)$ bringing information of the local field effects.

Unfortunately things get more complicated when dealing with two dimensional systems and eq. (3.21) does not apply any longer. The reason is that for 2D materials, the average that led to eq. (3.21) would be over a unit cell which is artificially elongated in the out-of-plane direction in order to separate the layer replica as discussed in the previous section. In the limit of large layer separation, most of the contribution to the average of the microscopic total potential would then stem from the vacuum, where the total potential is equal to the external one, and the macroscopic dielectric function would approach one independently of the $\mathbf{q}$-vector [76].

To avoid this problem it is reasonable to limit the out-of-plane average to a significant thickness d around the layer, i.e :

$$V^{\mathrm{Q2D}}_{\mathrm{tot}}(\mathbf{r}_\parallel,\omega;d) \equiv \frac{1}{\Omega_\parallel d}\int_{\Omega_\parallel(\mathbf{r}_\parallel)} d\mathbf{r}'_\parallel \int_{-d/2}^{d/2} dz' v_{\mathrm{tot}}(\mathbf{r}',\omega), \tag{3.22}$$

where z_0 is the out-of-plane coordinate of the layer center and the superscript Q2D (quasi-2D) indicates that the finite thickness of the 2D layer is taken into account. A physically sound value for d would be the actual out-of-plane extension of the electronic density. However since the latter requires ab-initio calculations, a good rule of thumb is to take the interlayer distance in the bulk form of the material. I will provide a more thorough discussion on the choice of d at the end of the section.

Following the same procedure as in eq. (3.18), it is straightforward to show that the new average leads to:

$$V^{\mathrm{Q2D}}_{\mathrm{tot}}(\mathbf{r}_\parallel,\omega;d) = \frac{1}{\Omega_\parallel}\sum_{\mathbf{q}_\parallel}^{\mathrm{BZ}}\frac{2}{d}\sum_{G_z} e^{iG_z z_0}\frac{\sin(G_z d/2)}{G_z} v^{\mathrm{tot}}_{0G_z}(\mathbf{q},\omega) e^{-\mathbf{i}\mathbf{q}_\parallel\cdot\mathbf{r}_\parallel}, \tag{3.23}$$

where I have adopted the notation $\mathbf{G} = \mathbf{G}_\parallel G_z$. Notice that the sum over the BZ vectors is only in the in-plane direction because with a really large simulation cell the BZ is practically flat and only a single out-of-plane q_z is used to represent it. If I now define $V^{\mathrm{Q2D}}_{\mathrm{tot}}(\mathbf{q}_\parallel,\omega;d) = \frac{2}{d}\sum_{G_z} e^{iG_z z_0}\frac{sin(G_z d/2)}{G_z} v^{\mathrm{tot}}_{0G_z}(\mathbf{q},\omega)$, use eq. (3.10) and keep in mind that only the $G' = 0$ component of the external potential contributes, I get:

$$V^{\mathrm{Q2D}}_{\mathrm{tot}}(\mathbf{q}_\parallel,\omega;d) = \frac{2}{d}\sum_{G_z} e^{iG_z z_0}\frac{\sin(G_z d/2)}{G_z}\epsilon^{-1}_{0G_z\,00}(\mathbf{q}_\parallel,\omega) V_{\mathrm{ext}}(\mathbf{q}_\parallel,\omega), \tag{3.24}$$

from which I can identify the Q2D macroscopic dielectric function:

$$\frac{1}{\epsilon^{\mathrm{Q2D}}_{\mathrm{M}}(\mathbf{q}_\parallel,\omega;d)} = \frac{2}{d}\sum_{G_z} e^{iG_z z_0}\frac{\sin(G_z d/2)}{G_z}\epsilon^{-1}_{0G_z\,00}(\mathbf{q}_\parallel,\omega). \tag{3.25}$$

The calculated static ($\omega = 0$) Q2D macroscopic dielectric function for monolayer MoS_2 and hBN are shown in fig. 3.3, together with their respective bulk dielectric function. From the figure it is clear that a monolayer is much less effective at screening compared to the bulk counterpart. In addition, the Q2D macroscopic dielectric function features a much stronger wavevector dependence compared to bulk, as it is forced to go to one for $\mathbf{q}_\parallel \to 0$. Therefore, while the dielectric properties of a bulk semiconductor can be well described with a dielectric constant $\epsilon = \epsilon_{\rm M}(\mathbf{q} \to 0)$, the same is not possible in 2D. It is important to stress that we numerically found $\epsilon_{\rm M}^{\rm Q2D}$ to be isotropic, i.e. the same in all the direction in the BZ. By further inspection of fig. 3.3 we can distinguish two different regimes, which are controlled by the dimensionless parameter $q_\parallel d$: a 3D regime, for $q_\parallel d \gg 1$, where the bulk-like behavior is recovered and a 2D one, for $q_\parallel d \ll 1$, where a linear approximation,

$$\epsilon_{\rm M}^{\rm Q2D}(\mathbf{q}_\parallel; d) \to \epsilon_{\rm M}^{\rm 2D}(\mathbf{q}_\parallel) = 1 + 2\pi\alpha q_\parallel, \tag{3.26}$$

describes the dielectric function well, as illustrated by the blue lines in fig. 3.3. The constant α is usually called the 2D polarizability constant and can be directly found as the slope of the linear expansion. Alternatively, α can be calculated directly from the reducible polarizability matrix. To show how this is done, I consider the $d \to 0$ limit (strict 2D limit) of the static version of the Q2D macroscopic dielectric function: $1/\epsilon_{\rm M}^{\rm Q2D}(\mathbf{q}_\parallel; d) \simeq \sum_{G_z} \epsilon^{-1}_{0G_z\,00}(\mathbf{q}_\parallel)$, where for simplicity I set $z_0 = 0$. Now, using the reciprocal space relation between dielectric matrix and the reducible polarizability matrix, i.e. $\epsilon^{-1}_{\mathbf{G},\mathbf{G}'}(\mathbf{q}_\parallel) = \delta_{\mathbf{G},\mathbf{G}'} + v_{\rm C}^{\rm trunc}(\mathbf{q}_\parallel + \mathbf{G})\chi_{\mathbf{G},\mathbf{G}'}(\mathbf{q}_\parallel)$, the Q2D macroscopic dielectric function becomes:

$$\begin{aligned}\frac{1}{\epsilon_{\rm M}^{\rm Q2D}(\mathbf{q}_\parallel; d)} &\simeq 1 + \sum_{G_z} v_{\rm C}^{\rm trunc}(\mathbf{q}_\parallel + \mathbf{G}_z)\chi_{0G_z\,00}(\mathbf{q}_\parallel) \\ &= 1 + v_{\rm C}^{\rm trunc}(\mathbf{q}_\parallel)\chi_{0\,0}(\mathbf{q}_\parallel) + \sum_{G_z \neq 0} v_{\rm C}^{\rm trunc}(\mathbf{q}_\parallel + \mathbf{G}_z)\chi_{0G_z\,00}(\mathbf{q}_\parallel).\end{aligned} \tag{3.27}$$

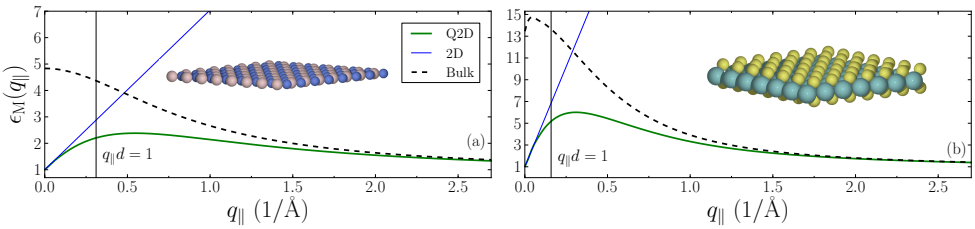

Figure 3.3: Figure adapted from Paper II. Macroscopic dielectric functions for (a) hBN and (b) MoS_2. The bulk (black), Q2D (green) and 2D (blue) static dielectric functions are shown. For more detail on the calculation check Paper II.

In the limit of zero thickness I expect the induced density to be non-zero only within the plane, in other words $\delta n(\mathbf{r}) \propto \delta(z)$, which implies $\chi(\mathbf{r},\mathbf{r}') \propto \delta(z)\delta(z')$. This condition translates to reciprocal space as $\chi_{\mathbf{G}\mathbf{G}'}(\mathbf{q}_\parallel)$ to be independent of the G_z and G'_z components, i.e. $\chi_{\mathbf{G}\mathbf{G}'}(\mathbf{q}_\parallel) = \chi_{\mathbf{G}_\parallel 0\, \mathbf{G}'_\parallel 0}(\mathbf{q}_\parallel)$. This given, the equation above can be further simplified:

$$\frac{1}{\epsilon_{\mathrm{M}}^{\mathrm{Q2D}}(\mathbf{q}_\parallel; d)} \simeq 1 + v_{\mathrm{C}}^{\mathrm{trunc}}(\mathbf{q}_\parallel)\chi_{0\,0}(\mathbf{q}_\parallel) + \chi_{0\,0}(\mathbf{q}_\parallel) \sum_{G_z \neq 0} v_{\mathrm{C}}^{\mathrm{trunc}}(\mathbf{q}_\parallel + \mathbf{G}_z). \tag{3.28}$$

Taking now the long wavelenght limit $\mathbf{q}_\parallel \to 0$, consistently with the $q_\parallel d \ll 1$ regime, and noticing that $v_{\mathrm{C}}^{\mathrm{trunc}}(\mathbf{q}_\parallel) \to 2\pi L/q_\parallel$, I get:

$$\frac{1}{\epsilon_{\mathrm{M}}^{\mathrm{Q2D}}(\mathbf{q}_\parallel; d)} \simeq 1 + \frac{2\pi L}{q_\parallel}\chi_{0\,0}(\mathbf{q}_\parallel) + \chi_{0\,0}(\mathbf{q}_\parallel) \sum_{G_z \neq 0} v_{\mathrm{C}}^{\mathrm{trunc}}(\mathbf{G}_z). \tag{3.29}$$

In this limit the third term on the RHS is clearly a higher order term in $q_\parallel$ and therefore can be neglected. Taking the reciprocal of the equation and using $1/(1+x) \sim 1 - x$, I arrive to:

$$\epsilon_{\mathrm{M}}^{\mathrm{Q2D}}(\mathbf{q}_\parallel; d) \simeq 1 - \frac{2\pi L}{q_\parallel}\chi_{0\,0}(\mathbf{q}_\parallel). \tag{3.30}$$

Since in the long wavelength limit $\chi^0_{0\,0}(q_\parallel) = \left.\frac{d^2\chi^0_{0\,0}(q_\parallel)}{d\mathbf{q}_\parallel^2}\right|_{\mathbf{q}_\parallel=0} + o(q_\parallel^2)$, as shown below eq. (3.11), I can assume the same behavior for the reducible polarizability and comparing to eq. (3.26), I can finally express the 2D polarizability as:

$$\alpha = -\frac{L}{2}\left.\frac{d^2\chi_{0\,0}(q_\parallel)}{d\mathbf{q}_\parallel^2}\right|_{\mathbf{q}_\parallel=0}. \tag{3.31}$$

In general, the linear behavior found for the 2D regime is in agreement with the macroscopic dielectric function typically used for 2D materials first derived by Cudazzo *et.al.* in Ref. [77].

Ending this section, I return to the problem of defining the thickness parameter d used for the average of the Q2D macroscopic dielectric function of MoS_2.

Figure 3.4 illustrates the effect of varying the averaging thickness d on the Q2D static dielectric function. The dashed lines indicate a variation in d of $\pm 10\%$ with respect to the interlayer distance in bulk MoS_2. Increasing (decreasing) d seems to decrease (increase) $\epsilon_{\mathrm{M}}^{\mathrm{Q2D}}$ in the $q_\parallel d \sim 1$ region. However, the 2D and 3D regimes are not affected by the choice of d. In the $q_\parallel d \ll 1$ limit, $\epsilon_{\mathrm{M}}^{\mathrm{Q2D}}$ is insensitive to d because the induced potential decays slowly outside the layer and therefore is pretty much constant over the averaging region. In the $q_\parallel d \gg 1$ limit, $\epsilon_{\mathrm{M}}^{\mathrm{Q2D}}$ is not affected as for large wavevectors the material is unresponsive and the induced potential is negligible.

3.4 Importance of Dielectric Function in Optical Response

Let us see how we can relate the response functions calculated in the previous sections to an experimental absorption spectrum. When perturbing a system with electromagnetic radiation, eq. (3.1) is, in principle, not sufficient to describe the perturbation. This is because the electromagnetic radiation is a transverse perturbation and therefore it cannot be represented only with a scalar potential. However, in the limit of long wavelength ($\mathbf{q} \to 0$) the velocity gauge (transverse perturbation) and the length gauge (longitudinal perturbation) are invariant and it becomes possible in this limit to show that transverse and longitudinal response coincide [78]. A simple and intuitive explanation of such a result is to consider an electron in the material with a velocity v_e perturbed by a field $\mathbf{E} \propto e^{\mathrm{i}(\mathbf{q}\cdot\mathbf{r}-\omega t)}$. The typical length experienced by the electron during its motion is $l_\mathrm{e} \sim v_\mathrm{e}/\omega$. Now if $l_\mathrm{e} \ll 1/q$ the electron cannot "feel" that the perturbation is a wave and as long as the field is locally the same, it cannot distinguish between a longitudinal and a transverse perturbation.

In an absorption experiment we are interested in the power dissipated per unit volume by the absorbing material. Such a quantity is given by:

$$\mathrm{p} = \frac{1}{V}\int_V d\mathbf{r}\, \mathbf{j}(\mathbf{r},t)\cdot\mathbf{E}(\mathbf{r},t). \tag{3.32}$$

with $\mathbf{j}(\mathbf{r},t)$ the current density and $\mathbf{E}(\mathbf{r},t)$ the total electric field in the material. These two quantities are further correlated to each other by the conductivity:

$$\mathbf{j}(\mathbf{r},t) = \int dt' \int_V d\mathbf{r}\, \sigma(\mathbf{r}-\mathbf{r}', t-t')\mathbf{E}(\mathbf{r}',t'). \tag{3.33}$$

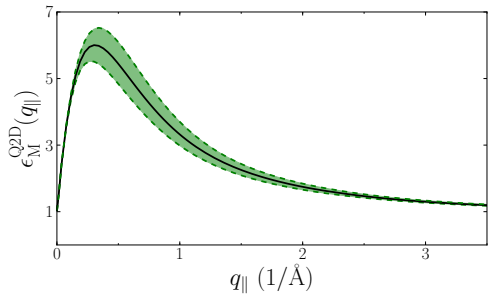

Figure 3.4: Effect of averaging thickness d variation on the Q2D macroscopic dielectric function in MoS_2. The continuous black lines are relative to $d = 6.29$Å (the interlayer distance in the bulk), while the dashed lines delimiting the shaded region are calculated with a variation of $\pm 10\%$ in d.

Note that in this relation it is assumed that the perturbation and the current density are longitudinal and in the same direction as the electric field. To continue, it is convenient to focus on the power dissipated by a total electric field with well defined Fourier components, i.e. $\mathbf{E}(\mathbf{r},t) = \mathbf{E}_0 e^{\mathrm{i}(\mathbf{q}\cdot\mathbf{r}-\omega t)} + c.c.$, where $\mathbf{E}_0$ is a real static vectors giving the magnitude of the field. With this particular form of the external field, eq. (3.33) can be simplified to:

$$\mathbf{j}(\mathbf{r},t) = \sigma(\mathbf{q},\omega)\mathbf{E}_0 e^{\mathrm{i}(\mathbf{q}\cdot\mathbf{r}-\omega t)} + c.c. \tag{3.34}$$

and consequently the power per unit volume dissipated becomes:

$$\mathrm{p} = 2\mathrm{Re}\left[\sigma(\mathbf{q},\omega)\right] E_0^2. \tag{3.35}$$

The next step is to relate the conductivity to the irreducible polarizability. This can be done by means of the continuity equation, which in Fourier space reads $n(\mathbf{q},\omega) = \frac{1}{\omega}\mathbf{q}\cdot\mathbf{j}(\mathbf{q},\omega)$. By expressing the density in terms of the reducible polarizability, $n(\mathbf{q},\omega) = P(\mathbf{q},\omega)V_{\mathrm{tot}}(\mathbf{q},\omega)$, and using that $E(\mathbf{q},\omega) = -\mathrm{i}\mathbf{q}V_{\mathrm{tot}}(\mathbf{q},\omega)$, the continuity equation yields the sought relationship:

$$\sigma(\mathbf{q},\omega) = -\mathrm{i}\frac{\omega}{q^2}P(\mathbf{q},\omega). \tag{3.36}$$

Inserting this in eq. (3.35), one gets $\mathrm{p} = -2\frac{\omega}{q^2}\mathrm{Im}\left[P(\mathbf{q},\omega)\right]E_0^2$. Essentially the power dissipated in the material per unit volume depends on the imaginary part of the irreducible polarizability.

In the case of the optical absorption, because photons carry negligible momentum, the long wavelength limit is satisfied and the absorption spectrum can be defined as:

$$\mathrm{ABS}(\omega) = \lim_{\mathbf{q}\to 0} -\frac{4\pi}{q^2}\mathrm{Im}\left[P(\mathbf{q},\omega)\right]. \tag{3.37}$$

I would like to stress that the prefactor $\frac{4\pi}{q^2}$ is the same regardless the dimensionality of the system, In the derivation above I made use of macroscopic quantities. In the case of bulk systems the absorption spectrum is often expressed in terms of the macroscopic dielectric function. Indeed, remembering that $\epsilon_{\mathrm{M}}(\mathbf{q},\omega) = 1 - 4\pi/q^2 P(\mathbf{q},\omega)$ and using eq. (3.21) one has:

$$\mathrm{ABS}^{\mathrm{3D}}(\omega) = \lim_{\mathbf{q}\to 0}\mathrm{Im}[\epsilon_{\mathrm{M}}^{\mathrm{3D}}(\mathbf{q},\omega)] = \lim_{\mathbf{q}\to 0}\mathrm{Im}\left[\frac{1}{\epsilon_{00}^{-1}}\right]. \tag{3.38}$$

However the same cannot be done in 2D since the Coulomb kernel linking the reducible polarizability to macroscopic dielectric function goes as $\sim 1/q$. Instead, one should make use of the fact that in 2D the macroscopic reducible and irreducible polarizabilities are the same in the long wavelength limit. To show this we consider the relation between the two macroscopic polarizabilities: $\chi(\mathbf{q}_\parallel,\omega) = P(\mathbf{q}_\parallel,\omega) + P(\mathbf{q}_\parallel,\omega)\frac{2\pi}{q_\parallel}\chi(\mathbf{q}_\parallel,\omega)$. Now in the long wavelength limit both P and χ go

as $q_\parallel^2$. This implies that the term $P(\mathbf{q}_\parallel,\omega)\frac{2\pi}{q_\parallel}\chi(\mathbf{q}_\parallel,\omega)$ goes as $q_\parallel^3$ and therefore can be neglected leading to $\lim_{q\to 0}\chi(\mathbf{q}_\parallel,\omega) = \lim_{q_\parallel\to 0} P(\mathbf{q}_\parallel,\omega)$. With the absorption spectrum in terms of χ, local field effects are readily included taking the $\mathbf{G}=\mathbf{G}'=0$ component:

$$\mathrm{ABS}^{\mathrm{2D}}(\omega) = \lim_{\mathbf{q}_\parallel\to 0}\mathrm{Im}[-\frac{4\pi}{q_\parallel^2}\chi_{\mathrm{M}}^{\mathrm{2D}}(\mathbf{q}_\parallel,\omega)] = \lim_{\mathbf{q}_\parallel\to 0}\mathrm{Im}\left[-\frac{4\pi}{q_\parallel^2}\chi_{00}^{\mathrm{2D}}(\mathbf{q}_\parallel,\omega)\right]. \tag{3.39}$$

In practice, χ^{2D} has to be calculated from the 3D counterpart since it is what we get from ab-initio calculations with 3D periodic boundary conditions. By definition $\chi_{00}^{\mathrm{2D}}(\mathbf{q}_\parallel,\omega) = \int dzdz'\chi_{\mathbf{G}_\parallel=0\mathbf{G}'_\parallel=0}(z,z',\mathbf{q}_\parallel,\omega)$, whereas $\chi_{00\,00}(\mathbf{q}_\parallel,\omega) = \frac{1}{L}\int_{-L/2}^{L/2} dzdz'$ $\chi_{\mathbf{G}_\parallel=0\mathbf{G}'_\parallel=0}(z,z',\mathbf{q}_\parallel,\omega)$. Since $\chi_{\mathbf{G}_\parallel=0\mathbf{G}'_\parallel=0}(z,z',\mathbf{q}_\parallel,\omega)$ is localized around the layer we can see that $\chi_{00}^{\mathrm{2D}}(\mathbf{q}_\parallel,\omega) = L\chi_{00\,00}(\mathbf{q}_\parallel,\omega)$.

3.5 Including Excitonic Effects: The Bethe-Salpeter Equation

When calculating the absorption spectrum of a semiconducting material within the RPA approximation as introduced in the previous section, or any other independent-particle approximation, the onset of the absorption coincides with the electronic direct gap. This can be inferred from the irreducible polarizability in eq. (3.5), which has poles only for frequencies matching the difference in eigenvalues. However, it is well known experimentally that a material can absorb light for frequencies lower than the electronic band gap. These apparently forbidden transitions arise from a many-body effect called the *exciton* [79, 80, 81]. In a simple picture an exciton is a particle-hole excitation which is created when an electron is excited from the valence to the conduction band leaving a hole behind. The attractive Coulomb interaction between the electron and hole leads to the formation of excitonic states that can potentially be optically active at frequencies lower that the electronic band gap. An illustration is reported in fig. 3.5 where the excitonic states are drawn as electronic states below the conduction band, but of course a symmetric picture for the hole would be valid as well.

In order to capture excitonic effects one has to get a better approximation for the irreducible polarization by including electron-hole interaction. Since an exciton can be depicted as two-particle many body problem, it is natural to introduce a quantity that is related to the two-particle Green function [42, 66, 82]:

$$L(1,2;3,4) = -\mathrm{i}G(1;3)G(4;2) + G_2(1,2;3,4). \tag{3.40}$$

Such a quantity is often referred to as a four-point reducible polarizability since it reduces to the reducible polarizability when its coordinates are contracted in the

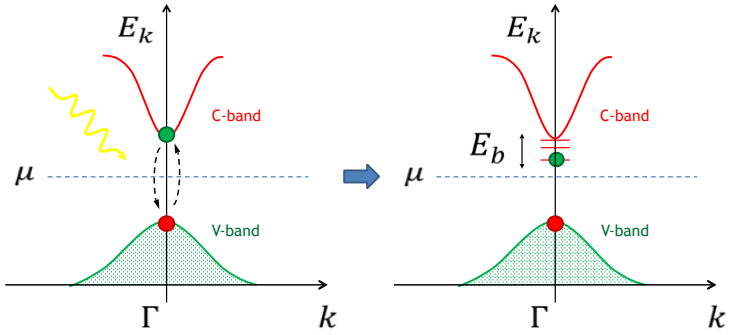

Figure 3.5: Schematic of the formation of an exciton. An exciton can be seen as electron-hole complex interacting via Coulomb interaction. Such interaction gives rise to states in the band gap that can be optically active. In the sketch the excitonic states are arbitrarily drawn as electron states, but a similar illustration for the hole would be valid as well.

following manner:

$$\chi(1;2) = L(1,1^+;2,2^+). \tag{3.41}$$

As shown by Bethe and Salpeter in 1951 [83], the four-point polarizability satisfies the following exact Dyson equation:

$$L(1,2;3,4) = L_0(1,2;3,4) + \int d5d6d7d8 L_0(1,2;5,6)K(5,6,7,8)L(7,8;3,4), \tag{3.42}$$

which goes under the name of Bethe-Salpeter equation (BSE). In particular, $L_0(1,2;3,4) \equiv -\mathrm{i}G(1;3)G(4;2)$ and the kernel $K(1,2,3,4)$ is a complicated object that carries information about the many-body effects in the system, and can be written as:

$$K(1,2,3,4) = v(1,3)\delta(1,2)\delta(3,4) + \mathrm{i}\frac{\delta\Sigma^{\mathrm{xc}}(1;2)}{\delta G(3;4)}. \tag{3.43}$$

A derivation of the Bethe-Salpeter equation can be found in appendix A.

Let us focus on the meaning of eq. (3.42). With the kernel equal to zero, the BSE reduces to $L = L_0$, which is essentially the four-point version of the RPA in eq. (2.45). The RPA consists of a simple product of electron and hole propagators (the Green functions), meaning that no electron-hole interaction is included. When the kernel is different from zero, instead, the independent particles picture is broken and the interaction between the electron and the hole is introduced self-consistently through the Dyson equation. To proceed further, one needs to specify an approximation for the exchange-correlation self-energy and evaluate its derivative with respect to the Green function. Employing the GW approximation and disregarding the variation of the screened interaction due to the excitation, i.e. $\frac{W(1;2)}{\delta G(3;4)} \simeq 0$, one can write

$\frac{\delta\Sigma^{xc}(1;2)}{\delta G(3;4)} \simeq \mathrm{i}\delta(1,3)\delta(2,4)W(1;2)$ and therefore rewrite the kernel as:

$$K(1,2,3,4) = \delta(1,2)\delta(3,4)v(1,3) - \delta(1,3)\delta(2,4)W(1,2). \tag{3.44}$$

The two terms on the RHS can be identified with the unscreened exchange interaction and screened direct interaction. While the distinction between screened and unscreened should be clear, the exchange and direct adjectives follow directly from the order of the variables in the delta functions. Solving eq. (3.42), even with the approximated kernel, is a demanding computational task and it is completely unaffordable for realistic systems (at least up to this date). A great simplification is obtained by considering only the static component of the screened interaction, i.e. $W(1,2) = 1/2\pi\, W(\mathbf{x}_1, \mathbf{x}_2, \omega = 0)\delta(t_1, t_2)$. Indeed, with the static approximation, the kernel is frequency independent and assuming the system to be homogeneous in time, the BSE can be rewritten as a simple product in frequency space:

$$\begin{aligned} L(\mathbf{x}_1, \mathbf{x}_2,&\mathbf{x}_3, \mathbf{x}_4; \omega) = L_0(\mathbf{x}_1, \mathbf{x}_2, \mathbf{x}_3, \mathbf{x}_4; \omega) + \\ &\int d\mathbf{x}_5 d\mathbf{x}_6 d\mathbf{x}_7 d\mathbf{x}_8 L_0(\mathbf{x}_1, \mathbf{x}_2, \mathbf{x}_5, \mathbf{x}_6; \omega) K(\mathbf{x}_5, \mathbf{x}_6, \mathbf{x}_7, \mathbf{x}_8) L(\mathbf{x}_7, \mathbf{x}_8, \mathbf{x}_3, \mathbf{x}_4; \omega). \end{aligned} \tag{3.45}$$

The validity of the static approximation is still a matter of research investigation, but it has been successful at describing dielectric properties of semiconductors. In Ref. [84], it is suggested that the good agreement with experiments on semiconductors is due to the cancellation of dynamical effects on the Green function and the self energy, but the same does not happen for metals, where instead the static approximation needs to be relaxed.

If I express the BSE in the schematic form $L(\omega) = L_0(\omega) + L_0(\omega)KL(\omega)$, then it is clear that the solution for the four-point polarizability is given by $L(\omega) = L_0(\omega)\left[1 - L_0(\omega)K\right]^{-1}$. Therefore, despite the simplification brought by the static approximation, the solution of the BSE still requires the inversion of the operator $[1 - L_0(\omega)K]$ for each single frequency. The standard trick [59, 85] that is used to overcome this problem, is to introduce a frequency independent two-particle Hamiltonian, $\mathcal{H}^{2p}$, and then use the spectral representation of its resolvent to calculate $L(\omega)$. This is more conveniently done in the so called transition space, where the basis functions are a product of two single-particle wave functions (the ones relative to the states taking part of the transition), namely $\psi_S(\mathbf{x}_1, \mathbf{x}_2) = \phi^*_{n_1\mathbf{k}}(\mathbf{x}_1)\phi_{n_2\mathbf{k}+\mathbf{q}}(\mathbf{x}_2)$. The real space four-point polarizability can be expanded in this space as:

$$L(\mathbf{x}_1, \mathbf{x}_2, \mathbf{x}_3, \mathbf{x}_4; \omega) = \sum_{\mathbf{q}}^{\mathrm{BZ}} \sum_{SS'} L_{SS'}(\mathbf{q})\psi_S(\mathbf{x}_1, \mathbf{x}_2)\psi^*_{S'}(\mathbf{x}_3, \mathbf{x}_4). \tag{3.46}$$

Interestingly, it is possible to show (see appendix A) that the transition space can be restricted to valence-conduction bands transitions only. Additionally, the fact that

$L_{SS'}(\mathbf{q})$ is diagonal in $\mathbf{q}$ follows from the translational invariance of the system. As anticipated above, $L_{SS'}(\mathbf{q},\omega)$ is found through the following spectral representation of $[(\omega+\mathrm{i}\eta)\hat{\mathbf{1}}-\mathcal{H}^{\mathrm{2p}}_{SS'}(\mathbf{q})]^{-1}$ (see appendix A):

$$L_{SS'}(\mathbf{q},\omega)=\sum_{\lambda\lambda'}\frac{A^S_\lambda(\mathbf{q})[A^{S'}_{\lambda'}(\mathbf{q})]^* N^{-1}_{\lambda\lambda'}(\mathbf{q})}{\omega-E_\lambda(\mathbf{q})+\mathrm{i}\eta}, \tag{3.47}$$

with $N_{\lambda\lambda'}(\mathbf{q})=(\mathbf{q})=\sum_S[A^S_\lambda(\mathbf{q})]^* A^S_{\lambda'}(\mathbf{q})$ the overlap matrix and $A^S_\lambda(\mathbf{q})$, $E_\lambda(\mathbf{q})$ the eigenfunctions and eigenvalues of the non-hermitian two particle Hamiltonian:

$$\mathcal{H}^{\mathrm{2p}}_{SS'}(\mathbf{q})=(\epsilon_{n_2\mathbf{k}+\mathbf{q}}-\epsilon_{n_1\mathbf{k}})\delta_{SS'}-(f_{n_2\mathbf{k}+\mathbf{q}}-f_{n_1\mathbf{k}})K_{SS'}(\mathbf{q}). \tag{3.48}$$

The diagonal part consists of single-particle transition energies while the off-diagonal terms are given by the BSE kernel $K_{SS'}(\mathbf{q})$ in the transition space.

At the end, the problem of inverting the operator $[1-L_0(\omega)K]$ at each frequency has been reduced to a once for all diagonalization of the two-particle Hamiltonian. Once again it is important to stress that the transitions can be safely restricted to valence-conduction transitions. To simplify the diagonalization even more, it is common to restrict the transition space even further to only the positive frequency transitions, i.e. transitions from valence to conduction band. This approximation is referred to as Tamm-Dancoff approximation and it has the advantage that in this subspace the two-particle Hamiltonian is hermitian [85].

Apart from giving access to the polarizability, the two-particle Hamiltonian is a source for physical insight. Indeed the eigenvalues $E_\lambda(\mathbf{q})$ are essentially the transition energies of the system accounting for the electron-hole interaction. Since such an interaction is attractive, the transitions energies become smaller, which is the reason why semiconductive material may be optically responsive at frequencies below the energy gap E_{G}. An important piece of information that can be extracted from the $E_\lambda(\mathbf{q})$ is the *exciton binding energy*: $E_{\mathrm{b}}=max\{E_{\mathrm{G}}-E_\lambda(\mathbf{q})\}$. This quantity describes how strong the exciton is bound, i.e. how strong the electron-hole interaction is. The eigenfunctions $A^S_{\lambda'}(\mathbf{q})$, often called exciton weights, are identified with the exciton wave functions in reciprocal space. Their connection to the real space exciton wave function is then given by $\Psi^{\mathrm{ex}}_\lambda(\mathbf{r}_{\mathrm{e}},\mathbf{r}_{\mathrm{h}},\mathbf{q})=\sum_S A^S_{\lambda'}(\mathbf{q})\psi_S(\mathbf{r}_{\mathrm{e}},\mathbf{r}_{\mathrm{h}})$. The exciton wave function has to be thought of as the probability of finding an electron in $\mathbf{r}_{\mathrm{e}}$ given a hole in $\mathbf{r}_{\mathrm{h}}$. In the description of optical experiments one is interested in the $\mathbf{q}\to 0$ limit and the $\mathbf{q}$-dependence of the excitonic properties is usually neglected. It is worth mentioning, however, that by solving the BSE at finite $\mathbf{q}$ one could extract, e.g., an excitonic band structure [86] or describe the propagation of excitons in inelastic scattering experiments [87].

So far I have not specified the origin of the single-particle transition energies appearing in the diagonal part of the two-particle Hamiltonian and of the wave function used to construct the transition space. In principle, to be consistent with the *GW* approximation made for σ^{xc} to get the BSE kernel, eigenvalues and wave function

should be obtained from the self-consistent GW (scGW) method. Unfortunately the computational cost of scGW is prohibitive for 2D crystals and "more importantly" is not implemented in GPAW. It is common practice, then, to employ G_0W_0 eigenvalues for the single-particle transitions and KS wave functions for the transition space. This poses the problem of initial state dependence of the BSE results as one could utilize KS wave function calculated with different exchange-correlation functionals. However this goes beyond the scope of this work and in the following LDA is chosen as starting point. An even easier approach is to add a constant shift Δ_s, the so called *scissor operator*, to the KS eigenvalues difference.

To conclude this section I report the final expression for the reducible polarizability matrix [59]:

$$\chi_{\mathbf{GG'}}(\mathbf{q},\omega) = \frac{1}{\Omega}\sum_{SS'} L_{SS'}(\mathbf{q},\omega)\rho_S(\mathbf{G})\rho_{S'}(\mathbf{G}), \tag{3.49}$$

where I used the charge-density matrix, defined in eq. (3.8), resulting from the planewave representation of the transition space basis function, whose spatial coordinates have been contracted according to eq. (3.41). From the knowledge of the reducible polarizability one can calculate the dielectric matrix and for example absorption spectra, which include excitonic effects. An example of absorption spectrum with and without excitonic effects is reported in fig. 3.6 for monolayer MoS_2. One can see that the spectrum is completely different when including excitons and the onset of the absorption is lower than the energy gap. In addition the excitons couple more strongly with light than the free electron-hole pairs as the absorption spectrum calculated using BSE has higher intensity than the corresponding RPA one. Finally

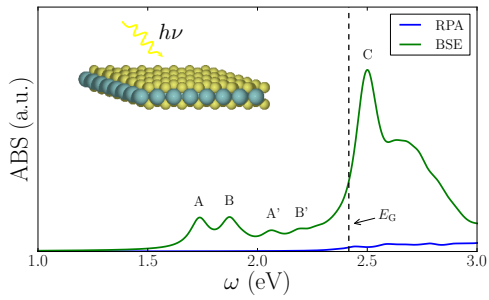

Figure 3.6: Absorption spectrum of MoS_2 with (BSE) and without (RPA) excitonic effects. For the BSE calculation the two topmost valence bands and the four lowermost conduction bands are used to construct the transition space and scissor operator of 0.8 eV is applied for the single-particle transitions. A 30×30 k-points mesh is used for both RPA and BSE. Spin-orbit coupling effects are accounted for non self-consistently..

one can distinguish several peaks associated to excitons: the ones corresponding to the lowest lying excitons (A and B), and the next excited excitonic states (A',B' and C) [27]. The split of the excitonic peaks in A and B is due to spin-orbit coupling effects. From this It is clear that excitonic effects are crucial for the description of optical properties of real materials.

For later purposes, it is instructive to write down the planewave representation of the exchange and screened Coulomb interaction in the kernel $K_{SS'}(\mathbf{q}) = v_{SS'}(\mathbf{q}) - W_{SS'}(\mathbf{q})$:

$$v_{SS'}(\mathbf{q}) = \frac{2}{\Omega}\sum_{\mathbf{G}} v(\mathbf{q}+\mathbf{G})\rho^{*}_{n_1\mathbf{k},n_2\mathbf{k}+\mathbf{q}}(\mathbf{G})\rho_{n_1'\mathbf{k},n_2'\mathbf{k}+\mathbf{q}}(\mathbf{G}), \tag{3.50}$$

$$W_{SS'}(\mathbf{q}) = \frac{1}{\Omega}\sum_{\mathbf{G}\mathbf{G}'} \rho^{*}_{n_1\mathbf{k},n_1'\mathbf{k}}(\mathbf{G})v(\mathbf{q}+\mathbf{G})\epsilon^{-1}_{\mathbf{G}\mathbf{G}'}(\mathbf{q},\omega=0)\rho_{n_2\mathbf{k}+\mathbf{q},n_2'\mathbf{k}+\mathbf{q}}(\mathbf{G}). \tag{3.51}$$

The factor two in the expression for the exchange interaction accounts for the spin and the assumption that only singlet transitions contribute to the transitions. The same factor is not present in the screened direct interaction since the spins are related to each other by the delta functions in the second term of eq. (3.44) and therefore they are not independent.

3.5.1 Remarks on BSE convergence

Doing a BSE calculation is extremely expensive in computational terms, the main two reasons being the diagonalization of the two-particle Hamiltonian and the calculation of the screened interaction. As I mentioned above, the two-particle Hamiltonian is represented on the transition space restricted to valence to conduction band transitions. Obviously even counting only these there are infinitely many transition and one has to come up with a significant subset that is enough to describe the relevant energy window. It turns out that for a semiconductor having non-degenerate highest valence band and lowest conduction band, it is enough to include only those two to get converged excitonic levels (at least for the lowest ones). If instead one is interested in the absorption spectrum up to several eV, the number of conduction and valence bands has to be increased. For example it is shown in Ref. [27] that in order to converge the MoS_2 absorption spectrum up to 3.5eV one has to include the last two valence bands and the first four conduction bands.

The other bottleneck of the BSE is the calculation of the screened interaction which in turn requires the calculation of the dielectric matrix at a RPA level. This stage of the computation is the limiting step in the case of two-dimensional materials. Two parameters play an important role: the cutoff energy that sets the number of unoccupied bands[3] for the calculation of the RPA dielectric matrix and the number

[3]The need of setting the number of unoccupied bands for the calculation of the RPA dielectric function follows from the sum over unoccupied states in eq. (3.8). It is important to stress that the number of unoccupied bands is not related to the number of conduction states included in the

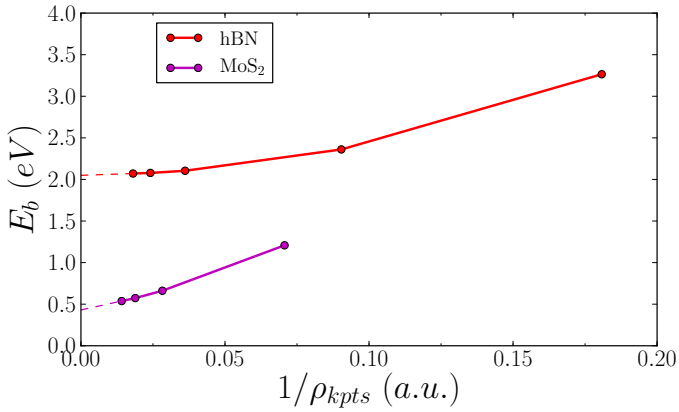

Figure 3.7: Convergence of the exciton binding energy for MoS_2 and h-BN. In this case the exchange contribution to the kernel has not been included. The markers, from left to right, are results from 60×60, 45×45, 30×30 and 12×12 k-points.

of k-points in the BZ. In fig. 3.7 I illustrate the convergence of the exciton binding energy in MoS_2 and h-BN as a function of k-point density in the two-dimensional BZ. The highest k-point density in the plot corresponds to a 60×60 k-point mesh, which according to the linear extrapolation in dashed line yields a converged result within ~ 0.1eV for MoS_2 and 0.03eV for hBN. The reason for such a slow convergence can be attributed to strong wavevector dependence of the dielectric function for 2D materials, as illustrated in fig. 3.3. In particular, a coarse k-point sampling of the dielectric function results in an underestimation of the screening and explains why the exciton binding energy goes up for smaller k-point density. It is important to mention that the same convergence issue appears in G_0W_0 calculations, since also in that case one needs to calculate the screened interaction.

two-particle Hamiltonian

CHAPTER 4

Modelling Excitons in 2D Materials

Band gaps in the visible range and strong light-matter interaction turned out to be the key to the success of two-dimensional (2D) semiconductors in (opto)-electronic applications [19, 24, 25]. The extensive theoretical and experimental investigation of the optical properties of these materials has demonstrated that the optical response is mainly governed by strongly bound excitons [26, 27, 29, 88, 89]. The formation of strongly bound excitons is unique to low-dimensional materials and it is a consequence of the poor electronic screening due to the reduced dimensionality. From a theoretical perspective, excitonic effects can be completely determined and understood in terms of the Bethe-Salpeter equation (BSE). Unfortunately, solving the BSE is a tremendous computational task, which becomes practically impossible in the case of complex materials such as van der Waals heterostructures. As an alternative to the BSE, it has been shown that under well-defined assumptions, the excitonic problem for bulk systems can be reduced to the solution of a hydrogenic-like Schrödinger equation, often referred to as the Mott-Wannier equation [90]:

$$\left[-\frac{\nabla^2}{2\mu_{\text{ex}}} - \frac{1}{\epsilon r}\right] F(\mathbf{r}) = E_{\text{b}} F(\mathbf{r}), \tag{4.1}$$

with μ_{ex} the exciton effective mass, ϵ the dielectric constant, E_{b} and $F(\mathbf{r})$ the exciton energies and wave functions respectively and $\mathbf{r}$ the electron-hole separation vector. This result agrees with the usual intuitive picture of an exciton as an electron and a hole interacting via a Coulomb interaction which is screened by all the other electrons in the material. However, as learned in the previous chapter, it is not clear how to define a dielectric constant, ϵ, for 2D materials. The standard approach [77,91,92] is to modify the electron-hole interaction using a linear approximation for the wavevector dependence of the dielectric function, exactly as in eq. (3.26). In this chapter I will provide a critical assessment of the standard approach, which is based on a strict 2D

picture of the material, by taking into account the intrinsic finite thickness of the 2D layer and including the full wavevector dependence of the screened electron-hole interaction. To conclude the chapter, I will show how, by a modified definition of a 2D effective dielectric constant, it is actually still possible to use the hydrogenic-like eq. (4.1) and find an analytic expression for the exciton binding energies.
The work presented in this chapter is based on Paper III and the first part of Paper II.

4.1 From BSE to the Mott-Wannier equations for 2D materials

As shown in the previous chapter, the solution of the BSE comes down to the diagonalization of the resonant part of the two-particle Hamiltonian. While, in principle, the two-particle Hamiltonian should be represented on a transition space consisting of all the available valence and conduction band pairs, the properties of the most strongly bound (lowest lying) excitons are usually well described by including only the highest lying valence band and lowest lying conduction band. This is valid as long as the two bands are well separated from all the others. Additionally, for optically generated excitons, it is enough to consider only vertical transitions, i.e. $\mathbf{q} \to 0$. The two-particle Hamiltonian in eq. (3.48) can then be rewritten as:

$$\mathcal{H}^{2\mathrm{p}}_{\substack{vc\mathbf{k}_\parallel \\ vc\mathbf{k}'_\parallel}} = (\epsilon_{c\mathbf{k}'_\parallel} - \epsilon_{v\mathbf{k}_\parallel})\delta_{\mathbf{k}_\parallel \mathbf{k}'_\parallel} + K_{\substack{vc\mathbf{k}_\parallel \\ vc\mathbf{k}'_\parallel}}, \tag{4.2}$$

with $\mathbf{k}_\parallel$ taken as a 2D vector in the 2D BZ. It is convenient to explicit the kernel in the reduced transition space:

$$\begin{aligned} K_{\substack{vc\mathbf{k}_\parallel \\ vc\mathbf{k}'_\parallel}} =& 2\int d\mathbf{r}d\mathbf{r}'\phi_{v\mathbf{k}_\parallel}(\mathbf{r})\phi^*_{c\mathbf{k}_\parallel}(\mathbf{r})v(\mathbf{r},\mathbf{r}')\phi^*_{v\mathbf{k}'_\parallel}(\mathbf{r}')\phi_{c\mathbf{k}'_\parallel}(\mathbf{r}') + \\ &- \int d\mathbf{r}d\mathbf{r}'\phi_{v\mathbf{k}_\parallel}(\mathbf{r})\phi^*_{c\mathbf{k}_\parallel}(\mathbf{r}')W(\mathbf{r},\mathbf{r}')\phi^*_{v\mathbf{k}'_\parallel}(\mathbf{r})\phi_{c\mathbf{k}'_\parallel}(\mathbf{r}'), \end{aligned} \tag{4.3}$$

where the KS superscript is omitted for ease of notation. The expression above clarifies even better than eq. (3.44) the reason why the first and the second terms on the RHS are referred to as exchange and direct screened interaction. According to our ab-initio solution of the BSE for two representative 2D semiconductors, namely MoS_2 (in the 2H phase) and hBN, the effect of the exchange interaction amounts to less than 5% of the exciton binding energy and therefore I will safely neglect it in the following.

Typical 2D materials feature excitons fairly delocalized in real space, or equivalently, fairly localized in reciprocal space. Technically speaking this means that the excitonic weights $A^{v(c)\mathbf{k}_\parallel}_{\lambda'}$, introduced in section 3.5, are non-zero only around the top

of the valence and bottom of the conduction band. This is illustrated in fig. 4.1, where the absolute squared value of the excitonic weights for the lowest lying excitons in MoS_2 and hBN are plotted as green circles, whose radius is proportional to their magnitude. It is evident that in both materials the exciton tends to localize around the K-point of the BZ. Since it is only the states around the extrema of the valence and conduction bands that matter, it is possible to approximate the bands as parabolic (red dashed lines in fig. 4.1), i.e. $\epsilon_{c(v)\mathbf{k}_\parallel} = \pm\frac{k^2}{2m_{\mathrm{e(h)}}}$, with $m_{\mathrm{e(h)}}$ the electron(hole) effective mass. It follows that the diagonal part of the two-particle Hamiltonian in eq. (4.2) can be expressed as $diag(\mathcal{H}^{\mathrm{2p}}_{\substack{vc\mathbf{k}_\parallel \\ vc\mathbf{k}'_\parallel}}) = \frac{k_\parallel^2}{2\mu_{\mathrm{ex}}}$, with the exciton mass defined as $\mu_{\mathrm{ex}}^{-1} = m_{\mathrm{e}}^{-1} + m_{\mathrm{h}}^{-1}$.

Since a parabolic energy dispersion is characteristic of free charges, it is justified to approximate valence and conduction Bloch wave functions as $\phi_{v(c)\mathbf{k}_\parallel}(\mathbf{r}) = \frac{e^{\mathrm{i}\mathbf{k}_\parallel\cdot\mathbf{r}_\parallel}}{\sqrt{\Omega_\parallel}}\phi_{v(c)\,\perp}(z)$, namely the product of an in-plane plane-wave normalized to the area of the unit cell $\Omega_\parallel$ and a distribution $\phi_{v(c)\,\perp}(z)$ for the out-plane direction. In particular for the latter, it is reasonable to choose the in-plane average of the valence (conduction) wave functions calculated at the point $\mathbf{k}_{\parallel\,0}$ of the BZ corresponding to the position of the bands extrema, in formula $\phi_{v(c)\,\perp}(z) = (\frac{1}{A}\int d\mathbf{r}_\parallel |\phi_{v(c)\mathbf{k}_{\parallel\,0}}(\mathbf{r})|^2)^{1/2}$. The square of the out-of-plane part of the valence and conduction wave functions in hBN and MoS_2 are illustrated in fig. 4.2.

Thanks to the discussed approximations, the kernel $K_{\substack{vc\mathbf{k}_\parallel \\ vc\mathbf{k}'_\parallel}}$ simplifies to:

$$K_{\substack{vc\mathbf{k}_\parallel \\ vc\mathbf{k}'_\parallel}} = -\frac{1}{\Omega_\parallel^2}\int d\mathbf{r}_\parallel d\mathbf{r}'_\parallel e^{\mathrm{i}(\mathbf{k}_\parallel-\mathbf{k}'_\parallel)\cdot\mathbf{r}_\parallel}\left[\int dz dz' |\phi_{c\,\perp}(z)|^2 W(\mathbf{r},\mathbf{r}')|\phi_{v\,\perp}(z')|^2\right] e^{-\mathrm{i}(\mathbf{k}_\parallel-\mathbf{k}'_\parallel)\cdot\mathbf{r}'_\parallel}. \tag{4.4}$$

Because $W(\mathbf{r},\mathbf{r}')$ is a function on a 2D periodic lattice it fulfills translational invariance and therefore satisfies a 2D version of eq. (3.7):

$$W(\mathbf{r},\mathbf{r}') = \frac{1}{\Omega_\parallel}\sum_{\mathbf{G}_\parallel,\mathbf{G}'_\parallel}\sum_{\mathbf{q}_\parallel}^{\mathrm{BZ}} e^{i(\mathbf{G}_\parallel+\mathbf{q}_\parallel)\cdot\mathbf{r}_\parallel} W_{\mathbf{G}_\parallel,\mathbf{G}'_\parallel}(z,z',\mathbf{q}_\parallel) e^{-i(\mathbf{q}_\parallel+\mathbf{G}'_\parallel)\cdot\mathbf{r}'}. \tag{4.5}$$

Inserting the last expression in eq. (4.4) and noting that the double integral over the exponential gives $\delta_{\mathbf{q}_\parallel\,\mathbf{k}'_\parallel-\mathbf{k}_\parallel}\delta_{G_\parallel\,0}\delta_{G'_\parallel\,0}$, I arrive at a very compact expression for the BSE kernel:

$$K_{\substack{vc\mathbf{k}_\parallel \\ vc\mathbf{k}'_\parallel}} = \frac{1}{\Omega_\parallel}\bar{W}(\mathbf{k}'_\parallel - \mathbf{k}_\parallel), \tag{4.6}$$

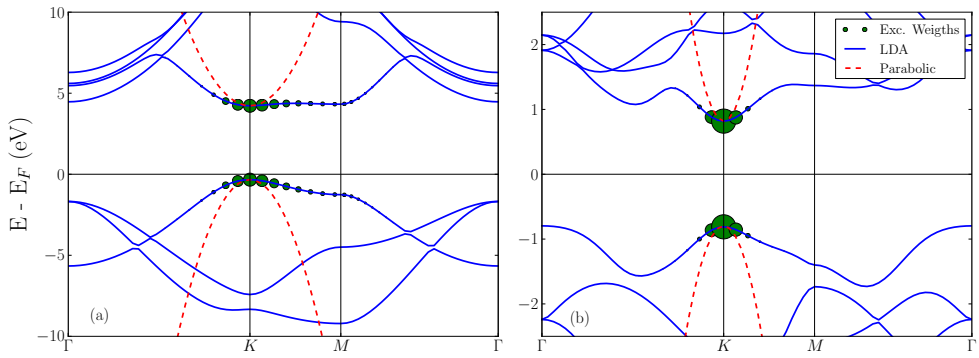

Figure 4.1: Absolute value squared of the excitonic weights of the lowest lying exciton for monolayer hBN (a) and MoS_2 (b) obtained as the solution to the BSE based on a LDA band structure. In both materials the exciton localizes at the K point. The parabolic approximation used in the Mott-Wannier equation is shown in red. The electron and hole masses calculated from LDA bands are respectively 0.93 a.u. and 0.62 a.u. for hBN and 0.61 a.u. and 0.49 a.u. for MoS_2.

where I defined the screened interaction energy in reciprocal space as

$$\begin{aligned}\bar{W}(\mathbf{q}_\parallel) &= \int dz dz' |\phi_{c\perp}(z)|^2 W_{00}(z,z',\mathbf{q}_\parallel)|\phi_{v\perp}(z')|^2 \\ &= \int dz dz' dz'' |\phi_{c\perp}(z)|^2 \epsilon^{-1}_{00}(z,z',\mathbf{q}_\parallel) v_{\mathrm{C}}(z'-z'',\mathbf{q}_\parallel)|\phi_{v\perp}(z'')|^2.\end{aligned} \tag{4.7}$$

The fact that only the $\mathbf{G}_\parallel = \mathbf{G}'_\parallel = 0$ component of the inverse dielectric function appears, means that the relevant screened interaction in the BSE Kernel is macroscopic in the in-plane direction (see section 3.3). Combining this result with the parabolic energy dispersion, the two-particle Hamiltonian becomes:

$$\mathcal{H}^{\mathrm{2p}}_{\substack{vc\mathbf{k}_\parallel \\ vc\mathbf{k}'_\parallel}} = \delta_{\mathbf{k}_\parallel \mathbf{k}'_\parallel} \frac{k_\parallel^2}{2\mu_{\mathrm{ex}}} + \frac{1}{\Omega_\parallel} \bar{W}(\mathbf{k}'_\parallel - \mathbf{k}_\parallel). \tag{4.8}$$

Finally, the BSE eigenproblem $\sum_{\mathbf{k}'} \mathcal{H}^{\mathrm{2p}}_{\substack{vc\mathbf{k}_\parallel \\ vc\mathbf{k}'_\parallel}} A^{\mathbf{k}'_\parallel} = E_{\mathrm{b}} A^{\mathbf{k}_\parallel}$ can be reformulated in real space as a *generalized* Mott-Wannier equation for 2D systems:

$$\left[-\frac{\nabla^2_{2D}}{2\mu_{\mathrm{ex}}} + \bar{W}(\mathbf{r}_\parallel) \right] F(\mathbf{r}_\parallel) = E_b F(\mathbf{r}_\parallel), \tag{4.9}$$

with $\mathbf{r}_\parallel$ the electron-hole separation vector, $F(\mathbf{r}_\parallel)$ the so called *envelope function*, defined as $F(\mathbf{r}_\parallel) = \frac{1}{\Omega_\parallel} \sum_{\mathbf{k}_\parallel} e^{-\mathrm{i}\mathbf{k}_\parallel \cdot \mathbf{r}_\parallel} A^{\mathbf{k}_\parallel}$ and $\bar{W}(\mathbf{r}_\parallel) = \frac{1}{\Omega_\parallel} \sum_{\mathbf{k}_\parallel} e^{-\mathrm{i}\mathbf{q}_\parallel \cdot \mathbf{r}_\parallel} \bar{W}(\mathbf{q}_\parallel)$. Because

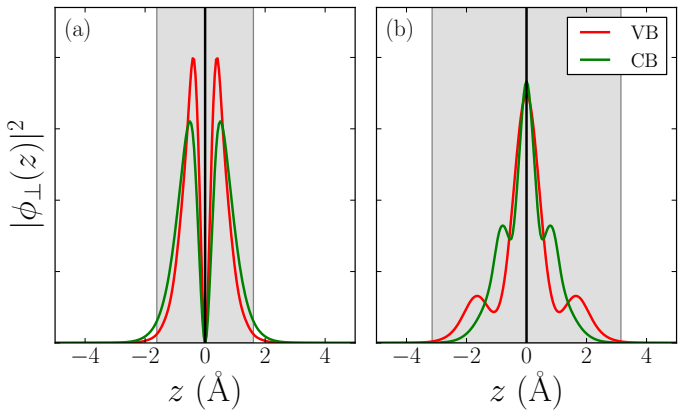

Figure 4.2: Valence (red) and conduction (green) out-of-plane wave function squared for (a) hBN and (b) MoS_2 calculated at $\mathbf{k}_{\parallel\,0} = K$. The grey shaded area represents the extension of the step function used to approximate the actual out-of-plane density distribution of the electron and the hole.

of the resemblance of eq. (4.9) with the Schrödinger equation for a 2D hydrogen atom, it is now evident why the Mott-Wannier equation is usually associated with a hydrogenic picture of the exciton. The reason why I used the term generalized is that compared to the original Mott-Wannier equation eq. (4.1), no approximation on the wavevector dependence of the electron-hole interaction energy has been made and the finite extension in the out-of-plane is effectively taken into account.

To conclude this section, let us consider the explicit expression of the electron-hole interaction energy in real space. Defining the electron (hole) charge density $\rho_{\mathrm{e(h)}}(\mathbf{r}) = \mp\delta(\mathbf{r}_\parallel - \mathbf{r}_{\mathrm{e(h)}\,\parallel})|\phi_{c(v)}(z)|^2$, it is straightforward to show:

$$\bar{W}(\mathbf{r}_{\mathrm{e}\,\parallel} - \mathbf{r}_{\mathrm{h}\,\parallel}) = \int d\mathbf{r} d\mathbf{r}' d\mathbf{r}'' \frac{\rho_{\mathrm{e}}(\mathbf{r})\epsilon_{\mathrm{M}}^{-1}(\mathbf{r} - \mathbf{r}')\rho_{\mathrm{h}}(\mathbf{r}'')}{|\mathbf{r}' - \mathbf{r}''|}. \tag{4.10}$$

Note that as argued below eq. (4.7) the dielectric function appearing in the expression above has to be macroscopic in-plane. Essentially, eq. (4.10) shows that $\bar{W}(\mathbf{r}_{\mathrm{e}\,\parallel}, \mathbf{r}_{\mathrm{h}\,\parallel})$ is nothing else but the screened classical electrostatic interaction energy associated with the electron and hole charge distributions.

4.2 Screened Coulomb Interaction

The main ingredients for the solution of the Mott-Wannier equation are the exciton effective mass, which is easily calculated from ab-initio band structures, and the screened electron-hole interaction energy, which will be the topic of this section.

Forgetting for a moment about the dielectric screening, it is instructive to see how the bare electron-hole interaction looks in reciprocal space in the case of a strict 2D system and a finite thickness layer (see sketch in fig. 4.3). For a 2D plane, the out-of-plane charge distribution for electron and hole reduces to a delta-function, meaning that one is left with the interaction energy of 2D point-charges (fig. 4.3 (a)), which is well known and reads:

$$\bar{V}_{\mathrm{2D}}(\mathbf{q}_\parallel) = -\frac{2\pi}{|\mathbf{q}_\parallel|}. \tag{4.11}$$

For an actual 2D material with finite thickness, the electron and hole should be rather thought as lines of charges (fig. 4.3 (b)) with an out-of-plane distribution given by $|\phi_{c(v)}(z)|^2$. By approximating the latter with a layer centered step-function of a thickness d, it is possible to obtain an analytic expression for the bare interaction energy in reciprocal space:

$$\bar{V}_{\mathrm{Q2D}}(\mathbf{q}_\parallel) = -\frac{4\pi}{d|\mathbf{q}_\parallel|^2}\left[1 - \frac{2}{|\mathbf{q}_\parallel|d}e^{-|\mathbf{q}_\parallel|d/2}\sinh\left(\frac{|\mathbf{q}_\parallel|d}{2}\right)\right]. \tag{4.12}$$

Details on the derivation of the above formula are given in Paper II. What is interesting to see is that the asymptotic limits:

$$\bar{V}_{\mathrm{Q2D}}(\mathbf{q}_\parallel) = \begin{cases} -\frac{2\pi}{|\mathbf{q}_\parallel|} & q_\parallel d \ll 1 \\ -\frac{4\pi}{|\mathbf{q}_\parallel|^2} & q_\parallel d \gg 1 \end{cases}, \tag{4.13}$$

are governed by the dimensionless parameter $q_\parallel d$, the same encountered in the previous chapter when discussing the Q2D macroscopic dielectric function. Once again, for $q_\parallel d \ll 1$ one recovers the 2D behavior, whereas for $q_\parallel d \gg 1$ the 3D limit is obtained.

Going back to the screened interaction energy, it is convenient to reformulate the reciprocal space expression in eq. (4.7) in the following way:

$$\bar{W}(\mathbf{q}_\parallel) = \int_{-\infty}^{\infty} dz dz' \rho_{\mathrm{e}}(z, \mathbf{q}_\parallel)\epsilon_{00}^{-1}(z, z', \mathbf{q}_\parallel)\varphi_{\mathrm{h}}(z', \mathbf{q}_\parallel). \tag{4.14}$$

In this form, the interaction energy can be seen as the electrostatic energy associated with an electron being in the field $\varphi_{\mathrm{h}}(z, \mathbf{q}_\parallel) = \int dz' v_{\mathrm{C}}(z - z', \mathbf{q}_\parallel)\rho_{\mathrm{h}}(z, \mathbf{q}_\parallel)$ generated by the hole. As explained in Paper II, the latter can be calculated numerically for an arbitrary out-of-plane hole distribution by solving the Poisson equation. The convenience of the equation above is clear when approximating the electron and hole out-of-plane distribution with a step-function. Indeed if I replace the potential $\varphi_{\mathrm{h}}(z, \mathbf{q}_\parallel)$ with its average values around the layer and follow the derivation in Paper II, the screened interaction energy becomes a simple product of the Q2D macroscopic dielectric function and the bare Coulomb interaction:

$$\bar{W}_{\mathrm{Q2D}}(\mathbf{q}_\parallel) = \epsilon_{\mathrm{Q2D}}^{-1}(\mathbf{q}_\parallel)\bar{V}_{\mathrm{Q2D}}(\mathbf{q}_\parallel), \tag{4.15}$$

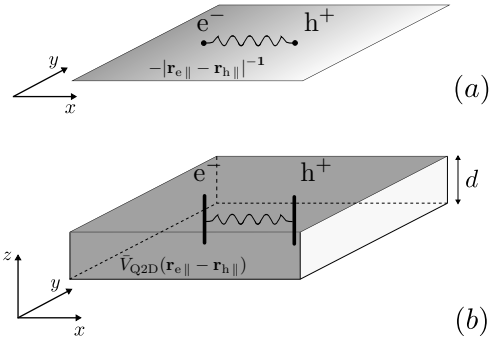

Figure 4.3: Sketch of the Coulomb interaction between (a) point-charges in a 2D plane and (b) quasi-2D point-charges, i.e. lines of charge extending along the thickness of the material.

where, for ease of notation, I used a slightly modified notation for the dielectric function compared to the original definition in section 3.3, i.e. $\epsilon_{\mathrm{Q2D}} = \epsilon^{\mathrm{Q2D}}$. Since both functions on the RHS reduce to their respective 2D asymptotic limit for $q_\parallel d \ll 1$, it is meaningful to define the $d \to 0$ limit of the screened interaction energy:

$$\bar{W}_{\mathrm{2D}}(\mathbf{q}_\parallel) = \epsilon_{\mathrm{2D}}^{-1}(\mathbf{q}_\parallel)\bar{V}_{\mathrm{2D}}(\mathbf{q}_\parallel). \tag{4.16}$$

This is the interaction standardly used in literature for excitons in 2D materials [77, 91, 92], but now directly derived from a microscopic approach as the $q_\parallel d \ll 1$ limit.

The advantage of the 2D approximation over the Q2D is that its real space equivalent has an analytic form:

$$\bar{W}_{\mathrm{2D}}(\mathbf{r}_\parallel) = \frac{1}{4\alpha}\left[H_0(x) - N_0(x)\right]_{x=r_\parallel/2\pi\alpha}, \tag{4.17}$$

with $H_0(x)$ and $N_0(x)$ the Struve and Neumann functions and α the 2D polarizability constant.

For the Q2D screened interaction energy, instead, only a semi-analytic expression can be found by integrating the angular part of the inverse Fourier transform of eq. (4.15):

$$W_{\mathrm{Q2D}}(\mathbf{r}_\parallel) = -\frac{2}{d}\int_0^\infty dq \frac{J_0(qr_\parallel)}{q}\epsilon_{\mathrm{Q2D}}^{-1}(q)\left[1 - \frac{2}{qd}e^{-qd/2}\sinh\left(\frac{qd}{2}\right)\right], \tag{4.18}$$

where the fact that the macroscopic dielectric function is isotropic has been used.

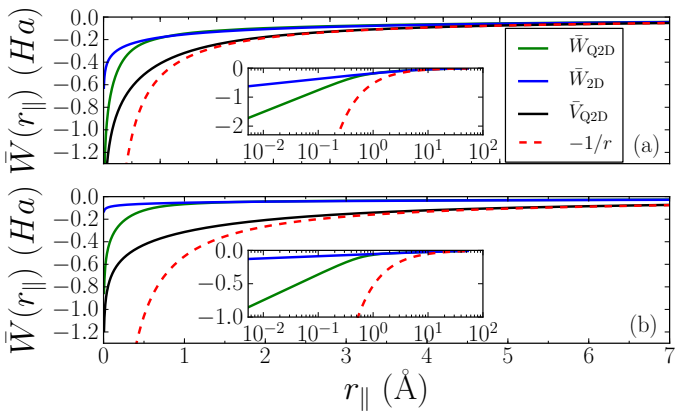

Figure 4.4: Q2D and 2D interaction energy for monolayer hBN (a) and MoS_2 (b)..

Figure 4.4 summarizes all the different screened and unscreened interaction energies introduced so far, for the specific case of hBN and MoS_2. First of all, the different interactions agree for large separation distances $r_\parallel$, meaning that screening is not effective on a long range and that the effect of finite thickness is irrelevant when $r_\parallel \gg d$. Comparing $V_{\rm Q2D}$ with $-1/r_\parallel$, one learns that the finite thickness of the layer in the Q2D picture modifies the interaction even at the unscreened level, at least for a distance smaller than the layer thickness ($d_{\rm MoS_2} = 6.29$Å and $d_{\rm hBN} = 3.22$Å). As expected, including screening reduces the interaction and it does it more for the strict 2D limit since $\epsilon_{\rm 2D}(\mathbf{q}_\parallel) > \epsilon_{\rm Q2D}(\mathbf{q}_\parallel)$ for all $\mathbf{q}_\parallel$. Overall the Q2D and 2D screened interaction energies agree very well, with the only deviation appearing for distances lower than ~ 1Å , a length scale much smaller than the typical exciton extension. Finally, it is of interest to notice that the asymptotic behavior for $r_\parallel \to 0$ is logarithmic for both the Q2D and 2D interactions. This is well understood considering that in both cases $W \propto 1/q_\parallel^2$ in the large $q_\parallel$ limit, which is the limit that determines the small separation distance behavior.

The are two main approximations going into eq. (4.15): the use of step-function distributions and, within that, the replacement of the hole induced potential $\varphi_{\rm h}(z, \mathbf{q}_\parallel)$ with its averaged value. While these approximations are handy to get a semi-analytic result, they might seem a bit extreme and their validity needs to be checked via numerical evaluation of eq. (4.14). The replacement of the potential of a step-function distributed hole with its average value can be avoided by numerically solving the Poisson equation for a step-function hole distribution. This leads to a screened interaction energy that I denote with $W_{\rm Q2D}(q_\parallel)^{\rm steps}$. Even more generally, the assumption of step-function distributions can be completely relaxed by using the actual charge densities, such as the ones in fig. 4.2, and obtain $W_{\rm Q2D}(q_\parallel)^{\rm wfs}$. I consider such an interaction energy the highest level of approximation reachable within the framework

introduced so far. I find it important to stress that the use of the Q2D subscript in the two new interaction energies is consistent with the fact that the finite thickness of the material is taken into account.

In order to compare the different screened interactions, it is convenient to define an effective Q2D macroscopic dielectric function as the ratio between the unscreened and screened interaction:

$$\epsilon^{\gamma}_{\mathrm{Q2D}}(\mathbf{q}_{\parallel}) = \frac{\langle \rho^{\gamma}_{\mathrm{e}}(\mathbf{q}_{\parallel}) | \phi^{\gamma}_{\mathrm{h}}(\mathbf{q}_{\parallel}) \rangle}{\langle \rho^{\gamma}_{\mathrm{e}}(\mathbf{q}_{\parallel}) | \epsilon^{-1}_{00}(\hat{z}, \hat{z}', \mathbf{q}_{\parallel}) | \phi^{\gamma}_{\mathrm{h}}(\mathbf{q}_{\parallel}) \rangle}, \tag{4.19}$$

with the bracket notation indicating the integration over z (and/or z') and $\gamma =$ steps,wfs. The calculated macroscopic dielectric functions for hBN and MoS_2 are shown in fig. 4.5. Whereas the deviation for $q_{\parallel}$ greater than the reciprocal space radius of the lowest lying exciton (indicated by the vertical line) is clear, the agreement for $q_{\parallel} < 1/R_{\mathrm{exc}}$ is practically perfect. This observation will be crucial for justifying the results on exciton binding energies in the following section.

4.3 Exciton Binding Energy: Quasi-2D Models vs 2D

A good way to test the different models described in the previous section, is to calculate the binding energy of the lowest lying exciton and benchmark it against the full BSE solution. Once again hBN and MoS_2 are chosen as test systems due to their rather different dielectric functions.

Considering that the interaction is isotropic, the Mott-Wannier equation can be conveniently reduced to a radial equation. In addition, to simplify the numerical

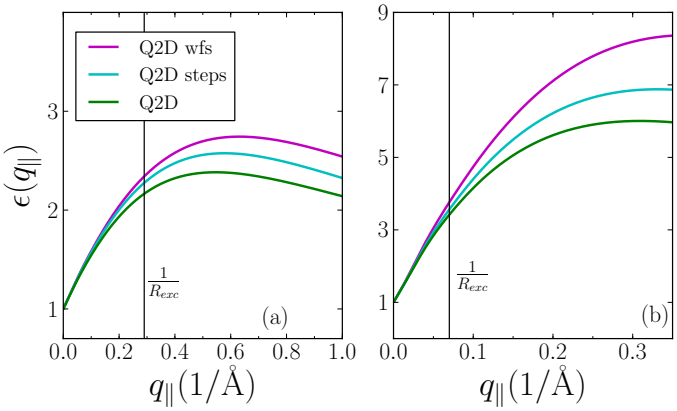

Figure 4.5: Macroscopic dielectric functions for (a) hBN and (b) MoS_2 calculated within different levels of approximation described in the text. The vertical line indicates the reciprocal space exciton radius.

treatment of the divergence of the interaction for small electron-hole separation, a logarithmic grid is employed. The results for the lowest lying exciton binding energy are given in table 4.1. All the approaches agree well with each other, and the agreement with the BSE benchmark can be considered really good given the simplicity of the models. Surprisingly the different level of approximation of the out-of-plane electron/hole distribution and related potentials, account for less than a few percents difference in binding energy. As anticipated above, this can be justified by means of fig. 4.5. Indeed, the wavevector values relevant for the description of the exciton are the ones smaller or comparable to its reciprocal space extension, regime for which the different effective macroscopic dielectric functions closely follow each other. A similar argument can be used to explain the practically perfect agreement between the Q2D and 2D approaches. In fact, for $q_{\parallel} < 1/R_{\mathrm{ex}}$, the Q2D dielectric functions are linear and therefore well represented by the linear approximation in the 2D model.

To conclude, solving the Mott-Wannier equation with the 2D screened interaction should be the method of choice in dealing with isolated layers since it is as accurate as the Q2D methods but easier to implement from a numerical point of view.

4.4 Simple Effectively Screened Hydrogenic Model

While the generalized Mott-Wannier equation is already a simplification of the BSE, it would be great if one could do even better by reducing the task of calculating exciton binding energies to the evaluation of a simple analytic expression. This is what is usually done in bulk systems where it is possible to define a static dielectric constant and therefore use the original form of the Mott-Wannier eq. (4.1), which can readily be solved to give:

$$E_{\mathrm{b}}^{\mathrm{3D}} = \frac{\mu_{\mathrm{ex}}}{2\epsilon_{\mathrm{3D}}^2}. \tag{4.20}$$

Getting exciton binding energies in 3D is then just a matter of calculating ab-initio effective masses and bulk dielectric constants.

In paper III we show that, despite the inherent non-locality of the dielectric screening, we can obtain a simple formula for the exciton binding energy even in the case of 2D materials. The key to get to such a result is to define an effective dielectric constant as the average screening felt by the exciton, in formula:

$$\epsilon_{\mathrm{eff}} = \frac{a_{\mathrm{eff}}^2}{\pi} \int_0^{2\pi} d\theta \int_0^{1/a_{\mathrm{eff}}} dq_{\parallel} q_{\parallel} \epsilon_{\mathrm{2D}}(\mathbf{q}_{\parallel}). \tag{4.21}$$

Here a_{eff} is the radius of the exciton in real space (equivalent to the R_{ex} used in the previous section). Borrowing the result for the ground state of the 2D hydrogen atom [93], the exciton radius a_{eff} can be expressed in terms of the effective dielectric constant as $a_{\mathrm{eff}} = \epsilon_{\mathrm{eff}}/2\mu_{\mathrm{ex}}$. This implies that eq. (4.21) has to be solved self-consistently. The use of the 2D macroscopic dielectric function, $\epsilon_{\mathrm{2D}}(\mathbf{q}_{\parallel}) = 1 + 2\pi\alpha q_{\parallel}$, beside giving a

Table 4.1: Numerical values for the energy of the lowest bound excitonic state at the direct gap. Both the BSE and the models are based on LDA ab-initio calculations. The exchange contribution to the BSE kernel is not included as justified in section 4.1.

	$\mathbf{E_b^{BSE}}$(eV)	$\mathbf{E_b^{Q2D}}$(eV)	$\mathbf{E_b^{2D}}$(eV)	$\mathbf{E_b^{steps}}$(eV)	$\mathbf{E_b^{wfs}}$(eV)
hBN	2.05	2.35	2.34	2.23	2.29
MoS_2	0.43	0.61	0.60	0.57	0.59

good description of screening in isolated 2D layers, allows for the calculation of the integral in eq. (4.21), specifically:

$$\epsilon_{\text{eff}} = \frac{1}{a_{\text{eff}}^2}\left(1 + \frac{4\pi\alpha}{3a_{\text{eff}}^2}\right). \tag{4.22}$$

Substituting the expression for a_{eff} I get:

$$\epsilon_{\text{eff}} = \frac{1}{2}\left(1 + 32\pi\alpha\mu_{\text{ex}}/3\right). \tag{4.23}$$

Using the result for the ground state energy of the 2D hydrogen [93] I finally arrive at:

$$E_{\text{b}}^{\text{eff}} = \frac{2\mu_{\text{ex}}}{\epsilon_{\text{eff}}^2} = \frac{8\mu_{\text{ex}}}{\left(1 + 32\pi\alpha\mu_{\text{ex}}/3\right)^2}, \tag{4.24}$$

which is the equivalent of eq. (4.20) for 2D materials.

The blue circles in fig. 4.6 illustrate the validity of eq. (4.24) for 51 isolated semiconducting transition metal dichalcogenides [21] by comparing to the exciton binding energies obtained from the solution of the generalized Mott-Wannier equation with a 2D interaction. I would like to point out that some of the 51 materials have indirect gap and therefore they can form *indirect* excitons, i.e. excitons where the electron and hole are localized in different points of the BZ. Indirect excitons and (direct) excitons can be treated on an equal footing, provided that the effective mass is calculated from the bands extrema hosting the electron and the hole. Overall the analytic formula performs really well, giving an excellent agreement for loosely bound exciton ($E_{\text{b}} \leq 0.5$eV) but a tendency to overestimate the more strongly bound ones.

An interesting feature of eq. (4.24) is that it becomes independent of the exciton effective mass for large values of $\alpha\mu_{\text{ex}}$, specifically:

$$E_{\text{b}}^{\text{eff}} \simeq \frac{3}{4\pi\alpha}, \qquad \text{for} \quad 32\pi\alpha\mu_{\text{ex}}/3 \gg 1. \tag{4.25}$$

Surprisingly this approximation performs almost as good as the original expression, as shown by the red squares in fig. 4.6. The independence from the mass can be explained in terms of the interplay of two opposing effects. While a higher effective

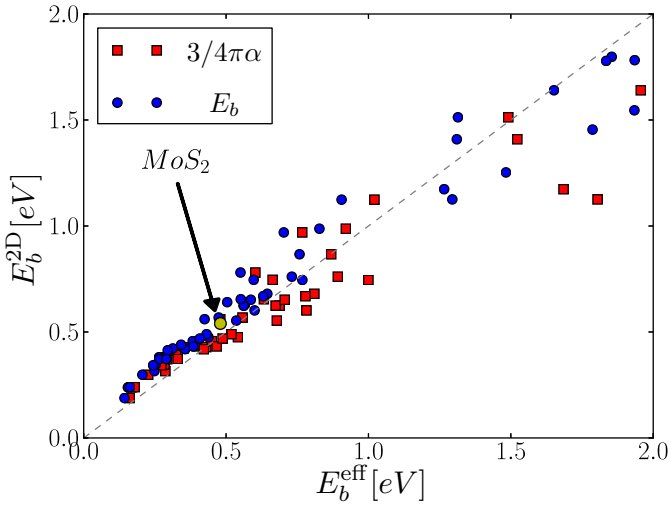

Figure 4.6: Effective dielectric constant model compared to the solution of the Mott-Wannier equation with a 2D screened electron-hole interaction. The exciton binding energies are calculated for 51 semiconducting transition metal dichalcogenides from Ref. [21].

mass tends to localize and bind the exciton more, the higher dielectric screening for localized excitons reduces the electron hole interaction, eventually compensating for the increase in the binding energy.

4.4.1 Linear scaling of the 2D polarizability constant with respect to the band gap

In Ref. [94] it is claimed that the exciton binding energy from BSE calculations scales linearly with the size of the band gap. If this is true, we expect the 2D polarizability constant to scale linearly with the inverse of the band gap, since according to eq. (4.25) $\alpha \propto 1/E_{\text{b}}^{\text{eff}}$. The values of the 2D polarizability constant for the 51 TMDs are plotted against the LDA band gaps in fig. 4.7, confirming a certain level of linear scaling. The scaling law can be argued by starting from the definition of the 2D polarizability constant in eq. (3.31). There, α is expressed in terms of the reducible polarizability, however if we neglect the effect of local field effects, which should not affect trends,

we can replace the reducible with the irreducible polarizability[1]

$$\alpha \simeq \alpha^{\mathrm{NLF}} = -\frac{L}{2}\left.\frac{d^2\chi^0_{0\,0}(q_\parallel)}{d\mathbf{q}_\parallel^2}\right|_{\mathbf{q}_\parallel=0}. \tag{4.26}$$

The advantage of having $\chi^0_{0\,0}(\mathbf{q}_\parallel)$ is that its reciprocal space representation, as it follows from eq. (3.8), can be readily expanded in power series of $q_\parallel$ around $q_\parallel = 0$, by approximating $e^{\pm i\mathbf{q}_\parallel\cdot\mathbf{r}} = 1 + q_\parallel\hat{q}_\parallel\cdot\mathbf{r} + o(q_\parallel^2)$:

$$\chi^0_{0\,0}(\mathbf{q}_\parallel) = \frac{2}{\Omega_\parallel L}\sum_{n}^{\mathrm{occ}}\sum_{n'}^{\mathrm{unocc}}\sum_{\mathbf{k}_\parallel}^{\mathrm{BZ}}\frac{|\langle\phi^{\mathrm{KS}}_{n\mathbf{k}_\parallel}|\hat{q}_\parallel\cdot\mathbf{r}|\phi^{\mathrm{KS}}_{n'\mathbf{k}_\parallel}\rangle|^2}{\epsilon^{\mathrm{KS}}_{n'\mathbf{k}_\parallel}-\epsilon^{\mathrm{KS}}_{n\mathbf{k}_\parallel}}q_\parallel^2 + o(q_\parallel^2). \tag{4.27}$$

To get this result the lowest order expansion of the wave functions and eigenvalue differences have been employed. In accordance to what was discussed in section 3.2, we find that $\chi^0_{0\,0}(\mathbf{q}_\parallel) \propto q_\parallel^2$. Finally, from the equation above, we can identify 2D

[1] This is easily proven by following the same steps leading to eq. (3.31), and keeping in mind that without local field effects, $\epsilon^{\mathrm{Q2D}}_{\mathrm{M}}(\mathbf{q}_\parallel,\omega;d) = \frac{2}{d}\sum_{G_z} e^{iG_z z_0}\frac{\sin(G_z d/2)}{G_z}\epsilon_{0G_z\,00}(\mathbf{q}_\parallel)$, and the dielectric matrix can be expressed in terms of the irreducible polarizability χ^0 through the RPA approximation (see eq. (3.9)).

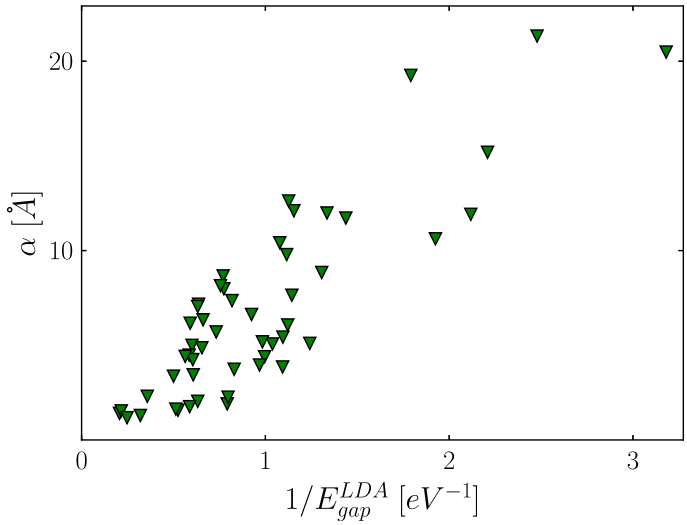

Figure 4.7: Close to linear scaling of the 2D polarizability constant with respect to LDA band gaps. Results are shown for 51 semiconducting transition metal dichalcogenides from Ref. [21].

polarizability constant as the second order coefficient of the expansion:

$$\alpha \simeq -\frac{2}{\Omega_\parallel}\sum_{n}^{\text{occ}}\sum_{n'}^{\text{unocc}}\sum_{\mathbf{k}_\parallel}^{\text{BZ}}\frac{|\langle\phi^{\text{KS}}_{n\mathbf{k}_\parallel}|\hat{q}_\parallel\cdot\mathbf{r}|\phi^{\text{KS}}_{n'\mathbf{k}_\parallel}\rangle|^2}{\epsilon^{\text{KS}}_{n'\mathbf{k}_\parallel}-\epsilon^{\text{KS}}_{n\mathbf{k}_\parallel}}. \tag{4.28}$$

It is now possible to see the explicit dependence on the inverse of the band gap and justify the results in fig. 4.7. This result then tells us that the linear scaling of the binding energy follows directly from α and not from the effective mass as argued in Ref. [94]

4.4.2 Non-hydrogenic Rydberg series

A well established peculiarity of 2D materials is that the excitonic spectrum (the collection of excited excitonic states) does not follow a standard hydrogen-like Rydberg series. As demonstrated by Chernikov *et.al.* in Ref. [95] for WS_2 supported on a SiO_2 substrate, the experimental energy levels corresponding to the excited excitonic s-like states are completely missed if the simple 2D hydrogenic eq. (4.1) is used. This is because the "non-hydrogenicity" is the result of the non-locality in the dielectric screening. In their paper, Chernikov *et.al.* show that the experimental non-hydrogenic series is well represented either by solving the 2D Mott-Wannier equation with a 2D screened electron-hole interaction and α used as a fitting parameter, or by using eq. (4.1) and introducing a fitted quantum state dependent effective dielectric constant. While I will show in the next chapter that to reproduce their experimental data from first-principles calculations the effect of the substrate has to be included, here we can naturally understand the quantum number dependence of the effective dielectric constant from our simple effectively screened hydrogenic model.

An excited excitonic state is characterized by a radius that is larger than for the lower lying states. Specifically for the s-states ($l = 0$), the solution of the 2D hydrogenic problem gives [93]:

$$a_{\text{eff},n} = \frac{3n(n-1)+1}{2\mu_{\text{ex}}}\epsilon_{\text{eff},n}, \tag{4.29}$$

with n the principal quantum number. Since the effective screening is defined in terms of the excitonic radius, the quantum number dependence is directly transferred to the dielectric constant, as given by the self-consistent solution of eq. (4.21):

$$\epsilon_{\text{eff},n} = \frac{1}{2}\left(1+\sqrt{1+\frac{32\alpha\mu_{\text{ex}}}{9n(n-1)+3}}\right). \tag{4.30}$$

With this expression one can then calculate the excited excitonic energies as [93]:

$$E^{\text{eff}}_n = -\frac{\mu_{\text{ex}}}{2(n-\frac{1}{2})^2\epsilon^2_{\text{eff},n}}. \tag{4.31}$$

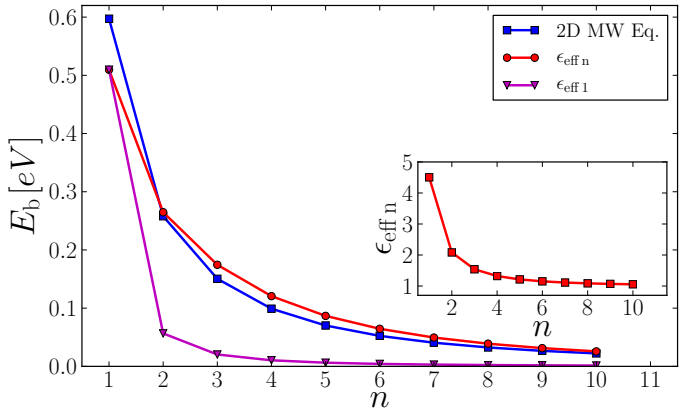

Figure 4.8: Rydberg series (excitonic spectrum) for monolayer 2H-WS_2 calculated from (blue) Mott-Wannier eq. (4.9) with a 2D screened interaction energy, (red) quantum number dependent dielectric constant model (eq. (4.31)) and (magenta) basic hydrogenic model (eq. (4.1)), where the effective dielectric constant is kept fixed and equal to the one for the ground state ϵ_1. The dependence of the effective dielectric constant on the quantum number is illustrated in the inset. Including such a dependence is crucial to reproduce the values from the 2D Mott-Wannier equation.

As mentioned before, Ref. [95] shows that the 2D Mott-Wannier equation successfully describes the non-hydrogenic behavior of the Rydberg series, and therefore we can use it to benchmark eq. (4.31). The Rydberg series for WS_2 is reported in fig. 4.8. A good agreement is found between the 2D Mott-Wannier equation values (blue line) and the effectively screened hydrogenic model (red line). The quantum number dependence of the effective dielectric constant is illustrated in the inset, and it is evident that the more the excitonic state is localized the higher is the screening that it experiences. To highlight the importance of this quantum state dependence, we report the hydrogenic Rydberg series obtained from a 2D hydrogenic equation with a fixed effective dielectric constant $\epsilon_{\text{eff},n} = \epsilon_{\text{eff},1}$ (magenta line). It is clear that such an approach cannot be applied to 2D materials.

As final remark one should notice that it would be straightforward to extend our effectively screened model to excitonic levels with non-zero angular momentum l. Indeed, it is enough to include the l dependence in the excitonic radius [93] and calculate a new effective dielectric constant to insert in the formula for the exciton energies. Since it can be shown that the higher angular momentum states are more extended, they would experience a lower effective screening and consequently a higher binding energy. Such a trend is in fact consistent with the findings in Ref. [96].

CHAPTER 5

Designing Excitons in van der Waals Heterostructures

The large and still growing family of two-dimensional materials is a great resource of building blocks for (opto)-electronic devices. Just as LEGO bricks, two-dimensional layers can be vertically stacked to create more complex structures named van der Waals heterostructures (vdWHs) [34, 97, 98]. The possibility of tuning vdWHs electronic and dielectric properties by combining layers with different properties and/or the order of the stack has lead to the fabrication of new efficient devices such as light emitting diodes [32], field effect transistors [99], ultrafast photodetectors [33,100] and so on. As for their monolayer constituents, the optical response of vdWHs is dictated by excitonic effects [32, 33, 34, 35, 36, 101]. Not only can vdWHs host electron-hole excitations within the constituent layers, but they are ideal for hosting excitations with the electron and the hole localized in distinct layers, namely interlayer excitons [102,103,104,105]. Compared to the isolated layers case, the dielectric screening in vdWHs is enhanced and it leads to the formation of more loosely bound excitons. This is a considerable advantage in opto-electronic devices, such as solar cells, where efficient electron-hole dissociation is required [34, 37]. Additional decrease in exciton binding energy is achievable for the interlayer excitons thanks to the spatial separation between the electron and the hole, which also entails longer exciton lifetimes [36, 102].

From an ab-initio point of view, the description of vdWHs is challenging, the main reasons being the following:

- Lattice mismatch among the layers: the use of supercells is often required, making the calculations particularly demanding;
- The number of layers of the stack could be large: as for the previous point this often leads to unfeasible calculations;
- Long range screening among the layers: including long range dielectric screening effects is not possible at the DFT level, and many-body perturbation theory

methods should be used instead.

It follows that standard ab-initio methods are limited to commensurable van der Waals stacks consisting of a few layers. In this chapter I will show how to overcome these limitations, by means of a multi-scale method, the quantum electrostatic heterostructure (QEH) method, which combines quantum accuracy at the monolayer level and macroscopic electrostatic coupling of the layers. The method builds upon the assumption that hybridization among the layers is negligible and therefore the dielectric response of the vdWH can be obtained from the dielectric response of the isolated layers. In other words the constituent monolayers can be mapped into dielectric building blocks which constitute the dielectric genome of the heterostructure. Once the dielectric function of the vdWH is known it can be, for example, used to calculate the screened electron-hole interaction and solve the generalized Mott-Wannier model (introduced in the previous chapter) to calculate intra and interlayer exciton binding energies. Furthermore the QEH approach can be combined with the G_0W_0 method to include the effect of interlayer screening in the electronic band structure and accurately calculate the band alignment in a vdWH, which is extremely relevant when it comes to device engineering.

The results and methodology discussed in this chapter are entirely based on Paper I, second part of Paper II and Paper IV. While in the following I will try to give a comprehensive overview, the reader interested in a more detailed explanation is referred to the papers.

5.1 The Quantum Electrostatic Heterostructure (QEH) Model

The goal of the Quantum Electrostatic Heterostructure Model (QEH) is to calculate the dielectric function of a vdWH directly from the dielectric response of the constituent monolayers. The main advantage of vdWHs is that the layers are held together via weak van der Waals interaction, with minimal or negligible hybridization. This means that it is fair to assume that the response to an external perturbation of each layer in the vdW stack is the same as the response in the freestanding condition and it can be condensed in a so called *dielectric building block*. Once the dielectric building blocks are calculated, they can be coupled together electrostatically in order to obtain the response of the full heterostructure. How this is done in practice is explained in the following.

In principle the response of the full heterostructure can be determined from eq. (2.38), which I rewrite here within the RPA approximation and in frequency space:

$$\chi(\mathbf{r}_1,\mathbf{r}_2;\omega) = \chi^0(\mathbf{r}_1,\mathbf{r}_2;\omega) + \int d\mathbf{r}_3 d\mathbf{r}_4 \chi^0(\mathbf{r}_1,\mathbf{r}_3;\omega) v_{\mathrm{C}}\mathbf{r}_3,\mathbf{r}_4)\chi(\mathbf{r}_4,\mathbf{r}_2;\omega). \tag{5.1}$$

Note that, for simplicity, I omitted the spin-variables. In this equation, the Coulomb interaction introduces correlation in the independent particle response χ_0 both at the intralayer and interlayer level. The main idea of the QEH approach is to simplify the solution of eq. (5.1) by including intra and interlayer correlation through two separate equations, as formally justified in the supplementary information of Paper I.

Because of the weak hybridization characteristic of vdWHs, the intralayer correlation can be calculated for each layer separately by solving eq. (5.1) in freestanding conditions and using a truncated Coulomb interaction. Next, for each layer, only the in-plane macroscopic component of the reducible polarizability is then considered. I denote the resulting reducible polarizability as $\tilde{\chi}_i(z, z'; \mathbf{q}_\parallel, \omega)$, with i being the layer index. Notice that while a real space representation is used for the out-of-plane direction, the in-plane dependence is treated in reciprocal space. To construct the building block, instead of keeping the full z, z' dependence of the response function we consider its multipole components:

$$\tilde{\chi}_{i\alpha}(\mathbf{q}_\parallel, \omega) = \int dz dz' (z - z_i)^\alpha \tilde{\chi}_i(z, z', \mathbf{q}_\parallel, \omega)(z' - z_i)^\alpha, \tag{5.2}$$

with $\alpha = 0,1, \ldots$ the multipole component index and z_i the center of the layer i. The reducible polarizability $\tilde{\chi}_{i\alpha}$ has to be interpreted as the α component of the response to an external field with a $e^{i\mathbf{q}_\parallel \cdot \mathbf{r}_\parallel}$-like variation in-plane and proportional to $(z - z_i)^\alpha$ in the out-of-plane direction. Specifically for the monopole and dipole components ($\alpha = 0$ and $\alpha = 1$ respectively), it follows that $\tilde{\chi}_{i\alpha}$ is the response function to a field which is constant or has a linear variation across the layer. To complete the building block, we one more ingredient that will be needed in the calculation of the interlayer Coulomb coupling (see eq. (5.5)). This is the out-of-plane shape of the density induced by the external perturbation. In particular recalling eq. (3.2), we can define the α multipole component of layer i as:

$$\rho_{i,\alpha}(z, \mathbf{q}_\parallel, \omega) = \frac{\int dz' \tilde{\chi}(z, z', \mathbf{q}_\parallel, \omega)\,(z' - z_i)^\alpha}{\tilde{\chi}_{i,\alpha}(\mathbf{q}_\parallel, \omega)}, \tag{5.3}$$

where the denominator guarantees the right normalization. An illustration of the monopole and dipole components of the induced densities is reported in blue lines in fig. 5.1 (b) for a typical transition metal dichalcogenide (TMD). In general we find $\rho_{i,\alpha}$ to be independent of frequency and it is therefore enough to only keep the static part ($\omega = 0$). Furthermore we limit our building blocks to the monopole and dipole components, as it turns out to be enough to describe all the systems we looked at. To summarize, to obtain a building block one first calculate $\tilde{\chi}_i(z, z'; \mathbf{q}_\parallel, \omega)$, which accounts for intralayer correlation, from there the multipole components of the response and the induced densities are obtained according to eq. (5.2) and eq. (5.3). The building blocks for more than 50 2D layers ranging from TMDs to hBN and graphene can be found in our computational material repository [106].

Once the building blocks for the layers in the vdWH are known, one can include the correlation at the interlayer level by coupling the building blocks by solving the

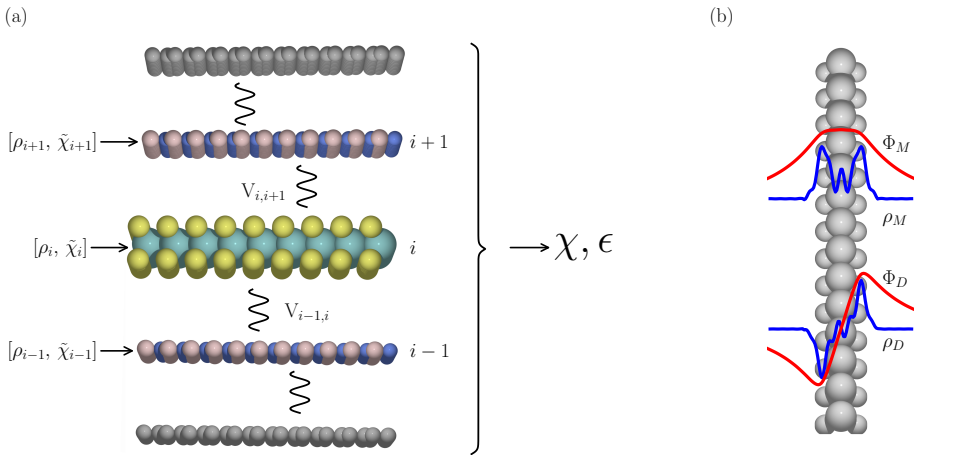

Figure 5.1: Panel (a): Schematic representation of the QEH model, where the two dimensional layers, whose dielectric response is calculated with quantum accuracy and condensed in dielectric building blocks, are coupled together macroscopically via a long range Coulomb interaction. Panel (b): Illustration of the monopole and dipole component of the induced density $\rho_{\mathrm{M/D}}(z)$ in red and corresponding monopole and dipole induced potentials $\phi_{\mathrm{M/D}}(z)$.

following Dyson equation in the QEH basis:

$$\chi_{i\alpha,j\beta}(\mathbf{q}_\parallel,\omega) = \tilde{\chi}_{i,\alpha}(\mathbf{q}_\parallel,\omega)\delta_{i\alpha,j\beta} + \tilde{\chi}_{i,\alpha}(\mathbf{q}_\parallel,\omega)\sum_{ki,\gamma} V^{\mathrm{inter}}_{i\alpha,k\gamma}(\mathbf{q}_\parallel)\,\chi_{k\gamma,j\beta}(\mathbf{q}_\parallel,\omega), \qquad (5.4)$$

with i,j,k layer indices and $\alpha,\beta,\gamma \in [0,1]$. The kernel $V^{\mathrm{inter}}_{i\alpha,k\gamma}(\mathbf{q}_\parallel)$ in the RHS accounts for the interlayer interaction and is defined as:

$$V^{\mathrm{inter}}_{i\alpha,k\gamma}(\mathbf{q}_\parallel) = (1-\delta_{i,k})\int dz \rho_{i,\alpha}(z,\mathbf{q}_\parallel)\Phi_{k\gamma}(z,\mathbf{q}_\parallel). \qquad (5.5)$$

where $\Phi_{k\gamma}(z,\mathbf{q}_\parallel)$ is the potential generated by the induced density $\rho_{k\gamma}(z,\mathbf{q}_\parallel)$ and it can be calculated by solving a simple Poisson equation. An example of the monopole and dipole components of such a potential is given by the red lines in fig. 5.1 (b). Equation (5.5) shows that the interlayer Coulomb kernel is nothing else than the overlap between the induced density and the potential generated by the induced density. The factor $(1-\delta_{i,k})$ guarantees that the intralayer Coulomb interaction, already accounted for in $\tilde{\chi}_{i,\alpha}$, is left out.

Finally, with the knowledge of the full reducible polarizability, the dielectric matrix

of the vdWH is obtained by the equivalent of eq. (2.40) in the QEH basis:

$$\epsilon^{-1}_{i\alpha,j\beta}(\mathbf{q}_\parallel,\omega) = \delta_{i\alpha,j\beta} + \sum_{k,\gamma} V_{i\alpha,k\gamma}(\mathbf{q}_\parallel)\chi_{k\gamma,j\beta}(\mathbf{q}_\parallel,\omega). \tag{5.6}$$

An illustration of the QEH model is sketched in fig. 5.1 (a). For more details on the derivation of the equations presented so far, the reader is referred to the supplementary information of Paper I. To conclude, the QEH provides a quantum mechanical description of the non-local screening and it can be applied to heterostructures of arbitrary composition and thickness. It is worth to mention that in a number of recent papers [88, 107, 108], the dielectric screening in heterostructures has been investigated using the dielectric continuum model proposed by Keldysh [109], where the screening properties of the layers are modified by the formation of image charges at the interfaces. This classical approach, however, neglects the intrinsic non-localities of the environmental screening, which are instead naturally included at a quantum mechanical level in our QEH model.

In the following I will present several examples where the QEH method is applied. We implemented the QEH method in GPAW and the python script that solves the electrostatic equation starting from the dielectric building blocks can be found in Ref. [106].

5.2 Dielectric Function in MoS_2: from 2D to 3D

In chapter 3, I discussed how the dielectric response of a bulk material differs from the response of a 2D layer. I showed that while for a bulk semiconductor the macroscopic static dielectric function can be replaced by a constant, this is not possible for a 2D semiconductor since the dielectric function is strongly dependent on the in-plane wavevector $\mathbf{q}_\parallel$. By means of the QEH model, it is now possible to investigate the transition between the 2D and 3D behavior. An example of such a transition is shown in fig. 5.2 (b) for the case of MoS_2. The figure shows the QEH macroscopic dielectric function for multi-layer MoS_2 together with the ab-initio results for monolayer, bilayer and bulk. In particular, the QEH macroscopic dielectric function is obtained as the average over the layers composing the stack. While the agreement with the monolayer ab-initio result is trivial, since the latter is used to define the dielectric building block, the agreement for the bilayer is remarkable considering that the effect of hybridization in bilayer MoS_2 is known to affect the electronic band structure [110]. Turning the argument around, this means that the dielectric properties are not that sensitive to hybridization. As the number of layers increases, the QEH dielectric function increases and approaches the bulk ab-initio result. However, for small values of $q_\parallel$, a linear drop towards unity is observed, with the drop becoming steeper for increasing N. This indicates that, exactly as for the isolated layer case, the dimensionless parameter $q_\parallel d$, with d thickness of the slab, sets whether the behavior of the dielectric function is 2D like ($q_\parallel d \ll 1$) or 3D like ($q_\parallel d \gg 1$). Finally it is worth noticing that

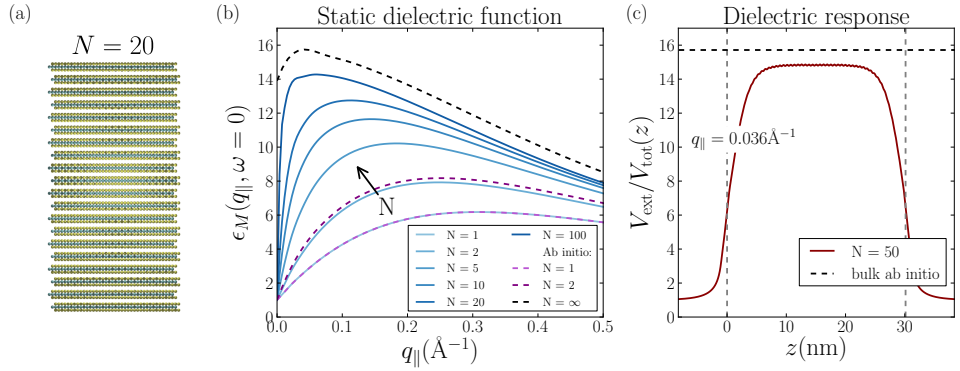

Figure 5.2: Panel (a): Cartoon of the MoS_2 multilayers. Panel (b): Dependence of the macroscopic static dielectric function $\epsilon_M(\mathbf{q}_\parallel, \omega = 0)$ on the number of MoS_2 layers N. The QEH dielectric function converges towards the bulk ab-initio result for large N. Panel (c): Effective local dielectric function, defined as $V_{ext}/V_{tot}(z)$, meaningful for the screening of constant external potential across a $N = 50$ layers stack. The external potential is proportional to $e^{i\mathbf{q}_\parallel \cdot \mathbf{r}_\parallel}$ in-plane direction, with $\mathbf{q}_\parallel = 0.036$Å^{-1}.

even for $N = 100$ the QEH dielectric function has not converged towards the bulk one. While this is partially due to hybridization effects, the slow convergence can be attributed to suppressed screening at the surfaces of the van der Waals stack. In fig. 5.2 (c) one can, in fact, see that the z-dependent local dielectric function defined as $\epsilon(z) = V_{ext}/V_{tot}(z)$ decreases towards the surfaces consequently lowering the contribution to the macroscopic screening.

5.3 Combining the QEH with the Mott-Wannier equation

Combining the QEH with the generalized Mott-Wannier eq. (4.9) allows us to describe excitonic effects in vdWHs. The screened electron-hole interaction energy given by eq. (4.14) is readily expressed in the QEH formalism as:

$$W(q_\parallel) = \underline{\rho}_e^{\mathrm{T}}(q_\parallel)\ \underline{\underline{\epsilon}}^{-1}(q_\parallel)\ \underline{\varphi}_h(q_\parallel), \tag{5.7}$$

with $\underline{\rho}_e$ ($\underline{\phi}_h$) being the electron density (hole induced potential) expanded in the basis set of monopole and dipole components of the induced density (induced potential). To be more specific, an arbitrary electron density $\underline{\rho}_e^{\mathrm{T}}(q_\parallel, z)$ can be written as $\underline{\rho}^{\mathrm{T}} = [\rho_{1M}, \rho_{1D}, \rho_{2M}, \rho_{2D}, \cdots, \rho_{nM}, \rho_{nD}]$ with $\rho_{i\alpha}$ the induced monopole/dipole density at

layer i. A similar expression can be formulated for the hole induced potential by using the basis of induced potentials instead. It is instructive to consider the practical example of a vdWH consisting of three layers hosting an intralayer exciton localized at layer $i = 1$. The electron density and hole potential would then be $\underline{\rho}^{\mathrm{T}} = [1, 0, 0, 0, 0, 0]$ and $\underline{\varphi}^{\mathrm{T}} = [1, 0, 0, 0, 0, 0]$ respectively. While it should be clear why only the layer $i = 1$ entries are non zero, the fact that I set the layer $i = 1$ dipole components to zero follows from the reasonable assumption that the electron and hole density distributions are symmetric around the layer, exactly as in fig. 4.2. Once the electron-hole interaction is known, it can be plugged in the Mott-Wannier equation. The other ingredient missing is the exciton effective mass. While, in principle, the effective mass should be obtained from the electron and hole effective masses calculated from the band structure of the vdWH, we assume that due to the weak hybridization the freestanding layer masses are preserved.

Before moving to the example sections, I would like to point out the screeened electron hole interaction obtained from the QEH is intrinsically of a quasi-2D (Q2D) type since the finite extension of the electron and the hole density distribution in the out-of-plane direction is taken into account through the QEH basis set. In the next section this will prove important for the right description of excitons in vdWH, where the condition $q_{\parallel} d \ll 1$ might no longer be satisfied.

5.3.1 The breakdown of the Linear Screening Model

In the previous chapter, I concluded that a linear approximation of the dielectric function is satisfying for describing the screening of the exciton electron-hole interaction in isolated 2D crystals. To demonstrate that this is not necessarily the case in vdWHs let us consider as a practical example a sandwich like heterostructure consisting of an MoS_2 layer encapsulated in n layers of hBN, as sketched in fig. 5.3 (a). To visualize the variation in dielectric screening felt by an exciton in a given layer it is convenient to extend the definition of effective macroscopic dielectric function in eq. (4.19) to vdWHs:

$$\epsilon(q_{\parallel}) = \frac{\underline{\rho}_e^{\mathrm{T}}(q_{\parallel})\ \underline{\varphi}_h(q_{\parallel})}{\underline{\rho}_e^{\mathrm{T}}(q_{\parallel})\ \underline{\underline{\epsilon}}^{-1}(q_{\parallel})\ \underline{\varphi}_h(q_{\parallel})}. \tag{5.8}$$

The effective dielectric function of MoS_2 in the sandwich structure as a function of a varying number of hBN layers is shown in fig. 5.3 (b) and it is referred to as Q2D. In the same plot the linear approximation, obtained as a fit of the Q2D dielectric function, is also reported and denoted by 2D. As was the case of multilayer MoS_2 for fig. 5.2, by increasing the thickness of the stack, i.e. adding more hBN layers, the screening becomes higher and the drop to unity becomes steeper. This is once again the result of the interplay between 2D and 3D behavior governed by the thickness of the heterostructure. The Q2D dielectric function and its linear approximation can be used to calculate the binding energy of the lowest lying exciton in the MoS_2 layer. The results are shown in fig. 5.3 (c). As one could expect, the increased screening

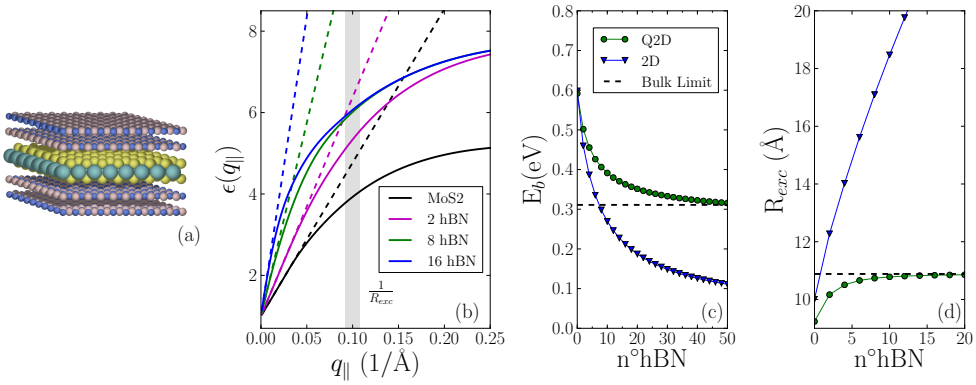

Figure 5.3: Panel (a): Sketch of the MoS2-hBN sandwich structure. Panel (b): Effective macroscopic dielectric function from eq. (5.8) (full line) compared to its linear approximation (dashed lines) for an increasing number of hBN layers. The shaded region indicates the range spanned by the inverse of the exciton radii in the considered structures. Panel (c) and (d): Binding energy and radii of the lowest lying excitons as function of hBN layers. The results calculated using the full $q_\parallel$-dependence and the linear approximation for the dielectric function are both shown.

leads to a reduction of the binding energy, which for the Q2D dielectric function converges towards a finite value of 0.31 eV, meaning that adding extra hBN at a large distance from the MoS_2 has no significant effect. On the other hand, the binding energy obtained from the linear approximation quickly diverges from the Q2D and eventually approaches zero. Accordingly, fig. 5.3 (d) shows that, while the radius for the Q2D reaches a constant value, the radius calculated with the linear approximation diverges. In the previous chapter, I established that the linear approximation performs well whenever the $q_\parallel d \ll 1$ and that the relevant $q_\parallel$ for the exciton are the ones smaller than the inverse of the excitonic radius, i.e. $q_\parallel < 1/R_{\text{exc}}$. Combining the two criteria one has that for excitons the linear approximation is expected to work for $R_{\text{exc}} > d$. While this condition is always satisfied for isolated layers, it is not necessarily true for vdWHs since their thickness can be indefinitely increased whereas the exciton radius eventually reaches a constant value. This explains why the linear approximation breaks down. This is confirmed by inspection of fig. 5.3 (b), where it is clear that the linear approximation significantly overshoots the Q2D dielectric function in the range of $q_\parallel$ lower than the inverse of the excitonic radius (indicated as a shaded region spanning the radii for the heterostructures with the different number of hBN).

While a 2D picture cannot always be applied to describe vdWHs, it is still possible

to reformulate the QEH model in terms of 2D building blocks as opposed to the Q2D ones in the original version (see sketch in fig. 5.4 (a)). Each layer is assumed to be infinitesimally thin and characterized by a linear macroscopic dielectric function $\epsilon^{2\mathrm{D}}(q_\parallel) = 1 + 2\pi\alpha q_\parallel$. Without considering the out-of-plane extension of the layer, only the monopole components of the induced density and response function have an obvious definition. Given a layer i, the induced density is indeed just a delta function at the layer center z_i, while the response function is obtained directly from the 2D dielectric function of the isolated layer:

$$\tilde{\chi}^{2\mathrm{D}}_{i\mathrm{M}}(q_\parallel) = \frac{q_\parallel}{2\pi}\left[\epsilon_i^{-1\,2\mathrm{D}}(q_\parallel) - 1\right] = -\frac{\alpha_i q_\parallel^2}{1 + 2\pi\alpha_i q_\parallel}, \tag{5.9}$$

where I used that the Coulomb potential in 2D is $2\pi/q_\parallel$. This strict 2D picture has then the advantage that the interlayer Coulomb kernel in eq. (5.5) can be worked out analytically:

$$V_{iM,kM}(q_\parallel) = (1 - \delta_{i,k})\frac{2\pi e^{-q_\parallel |z_i - z_k|}}{q_\parallel}. \tag{5.10}$$

The validity of the QEH model based on 2D building blocks is assessed against the standard QEH for heterostructures consisting of monolayer MoS_2 supported on a varying number of hBN layers (see fig. 5.4 (b)). Interestingly, even by starting from building blocks with a linear dielectric function, the interlayer screening induces non-linearities in the effective dielectric functions for $q_\parallel < 1/R_{\mathrm{exc}}$, as it can be seen in fig. 5.4 (c). The deviation from the linear behavior brings the QEH@2D dielectric functions closer to the QEH@Q2D ones (check Paper II for the results obtained with the QEH@Q2D on this specific structure) and leads to an exciton binding energy which, unlike the one from the linear screening approximation, converges to a finite value for increasing number of hBN layers, as shown in fig. 5.4 (d). However one can observe that the reduction in binding energy predicted by the QEH@2D is around 50% smaller than the one predicted by the QEH@Q2D approach, meaning that within the QEH@2D the interlayer screening is underestimated. This can be ascribed both to the fact that strict 2D building blocks are less effective at screening because the induced potentials away from the layer decays faster than it should and to the fact that the dipole component of the response is neglected. To conclude, even if the QEH based on strict 2D building blocks is formally and practically much simpler, it is not as accurate as the Q2D counterpart.

5.3.2 Non-hydrogenic Rydberg Series in supported WS_2

Accounting for environmental screening is not only relevant for vdWHs. It is often the case that optical measurements on 2D materials are performed in the presence of a substrate and, as demonstrated in the previous section, this could significantly alter the excitonic properties of the material under investigation. As I anticipated in section 4.4, the inclusion of dielectric screening due to substrate is necessary for

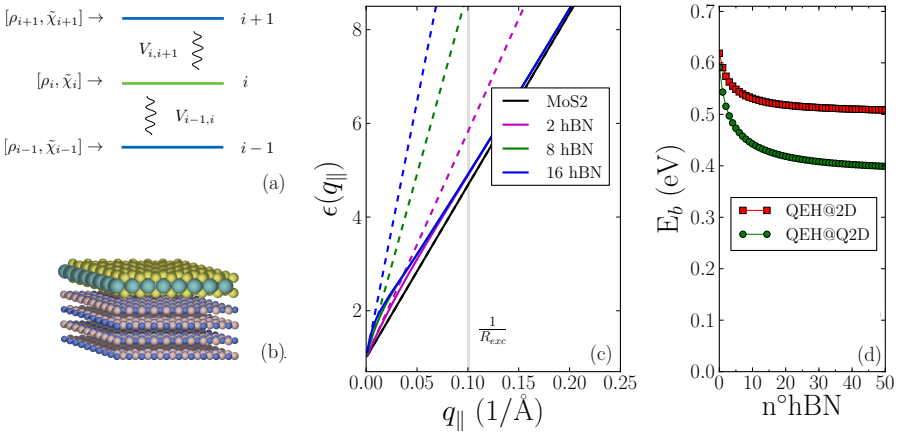

Figure 5.4: Comparison between QEH@Q2D and QEH@2D approches. Panel (a) Sketch of the QEH approach with two-dimensional building blocks (QEH@2D). Panel (b) MoS_2 supported on hBN layers structure. Panel (c) effective macroscopic dielectric function obtained from the QEH@2D and its linear approximation. The shaded region indicates the range of the inverse of the excitonic radii for the different 'on top' structures. Panel (d) binding energy for the lowest lying exciton calculated with the QEH@Q2D and QEH@2D for the 'on-top' configuration.

a quantitative description of the non-hydrogenic Rydberg series in WS_2 measured in ref. [95]. In that particular experiment, indeed, the optical measurements were performed on WS_2 supported on a SiO_2 substrate. In order to simulate the effect of the substrate with the QEH model, we place a WS_2 layer on top of a 100 hBN layers slab as sketched in fig. 5.5 (a). The choice of hBN instead of SiO_2 is dictated by the limitation of the QEH to layered structure. However, considering that hBN and SiO_2 have similar bulk dielectric constant, it is fair to assume that the dielectric behavior is the same. The experimental Rydberg series together with the ones calculated with the QEH for the freestanding and supported layer are plotted in fig. 5.5 (c). To highlight the non-hydrogenicity peculiar of 2D materials, in the same panel I report the Rydberg series obtained from a hydrogenic model with a fixed dielectric constant (fitted to reproduce the highest experimental excitonic state). Without any doubt, the agreement with the experimental values is improved with the inclusion of the substrate. In addition, the relative deviation between the freestanding and supported case is different for different excitonic states. This is an indication of the non-locality in the environmental screening, which is confirmed in fig. 5.5 (b) where it is shown that the difference in screened-electron hole interaction for the supported and freestanding WS_2 is larger for intermediate electron-hole separation. Since the spatial distribution

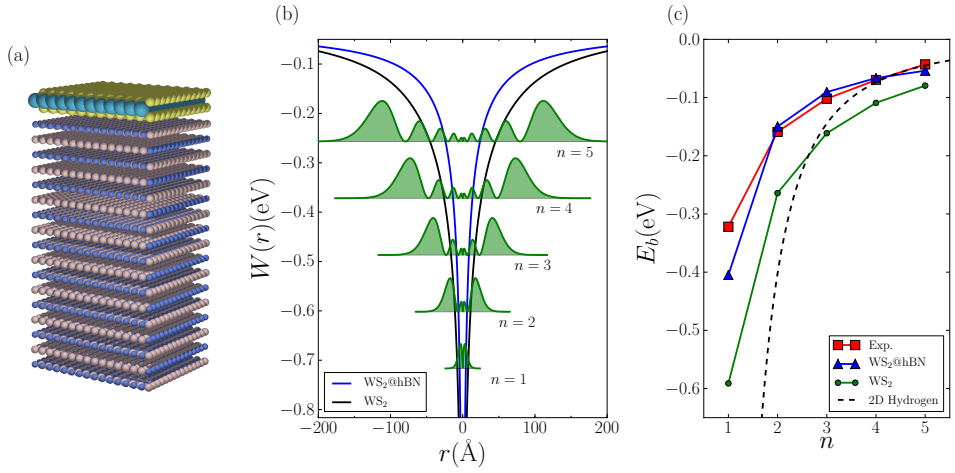

Figure 5.5: Excitonic Rydberg series in supported WS_2. Panel (a): WS_2 supported on a hBN substrate. Panel (b): screened electron-hole interaction energy in the supported (blue line) and free standing (black line) WS_2. The same panel shows the radial probability distribution, $r|F(r)|^2$, of the first five excitonic states. The normalization is arbitrary. Panel (c): The Rydberg series calculated with the QEH for freestanding WS_2 (green) and WS_2 on hBN (blue) are compared to the experimental data from Ref. [95] for WS_2 on SiO_2 (red). The hydrogenic Rydberg series obtained for a constant $\epsilon = 1.7$ is also displayed for reference.

of the intermediate excited excitonic states is mainly localized in the region where the screened interaction in the freestanding and supported layers differ the most (see fig. 5.5 (b)), it is the energy of these states that is affected the most. A more detailed analysis can be found in Paper III.

5.3.3 Excitons in MoS_2: from 2D to 3D

It is well known that when going from monolayer to bulk MoS_2, the binding energy of the exciton at the direct band gap is reduced by almost an order of magnitude and such an effect is usually attributed to quantum confinement. In this section I will show that combining the QEH with the generalized Mott-Wannier equation for 2D materials we are able to describe the transition from 2D to 3D behavior. At first glance, it might seem abusive to use the generalized Mott-Wannier equation for 2D materials to account for excitons in 3D systems since the motion in the out-of-plane

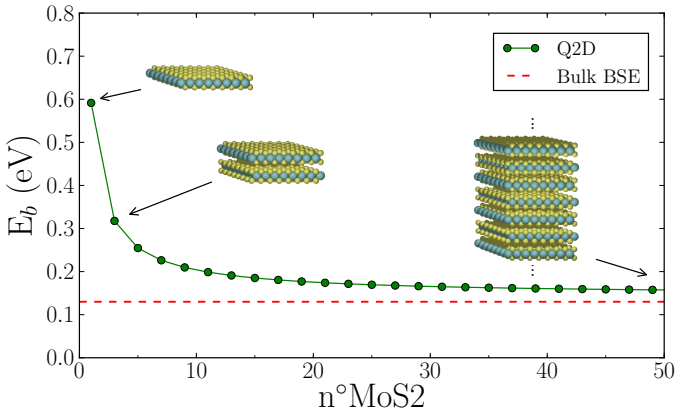

Figure 5.6: Binding energy of the most strongly bound exciton in multilayer MoS_2 calculated with the QEH method. The exciton is placed in the central MoS_2 layer and the reduction in the binding energy with the increase in number of layers is due to environmental screening. The bulk result calculated with BSE in Ref. [111] is almost completely recovered for 50 MoS_2 layers.

direction should be included. Specifically one should solve the following equation:

$$\left[-\frac{\nabla_{\parallel}^2}{2\mu_{\parallel}^{ex}} - \frac{\nabla_{\perp}^2}{2\mu_{\perp}^{ex}} + W(\mathbf{r})\right] F(\mathbf{r}) = E_b F(\mathbf{r}). \tag{5.11}$$

However for layered materials the out-of-plane exciton effective mass is much larger than the in-plane one, i.e $\mu_{\perp}^{ex} \gg \mu_{\parallel}^{ex}$. Therefore the kinetic energy contribution in the out-of-plane direction can be left out and the 2D Mott-Wannier equation is recovered. Since $\mu_{\parallel}^{ex}$ does not change considerably from monolayer to bulk MoS_2, as shown in Ref. [112], the variation in binding energy as a function of number of MoS_2 layers can only result from interlayer screening. To check the validity of this argument, we used the QEH to calculate the screened electron-hole interaction for an exciton localized in the central layer of MoS_2 slabs with a varying number of layers and then solved the Mott-Wannier equation to get exciton binding energies. The calculated values are shown in fig. 5.6. Going from 2D to 3D, the binding energy decreases continuously, eventually getting as close as $0.03eV$ to the value calculated with BSE for bulk MoS_2 [111]. This confirms that the reduction in exciton binding energy can be almost completely ascribed to interlayer screening rather than quantum confinement effects.

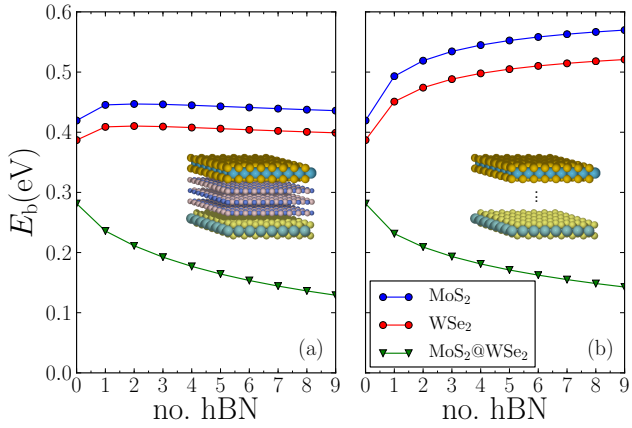

Figure 5.7: Intra and Interlayer exciton binding energy as a function of number of intercalating hBN (a) and vacuum (b) layers. The width of the vacuum layers is chosen to be the same as the hBN one.

5.3.4 Interlayer Excitons

As mentioned in the introduction, vdWHs can host electron-hole excitations with the two charges localized in different layers. The spatial separation between the electron and the hole can be used as a new degree of freedom in designing excitons in vdWHs. For example one could imagine that separating the two layers hosting the electron and the hole by intercalating other 2D materials could be a way to engineer exciton binding energies. In this section, I investigate this particular problem for the case of MoS_2/WSe_2 bilayers intercalated with hBN.

The generalization of the QEH formalism to the calculation of the screened-electron hole interaction for interlayer excitons is straightforward. Indeed it is enough to correctly represent the electron density and the hole induced potential in the QEH basis so that the two quantities are centered on the layers hosting the electron and the hole respectively. Let us consider the MoS_2/WSe_2 bilayer. Since, as I will justify in the next section, this structure is characterized by interlayer excitons with the electron sitting on MoS_2 and the hole on WSe_2, the electron density takes the form $\underline{\rho_e}^{\mathrm{T}} = [1,0,0,0]$, while the potential induced by the hole can be written as $\underline{\phi_h}^{\mathrm{T}} = [0,0,1,0]$. Next, the use of the generalized 2D Mott-Wannier for describing interlayer excitons is justified by the fact that the electron and hole motion is still along the in-plane direction, even if the two charges confined in distinct layers. The electron-hole out-of-plane separation naturally enters the screened electron-hole interaction. Additionally, the interlayer effective mass has to be calculated for the the electron and the hole from the WSe_2 and MoS_2 valence and conduction bands respectively.

The binding energy of the lowest lying interlayer exciton for the MoS_2/hBN/WSe_2 heterostructures are plotted in fig. 5.7 (a). In the same plot the binding energy for the MoS_2 and WSe_2 intralayer excitons are also reported. It is evident that the intralayer exciton binding energies remains more or less constant with the addition of hBN layers. This can be explained by a compensation between the increased dielectric screening due to the intercalation of hBN and the reduction of dielectric screening following the separation between the MoS_2 and WSe_2 which are the layers that are better at screening. The interlayer exciton binding energy in the bilayer is strongly reduced compared to the intralayer ones and it keeps decreasing as the number of hBN layers is increased. To separate the effect of screening induced by the hBN from the effect of spatial separation we perform similar calculations where the MoS_2 and WSe_2 layers are separated by vacuum as shown in fig. 5.7 (b). It is evident that the behavior of the interlayer exciton binding energy is the same, clearly indicating that the main effect of intercalating hBN is the increase in the electron-hole spatial separation. Finally, as expected, the binding energies of the intralayer exciton in MoS_2 and WSe_2 slowly approach their freestanding layer values with increasing vacuum. The slow recovery is a consequence of the long range nature of the dielectric screening.

5.4 Band Alignment in vdWHs: the G_0W_0-QEH approach

In order for a vdWH to feature interlayer excitons, a type II electronic band alignment between the layers hosting the excitation is strictly necessary [102]. Thus, a proper design of interlayer excitons has to start from an accurate description of the position of the electronic bands in the heterostructure. Accurate band structure calculations require high-level theoretical methods, such as G_0W_0, which are far from being applicable to realistic vdWHs. It would then be ideal to predict the electronic bands of a vdWH by performing band structure calculations for the monolayer constituents only. One of the main issues with this approach is hybridization effects, which, differently from the case of the dielectric response, are usually significant for electronic bands. The other main issue is, instead, the effect of interlayer dielectric screening on the electronic excitations. In this section I address these problems in the case of MoS_2/WSe_2 based heterostructures. The choice of these specific systems embraces both the lattice mismatch and large number of layers challenges and allows us to benchmark our results on band alignment and interlayer exciton binding energies (from the previous section) with available photoluminescence measurements from Ref. [104].

I start out by performing band structure calculations on bilayer MoS_2/WSe_2 at the LDA level in order to investigate the importance of hybridization between the layers. Since MoS_2 and WSe_2 layers are incommensurable (see fig. 5.8 (b)), the use of a supercell is required, since straining the layers to match the lattice would artificially affect the electronic bands (see Supplementary Information of Paper IV). The use

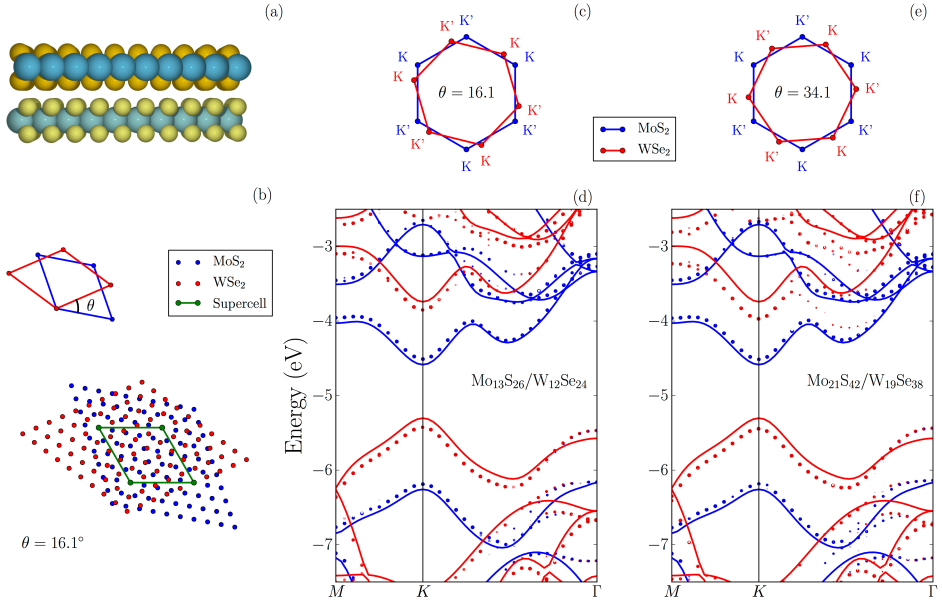

Figure 5.8: Panel (a): MoS_2-WSe_2 bilayer. Panel (b): Illustration of the primitive and super cells for the specific twisting angle $\theta = 16.1°$. Panels (c) and (e) show the geometrical relation between the BZs of the two material for two twisting angles, θ, 16.1° (a) and 34.4° respectively. Panel (d) and (f) show the LDA band structures of the MoS_2/WSe_2 bilayer for $\theta = 16.1°$ and $\theta = 34.4°$ respectively. The energy is taken with respect to vacuum. The bands of the bilayers (circles) are unfolded and projected to the respective layers. The isolated layers bands are shown for comparison (continuous lines). For simplicity spin-orbit coupling is not included.

of supercells makes it also possible to set up structures where the two layers are twisted with respect to each other, a configuration which is closer to the experimental situation where the alignment angle between the layers is not necessarily controlled. However, the use of supercells requires the unfolding of the band structure in order to compare to freestanding layer calculations. By following the method proposed in Ref. [113], which only relies on eigenvalues and wave functions obtained from the supercell calculation, I implemented a routine in GPAW to unfold any given supercell band structure to the corresponding primitive cell. To analyze the dependence of the electronic bands on the alignment angle θ, I setup MoS_2/WSe_2 bilayers for $\theta \sim 16.1°$ and $\theta \sim 34.4°$. The choice of these values is dictated by having a strain less than 1% and a minimal number of atoms in the supercell. The MoS_2 and WSe_2 BZs for the two twisted structures are shown in fig. 5.8 (c) and (e). The fact that the BZs of the two materials are different in size and rotated with respect to each other adds an

extra complication to the unfolding procedure. Indeed one has to unfold the supercell bands to two different primitive BZs and subsequently project the bands on the layer to which they belong. The projection is performed by iterating over the eigenvalues along the band path and assigning them to the appropriate layer according to the weight of the corresponding wave function on the two different layers. The unfolded band structures obtained with the above procedure for the two different alignment angles are plotted with colored circles in fig. 5.8 (d) and (f). For comparison with the isolated layers bands are shown with continuous lines. The main observation here is that the unfolded bands for the two bilayers are essentially the same, and because the alignment angles are arbitrarily chosen it is safe to state that the band structure is not dependent on the alignment angle. When comparing the bilayer bands to the isolated layer ones the agreement is not stunning and two main effects can be distinguished: a constant shift in energy throughout the BZ, up in energy for MoS_2 and down for WSe_2, and shape modification of the bands around the Γ point. The asymmetric energy shift is a clear signature of charge transfer between the layers. Indeed, because of the mismatch of the energy of the band gap centers of the two layers, the electron distribution rearranges at the interface leading to the formation of an interface dipole. This, in turn, generates an electrostatic potential that shifts the energy levels of the two layers asymmetrically. At the Γ point, instead, we observe more than just a simple shift as the shape of the bands is altered. We ascribe such an effect to hybridization of the wave functions of the two monolayers. For a more detailed investigation of the charge transfer and hybridization effect check the Supplementary Information of Paper IV. Importantly, as far as the interlayer exciton formation is concerned, a clear type II band alignment exists between the MoS_2 and WSe_2 layers, with the top of the valence band localized on WSe_2 and the bottom of the conduction band on MoS_2. Since the two relevant band edges reside at the K-point of the BZs, hybridization effects are minimal and therefore I can conclude that, at the LDA level, the band structure of the bilayer MoS_2/WSe_2 can be obtained as superposition of the freestanding layers bands and the effect of charge transfer can be accounted for by adding a constant asymmetric shift.

While the use of DFT is advantageous in terms of computational demand, it often yields a poor quantitative description of band gaps and band alignment, and higher level methods, such as G_0W_0, are needed. To show that this is the case also for the MoS_2/WSe_2 bilayer, the freestanding layers band structure calculated within the G_0W_0 approximation (described in section 2.3.2.1) and LDA are compared in fig. 5.9 (a). In this case spin-orbit coupling is included. Apart from the qualitative type II band alignment predicted by both LDA and G_0W_0, the LDA fails at describing both the size of the band gaps and the level alignment. Since it could be argued that the failure of the LDA is a consequence of the poor approximation for the exchange-correlation functional rather than the DFT approach itself, I calculated the band edges for MoS_2 and WSe_2 using the HSE hybrid functional, which is known to be more reliable for the scope. The band edges within the different approximations are shown in fig. 5.9 (b). While the improvement over the LDA result is considerable, the HSE band edges are not yet as accurate as the G_0W_0 ones. Not surprisingly, we learn

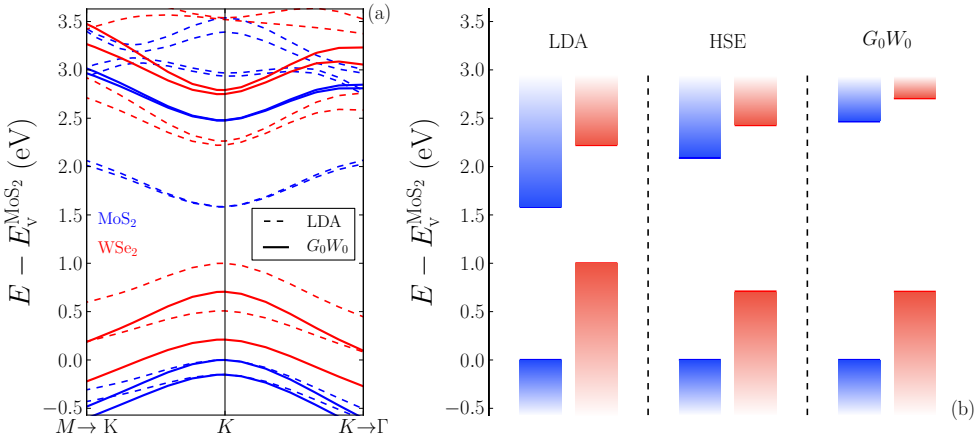

Figure 5.9: Panel (a): LDA and G_0W_0 band structure for the freestanding MoS_2 and WSe_2 layers. Only the portion of the BZ around the K-point is shown. Panel (b): comparison of the LDA, HSE (HSE06) and G_0W_0 band edges. We chose the top of the valence band in MoS_2 as reference energy to align the bands because of the uncertainty of the G_0W_0 vacuum levels. Spin-orbit effects are included in the calculations.

that G_0W_0 has to be the method of choice if high accuracy is crucial. Furthermore it should be noted that the G_0W_0, or similarly the HSE, band alignment yields a difference of the band gap centers of ~ 0.3 eV as opposed to the ~ 1 eV given by the LDA. Since it is the mismatch in band gap centers that drives the charge rearrangement at the bilayer interface, it means we should safely expect the charge transfer to be negligible and no shift of the monolayer bands has to be applied to describe the vdWH band structure.

Now that we know that hybridization and charge transfer effects can be neglected at the band edges, we are only left with the problem of accounting for interlayer screening on the electronic bands. The natural way to include interlayer screening would be performing a G_0W_0 calculation for the full vdWH, but this is clearly not a viable solution. However, we can combine the QEH model with monolayer G_0W_0 calculations and include the macroscopic contribution of the interlayer screening. Specifically, we can modify the screened electron-electron interaction of a given layer by adding the extra screening coming from the neighboring layers. In formulas:

$$W^{\text{vdWH}}_{\mathbf{GG'}}(\mathbf{q},\omega) = W^{\text{free}}_{\mathbf{GG'}}(\mathbf{q},\omega) + \delta W(\mathbf{q},\omega)\delta_{\mathbf{G}0}\delta_{\mathbf{G'}0}, \tag{5.12}$$

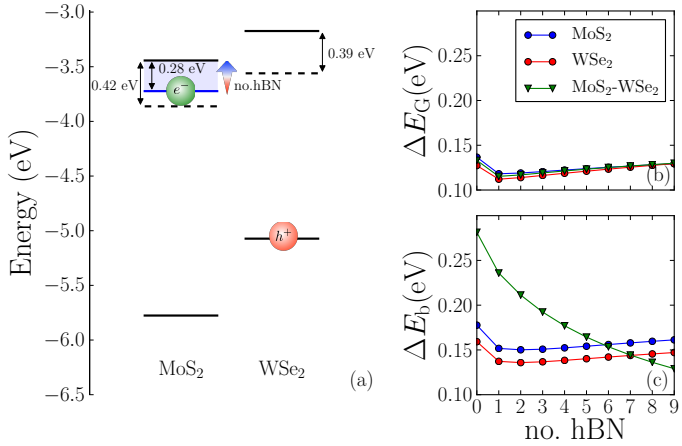

Figure 5.10: Panel (a): Band alignment diagram for bilayer MoS_2-WSe_2 calculated with the G_0W_0-QEH method. In the same diagram the energy levels associated to the lowest intra and inter-layer excitonic levels are shown. The shaded region and the arrow indicates the reduction of interlayer exciton binding energy due to the intercalation of hBN. Panel (b) and (c) show the variation of intra and interlayer gaps and exciton binding energies respectively. The variation is taken with respect to the separated layers.

where $W^{\text{free}}_{\mathbf{G}\mathbf{G}'}(\mathbf{q},\omega)$ accounts for the intra layer screening, as in any monolayer G_0W_0 calculation, and $\delta W(\mathbf{q},\omega)$ is the correction due to interlayer screening. Such a correction is readily calculated with the QEH. First, the screened electron-electron interaction is calculated for the isolated layer and for the layer embedded in the heterostructure by using eq. (5.7) with $\underline{\varphi}_e$ instead of $\underline{\varphi}_h$[1]. Then, taking the difference between these two different interactions, $\delta W(\mathbf{q},\omega)$ is obtained. As briefly mentioned, only the macroscopic part of the dielectric screening is included, as inferred from the $\delta_{\mathbf{G}0}\delta_{\mathbf{G}'0}$ in eq. (5.12). This is a reasonable approximation since we verified that the $\mathbf{G},\mathbf{G}' \neq 0$ components rapidly decay outside the layer and therefore do not play a relevant role in the interlayer screening. This G_0W_0-QEH approach, reduces the task of calculating the band structure for the full vdWHs to at most N-G_0W_0 monolayer calculations, with N the number of layers in the heterostructure.

Next I apply the newly developed method, to the MoS_2/WSe_2 based heterostructures and finally get an accurate energy levels diagram including all the relevant effects, see fig. 5.10 (a). The G_0W_0-QEH can be further exploited to evaluate the effect of hBN intercalation on intra and interlayer gap. The results are shown in

[1]Since in the QEH both electrons and holes are represented with the monopole component of the induced density, the only difference between $\underline{\varphi}_h$ and $\underline{\varphi}_e$ is a sign.

fig. 5.10 (b) where the variation of the band gaps with respect to the isolated layers is plotted. Although the band gap renormalization is noticeable when going from monolayers to bilayer, the intercalation of h-BN does not have a considerable effect. For comparison, the variation of intra and interlayer exciton binding energy is reported in fig. 5.10 (b). The effect of interlayer screening on both intra and interlayer gaps is of the same order of magnitude as the effect on intralayer exciton binding energy. Differently from the interlayer exciton case, no dependence on the MoS_2-WSe_2 distance is observed for interlayer gap.

The ultimate test for the methodologies introduced so far is to benchmark the results on band edges and exciton binding energies for the MoS_2/hBN/WSe_2 heterostructures with experimental measurements on interlayer exciton photoluminescence (PL) from Ref. [104]. In particular, we can estimate the position of the PL peaks of the lowest lying interlayer excitons as:

$$E_{\mathrm{PL}} = E_{\mathrm{IG}} - E_{\mathrm{b}}^{\mathrm{Inter}}, \tag{5.13}$$

with E_{IG} the interlayer band gap and $E_{\mathrm{b}}^{\mathrm{Inter}}$ the interlayer exciton binding energy. The position of the photoluminesce peaks calculated with the G_0W_0-QEH together with the photoluminence spectra are plotted in fig. 5.11 for the isolated monolayers (left panel) and MoS_2/hBN/WSe_2 heterostructures (right panel). For the isolated layers the PL signal is due to the intralayer excitons and therefore the peak positions are calculated with the equivalent of eq. (5.13) for intralayer quantities. Because the experimental measurements are performed on heterostructures supported on SiO_2, we simulated the effect of the substrate with 30 layers of hBN, which has a similar bulk dielectric constant to SiO_2. Compared to the freestanding case, the substrate does not seem to considerably affect the PL peaks position. In general the agreement with the experimental data for both isolated layers and heterostructures is remarkable and it is further highlighted by the inset, where a shift in energy of only 0.13 eV has been applied to match the experimental results. It has to be mentioned, though, that interpretation of the PL peaks in Ref. [104] is ambiguous. Indeed, while it is claimed that the PL peak for the bilayer without hBN is a clear signature of interlayer exciton, for the MoS_2/hBN/WSe_2 and MoS_2/3hBN/WSe_2 the interlayer exciton peak could be mixed with the WSe_2 intralayer exciton one.

Finally, to demonstrate that the treatment of the band edges at the G_0W_0 is key to the agreement with experiment, the PL peaks calculated from for LDA and HSE band edges are also shown in fig. 5.11. While HSE results are reasonably close to the G_0W_0 ones, the LDA dramatically misses the experimental values. The reason why not even the trend of the PL peaks is correctly described with LDA is that charge transfer effects cannot be neglected. Charge transfer, indeed, opens the interlayer band gap shifting the PL peaks up in energy. Increasing the number of hBN layers, the charge transfer is hindered and consequently the shift of the PL peaks decreases, which explains the incorrect trend.

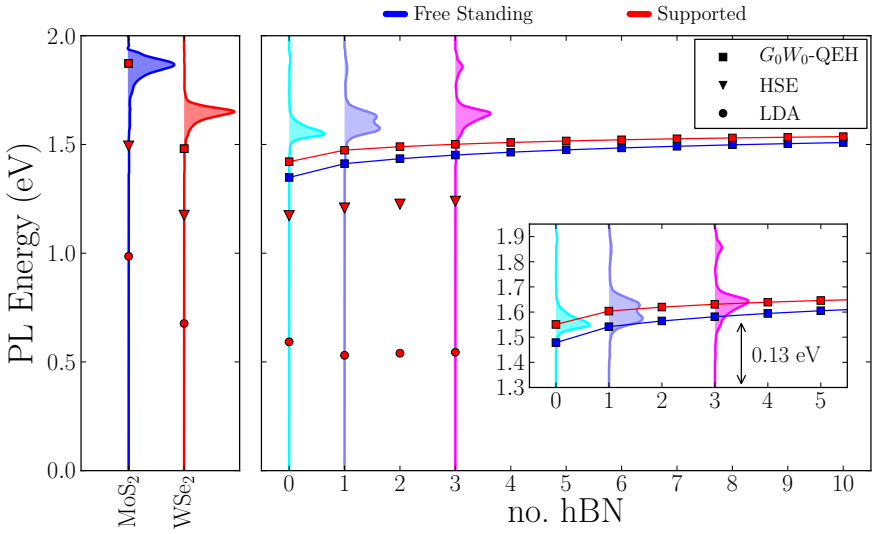

Figure 5.11: Photoluminescence experimental spectra and calculated peak positions for isolated layers (left panel) and MoS_2/hBN/WSe_2 based heterostructures (right panel). While the signal in the isolated layers is due to intralayer excitons, the ones for the heterostructure are associated to the interlayer ones (at least up to one hBN layer). The peak positions are calculated at different level of approximation for supported and freestanding heterostructures. The inset shows how with a shift of only 0.13 eV the G_0W_0-QEH perfectly reproduce the experimental trend.

CHAPTER 6

Exciton Dissociation

Devices such as solar cells or photodetectors, which convert photons into electrical current, rely on the formation and subsequent dissociation of excitons. We have seen in chapter 3 that the formation of excitons in 2D semiconductors is an efficient process thanks to the strong coupling with light. Additionally, in chapter 4, we learned that due to the reduced dielectric screening, in 2D excitons are strongly bound. The latter represents a disadvantage when the excitons have to be dissociated into free electron-hole pairs that could be detected/collected at the contacts. For this reason photodetectors based on 2D materials cannot rely on thermal dissociation of the excitons but require a field-assisted exciton ionization instead. This has been demonstrated in Ref. [114], where exciton related photocurrent in MoS_2 is observed only if a finite bias is applied to the crystal.

Here I present the calculations we performed on Stark shift and dissociation of the lowest lying exciton in monolayer MoS_2 under the effect of a constant in-plane electric field. In addition to that, I show how these quantities are affected when combining MoS_2 with hBN in ultra-thin vdWHs. We calculate the Stark shift and the dissociation rate from the energy and the lifetime of the resonant state associated with the lowest lying exciton. The resonant state, in turn, is obtained by applying the complex scaling technique to the 2D Mott-Wannier Hamiltonian in eq. (4.9). For the ultra-thin heterostructures the effect of interlayer screening is included by calculating the screened electron-hole interaction through the QEH model, following the procedure described in the previous chapter. We demonstrate that field-induced exciton dissociation in MoS_2 can be faster than intrinsic excitonic decay mechanisms and that it is significantly facilitated when embedding the semiconducting layer in hBN.

This chapter is fully based on Paper V, but I would like to point out that results on exciton dissociation rates for in-plane and out-of-plane electric fields in multilayer TMDs are presented in Paper VI. However, since my contribution to Paper VI was limited to the calculation of the ab-initio parameters used in the model, the results are not presented here.

6.1 Definition of a Resonance

The first step towards the calculation of the dissociation rate is the identification of a resonant state associated with the exciton. Consider fig. 6.1 where the potential energy landscape experienced by the electron involved in the exciton is sketched with and and without electric field in panel (a) and (b) respectively. When no electric field is applied, the electron is "trapped" by the screened Coulomb potential generated by the hole and it occupies the lowest energy state. Such a state is a bound state localized around the hole and characterized by a real eigenvalue, as illustrated in fig. 6.1 (a). In the presence of the electric field the situation is different. The electron can now tunnel out of the potential generated by the hole. Bound states are no longer eigenstates of the Mott-Wannier Hamiltonian as they are now coupled to the continuum states made accessible by the electric field. One way to describe the dynamics of electron "escaping" from the hole is to look for the so called resonant states, or simply resonances. A resonance is defined as a solution of the stationary Schrödinger equation with the following boundary conditions:

$$\lim_{r\to\infty} \psi(\mathbf{r}) = Ae^{i\mathbf{K}\cdot\mathbf{r}}, \qquad \text{with} \quad \mathrm{Re}\left[\mathbf{K}\cdot\hat{r}\right] > 0. \tag{6.1}$$

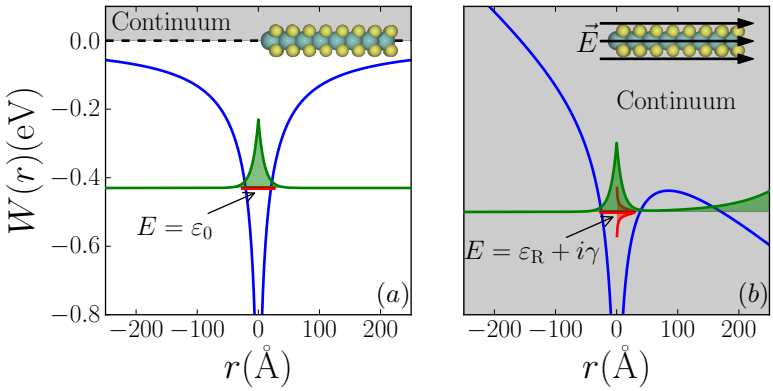

Figure 6.1: Illustration of an excitonic state with and without electric field. Panel (a): The lowest lying excitonic state is represented as the lowest energy level associated to the electron trapped by the screened Coulomb potential (in blue) generated by the hole. Such a state is a bound state with a real eigenvalue and is confined by the Coulomb potential as shown by wave function (in green). Panel (b): the same excitonic state in the presence of a in-plane electric field. The state is not bound since the electron can now leak out of the attractive potential generated by the hole. Such a state is, instead, a resonant state whose energy is complex valued.

Here $\hat{r}$ is the unit position vector and the absolute value of momentum $\mathbf{K}$ is related to the energy of the state by $K = \sqrt{2m_e\epsilon}$. These boundary conditions, originally proposed by Siegert [115], impose that the allowed eigenfunctions are outgoing waves. This corresponds to the assumption that the system is open and that charge can leak out. If there exists a solution to the Schrödinger equation satisfying such conditions, it can be formally shown (see e.g. [116]) the Hamiltonian of the system is non-Hermitian and consequently admits complex eigenvalues $\epsilon = \epsilon_R + i\gamma$, with $\epsilon_R, \gamma \in \mathbb{R}$ corresponding to the energy and the lifetime of the resonance respectively. It is worth it to stress that, even if it might seem unphysical, a non-Hermitian Hamiltonian is common in open quantum systems. Molecular junctions, e.g., can be fully described by an Hamiltonian containing only the degrees of freedom of the molecule but accounting for the flow of charge to and from the contacts through a complex-valued embedding self-energy [42]. Importantly, it should be noted that an outgoing state with complex eigenvalue, such as the resonance, is divergent and thus not square-integrable (see the wave function in fig. 6.1 (b)). This poses a problem in finding resonant states by means of standard methods, such as direct diagonalization of the Hamiltonian, which are based on square-integrability and zero boundary conditions. Moreover, an extra complication arises from the boundary conditions in eq. (6.1) which depend on the energy of the resonance through $\mathbf{K}$. In next section I describe how this issue can be solved using the complex scaling method.

6.2 Complex Scaling Method: A short Introduction

The underlying idea of the complex scaling technique is to cancel the divergence of resonant states by mapping the real spatial coordinates into the complex plane. This approach, originally proposed in Ref. [117], has a dual advantage: it transforms the resonant states into square-integrable functions and it suppresses the energy dependence of their boundary conditions. Ultimately, this allows for resonant states to be accessible with standard solution schemes for the stationary Schrödinger equation. In this section I present an introduction to the basic concepts of the complex scaling method, closely following Ref. [118].

Let us consider a generic single-particle stationary Schrödinger equation in real space:

$$\mathbf{H}(\mathbf{r})\psi(\mathbf{r}) = \epsilon\psi(\mathbf{r}), \tag{6.2}$$

with $\mathbf{H}(\mathbf{r}) = -\frac{1}{2}\nabla^2 + v(\mathbf{r})$ and $v(\mathbf{r})$ the trapping potential. The complex scaling technique requires the potential $v(\mathbf{r})$ to be dilation analytic. For the present discussion it is enough to know that the Coulomb potential satisfies this condition [117] and that the potential associated to the constant electric field, even if not dilation analytic, is a particular case for which the complex scaling technique can be applied anyway [119].

The complex scaling transformation is essentially a rotation of the real space coordinates into the complex space. In practice, the position and momentum operators

are modified according to:

$$\mathrm{i}\nabla \to e^{-\mathrm{i}\theta}\mathrm{i}\nabla, \tag{6.3}$$

$$\mathbf{r} \to \mathbf{r}e^{\mathrm{i}\theta}, \tag{6.4}$$

where θ is the rotation angle and it has to be thought as a fixed parameter. Applying this transformations to eq. (6.2) we obtain the complex scaled Schrödinger equation:

$$\mathbf{H}_\theta(\mathbf{r})\psi_\theta(\mathbf{r}) = \epsilon_\theta\psi_\theta(\mathbf{r}), \tag{6.5}$$

with

$$\mathbf{H}_\theta(\mathbf{r}) = -\frac{1}{2}e^{-\mathrm{i}2\theta}\nabla^2 + v(\mathbf{r}e^{\mathrm{i}\theta}) \qquad \text{and} \qquad \psi_\theta(\mathbf{r}) = e^{\mathrm{i}N\theta/2}\psi(\mathbf{r}e^{\mathrm{i}\theta}), \tag{6.6}$$

where N is the number of dimensions (in our case $N = 2$). The complex scaling operation transformed the original Hamiltonian $\mathbf{H}$ into a non-Hermitian Hamiltonian $\mathbf{H}_\theta$ which now admits complex eigenvalues ϵ_θ. For sufficiently large θ, the analytic continuation of the wave function $\psi(\mathbf{r})$ in the complex plane suppresses the divergence of resonant states and therefore they can be now found by solving eq. (6.5) with zero boundary conditions.

It is of interest to investigate how the spectrum of $\mathbf{H}$ is affected by the complex scaling. Let us consider the expectation value of $\mathbf{H}$ over the state $\psi(\mathbf{r})$:

$$\epsilon = \int d\mathbf{r}\, \psi^*(\mathbf{r})\mathbf{H}(\mathbf{r})\psi(\mathbf{r}). \tag{6.7}$$

If the integrand is analytic and its analytic continuation dies out (sufficiently quickly) for $r \to \infty$, the integration path can be rotated into the complex plane by θ without altering the result. This is indeed the case for bound states, which are expected to be localized. This conditions are satisfied by bound states and it can be shown that $\epsilon_\theta = \epsilon$ for all θ[1]. Indeed:

$$\begin{aligned}
\epsilon &= \int e^{\mathrm{i}N\theta} d\mathbf{r}\, \psi^*(e^{\mathrm{i}\theta}\mathbf{r})\mathbf{H}(e^{\mathrm{i}\theta}\mathbf{r})\psi(e^{\mathrm{i}\theta}\mathbf{r}) \\
&= \int d\mathbf{r}\, e^{\mathrm{i}N\theta/2}\psi^*(e^{\mathrm{i}\theta}\mathbf{r})\mathbf{H}(e^{\mathrm{i}\theta}\mathbf{r})e^{\mathrm{i}N\theta/2}\psi(e^{\mathrm{i}\theta}\mathbf{r}) \\
&= \int d\mathbf{r}\, \bar{\psi}_\theta(\mathbf{r})\mathbf{H}_\theta(\mathbf{r})\psi_\theta(\mathbf{r}) = \epsilon_\theta,
\end{aligned} \tag{6.8}$$

where I defined $\bar{\psi}_\theta(\mathbf{r}) = e^{\mathrm{i}N\theta}\psi^*(e^{\mathrm{i}\theta}\mathbf{r})$ and in the first I used the fact that the integration path can be safely rotated. In practice this result means that the eigenvalues of the bound states are untouched by the complex scaling and they keep lying on the real axis.

The situation is different for the continuum states as they are not localized and therefore the equivalence between the integration along the real path and the rotated

[1] As long as the state is analytic.

one does not hold. In order to understand the effect of complex scaling on continuum states we consider their asymptotic behavior and assume that it is not significantly affected by the potential $v(\mathbf{r})$. Then, for $r \to \infty$ the complex scaled continuum states can be found from:

$$-\frac{1}{2}e^{-\mathrm{i}2\theta}\nabla^2\psi_\theta(\mathbf{r}) = \epsilon_\theta\psi_\theta(\mathbf{r}). \tag{6.9}$$

Clearly this equation is equivalent to the non-scaled one and they both yield the same eigenstate, i.e. $\psi_\theta(\mathbf{r}) = \psi(\mathbf{r})$. It is only the eigenvalues that are affected by the complex scaling, i.e. $\epsilon_\theta = e^{\mathrm{i}2\theta}\epsilon = e^{\mathrm{i}2\theta}\frac{1}{2}k^2$ with $k \in \mathbb{R}$. Hence, the effect of complex scaling on the continuum states is a rotation of -2θ into the complex plane of the non-scaled eigenvalues.

To better illustrate what has been discussed so far I report the spectrum of the complex scaled Mott-Wannier Hamiltonian for MoS_2 in absence of field in fig. 6.2. The figure shows that for the three different values of θ the bound states are unaffected, whereas the continuum states are rotated by -2θ as explained above. The reason why the continuum does not start at $\mathrm{Re}[E] = \mathrm{Im}[E] = 0$ is a consequence of the finite size of the simulation box.

The last type of states we need to analyze are the resonances. As described in the previous section a resonant state is defined as such a state that satisfies the outgoing boundary conditions in eq. (6.1). Applying the complex scaling transformation to the

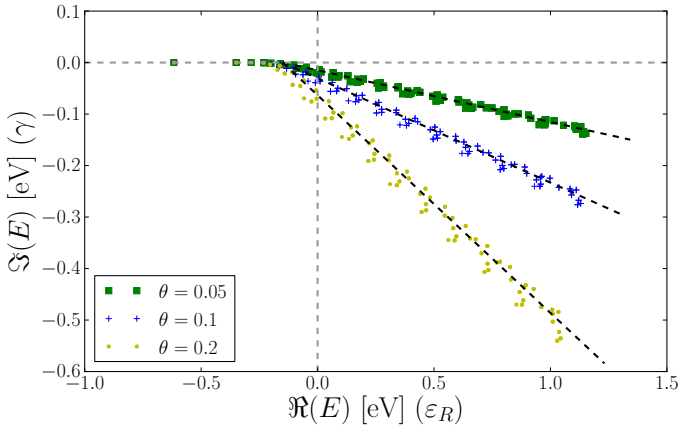

Figure 6.2: Illustration of the effect of complex scaling on the bound and continuum states of the Mott-Wannier Hamiltonian for an exciton in MoS_2 in absence of external field. While the bound states are not altered, the continuum states rotate by an angle of -2θ. The fact that the continuum does not start at zero is a consequence of the finite size of the simulation box.

outgoing resonant state for $r \to \infty$, one has:

$$\begin{aligned}\psi_\theta(\mathbf{r}) &= e^{\mathrm{i}N\theta/2}\psi_\theta(e^{\mathrm{i}\theta}\mathbf{r}) = e^{\mathrm{i}N\theta/2}e^{\mathrm{i}\mathbf{K}\cdot\mathbf{r}e^{\mathrm{i}\theta}} = e^{\mathrm{i}N\theta/2}e^{\mathrm{i}(\mathbf{P}-\mathrm{i}\mathbf{Q})\cdot\mathbf{r}e^{\mathrm{i}\theta}} \\ &= e^{\mathrm{i}N\theta/2}e^{\mathrm{i}(\mathbf{P}\cos\theta+\mathbf{Q}\sin\theta)\cdot\mathbf{r}}e^{\mathrm{i}(-\mathbf{P}\sin\theta+\mathbf{Q}\cos\theta)\cdot\mathbf{r}},\end{aligned} \tag{6.10}$$

where I used $\mathbf{K} = \mathbf{P} - \mathrm{i}\mathbf{Q}$, with $\mathbf{P}, \mathbf{Q} \in \mathbb{R}^N$. From the expression above we can infer that the resonant state becomes square-integrable only for values of θ such as $(-\mathbf{P}\sin\theta + \mathbf{Q}\cos\theta)\cdot\hat{r} < 0$, i.e $\theta > \tan^{-1}(\mathbf{Q}\cdot\hat{r}/\mathbf{P}\cdot\hat{r})$. Practically speaking this means that one has to solve eq. (6.5) with increasing values of θ until resonances appear. Once appeared, the resonances eigenvalues are independent of θ. Finally, note that because no external field is applied, resonant states do not appear in fig. 6.2.

6.3 Exciton life-time and Stark shift in ultra-thin vdHWs

From the previous section we learned that through the complex scaling method, resonant states are transformed into square-integrable functions which can be found by numerically solving eq. (6.5), e.g., by iterative diagonalization. In the following I discuss how we applied the complex scaling to the 2D Mott-Wannier Hamiltonian to calculate the dissociation rate and Stark shift of excitons in MoS_2 due to a constant in-plane electric field. To determine the effect of environmental screening, we study the case of freestanding MoS_2 monolayer and MoS_2 embedded in ultrathin vdWHs with hBN, in particular MoS_2-hBN and hBN-MoS_2-hBN.

To describe the effect of the constant electric field on the excitons, we employ the usual 2D Mott-Wannier Hamiltonian in eq. (4.9) and add the electric potential associated with the external in-plane electric field. We assume that the field does not affect the exciton effective mass. Regarding the screened electron-hole interaction, we use the 2D expression in eq. (4.17), which, I recall, relies on the linear approximation of the dielectric function. The 2D polarizability constant is calculated from the linear fit of the full wave vector dependent Q2D dielectric function and in the case of vdWHs it is calculated with the QEH. We have seen in section 5.3.1 that although a linear dielectric constant approximation is not appropriate for vdWHs, it is acceptable for heterostructure that are ultrathin, i.e. consisting of a very few layers, such as the ones investigated in this section. The advantage of using the 2D interaction energy is the availability of an explicit analytic form which can be directly complex scaled by applying the transformation in eq. (6.4). Contrastingly the use of the full q-vector dependent Q2D dielectric function would require a non trivial numerical continuation into the complex plane. Once the Mott-Wannier Hamiltonian is complex scaled, it is diagonalized iteratively for different θ and the resonant excitonic states are found.

The eigenvalue of the resonance carries information on both the Stark shift and the lifetime of the excitonic state. Taking the difference between the real part of the lowest resonant state, i.e. the resonance with the lowest real part of the energy, and the binding energy of the lowest lying exciton we can calculate the Stark shift. Note that the complex scaling method is a non-perturbative method as opposed to

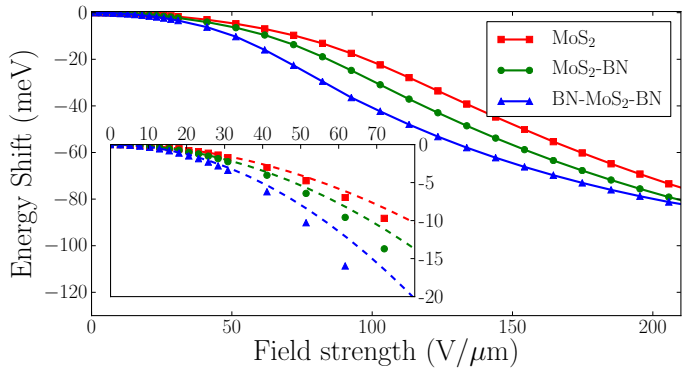

Figure 6.3: Exciton Stark shift in the MoS_2 based structures as a function of field strength calculated through complex scaling. Inset: the shift predicted by our simple hydrogenic model(dashed lines) agrees well with the complex scaling results for small fields.

the perturbative techniques usually employed to calculate the Stark shift. Figure 6.3 shows the Stark shift of the exciton binding energy as a function of field strength for the three different structures. The Stark shift becomes larger with increasing field strength and it shows a parabolic behavior for small fields. The parabolic behavior is what one would expect from standard perturbation theory since the Stark shift is a second order effect. To confirm this, we apply second order perturbation theory to the simple effectively screened hydrogenic model discussed in section 4.4. An analytic expression for the energy shift can be worked out and it reads:

$$\Delta E = -\frac{21}{64}\frac{\epsilon_{\text{eff}}^4}{\mu^3}E^2, \tag{6.11}$$

with ϵ_{eff} defined in eq. (4.23), μ the exciton effective mass and E the field strength. The validity of this expression for very low field strength is verified in the inset of fig. 6.3. Additionally, eq. (6.11) help us understand why the Stark shift is higher for the vdWHs. Indeed $\Delta E \propto \epsilon_{\text{eff}}^4$, and adding hBN to MoS_2 increases the environmental screening encoded in ϵ_{eff}.

Finally fig. 6.4 reports the field-induced exciton dissociation rate, evaluated as $1/\gamma$ where γ is the lifetime (imaginary part of the eigenvalue) of the resonant state with the lowest real part of the eigenvalue. While it is not surprising that the dissociation is faster for increasing field strength, the noticeable result here is that the dissociation rate can be largely tuned by modifying the dielectric environment. It is indeed seen in fig. 6.4 that the dissociation rate increases when going from MoS_2 to MoS_2-hBN and it increases even more for the hBN-MoS_2-hBN structure. Such a behavior is a consequence of the increased environmental screening that weakens the binding of the electron-hole pair, making the exciton more prone to dissociate. The

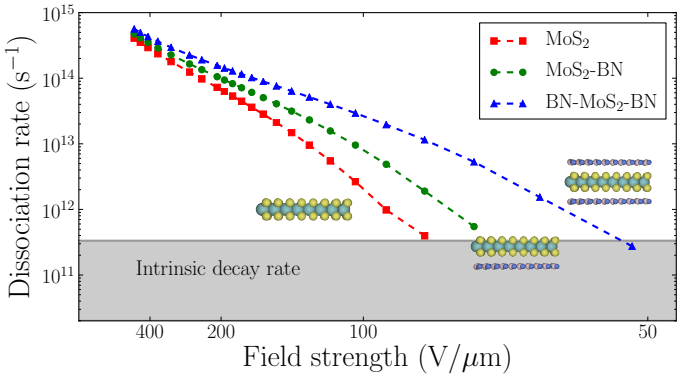

Figure 6.4: In-plane field-dependent dissociation rate of an exciton localized in the MoS2 layer for the three different structures. The shaded region represents the range of typical dissociation rates associated with intrinsic exciton decay processes.

field-induced dissociation is not the only process that causes the exciton to decay. In an actual device processes such as radiative recombination [36], defect-assisted recombination [120], and exciton-exciton annihilation [121] all contribute to intrinsic exciton decay and the relative importance of these effects depends on temperature, defect concentration and exciton density. The typical decay rates associated with these processes are indicated by the shaded region in fig. 6.4. We estimate that a field-strength of 0.1 V/nm can be reasonably achieved at the contact-MoS_2 interface under experimental condition. For such a value of field, we see that the dissociation process dominates over the other intrinsic decay mechanisms. We then conclude that exciton dissociation via external field can be a viable route to separating electron-hole pairs, and it is an even more efficient process if the active material, in this case MoS_2, is encapsulated in vdWHs.

CHAPTER 7

Conclusion

In this thesis I presented a comprehensive framework to calculate properties of excitons in 2D materials and their heterostructures. I discussed how the daunting task of solving the Bethe-Salpeter equation is rephrased in terms of a generalized Mott-Wannier equation where the main ingredient is the screened electron-hole interaction. The screened electron-hole interaction, in turn, is obtained with quantum accuracy from the dielectric response of the material. For 2D semiconductors, as opposed to bulk, I showed that the correct description of the excitons requires to take into account the non-locality of the dielectric function, which manifests itself with a strong dependence on the in-plane wave-vector $\mathbf{q}_\parallel$. With our quasi-2D (Q2D) picture of a 2D material, i.e. by accounting for the finite out-of-plane extension of the layer, we were able to calculate the full $\mathbf{q}_\parallel$ dependence of the dielectric function. We then demonstrated that in the limit $q_\parallel d \ll 1$, with d the thickness of the slab, the, commonly used linear approximation for the dielectric function is completely justified. Since the relevant range of $\mathbf{q}_\parallel$ for excitons in isolated 2D crystals satisfies the $q_\parallel d \ll 1$ condition, we found that solving the Mott-Wannier equation with either a Q2D or a linearly screened electron-hole interaction yields the same excitonic properties, such as the binding energy. The linear behavior of the dielectric function is advantageous when reducing the generalized Mott-Wannier equation to an effectively screened hydrogenic equation. Indeed defining an effective dielectric constant in terms of a linear dielectric function allows us to construct an analytic expression for the energies of the excitonic states in 2D semiconductors in terms of the 2D polarizability constant and the effective mass. The non-locality of the dielectric screening in 2D materials extends to their van der Waals heterostructure. While standard ab-initio methods can be directly applied to the calculation of the dielectric response of isolated 2D crystals, they are computationally unfeasible for complex multilayer heterostructures. This, however, did not stop us but, instead, motivated the development of a first-principles multi-scale method, the QEH model, which can accurately and efficiently determine the dielectric response of a generic vdWH from the dielectric properties of the constituent layers. This is done by first encoding the dielectric response of each layer into a dielectric building block and second coupling the building blocks by solving the electrostatic Dyson equation in a discrete monopole/dipole basis. The QEH approach enabled us to calculate dielectric, electronic and excitonic properties of realistic heterostructures at an extremely reduced computational cost and with high accuracy. For example, we showed that combining the QEH with the Mott-Wannier equation we could describe the 2D to 3D transition of the exciton binding energy in MoS_2 and

reproduce the experimental non-hydrogenic Rydberg series of the excitons in supported WS_2. We found out that the linear approximation, successful for excitons in isolated 2D crystals, breaks down in several-layer vdWHs and that the out-of-plane extension of the layers has to be taken into account. Our framework allowed us to even account for more exotic excitations in vdWHs such as interlayer excitons. By calculating interlayer exciton binding energies and electronic band edges taking interlayer screening into account in both cases, we completely determined the energy levels alignment in complex MoS_2-hBN-WSe_2 based heterostructure. This represents a first step towards the understanding of processes at the interfaces between the layers and allowed us to reproduce experimental results on interlayer exciton pholuminescence. Finally, I presented how complex scaling the Mott-Wannier Hamiltonian can give us access to the rate of field-assisted exciton dissociation in freestanding monolayer MoS_2 or in ultra-thin vdWHs hBN/MoS_2 and hBN/MoS_2/hBN. While we estimated the field-assisted dissociation to be faster than intrinsic exciton decay for a freestanding MoS_2 layer, we demonstrated that the dissociation rate can be significantly increased by embedding MoS_2 in ultra-thin vdWHs.

In my vision, the future of vdWHs looks bright but still a lot needs to be understood if we want vdWHs to revolutionize nanoelectronics. In this work, we took the first steps towards the understanding of the dielectric response of these innovative materials and how this affects the energy and the lifetime of the excitons. However problems such as the control of absorption, photoluminescence, charge transfer at the interface and defects are still unsolved. There is still plenty of room for the development of new ab-initio schemes, most likely based on a multi-scale approach, that could give a solution to these open issues. For example a starting point to the understanding of photoluminescence of interlayer excitons in complex vdHWs structures could be calculating the transition dipole moments of the initial and final excitonic states and study how that depends on the alignment angle or distance between the layers hosting the excitation.

A much more ambitious project would instead be the development of time dependent methods based on non-equilibrium Green's functions which include all the intimate processes in the material, such as electron-electron, electron-phonon and electron-defect scattering. This would give us direct access to the real time dynamics of electrons and nuclei which could support the incredible amount of data produced by ultra-fast pump and probe experiments in the past few years. At the same time, being able to say something about the time scale of physical processes such as exciton recombination, charge extraction at the contacts of a device or on-off switching of transistors would be of a great importance for the engineering of the ultimate high-performance (opto)-electronic device.

APPENDIX A

Derivation of the Bethe Salpeter Equation

A.1 Bethe-Salpeter Equation

As we saw in chapter 2, a higher level of approximation in many-body interaction can be obtained by iterating Hedin's equations once more [122]. The way to go is to plug the GW expression for the exchange correlation self-energy in the equation for the vertex. We then need to calculate $\frac{\delta\Sigma^{xc}(1;2)}{\delta G(4;5)}$. Disregarding the variation of the screened interaction due to the excitation, i.e. $\frac{W(1;2)}{\delta G(4;5)} \simeq 0$, we can write $\frac{\delta\Sigma^{xc}(1;2)}{\delta G(4;5)} \simeq \mathrm{i}\delta(1,4)\delta(2,5)W(1;2)$ and therefore express the vertex as:

$$\Gamma(1,2;3) = \delta(1;2)\delta(1;3) + \mathrm{i}\int d6d7W(1;2)G(1;6)G(7;2)\Gamma(6,7;3). \tag{A.1}$$

Inserting the relation above back into the equation for the irreducible polarizability (eq. (2.43)) we get:

$$P(1;2) = -\mathrm{i}G(1;2)G(2;1) + \int d4d5d6d7G(1;4)G(5;1)W(4;5)G(4;6)G(7;5)\Gamma(6,7;2). \tag{A.2}$$

If we now define a three-points irreducible polarizability as:

$$^3P(1,2;3) = -\mathrm{i}\int d5d6G(1;5)G(6;2)\Gamma(5,6;3), \tag{A.3}$$

eq. (A.2) can be generalized to:

$$^3P(1,2;3) = -\mathrm{i}G(1;3)G(3;2) + \mathrm{i}\int d4d5G(1;4)G(5;2)W(4;5)^3P(4,5;3). \tag{A.4}$$

The two-points irreducible polarizability can be easily recovered by the three-point one, since $P(1;2) =^3 P(1,1^+;2)$. To make the last equation even more appealing we can introduce a new quantity:

$$L_0(1,2;3,4) = -\mathrm{i}G(1;3)G(4;2) \tag{A.5}$$

and further generalize the irreducible polarizability to a four-point function:

$$^4P(1,2;3,4) = L_0(1,2;3,4) - \int d5d6d7d8 L_0(1,2;5,6)\,^4W(5,6,7,8)\,^4P(7,8;3,4), \tag{A.6}$$

where I defined $^4W(1,2,3,4) = W(1,2)\delta(1,3)\delta(2,4)$. Once again, the two-point irreducible polarizability can be retrieved by contracting the four-point one: $P(1;2) =^4 P(1,1^+;2,2^+)$.

To proceed even further, the four-point irreducible polarizability can be related to the four-point reducible polarizability, usually indicated with L(1,2;3,4), by generalizing the Dyson eq. (2.38) to four-point functions:

$$L(1,2;3,4) =^4 P(1,2;3,4) + \int d5d6d7d8\,^4P(1,2;5,6)\,^4v(5,6,7,8)L(7,8;3,4), \tag{A.7}$$

with ^4v defined by $^4v(1,2,3,4) = v(1,3)\delta(1,2)\delta(3,4)$. Using this equation and eq. (A.6) we can finally arrive to the Bethe-Salpeter equation (BSE) [83] within the GW approximation:

$$L(1,2;3,4) = L_0(1,2;3,4) + \int d5d6d7d8 L_0(1,2;5,6)K(5,6,7,8)L(7,8;3,4), \tag{A.8}$$

where I defined the kernel:

$$K(1,2,3,4) = v(1,3)\delta(1,2)\delta(3,4) - W(1,2)\delta(1,3)\delta(2,4). \tag{A.9}$$

In the next section I will show how eq. (A.8) can be solved in practice by using an effective two-particles Hamiltonian.

A.2 From BSE to the two-particle Hamiltonian

Within the static kernel approximation introduced in section 3.5, eq. (A.10) is better tractable in frequency space and it reads:

$$L(\mathbf{r}_1,\mathbf{r}_2,\mathbf{r}_3,\mathbf{r}_4;\omega) = L_0(\mathbf{r}_1,\mathbf{r}_2,\mathbf{r}_3,\mathbf{r}_4;\omega) + \int d\mathbf{r}_5 d\mathbf{r}_6 d\mathbf{r}_7 d\mathbf{r}_8 L_0(\mathbf{r}_1,\mathbf{r}_2,\mathbf{r}_5,\mathbf{r}_6;\omega)K(\mathbf{r}_5,\mathbf{r}_6,\mathbf{r}_7,\mathbf{r}_8)L(\mathbf{r}_7,\mathbf{r}_8,\mathbf{r}_3,\mathbf{r}_4;\omega). \tag{A.10}$$

The advantage of working in frequency space is that one can easily get an explicit form for L_0 just by generalizing eq. (3.5) to four-coordinates:

$$L_0(\mathbf{r}_1,\mathbf{r}_2,\mathbf{r}_3,\mathbf{r}_4;\omega) = 2\sum_{n_1 n_2}\sum_{\mathbf{kq}}^{\mathrm{BZ}}(f_{n_1\mathbf{k}} - f_{n_2\mathbf{k+q}})\frac{\phi^*_{n_1\mathbf{k}}(\mathbf{r}_1)\phi_{n_2\mathbf{k+q}}(\mathbf{r}_2)\phi_{n_1\mathbf{k}}(\mathbf{r}'_4)\phi^*_{n_2\mathbf{k+q}}(\mathbf{r}'_5)}{\omega + \epsilon_{n_1\mathbf{k}} - \epsilon_{n_2\mathbf{k+q}} + \mathrm{i}\eta}. \tag{A.11}$$

A discussion of what wave functions and eigenvalues to use is provided in the main text in section 3.5.

To make the solution of eq. (A.10) more practical, the four-points reducible polarizability can be represented in the so called transition space according to:

$$L(\mathbf{r}_1, \mathbf{r}_2, \mathbf{r}_3, \mathbf{r}_4; \omega) = \sum_{\mathbf{q}}^{\mathrm{BZ}} \sum_{SS'} L_{SS'}(\mathbf{q}, \omega) \psi_S(\mathbf{r}_1, \mathbf{r}_2) \psi^*_{S'}(\mathbf{r}_3, \mathbf{r}_4), \tag{A.12}$$

with the super-indices $S = n_1 n_2$ and $S' = n_3 n_4$ and the transition basis function defined by $\psi_S(\mathbf{r}_1, \mathbf{r}_2) = \phi^*_{n_1 \mathbf{k}}(\mathbf{r}_1) \phi_{n_2 \mathbf{k}+\mathbf{q}}(\mathbf{r}_2)$. The fact that $L_{SS'}(\mathbf{q})$ is diagonal in $\mathbf{q}$ follows from the translational invariance of the system. The idea of defining such a transition space is not completely out of the box but it follows from the fact that L_0 assumes a really simple form in this basis:

$$L_{0\,SS'}(\mathbf{q}, \omega) = \frac{f_S(\mathbf{q})}{\omega - \epsilon_S + \mathrm{i}\eta} \delta_{SS'}, \tag{A.13}$$

which can be directly verified from eq. (A.11) and introducing $f_S(\mathbf{q}) = f_{n_2 \mathbf{k}+\mathbf{q}} - f_{n_1 \mathbf{k}}$ and $\epsilon_S(\mathbf{q}) = \epsilon_{n_2 \mathbf{k}+\mathbf{q}} - \epsilon_{n_1 \mathbf{k}}$.

With the previous two expressions and a bit of algebra [85], the BSE becomes a trivial matrix equation for $L_{SS'}(\mathbf{q})$ and the solution can be conveniently written in terms of the resolvent of an auxiliary non-hermitian two-particles hamiltonian $\mathcal{H}^{2p}(\mathbf{q})$:

$$L_{SS'}(\mathbf{q}, \omega) = \left[\mathcal{H}^{2p}(\mathbf{q}) - (\omega + \mathrm{i}\eta) 1\right]^{-1}_{SS'} f_{S'}(\mathbf{q}), \tag{A.14}$$

with 1 the identity matrix and $\mathcal{H}^{2p}(\mathbf{q})$ given by:

$$\mathcal{H}^{2p}_{SS'}(\mathbf{q}) = \epsilon_S(\mathbf{q}) \delta_{SS'} - f_S K_{SS'}(\mathbf{q}). \tag{A.15}$$

The advantage of writing the polarizability in terms of a resolvent is that one can avoid inverting of a matrix for each frequency and instead just diagonalize the two-particles Hamiltonian once for all. This is done by using the spectral representation of the resolvent:

$$\left[\mathcal{H}^{2p}(\mathbf{q}) - (\omega + \mathrm{i}\eta) 1\right]^{-1}_{SS'} = \sum_{\lambda\lambda'} \frac{A^S_\lambda(\mathbf{q}) [A^{S'}_{\lambda'}(\mathbf{q})]^* N^{-1}_{\lambda\lambda'}}{\omega - E_\lambda(\mathbf{q}) + \mathrm{i}\eta}, \tag{A.16}$$

where A_λ and E_λ denote the eigenstates and eigenvalues of the two-particles hamiltonian and $N_{\lambda\lambda'}$ is the eigenstates overlap matrix, in formula:

$$\mathcal{H}^{2p}(\mathbf{q}) A_\lambda(\mathbf{q}) = E_\lambda(\mathbf{q}) A_\lambda(\mathbf{q}), \qquad N_{\lambda\lambda'}(\mathbf{q}) = \sum_S [A^S_\lambda(\mathbf{q})]^* A^S_{\lambda'}(\mathbf{q}). \tag{A.17}$$

Just by making use of the delta function $\delta_{SS'}$ and the occupation factor f_S in the definition in eq. (A.15), the two-particle Hamiltonian assumes a peculiar structure [122]:

$$\mathcal{H}^{2p}_{SS'} = \left(\begin{array}{c|cccc} & \{vc\}' & \{cv\}' & \{vv\}' & \{cc\}' \\ \hline \{vc\} & \mathcal{H}^{2p,\,\mathrm{Res}} & K & K & K \\ \{cv\} & -K^* & -[\mathcal{H}^{2p,\,\mathrm{Res}}]^* & -K & -K \\ \{vv\} & 0 & 0 & \epsilon_{\{vv\}}\delta_{\{vv\}\{vv\}'} & 0 \\ \{cc\} & 0 & 0 & 0 & \epsilon_{\{vv\}}\delta_{\{vv\}\{vv\}'} \end{array}\right), \tag{A.18}$$

where v and c indicate occupied (valence) and unoccupied (conduction) states respectively. Because of the upper block triangular structure and the occupation factor $f_{S'}$ in eq. (A.14), the only part of $\mathcal{H}^{2p}$ that needs to be diagonalize is the one that involves electron-hole transitions, i.e. the upper left block. The latter can be further divided into four blocks: the resonant part, $\mathcal{H}^{2p,\,\mathrm{Res}}$, which involves positive frequencies transitions (from valence to conduction states), the anti-resonant part, $[\mathcal{H}^{2p,\,\mathrm{Res}}]^*$ and the coupling between the two. It is standard procedure to apply the Tamm-Dancoff approximation [43] which consists in retaining only the resonant part and neglecting the coupling terms. This leads to an extreme simplification of the diagonalization since now the two-particle hamiltonian is represented only in the subspace of electron-hole transitions and is hermitian.

Bibliography

[1] E. Braun and S. MacDonald, *Revolution in miniature: The history and impact of semiconductor electronics*. Cambridge University Press, 1982.

[2] J. Bardeen and W. H. Brattain, "The transistor, a semi-conductor triode," *Physical Review*, vol. 74, no. 2, p. 230, 1948.

[3] G. E. Moore, "Cramming more components onto integrated circuits," *Electronics Magazine*, p. 4, 1965.

[4] J. D. Meindl, Q. Chen, and J. A. Davis, "Limits on silicon nanoelectronics for terascale integration," *Science*, vol. 293, no. 5537, pp. 2044–2049, 2001.

[5] K. S. Novoselov, A. K. Geim, S. V. Morozov, D. Jiang, Y. Zhang, S. V. Dubonos, I. V. Grigorieva, and A. A. Firsov, "Electric field effect in atomically thin carbon films," *science*, vol. 306, no. 5696, pp. 666–669, 2004.

[6] A. A. Balandin, S. Ghosh, W. Bao, I. Calizo, D. Teweldebrhan, F. Miao, and C. N. Lau, "Superior thermal conductivity of single-layer graphene," *Nano letters*, vol. 8, no. 3, pp. 902–907, 2008.

[7] A. S. Mayorov, R. V. Gorbachev, S. V. Morozov, L. Britnell, R. Jalil, L. A. Ponomarenko, P. Blake, K. S. Novoselov, K. Watanabe, T. Taniguchi, *et al.*, "Micrometer-scale ballistic transport in encapsulated graphene at room temperature," *Nano letters*, vol. 11, no. 6, pp. 2396–2399, 2011.

[8] K. S. Novoselov, Z. Jiang, Y. Zhang, S. Morozov, H. Stormer, U. Zeitler, J. Maan, G. Boebinger, P. Kim, and A. Geim, "Room-temperature quantum Hall effect in graphene," *Science*, vol. 315, no. 5817, pp. 1379–1379, 2007.

[9] M. Katsnelson, K. Novoselov, and A. Geim, "Chiral tunnelling and the Klein paradox in graphene," *Nature physics*, vol. 2, no. 9, pp. 620–625, 2006.

[10] W. Han, R. K. Kawakami, M. Gmitra, and J. Fabian, "Graphene spintronics," *Nature nanotechnology*, vol. 9, no. 10, pp. 794–807, 2014.

[11] A. Rycerz, J. Tworzydło, and C. Beenakker, "Valley filter and valley valve in graphene," *Nature Physics*, vol. 3, no. 3, pp. 172–175, 2007.

[12] M. Y. Han, B. Özyilmaz, Y. Zhang, and P. Kim, "Energy band-gap engineering of graphene nanoribbons," *Physical review letters*, vol. 98, no. 20, p. 206805, 2007.

[13] R. Balog, B. Jørgensen, L. Nilsson, M. Andersen, E. Rienks, M. Bianchi, M. Fanetti, E. Lægsgaard, A. Baraldi, S. Lizzit, *et al.*, "Bandgap opening in graphene induced by patterned hydrogen adsorption," *Nature materials*, vol. 9, no. 4, pp. 315–319, 2010.

[14] T. G. Pedersen, C. Flindt, J. Pedersen, N. A. Mortensen, A.-P. Jauho, and K. Pedersen, "Graphene antidot lattices: designed defects and spin qubits," *Physical Review Letters*, vol. 100, no. 13, p. 136804, 2008.

[15] C. R. Dean, A. F. Young, I. Meric, C. Lee, L. Wang, S. Sorgenfrei, K. Watanabe, T. Taniguchi, P. Kim, K. Shepard, *et al.*, "Boron nitride substrates for high-quality graphene electronics," *Nature nanotechnology*, vol. 5, no. 10, pp. 722–726, 2010.

[16] L. Ponomarenko, A. Geim, A. Zhukov, R. Jalil, S. Morozov, K. Novoselov, I. Grigorieva, E. Hill, V. Cheianov, V. Fal'Ko, *et al.*, "Tunable metal-insulator transition in double-layer graphene heterostructures," *Nature Physics*, vol. 7, no. 12, pp. 958–961, 2011.

[17] L. Britnell, R. V. Gorbachev, R. Jalil, B. D. Belle, F. Schedin, M. I. Katsnelson, L. Eaves, S. V. Morozov, A. S. Mayorov, N. M. Peres, *et al.*, "Electron tunneling through ultrathin boron nitride crystalline barriers," *Nano letters*, vol. 12, no. 3, pp. 1707–1710, 2012.

[18] B. Radisavljevic, A. Radenovic, J. Brivio, i. V. Giacometti, and A. Kis, "Single-layer MoS_2 transistors," *Nature nanotechnology*, vol. 6, no. 3, pp. 147–150, 2011.

[19] Q. H. Wang, K. Kalantar-Zadeh, A. Kis, J. N. Coleman, and M. S. Strano, "Electronics and optoelectronics of two-dimensional transition metal dichalcogenides," *Nature nanotechnology*, vol. 7, no. 11, pp. 699–712, 2012.

[20] K. Novoselov, D. Jiang, F. Schedin, T. Booth, V. Khotkevich, S. Morozov, and A. Geim, "Two-dimensional atomic crystals," *Proceedings of the National Academy of Sciences of the United States of America*, vol. 102, no. 30, pp. 10451–10453, 2005.

[21] F. A. Rasmussen and K. S. Thygesen, "Computational 2D Materials Database: Electronic Structure of Transition Metal Dichalcogenides and Oxides," *The Journal of Physical Chemistry C*, 2015.

[22] M. M. Ugeda, A. J. Bradley, Y. Zhang, S. Onishi, Y. Chen, W. Ruan, C. Ojeda-Aristizabal, H. Ryu, M. T. Edmonds, H.-Z. Tsai, *et al.*, "Characterization of collective ground states in single-layer $NbSe_2$," *Nature Physics*, vol. 12, no. 1, pp. 92–97, 2016.

[23] K. F. Mak, C. Lee, J. Hone, J. Shan, and T. F. Heinz, "Atomically thinMoS_2: a new direct-gap semiconductor," *Physical Review Letters*, vol. 105, no. 13, p. 136805, 2010.

[24] A. Splendiani, L. Sun, Y. Zhang, T. Li, J. Kim, C.-Y. Chim, G. Galli, and F. Wang, "Emerging photoluminescence in monolayer MoS_2," *Nano letters*, vol. 10, no. 4, pp. 1271–1275, 2010.

[25] K. F. Mak, C. Lee, J. Hone, J. Shan, and T. F. Heinz, "Atomically thin MoS_2: A new direct-gap semiconductor," *Phys. Rev. Lett.*, vol. 105, p. 136805, Sep 2010.

[26] A. Ramasubramaniam, "Large excitonic effects in monolayers of molybdenum and tungsten dichalcogenides," *Phys. Rev. B*, vol. 86, p. 115409, Sep 2012.

[27] D. Y. Qiu, H. Felipe, and S. G. Louie, "Optical spectrum of MoS_2: many-body effects and diversity of exciton states," *Physical review letters*, vol. 111, no. 21, p. 216805, 2013.

[28] M. M. Ugeda, A. J. Bradley, S.-F. Shi, H. Felipe, Y. Zhang, D. Y. Qiu, W. Ruan, S.-K. Mo, Z. Hussain, Z.-X. Shen, *et al.*, "Giant bandgap renormalization and excitonic effects in a monolayer transition metal dichalcogenide semiconductor," *Nature materials*, 2014.

[29] K. He, N. Kumar, L. Zhao, Z. Wang, K. F. Mak, H. Zhao, and J. Shan, "Tightly bound excitons in monolayer WSe_2," *Phys. Rev. Lett.*, vol. 113, p. 026803, Jul 2014.

[30] K. Novoselov, A. Mishchenko, A. Carvalho, and A. C. Neto, "2d materials and van der Waals heterostructures," *Science*, vol. 353, no. 6298, p. aac9439, 2016.

[31] L. Britnell, R. Gorbachev, R. Jalil, B. Belle, F. Schedin, A. Mishchenko, T. Georgiou, M. Katsnelson, L. Eaves, S. Morozov, *et al.*, "Field-effect tunneling transistor based on vertical graphene heterostructures," *Science*, vol. 335, no. 6071, pp. 947–950, 2012.

[32] F. Withers, O. Del Pozo-Zamudio, A. Mishchenko, A. P. Rooney, A. Gholinia, K. Watanabe, T. Taniguchi, S. J. Haigh, A. K. Geim, A. I. Tartakovskii, and K. S. Novoselov, "Light-emitting diodes by band-structure engineering in van der Waals heterostructures," *Nat. Mater.*, vol. 14, pp. 301–306, 03 2015.

[33] M. Massicotte, P. Schmidt, F. Vialla, K. Schädler, A. Reserbat-Plantey, K. Watanabe, T. Taniguchi, K. Tielrooij, and F. Koppens, "Picosecond photoresponse in van der Waals heterostructures," *Nature nanotechnology*, vol. 11, no. 1, pp. 42–46, 2016.

[34] L. Britnell, R. Ribeiro, A. Eckmann, R. Jalil, B. Belle, A. Mishchenko, Y.-J. Kim, R. Gorbachev, T. Georgiou, and S. Morozov, "Strong light-matter interactions in heterostructures of atomically thin films," *Science*, vol. 340, no. 6138, pp. 1311–1314, 2013.

[35] M. Bernardi, M. Palummo, and J. C. Grossman, "Extraordinary sunlight absorption and one nanometer thick photovoltaics using two-dimensional monolayer materials," *Nano letters*, vol. 13, no. 8, pp. 3664–3670, 2013.

[36] M. Palummo, M. Bernardi, and J. C. Grossman, "Exciton radiative lifetimes in two-dimensional transition metal dichalcogenides," *Nano letters*, vol. 15, no. 5, pp. 2794–2800, 2015.

[37] C.-H. Lee, G.-H. Lee, A. M. Van Der Zande, W. Chen, Y. Li, M. Han, X. Cui, G. Arefe, C. Nuckolls, and T. F. Heinz, "Atomically thin p–n junctions with van der Waals heterointerfaces," *Nature nanotechnology*, vol. 9, no. 9, pp. 676–681, 2014.

[38] J. S. Ross, P. Klement, A. M. Jones, N. J. Ghimire, J. Yan, D. Mandrus, T. Taniguchi, K. Watanabe, K. Kitamura, W. Yao, *et al.*, "Electrically tunable excitonic light-emitting diodes based on monolayer WSe_2 pn junctions," *Nature nanotechnology*, vol. 9, no. 4, pp. 268–272, 2014.

[39] A. Pospischil, M. M. Furchi, and T. Mueller, "Solar-energy conversion and light emission in an atomic monolayer pn diode," *Nature nanotechnology*, vol. 9, no. 4, pp. 257–261, 2014.

[40] O. Lopez, D. Lembke, M. Kayci, A. Radenovic, and A. Kis, "Ultrasensitive photodetectors based on monolayer MoS_2," *Nature nanotechnology*, vol. 8, no. 7, pp. 497–501, 2013.

[41] M. Born and R. Oppenheimer, "Zur quantentheorie der molekeln," *Annalen der Physik*, vol. 389, no. 20, pp. 457–484, 1927.

[42] G. Stefanucci and R. van Leeuwen, *Nonequilibrium Many-Body Theory of Quantum Systems: A Modern Introduction*. Cambridge University Press, 2013.

[43] A. Fetter and J. Walecka, *Quantum Theory of Many-Particle Systems*. Dover Books on Physics, DOVER PUBN Incorporated, 2003.

[44] L. H. Thomas, "The calculation of atomic fields," in *Mathematical Proceedings of the Cambridge Philosophical Society*, vol. 23, pp. 542–548, Cambridge Univ Press, 1927.

[45] E. Fermi, "Un metodo statistico per la determinazione di alcune priorieta dell'atomo," *Rend. Accad. Naz. Lincei*, vol. 6, no. 602-607, p. 32, 1927.

[46] P. Hohenberg and W. Kohn, "Inhomogeneous electron gas," *Physical review*, vol. 136, no. 3B, p. B864, 1964.

[47] W. Kohn and L. J. Sham, "Self-consistent equations including exchange and correlation effects," *Physical review*, vol. 140, no. 4A, p. A1133, 1965.

[48] R. M. Dreizler and E. K. Gross, *Density functional theory: an approach to the quantum many-body problem*. Springer Science & Business Media, 2012.

[49] M. Lüders, A. Ernst, W. Temmerman, Z. Szotek, and P. Durham, "Ab initio angle-resolved photoemission in multiple-scattering formulation," *Journal of Physics: Condensed Matter*, vol. 13, no. 38, p. 8587, 2001.

[50] D. M. Ceperley and B. Alder, "Ground state of the electron gas by a stochastic method," *Physical Review Letters*, vol. 45, no. 7, p. 566, 1980.

[51] K. Capelle, "A bird's-eye view of density-functional theory," *arXiv preprint cond-mat/0211443*, 2002.

[52] J. Kohanoff, *Electronic structure calculations for solids and molecules: theory and computational methods*. Cambridge University Press, 2006.

[53] J. J. Mortensen, L. B. Hansen, and K. W. Jacobsen, "Real-space grid implementation of the projector augmented wave method," *Physical Review B*, vol. 71, no. 3, p. 035109, 2005.

[54] J. Enkovaara, C. Rostgaard, J. J. Mortensen, J. Chen, M. Dułak, L. Ferrighi, J. Gavnholt, C. Glinsvad, V. Haikola, H. Hansen, *et al.*, "Electronic structure calculations with GPAW: a real-space implementation of the projector augmented-wave method," *Journal of Physics: Condensed Matter*, vol. 22, no. 25, p. 253202, 2010.

[55] P. E. Blöchl, "Projector augmented-wave method," *Physical Review B*, vol. 50, no. 24, p. 17953, 1994.

[56] J. Yan, J. J. Mortensen, K. W. Jacobsen, and K. S. Thygesen, "Linear density response function in the projector augmented wave method: Applications to solids, surfaces, and interfaces," *Physical Review B*, vol. 83, no. 24, p. 245122, 2011.

[57] F. Hüser and K. S. Thygesen, *Quasiparticle GW calculations within the GPAW electronic structure code*. PhD thesis, Technical University of DenmarkDanmarks Tekniske Universitet, CenterCenters, Center for Atomic-scale Materials DesignCenter for Atomic-scale Materials Design, 2013.

[58] F. A. Rasmussen and K. S. Thygesen, *First Principle Calculations of Electronic Excitations in 2D Materials*. PhD thesis, Technical University of DenmarkDanmarks Tekniske Universitet, CenterCenters, Center for Atomic-scale Materials DesignCenter for Atomic-scale Materials Design, 2016.

[59] J. Yan, K. W. Jacobsen, and K. S. Thygesen, "Optical properties of bulk semiconductors and graphene/boron nitride: The Bethe-Salpeter equation with derivative discontinuity-corrected density functional energies," *Physical Review B*, vol. 86, no. 4, p. 045208, 2012.

[60] J. Schwinger, "On the Green's functions of quantized fields. i," *Proceedings of the National Academy of Sciences*, vol. 37, no. 7, pp. 452–455, 1951.

[61] P. C. Martin and J. Schwinger, "Theory of Many-Particle systems. i," *Phys. Rev.*, vol. 115, pp. 1342–1373, Sep 1959.

[62] R. Kubo, "Statistical-mechanical theory of irreversible processes. i. general theory and simple applications to magnetic and conduction problems," *Journal of the Physical Society of Japan*, vol. 12, no. 6, pp. 570–586, 1957.

[63] G.-C. Wick, "The evaluation of the collision matrix," *Physical review*, vol. 80, no. 2, p. 268, 1950.

[64] H. Lehmann, "Über eigenschaften von ausbreitungsfunktionen und renormierungskonstanten quantisierter felder," *Il Nuovo Cimento (1943-1954)*, vol. 11, no. 4, pp. 342–357, 1954.

[65] L. Hedin, "New method for calculating the one-particle Green's function with application to the electron-gas problem," *Physical Review*, vol. 139, no. 3A, p. A796, 1965.

[66] G. Strinati, "Application of the Green's functions method to the study of the optical properties of semiconductors," *La Rivista del Nuovo Cimento (1978-1999)*, vol. 11, no. 12, pp. 1–86, 1988.

[67] F. Caruso, *Self-consistent GW approach for the unified description of ground and excited states of finite systems*. PhD thesis, Freie Universität Berlin, 2013.

[68] K. S. Thygesen and A. Rubio, "Renormalization of molecular quasiparticle levels at metal-molecule interfaces: trends across binding regimes," *Physical review letters*, vol. 102, no. 4, p. 046802, 2009.

[69] J. Garcia-Lastra and K. S. Thygesen, "Renormalization of optical excitations in molecules near a metal surface," *Physical review letters*, vol. 106, no. 18, p. 187402, 2011.

[70] L. Sham and M. Schlüter, "Density-functional theory of the energy gap," *Physical Review Letters*, vol. 51, no. 20, p. 1888, 1983.

[71] M. Hellgren and U. von Barth, "Correlation potential in density functional theory at the *gwa* level: Spherical atoms," *Physical Review B*, vol. 76, no. 7, p. 075107, 2007.

[72] M. Grüning, A. Marini, and A. Rubio, "Density functionals from many-body perturbation theory: The band gap for semiconductors and insulators," *The Journal of chemical physics*, vol. 124, no. 15, p. 154108, 2006.

[73] S. L. Adler, "Quantum theory of the dielectric constant in real solids," *Physical Review*, vol. 126, no. 2, p. 413, 1962.

[74] N. Wiser, "Dielectric constant with local field effects included," *Physical Review*, vol. 129, no. 1, p. 62, 1963.

[75] C. A. Rozzi, D. Varsano, A. Marini, E. K. Gross, and A. Rubio, "Exact coulomb cutoff technique for supercell calculations," *Physical Review B*, vol. 73, no. 20, p. 205119, 2006.

[76] F. Hüser, T. Olsen, and K. S. Thygesen, "How dielectric screening in two-dimensional crystals affects the convergence of excited-state calculations: Monolayer MoS_2," *Physical Review B*, vol. 88, no. 24, p. 245309, 2013.

[77] P. Cudazzo, I. V. Tokatly, and A. Rubio, "Dielectric screening in two-dimensional insulators: Implications for excitonic and impurity states in graphane," *Physical Review B*, vol. 84, no. 8, p. 085406, 2011.

[78] R. Del Sole and R. Girlanda, "Optical properties of semiconductors within the independent-quasiparticle approximation," *Physical Review B*, vol. 48, no. 16, p. 11789, 1993.

[79] S. Albrecht, L. Reining, R. Del Sole, and G. Onida, "Ab initio calculation of excitonic effects in the optical spectra of semiconductors," *Physical review letters*, vol. 80, no. 20, p. 4510, 1998.

[80] L. X. Benedict, E. L. Shirley, and R. B. Bohn, "Optical absorption of insulators and the electron-hole interaction: An ab-initio calculation," *Physical review letters*, vol. 80, no. 20, p. 4514, 1998.

[81] M. Rohlfing and S. G. Louie, "Electron-hole excitations in semiconductors and insulators," *Physical review letters*, vol. 81, no. 11, p. 2312, 1998.

[82] M. Gatti, "Correlation effects in valence electron spectroscopy of transition metal oxides: many-body perturbation theory and alternative approaches," *L'École Polytechnique*, 2007.

[83] E. E. Salpeter and H. A. Bethe, "A relativistic equation for bound-state problems," *Physical Review*, vol. 84, no. 6, p. 1232, 1951.

[84] A. Marini and R. Del Sole, "Dynamical excitonic effects in metals and semiconductors," *Physical review letters*, vol. 91, no. 17, p. 176402, 2003.

[85] G. Onida, L. Reining, and A. Rubio, "Electronic excitations: density-functional versus many-body Green's-function approaches," *Reviews of Modern Physics*, vol. 74, no. 2, p. 601, 2002.

[86] P. Cudazzo, L. Sponza, C. Giorgetti, L. Reining, F. Sottile, and M. Gatti, "Exciton band structure in two-dimensional materials," *Physical review letters*, vol. 116, no. 6, p. 066803, 2016.

[87] G. Fugallo, M. Aramini, J. Koskelo, K. Watanabe, T. Taniguchi, M. Hakala, S. Huotari, M. Gatti, and F. Sottile, "Exciton energy-momentum map of hexagonal boron nitride," *Physical Review B*, vol. 92, no. 16, p. 165122, 2015.

[88] C. Zhang, H. Wang, W. Chan, C. Manolatou, and F. Rana, "Absorption of light by excitons and trions in monolayers of metal dichalcogenide MoS_2: Experiments and theory," *Physical Review B*, vol. 89, no. 20, p. 205436, 2014.

[89] T. C. Berkelbach, M. S. Hybertsen, and D. R. Reichman, "Theory of neutral and charged excitons in monolayer transition metal dichalcogenides," *Phys. Rev. B*, vol. 88, p. 045318, Jul 2013.

[90] G. Grosso and G. Parravicini, *Solid State Physics*. Elsevier Science, 2000.

[91] P. Cudazzo, C. Attaccalite, I. V. Tokatly, and A. Rubio, "Strong Charge-Transfer Excitonic Effects and the Bose-Einstein Exciton Condensate in Graphane," *Phys. Rev. Lett.*, vol. 104, p. 226804, Jun 2010.

[92] O. Pulci, P. Gori, M. Marsili, V. Garbuio, R. Del Sole, and F. Bechstedt, "Strong excitons in novel two-dimensional crystals: Silicane and germanane," *EPL (Europhysics Letters)*, vol. 98, no. 3, p. 37004, 2012.

[93] X. Yang, S. Guo, F. Chan, K. Wong, and W. Ching, "Analytic solution of a two-dimensional hydrogen atom. i. nonrelativistic theory," *Physical Review A*, vol. 43, no. 3, p. 1186, 1991.

[94] J.-H. Choi, P. Cui, H. Lan, and Z. Zhang, "Linear scaling of the exciton binding energy versus the band gap of two-dimensional materials," *Physical review letters*, vol. 115, no. 6, p. 066403, 2015.

[95] A. Chernikov, T. C. Berkelbach, H. M. Hill, A. Rigosi, Y. Li, O. B. Aslan, D. R. Reichman, M. S. Hybertsen, and T. F. Heinz, "Exciton binding energy and nonhydrogenic rydberg series in monolayer WS_2," *Physical review letters*, vol. 113, no. 7, p. 076802, 2014.

[96] Z. Ye, T. Cao, K. O'Brien, H. Zhu, X. Yin, Y. Wang, S. G. Louie, and X. Zhang, "Probing excitonic dark states in single-layer tungsten disulphide," *Nature*, vol. 513, no. 7517, pp. 214–218, 2014.

[97] A. Geim and I. Grigorieva, "Van der waals heterostructures," *Nature*, vol. 499, no. 7459, pp. 419–425, 2013.

[98] H. Terrones, F. López-Urías, and M. Terrones, "Novel hetero-layered materials with tunable direct band gaps by sandwiching different metal disulfides and diselenides," *Scientific reports*, vol. 3, 2013.

[99] X. Cui, G.-H. Lee, Y. D. Kim, G. Arefe, P. Y. Huang, C.-H. Lee, D. A. Chenet, X. Zhang, L. Wang, F. Ye, *et al.*, "Multi-terminal transport measurements of MoS_2 using a van der Waals heterostructure device platform," *Nature nanotechnology*, vol. 10, no. 6, pp. 534–540, 2015.

[100] Q. Ma, T. I. Andersen, N. L. Nair, N. M. Gabor, M. Massicotte, C. H. Lui, A. F. Young, W. Fang, K. Watanabe, and T. Taniguchi, "Tuning ultrafast electron thermalization pathways in a van der Waals heterostructure," *Nature Physics*, vol. 12, no. 1, pp. 455–459, 2016.

[101] X. Hong, J. Kim, S.-F. Shi, Y. Zhang, C. Jin, Y. Sun, S. Tongay, J. Wu, Y. Zhang, and F. Wang, "Ultrafast charge transfer in atomically thin MoS_2/WS_2 heterostructures," *Nature nanotechnology*, vol. 9, no. 1, pp. 682–686, 2014.

[102] P. Rivera, J. R. Schaibley, A. M. Jones, J. S. Ross, S. Wu, G. Aivazian, P. Klement, K. Seyler, G. Clark, and N. J. Ghimire, "Observation of long-lived interlayer excitons in monolayer $MoSe_2$-WSe_2 heterostructures," *Nature communications*, vol. 6, 2015.

[103] P. Rivera, K. L. Seyler, H. Yu, J. R. Schaibley, J. Yan, D. G. Mandrus, W. Yao, and X. Xu, "Valley-polarized exciton dynamics in a 2D semiconductor heterostructure," *Science*, vol. 351, no. 6274, pp. 688–691, 2016.

[104] H. Fang, C. Battaglia, C. Carraro, S. Nemsak, B. Ozdol, J. S. Kang, H. A. Bechtel, S. B. Desai, F. Kronast, and A. A. Unal, "Strong interlayer coupling in van der Waals heterostructures built from single-layer chalcogenides," *Proceedings of the National Academy of Sciences*, vol. 111, no. 17, pp. 6198–6202, 2014.

[105] H. Heo, J. H. Sung, S. Cha, B.-G. Jang, J.-Y. Kim, G. Jin, D. Lee, J.-H. Ahn, M.-J. Lee, and J. H. Shim, "Interlayer orientation-dependent light absorption and emission in monolayer semiconductor stacks," *Nature communications*, vol. 6, 2015.

[106] "The dielectric building blocks and the qeh software can be downloaded from:." `https://cmr.fysik.dtu.dk/vdwh/vdwh.html`. Accessed: 2015-08-18.

[107] A. Steinhoff, J.-H. Kim, F. Jahnke, M. Rösner, D.-S. Kim, C. Lee, G. H. Han, M. S. Jeong, T. O. Wehling, and C. Gies, "Efficient Excitonic Photoluminescence in Direct and Indirect Band Gap Monolayer MoS_2," *Nano letters*, vol. 15, no. 10, pp. 6841–6847, 2015.

[108] M. Rösner, E. Şaşıoğlu, C. Friedrich, S. Blügel, and T. Wehling, "Wannier function approach to realistic Coulomb interactions in layered materials and heterostructures," *Physical Review B*, vol. 92, no. 8, p. 085102, 2015.

[109] L. V. Keldysh *JETP Lett.*, vol. 29, p. 658, 1979.

[110] T. Cheiwchanchamnangij and W. R. L. Lambrecht, "Quasiparticle band structure calculation of monolayer, bilayer, and bulk MoS_2," *Phys. Rev. B*, vol. 85, p. 205302, May 2012.

[111] H.-P. Komsa and A. V. Krasheninnikov, "Effects of confinement and environment on the electronic structure and exciton binding energy of MoS_2 from first principles," *Phys. Rev. B*, vol. 86, p. 241201, Dec 2012.

[112] H. Peelaers and C. G. Van de Walle, "Effects of strain on band structure and effective masses in MoS_2," *Phys. Rev. B*, vol. 86, p. 241401, Dec 2012.

[113] V. Popescu and A. Zunger, "Extracting e versus $\bar{k}$ effective band structure from supercell calculations on alloys and impurities," *Physical Review B*, vol. 85, no. 8, p. 085201, 2012.

[114] A. Klots, A. Newaz, B. Wang, D. Prasai, H. Krzyzanowska, J. Lin, D. Caudel, N. Ghimire, J. Yan, B. Ivanov, *et al.*, "Probing excitonic states in suspended two-dimensional semiconductors by photocurrent spectroscopy," *Scientific reports*, vol. 4, 2014.

[115] A. J. Siegert, "On the derivation of the dispersion formula for nuclear reactions," *Physical Review*, vol. 56, no. 8, p. 750, 1939.

[116] N. Hatano, K. Sasada, H. Nakamura, and T. Petrosky, "Some properties of the resonant state in quantum mechanics and its computation," *Progress of theoretical physics*, vol. 119, no. 2, pp. 187–222, 2008.

[117] B. Simon, "Resonances in n-body quantum systems with dilatation analytic potentials and the foundations of time-dependent perturbation theory," *Annals of Mathematics*, pp. 247–274, 1973.

[118] A. H. Larsen, U. De Giovannini, and A. Rubio, "Dynamical Processes in Open Quantum Systems from a TDDFT perspective: Resonances and electron photoemission," in *Density-Functional Methods for Excited States*, pp. 219–271, Springer, 2015.

[119] I. Herbst and B. Simon, "Stark effect revisited," *Physical Review Letters*, vol. 41, no. 2, p. 67, 1978.

[120] H. Shi, R. Yan, S. Bertolazzi, J. Brivio, B. Gao, A. Kis, D. Jena, H. G. Xing, and L. Huang, "Exciton dynamics in suspended monolayer and few-layer MoS_2 2D crystals," *ACS nano*, vol. 7, no. 2, pp. 1072–1080, 2013.

[121] D. Sun, Y. Rao, G. A. Reider, G. Chen, Y. You, L. Brézin, A. R. Harutyunyan, and T. F. Heinz, "Observation of rapid exciton–exciton annihilation in monolayer molybdenum disulfide," *Nano letters*, vol. 14, no. 10, pp. 5625–5629, 2014.

[122] F. Sottile, *Response functions of semiconductors and insulators: from the Bethe-Salpeter equation to time-dependent density functional theory*. PhD thesis, Ecole Polytechnique X, 2003.

Papers

Paper I

Dielectric Genome of van der Waals Heterostructures
Kirsten Andersen, Simone Latini and Kristian S. Thygesen, *Nano Lett.*, **15** (7), pp 4616–4621 (2015).

NANO LETTERS

Letter

pubs.acs.org/NanoLett

Dielectric Genome of van der Waals Heterostructures

Kirsten Andersen,*[†] Simone Latini,[†,‡] and Kristian S. Thygesen*[†,‡]

[†]Center for Atomic-scale Materials Design, Department of Physics, and [‡]Center for Nanostructured Graphene, Technical University of Denmark, DK-2800 Kgs. Lyngby, Denmark

Supporting Information

ABSTRACT: Vertical stacking of two-dimensional (2D) crystals, such as graphene and hexagonal boron nitride, has recently lead to a new class of materials known as van der Waals heterostructures (vdWHs) with unique and highly tunable electronic properties. Ab initio calculations should in principle provide a powerful tool for modeling and guiding the design of vdWHs, but in their traditional form such calculations are only feasible for commensurable structures with a few layers. Here we show that the dielectric properties of realistic, incommensurable vdWHs comprising hundreds of layers can be efficiently calculated using a multiscale approach where the dielectric functions of the individual layers (the dielectric building blocks) are computed ab initio and coupled together via the long-range Coulomb interaction. We use the method to illustrate the 2D−3D transition of the dielectric function of multilayer MoS_2 crystals, the hybridization of quantum plasmons in thick graphene/hBN heterostructures, and to demonstrate the intricate effect of substrate screening on the non-Rydberg exciton series in supported WS_2. The dielectric building blocks for a variety of 2D crystals are available in an open database together with the software for solving the coupled electrodynamic equations.

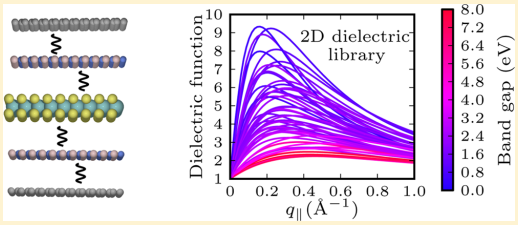

KEYWORDS: *van der Waals heterostructures, 2D materials, density functional theory, dielectric function, excitons, plasmons*

The class of 2D materials, which started with graphene, is rapidly expanding and now includes metallic and semiconducting transition metal dichalcogenides[1] in addition to group III−V semimetals, semiconductors, and insulators.[2] These atomically thin materials exhibit unique optoelectronic properties with high technological potential.[3−7] However, the 2D materials only form the basis of a new and much larger class of materials consisting of vertically stacked 2D crystals held together by weak van der Waals forces. In contrast to conventional heterostructures that require complex and expensive crystal-growth techniques to epitaxially grow the single-crystalline semiconductor layers, van der Waals heterostructures (vdWHs) can be stacked in ambient conditions with no requirements of lattice matching. The latter implies a weaker constraint, if any, on the choice of materials that can be combined into vdWHs.

The weak interlayer binding suggests that the individual layers of a vdWH largely preserve their original 2D properties modified only by the long-range Coulomb interaction with the surrounding layers. Turning this argument around, it should be possible to predict the overall properties of a vdWH from the properties of the individual layers. In this Letter we show that this can indeed be achieved for the dielectric properties. Conceptually, this extends the Lego brick picture used by Geim and Grigorieva[8] for the atomic structure of a vdWH, to its dielectric properties. Specifically, we develop a semiclassical model that takes as input the dielectric functions of the individual isolated layers computed fully quantum mechanically and condensed into the simplest possible representation, and couples them together via the Coulomb interaction, see Figure 1. Despite the complete neglect of interlayer hybridization, the model provides an excellent account of both the spatial and dynamical dielectric properties of vdWHs. The condensed representation of the dielectric functions of the 2D crystals can thus be regarded as the dielectric genome of the vdWH.

In addition to its conceptual value, our approach overcomes a practical limitation of conventional first-principles methods. Such methods are not only computationally demanding, but also rely on periodic boundary conditions, which are incompatible with the incommensurable interfaces found in vdWHs. In fact, for many purposes, an in-plane lattice mismatch between neighboring 2D crystals is preferred because it reduces the interlayer coupling, and thus minimizes the risk of commensurate−incommensurate transitions,[9] and formation of Moire patterns[10] and associated band structure reconstructions,[11] which are typical for systems with similar lattice constants. This emphasizes the need for alternative approaches for modeling vdWHs.

The dielectric function is one of the most important material response functions. It determines the effective interaction between charged particles in the material, contains information about the collective oscillations of the electron gas (plasmons),[12] and enters as a fundamental ingredient in many-body calculations of, e.g., excitons and quasiparticle

Received: March 31, 2015
Revised: June 3, 2015
Published: June 5, 2015

DOI: 10.1021/acs.nanolett.5b01251
Nano Lett. 2015, 15, 4616−4621

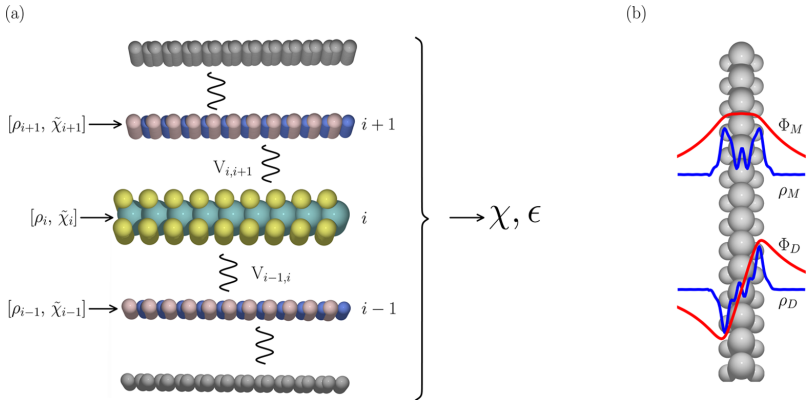

Figure 1. Schematic of the QEH model. (a) The density response function and dielectric function of the heterostructure are calculated from the dielectric building blocks of the individual layers assuming a purely electrostatic interaction between the layers. The dielectric building blocks are calculated ab initio for the isolated layers. They comprise the monopole and dipole components of the density response function, $\tilde{\chi}_{M/D}$, together with the spatial shape of the electron density, $\rho_{M/D}(z)$, induced by a constant and linear applied potential, respectively. (b) Monopole and dipole induced densities (blue) together with the associated potentials (red) for monolayer MoS_2.

band structures.[13,14] We stress that in this work we consider only the electronic contributions to the dielectric properties. In particular, when referring to the static dielectric function we mean the dielectric function at frequencies smaller than any electronic transition energy but larger than the vibrational energies of the system.

The (inverse) dielectric function is related to the electron density response function, χ, via

$$\epsilon^{-1}(\mathbf{r}, \mathbf{r}', \omega) = \delta(\mathbf{r} - \mathbf{r}') + \int \frac{1}{|\mathbf{r} - \mathbf{r}''|}\chi(\mathbf{r}'', \mathbf{r}', \omega)\, \mathrm{d}\mathbf{r}'' \tag{1}$$

In our quantum-electrostatic heterostructure (QEH) model the calculation of the dielectric function is divided into two parts. In the first part the in-plane averaged density response functions of the freestanding layers, $\chi_i(z, z', \mathbf{q}_\parallel, \omega)$, are obtained from ab initio calculations. In practice we treat the in-plane momentum transfer, $\mathbf{q}_\parallel$, as a scalar since most 2D materials are isotropic within the plane. From χ_i we calculate the magnitude of the monopole/dipole component of the density induced by a potential with a constant/linear variation across the layer and in-plane variation $\exp(i\mathbf{r}_\parallel \cdot \mathbf{q}_\parallel)$

$$\tilde{\chi}_{i\alpha}(\mathbf{q}_\parallel, \omega) = \int z^\alpha \chi_i(z, z', \mathbf{q}_\parallel, \omega) z'^\alpha \, \mathrm{d}z\mathrm{d}z' \tag{2}$$

Here α = 0,1 for the monopole and dipole components, respectively. In addition we calculate the spatial form of the induced density, $\rho_{i\alpha}(z,\mathbf{q}_\parallel)$. With a proper normalization of $\rho_{i\alpha}$ we can then write

$$\int \chi_i(z, z', \mathbf{q}_\parallel, \omega) z'^\alpha \, \mathrm{d}z' = \tilde{\chi}_{i\alpha}(\mathbf{q}_\parallel, \omega)\rho_{i\alpha}(z, \mathbf{q}_\parallel) \tag{3}$$

We have found that while $\tilde{\chi}_{i\alpha}$ depends strongly on frequency, $\rho_{i\alpha}$ does not. The data set $(\tilde{\chi}_{i\alpha}, \rho_{i\alpha})$ with α = 0,1 or equivalently $\alpha = M,D$ constitutes the dielectric building block of layer i, as illustrated in Figure 1. According to eq 3 the dielectric building block allows us to obtain the density induced in the (isolated) layer i by a constant/linear potential. It is straightforward to extend the dielectric building blocks to account for higher-order moments in the induced density described by $\alpha > 1$, but we have found the dipole approximation to be sufficient in all cases considered.

In the second part of the QEH model, the density response function of the vdWH in the discrete monopole/dipole representation is obtained by solving a Dyson-like equation that couples the dielectric building blocks together via the Coulomb interaction. The Dyson equation for the full density response function giving the magnitude of the monopole/dipole density on layer i induced by a constant/linear potential applied to layer j reads (omitting the $\mathbf{q}_\parallel$ and ω variables for simplicity)

$$\chi_{i\alpha,j\beta} = \tilde{\chi}_{i\alpha}\delta_{i\alpha,j\beta} + \tilde{\chi}_{i\alpha}\sum_{k\neq i,\gamma} V_{i\alpha,k\gamma}\chi_{k\gamma,j\beta} \tag{4}$$

The Coulomb matrices are defined as

$$V_{i\alpha,k\gamma}(\mathbf{q}_\parallel) = \int \rho_{i\alpha}(z, \mathbf{q}_\parallel)\Phi_{k\gamma}(z, \mathbf{q}_\parallel)\, \mathrm{d}z \tag{5}$$

where $\Phi_{k\gamma}$ is the potential associated with the induced density, $\rho_{k\gamma}$, which we calculate on a uniform grid by solving a 1D Poisson equation. Note that we leave out the self-interaction terms in eq 4 since the intralayer Coulomb interaction is already accounted for by the uncoupled $\tilde{\chi}_{i\alpha}$. The (inverse) dielectric function of eq 1 in the monopole/dipole basis becomes

$$\epsilon^{-1}_{i\alpha,j\beta}(\mathbf{q}_\parallel, \omega) = \delta_{i\alpha,j\beta} + \sum_{k\gamma} V_{i\alpha,k\gamma}(\mathbf{q}_\parallel)\chi_{k\gamma,j\beta}(\mathbf{q}_\parallel, \omega) \tag{6}$$

More details on the method and computations are provided in the Supporting Information.

A database containing the dielectric building blocks of a large collection of 2D materials has been constructed and is available from our Web site.[15] It presently contains more than 50 transition metal dichalcogenides and oxides, graphene at different doping levels, and hBN, and more materials are being added. From here the data files can be downloaded together with a Python module for calculating the dielectric function and associated properties of any combination of these materials. QEH model calculations for vdWHs containing a few

DOI: 10.1021/acs.nanolett.5b01251
Nano Lett. 2015, 15, 4616−4621

hundred layers can be performed on a standard PC. To illustrate the variation in the dielectric properties of the 2D semiconductors, Figure 2 shows the $\mathbf{q}_\parallel$-dependent static

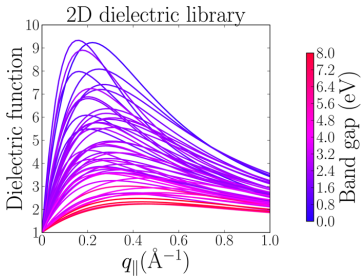

Figure 2. Static dielectric function $\epsilon(\mathbf{q}_\parallel,\omega = 0)$ of the 51 transition metal dichalcogenides and oxides included in the database. As expected, the magnitude of the dielectric function is seen to correlate with the size of the band gap indicated by the color. The band gaps are calculated with G_0W_0 in ref 16.

dielectric functions of the monolayer transition metal dichalcogenides and -oxides presently contained in our database (for a complete overview of the materials see ref 16). All the dielectric functions show the same qualitative form, in particular they become 1 for $\mathbf{q}_\parallel \to 0$ and $\mathbf{q}_\parallel \to \infty$; however, there is quite some variation in their magnitude. As expected the size of the dielectric function correlates well with the size of the band gap of the material indicated by the color.

First-principles calculations were performed with the GPAW code.[17,18] Single-particle wave functions and energies were calculated within the local density approximation (LDA) using 400 eV plane wave cutoff and at least 45 × 45 sampling of the 2D Brillouin zone. Density response functions and dielectric functions were calculated within the random phase approximation (RPA). The RPA does not include (direct) electron−hole interaction, but generally yields good results for the static dielectric properties of semiconductors and dynamical response of metals. Except for MoS_2 bulk, we included at least 15 Å of vacuum in the super cells perpendicular to the layers and applied a truncated Coulomb kernel to avoid long-range screening between periodically repeated structures. All response functions were calculated in a plane wave basis including reciprocal lattice vectors up to at least 50 eV. A similar cut off was used for the sum over empty states, and convergence was carefully checked. The frequency dependence of the response functions was represented on a nonlinear frequency grid ranging from 0 to 35 eV, with an initial grid spacing of 0.02 eV. All details of the calculations and atomic structure geometries are provided in the Supporting Information.

As a first application of the QEH model, we study how the (static) dielectric function of a 2D material evolves as the layer thickness increases toward the bulk. One of the most characteristic differences between 2D and 3D materials is the behavior of the dielectric function in the long wavelength limit: For a bulk semiconductor, the dielectric function $\epsilon(\mathbf{q})$ tends smoothly to a value larger than unity as $\mathbf{q} \to 0$. This is the static dielectric constant of the material, ϵ_∞. In contrast $\epsilon(\mathbf{q}_\parallel) = 1 + O(\mathbf{q}_\parallel)$ for a 2D semiconductor implying a complete absence of screening in the long wavelength limit.[19,20] Consequently, the concept of the dielectric *constant* does not exist for a freestanding 2D semiconductor.

Ab initio calculations were performed for the dielectric function of MoS_2 monolayer, bilayer, and bulk, and the QEH model was used for multilayer structures up to 100 layers. Figure 3b shows the dielectric functions averaged over the slabs, i.e., the macroscopic dielectric function, as a function of the in-plane momentum transfer. For large $\mathbf{q}_\parallel$ the dielectric functions show similar behavior. However, whereas $\epsilon(0) = 14$ for the bulk, the dielectric functions of the slabs decrease sharply to 1 for small $\mathbf{q}_\parallel$. This demonstrates that the dielectric properties of a vdWH of thickness L are 2D like for $q_\parallel \ll 1/L$ and 3D like for $q_\parallel \gg 1/L$. Interestingly, also the result for bulk MoS_2 shows reminiscence of the 2D nature of the constituent layers, where the magnitude of the dielectric function has a slight drop when $q_\parallel \to 0$.

The QEH model describes the change in the dielectric function from mono- to bilayer very accurately in spite of the well-known differences between the mono- and bilayer band

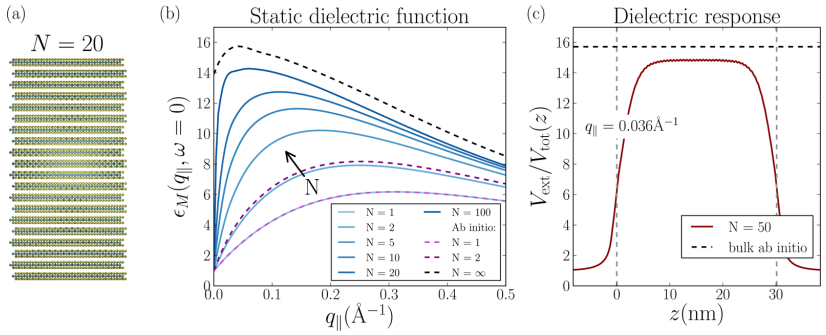

Figure 3. Two-dimensional to three-dimensional transition of the dielectric function. (a) Atomic structure of a 20 layer MoS_2 slab. (b) The macroscopic static dielectric function $\epsilon_M(q_\parallel,\omega = 0)$ as a function of the in-plane momentum transfer for different number of layers, N. The macroscopic dielectric function relates the total potential averaged over the width of the slab to an external potential of the form $V_{ext}(r_\parallel,z) = \exp(i\mathbf{r}_\parallel \cdot \mathbf{q}_\parallel)$. The dielectric functions increase monotonically with N converging slowly toward the dielectric function of bulk MoS_2 obtained from an ab initio calculation. Excellent agreement between the QEH model and the ab initio results are seen for $N = 1,2$. The slow convergence toward the bulk result is due to the strong spatial variation of the induced potential in the surface region of the slabs. This can be seen in panel (c), which shows $V_{ext}/V_{tot}(z)$, i.e., the local dielectric function, for an external potential constant across the slab and with in-plane wave vector $\mathbf{q}_\parallel = 0.036$ Å^{-1} for $N = 50$.

DOI: 10.1021/acs.nanolett.5b01251
Nano Lett. 2015, 15, 4616−4621

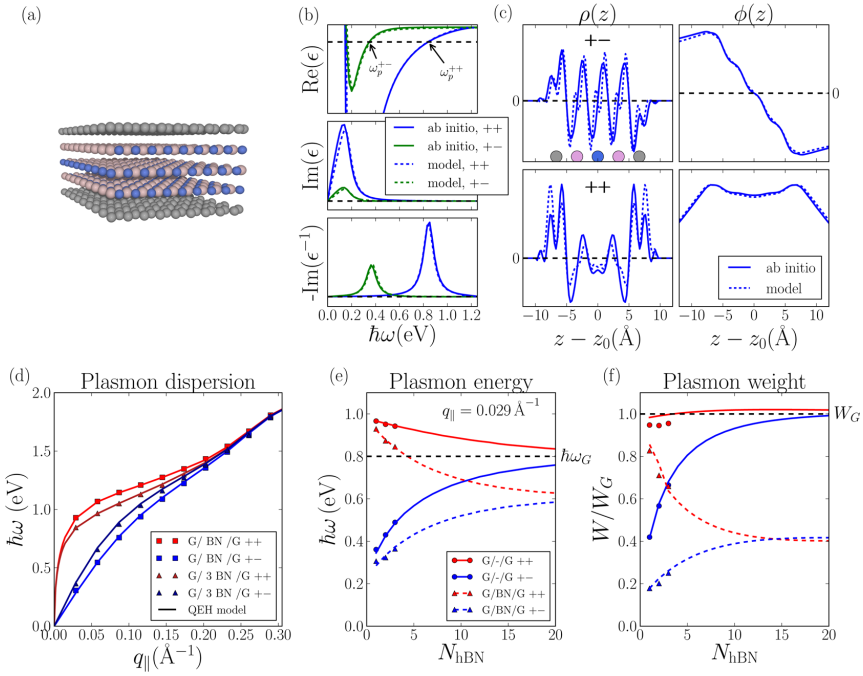

Figure 4. Plasmons in graphene/hBN heterostructures. (a) Two graphene sheets separated by three layers of hBN. (b) Eigenvalues of the heterostructure dielectric function $\epsilon(\omega)$. Only the two eigenvalue curves that fulfill the plasmon condition $\mathrm{Re}\epsilon_n(\omega_P) = 0$ are shown. (c) The eigenpotential, $\psi(\omega_P)$, and associated density, $\rho(\omega_P)$, of the plasmon modes. The plasmons correspond to the antisymmetric (+−) and symmetric (+ +) combinations of the isolated graphene plasmons. (d) Plasmon dispersion for heterostructures containing 1 and 3 layers of hBN. Full lines denote the QEH model while ab initio results are denoted by symbols. (e,f) Energy and weight of the plasmon modes for up to 20 layers hBN between the graphene sheets. Results for equivalent structures with vacuum filling the gap are also shown. Dashed black lines indicate the plasmon energy and weight in an isolated graphene sheet. Overall, the QEH model is in excellent agreement with the full ab initio calculations performed for up to 3 layers of hBN.

structures.[21] This shows that hybridization driven band structure effects, i.e., quantum confinement, have negligible influence on the dielectric properties of a vdWH which is the main reason for the success of the QEH model. The model result seems to converge toward the ab initio bulk result; however, convergence is not fully reached even for $N = 100$. The slow convergence toward the bulk result is mainly due to the spatial variation of the induced potential across the slab. In Figure 3c we show the z-dependent dielectric function defined as $\epsilon(z) = V_{ext}/V_{tot}(z)$, for a constant (along z) external potential with a long wavelength in-plane variation for $N = 50$. Although $\epsilon(z)$ is close to the ab initio bulk value (dashed line) in the middle of the slab, screening is strongly suppressed in the surface region. Increasing the slab thickness beyond 50 layers brings the QEH result even closer to the bulk result in the middle of the slab, but a small underestimation remains originating from the difference in the band structures of the monolayer and bulk systems. The suppressed screening in the surface region is a direct consequence of the anisotropic nature of the layered MoS_2 crystals, which limits the screening of perpendicular fields relative to in-plane fields, and is expected to be a general property of vdWHs.

The model can also be used to calculate the response to fields polarized along the z-direction, i.e., perpendicular to the layers. In this case the perpendicular component, $\epsilon_{zz}(\omega = 0)$, can be calculated by applying an external potential with a linear variation along z. In the discrete basis of the QEH model, such a field is represented by a vector with 0 for all monopole components and 1 for all dipole components. Comparing the averaged slope of the total potential to the slope of the applied linear potential for a slab of $N = 100$ layers of MoS_2 yields $\epsilon_{zz} = 7.8$. This value is somewhat larger than the bulk value of 6.03; however, due to long-range surface effects the two numbers should not necessarily coincide. In fact, we find excellent agreement between the QEH model and full ab initio calculation of ϵ_{zz} for a four layer MoS_2 slab (see Supporting Information).

Next, we consider the hybridization of plasmons in graphene sheets separated by a hBN buffer layer of varying thickness, see Figure 4a. Plasmons in graphene on hBN were recently found to propagate with low loss,[6] and the close to perfect lattice match between graphene and hBN enables full ab initio calculations for the thinnest heterostructures. Here we use doped graphene that has a finite density of states at the Fermi level, giving rise to metallic sheet plasmons with energies in the regime 0−2 eV. The plasmon energies go to zero in the optical limit, $\mathbf{q}_\parallel \to 0$, as characteristic for plasmons in 2D metals.[22,23] We calculate the effect of hBN on the plasmons using the QEH model for up to 20 layers of hBN and compare to full ab initio calculations for 1−3 layers of hBN.

DOI: 10.1021/acs.nanolett.5b01251
Nano Lett. 2015, 15, 4616−4621

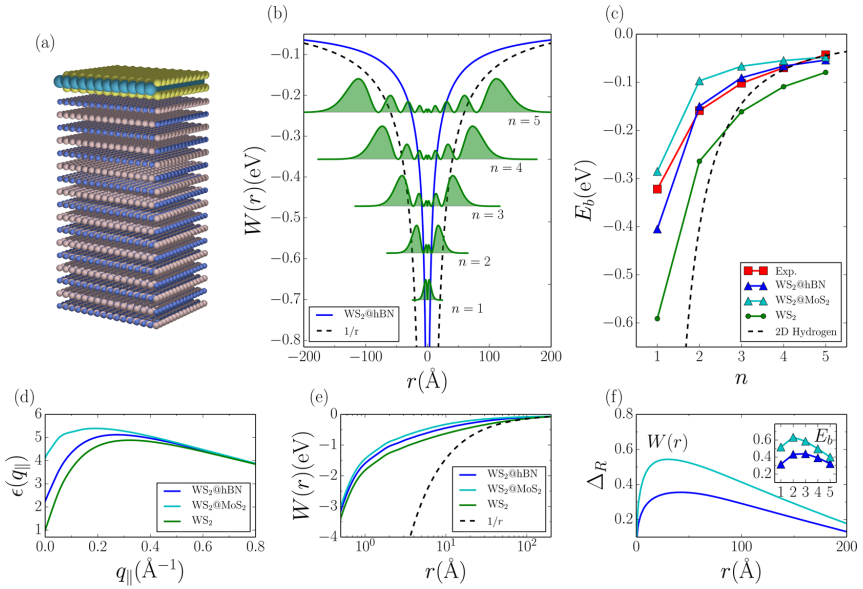

Figure 5. Excitons in supported WS_2. (a) Monolayer WS_2 adsorbed on a hBN substrate. (b) The screened interaction between an electron and a hole localized within a WS_2 monolayer adsorbed on hBN. For comparison the unscreened $1/r$ potential is shown. The radial probability distribution of the first five excitons, $r|F(r)|^2$, are also shown (arbitrary normalization). (c) The calculated binding energies of the lowest five excitons in freestanding WS_2 (green) and WS_2 on hBN (blue) and MoS_2 (cyan). Experimental values from ref 26 for WS_2 on SiO_2 are shown in red. The 2D hydrogen model with a $1/\epsilon r$ potential is shown for $\epsilon = 1.7$. (d) The dielectric function of the WS_2 layer defined as $\epsilon(q_\parallel) = V(q_\parallel)/W(q_\parallel)$, where $V(q)$ and $W(q)$ are the bare and screened interaction in the WS_2 layer, respectively. (e) The screened interaction in the WS_2 layer as a function of $\log(r)$. (f) The relative difference between the screened interaction in the supported and freestanding WS_2. Inset shows the relative difference between E_b for the supported and freestanding WS_2.

To identify the plasmons of the heterostructure we follow ref 24. In brief, we compute the eigenvalues, $\epsilon_n(\omega)$, of the heterostructure dielectric function for each frequency point and identify a plasmon energy, $\hbar\omega_P$, from the condition $\mathrm{Re}\epsilon_n(\omega_P) = 0$, see Figure 4b. The corresponding eigenvector, $\phi_n(\omega_P)$, represents the potential associated with the plasmon oscillation, see panel c. This analysis identifies two plasmons corresponding to the symmetric (++) and antisymmetric (+−) combinations of the graphene plasmons as previously found for two freestanding graphene sheets.[25] For 1−3 hBN layers, the QEH model perfectly reproduces the ab initio results for the dielectric eigenvalues, plasmon energies, and weights. The weight is defined as the area under the peaks in the loss function $-\mathrm{Im}\epsilon^{-1}(\mathbf{q}_\parallel,\omega)$, see panel b. The densities and potentials of the plasmon eigenmodes shown in panel c are also reproduced fairly accurately by the model, where the qualitative differences for the induced densities, $\rho(z)$, are due to the use of a limited basis of the monopole and dipole response for each layer. In panels e and f the result of full ab initio calculations are shown by triangles, while the QEH results are shown by continuous lines. The effect of the hBN buffer (dashed lines) is to red shift and dampen the plasmons compared to the result for two graphene sheets separated by the same amount of vacuum (full lines). This is also reflected by the relatively large amount of electron density located on the hBN during the plasma oscillation, see panel c.

Finally, we explore some characteristic features of excitons in freestanding and supported 2D semiconductors. A straightforward generalization of the well-known Mott−Wannier model[27] leads to the following eigenvalue equation for the excitons of a 2D semiconductor[19,28]

$$\left[-\frac{\nabla_{2D}^{\ 2}}{2\mu_{ex}} + W(\mathbf{r})\right]F(\mathbf{r}) = E_b F(\mathbf{r}) \tag{7}$$

where E_b is the exciton binding energy, $F(\mathbf{r})$ is the wave function, μ_{ex} is the effective mass, and $W(\mathbf{r})$ is the screened electron−hole interaction. Assuming that the electron and hole are localized in layer 1, the Fourier transformed screened electron−hole interaction is obtained from the static ($\omega = 0$) response function (eq 4) and Coulomb interaction matrix (eq 5) of the QEH model

$$W(\mathbf{q}_\parallel) = V_{1M,1M}(\mathbf{q}_\parallel) + \sum_{i\alpha,j\beta} V_{1M,j\beta}(\mathbf{q}_\parallel)\chi_{j\beta,i\alpha}(\mathbf{q}_\parallel)V_{i\alpha,1M}(\mathbf{q}_\parallel) \tag{8}$$

The first term is the bare, i.e., unscreened, electron−hole interaction in layer 1 under the assumption that the electron and hole densities can be represented by the induced monopole density, $\rho_{1M}(z)$. The second term describes the screening from the surrounding layers and layer 1 itself. Note that the above equation can be easily generalized to describe the screened interaction between charges localized in different layers (relevant for indirect excitons).

In ref 26 Chernikov et al. observed a peculiar non-hydrogenic Rydberg series for the excitons in a single layer of WS_2 adsorbed on a SiO_2 substrate. Here we use the QEH model to calculate the screened electron−hole interaction within the

DOI: 10.1021/acs.nanolett.5b01251
Nano Lett. 2015, 15, 4616−4621

WS_2 layer from the dielectric function of the full heterostructure. Since the QEH is applicable only to layered materials we place WS_2 on a 100 layer thick slab of hBN, which has dielectric constant very similar to that of SiO_2 (both around 4). For comparison we performed similar calculations using MoS_2 as substrate (dielectric constant larger than SiO_2). Figure 5c shows the five lowest *s*-excitons calculated from eq 7 for both freestanding and supported WS_2. For freestanding WS_2, we obtain E_b = 0.59 eV for the lowest exciton in good agreement with previous ab initio calculations.[29] The enhanced screening from the substrate lowers the exciton binding energies bringing the entire series closer to the experimental values (red), in particular for the hBN substrate.

The dielectric function of the WS_2 layer is defined as $\epsilon(q_\parallel) = V(q_\parallel)/W(q_\parallel)$, where $V(q_\parallel)$ and $W(q_\parallel)$ are the bare and screened interaction in the WS_2 layer, respectively. Figure 5d shows that the dielectric function of the supported WS_2 layer exceeds unity in the $\mathbf{q}_\parallel \to 0$ limit. For structures of finite width, L, the dielectric function will in fact tend to unity for very small $q_\parallel \ll 1/L$. Here the results have been extrapolated to infinite substrate thickness, where $\epsilon(\mathbf{q}_\parallel)$ tends to a value larger than unity (in practice the extrapolation has no influence on the calculated exciton energies, i.e., they are well converged for N = 100). This means that the nature of the screening within the layer is not strictly 2D because the bulk substrate is able to screen the long wavelength fields. In real space, the screened potentials diverge as $\log(r)$ for small r and decay as $1/r$ for large r, see panel e. In panel f we show how the substrate affects $W(r)$: The relative deviation from $W(r)$ of the freestanding layer vanishes for small and large r but becomes significant at intermediate distances. As a consequence, the substrate-induced change in the exciton binding energy is relatively larger for intermediate exciton sizes. These results clearly demonstrate the profound, nonlocal influence of substrates on the dielectric screening and excitations in 2D materials.

In conclusion, we have demonstrated that the spatial and dynamical dielectric properties of a vdWH can be accurately and efficiently obtained from the dielectric properties of its constituent 2D crystals. The presented quantum-electrostatic heterostructure model (QEH) exploits this feature and enables the calculation of the dielectric properties and collective electronic excitations of realistic incommensurable heterostructures with ab initio precision. The dielectric building blocks for more than 50 different 2D materials are available in an open database allowing 2D materials researchers to efficiently predict and design the dielectric properties of realistic vdWHs.

■ ASSOCIATED CONTENT

Supporting Information

Detailed description of our quantum-electrostatic heterostructure (QEH) model and the computational details for all the ab initio calculations. The Supporting Information is available free of charge on the ACS Publications website at DOI: 10.1021/acs.nanolett.5b01251.

■ AUTHOR INFORMATION

Corresponding Authors

*E-mail: kiran@fysik.dtu.dk.
*E-mail: thygesen@fysik.dtu.dk.

Notes

The authors declare no competing financial interest.

■ ACKNOWLEDGMENTS

The authors thank Karsten Jacobsen for inspiring discussions. The authors acknowledge support from the Danish Council for Independent Research's Sapere Aude Program through grant no. 11-1051390. The Center for Nanostructured Graphene (CNG) is sponsored by the Danish National Research Foundation, Project DNRF58.

■ REFERENCES

(1) Wang, Q. H.; Kalantar-Zadeh, K.; Kis, A.; Coleman, J. N.; Strano, M. S. *Nat. Nanotechnol.* **2012**, *7*, 699−712.
(2) Şahin, H.; Cahangirov, S.; Topsakal, M.; Bekaroglu, E.; Akturk, E.; Senger, R. T.; Ciraci, S. *Phys. Rev. B* **2009**, *80*, 155453.
(3) Britnell, L.; Ribeiro, R. M.; Eckmann, a.; Jalil, R.; Belle, B. D.; Mishchenko, a.; Kim, Y.-J.; Gorbachev, R. V.; Georgiou, T.; Morozov, S. V.; Grigorenko, a. N.; Geim, a. K.; Casiraghi, C.; Castro Neto, a. H.; Novoselov, K. S. *Science* **2013**, *340*, 1311−4.
(4) Sup Choi, M.; Lee, G.-H.; Yu, Y.-J.; Lee, D.-Y.; Hwan Lee, S.; Kim, P.; Hone, J.; Jong Yoo, W. *Nat. Commun.* **2013**, *4*, 1624.
(5) Shih, C. J.; Wang, Q. H.; Son, Y.; Jin, Z.; Blankschtein, D.; Strano, M. S. *ACS Nano* **2014**, *8*, 5790−5798.
(6) Woessner, A.; Lundeberg, M. B.; Gao, Y.; Principi, A.; Alonso-González, P.; Carrega, M.; Watanabe, K.; Taniguchi, T.; Vignale, G.; Polini, M.; Hone, J.; Hillenbrand, R.; Koppens, F. H. L. *Nat. Mater.* **2015**, *14*, 421−425.
(7) Withers, F.; del Pozo-Zamudio, O.; Mishchenko, A.; Rooney, A. P.; Gholinia, A.; Watanabe, K.; Taniguchi, T.; Haigh, S. J.; Geim, A. K.; Tartakovskii, A. I.; Novoselov, K. S. *Nat. Mater.* **2015**, *14*, 301−306.
(8) Geim, a. K.; Grigorieva, I. V. *Nature* **2013**, *499*, 419−25.
(9) Woods, C. R.; et al. *Nat. Phys.* **2014**, *10*, 451−456.
(10) Kang, J.; Li, J.; Li, S. S.; Xia, J. B.; Wang, L. W. *Nano Lett.* **2013**, *13*, 5485−5490.
(11) Lu, C.-P.; Li, G.; Watanabe, K.; Taniguchi, T.; Andrei, E. *Phys. Rev. Lett.* **2014**, *113*, 156804.
(12) Pitarke, J. M.; Silkin, V. M.; Chulkov, E. V.; Echenique, P. M. *Rep. Prog. Phys.* **2007**, *70*, 1−87.
(13) Onida, G.; Reining, L.; Rubio, A. *Rev. Mod. Phys.* **2002**, *74*, 601−659.
(14) Hybertsen, M. S.; Louie, S. G. *Phys. Rev. B* **1986**, *34*, 5390.
(15) The dielectric building blocks and QEH software can be downloaded at https://cmr.fysik.dtu.dk/vdwh/vdwh.html.
(16) Rasmussen, F. A.; Thygesen, K. S. *J. Phys. Chem. C* **2015**, DOI: 10.1021/acs.jpcc.5b02950.
(17) Enkovaara, J.; et al. *J. Phys. Condens. Mater.* **2010**, *22*, 253202.
(18) Yan, J.; Mortensen, J. J.; Jacobsen, K. W.; Thygesen, K. S. *Phys. Rev. B* **2011**, *83*, 245122.
(19) Cudazzo, P.; Tokatly, I. V.; Rubio, A. *Phys. Rev. B* **2011**, *84*, 085406.
(20) Hüser, F.; Olsen, T.; Thygesen, K. S. *Phys. Rev. B* **2013**, *87*, 1−14.
(21) Cheiwchanchamnangij, T.; Lambrecht, W. R. L. *Phys. Rev. B* **2012**, *85*, 1−4.
(22) Hwang, E.; Sarma, S. *Phys. Rev. B* **2007**, *75*, 205418.
(23) Shin, S. Y.; Kim, N. D.; Kim, J. G.; Kim, K. S.; Noh, D. Y.; Kim, K. S.; Chung, J. W. *Appl. Phys. Lett.* **2011**, *99*, 082110.
(24) Andersen, K.; Jacobsen, K. W.; Thygesen, K. S. *Phys. Rev. B* **2012**, *86*, 245129.
(25) Hwang, E.; Das Sarma, S. *Phys. Rev. B* **2009**, *80*, 205405.
(26) Chernikov, A.; Berkelbach, T. C.; Hill, H. M.; Rigosi, A.; Li, Y.; Aslan, O. B.; Reichman, D. R.; Hybertsen, M. S.; Heinz, T. F. *Phys. Rev. Lett.* **2014**, *113*, 076802.
(27) Wannier, G. H. *Phys. Rev.* **1937**, *52*, 191.
(28) Berkelbach, T. C.; Hybertsen, M. S.; Reichman, D. R. *Phys. Rev. B* **2013**, *88*, 045318.
(29) Shi, H.; Pan, H.; Zhang, Y.-W.; Yakobson, B. I. *Phys. Rev. B* **2013**, *87*, 155304.

DOI: 10.1021/acs.nanolett.5b01251
Nano Lett. 2015, 15, 4616−4621

Supporting Information for: Dielectric genome of van der Waals Heterostructures

Kirsten Andersen*
Center for Atomic-scale Materials Design, Department of Physics
Technical University of Denmark, DK - 2800 Kgs. Lyngby, Denmark

Simone Latini and Kristian S. Thygesen†
Center for Atomic-scale Materials Design, Department of Physics, and Center for Nanostructured Graphene
Technical University of Denmark, DK - 2800 Kgs. Lyngby, Denmark

In this Supporting Information we provide a detailed description of our quantum-electrostatic heterostructure (QEH) model including the precise definition of the dielectric building blocks. In addition we detail the spectral analysis used to identify the plasmon eigenmodes for the graphene/hBN structures and describe the calculation of the screened electron-hole interaction used in the 2D exciton model. Also, we describe how the model can be applied to calculate the response to fields with a variation perpendicular to the layers. Finally, we provide computational details for all the ab-initio calculations presented in the Letter.

I. FORMAL MATTERS

Within linear response theory, the induced density due to an external field of the form $V_{ext}(\mathbf{r},t) = V_{ext}(\mathbf{r},\omega)e^{i\omega t}$, is described by the density response function, $\chi(\mathbf{r},\mathbf{r}',\omega)$:

$$n_{\mathrm{ind}}(\mathbf{r},\omega) = \int dr' \chi(\mathbf{r},\mathbf{r}',\omega) V_{ext}(\mathbf{r}',\omega), \tag{1}$$

The density response function can be obtained from its non-interacting counterpart, $\chi^0(\mathbf{r},\mathbf{r}',\omega)$, that gives the response to the *total* field, by solving the Dyson equation in the random phase approximation (RPA):

$$\chi(\mathbf{r},\mathbf{r}',\omega) = \chi^0(\mathbf{r},\mathbf{r}',\omega) + \int\int d\mathbf{r}_1 d\mathbf{r}_2 \chi^0(\mathbf{r},\mathbf{r}_1,\omega)\frac{1}{|\mathbf{r}_1-\mathbf{r}_2|}\chi(\mathbf{r}_2,\mathbf{r}',\omega). \tag{2}$$

For modelling of vdWHs, this equation is favourably split into two parts, namely the intra-layer and inter-layer parts, as described below.

We are assuming a basis set consisting of layer centred functions, $\{\phi_{i\alpha}\}$, where i denotes the layer. Defining the Coulomb matrix as

$$\mathbf{V}_{i\alpha,j\beta} = \int d\mathbf{r} d\mathbf{r}' \phi_{i\alpha}(\mathbf{r})\frac{1}{|\mathbf{r}-\mathbf{r}'|}\phi_{j\beta}(\mathbf{r}') \tag{3}$$

we can divide the Coulomb interaction into its intra- and interlayer parts: $\mathbf{V} = \tilde{\mathbf{V}} + \mathbf{V^I}$. The Dyson equation Eq. 2 can then be separated into the following two matrix equations

$$\tilde{\boldsymbol{\chi}} = \boldsymbol{\chi^0} + \boldsymbol{\chi^0}\tilde{\mathbf{V}}\tilde{\boldsymbol{\chi}} \tag{4}$$

$$\boldsymbol{\chi} = \tilde{\boldsymbol{\chi}} + \tilde{\boldsymbol{\chi}}\mathbf{V^I}\boldsymbol{\chi}. \tag{5}$$

To see this, simply insert Eq. 4 into Eq. 5

$$\begin{aligned}\boldsymbol{\chi} &= \boldsymbol{\chi^0} + \boldsymbol{\chi^0}\tilde{\mathbf{V}}\tilde{\boldsymbol{\chi}} + \boldsymbol{\chi^0}\mathbf{V^I}\boldsymbol{\chi} + \boldsymbol{\chi^0}\tilde{\mathbf{V}}\tilde{\boldsymbol{\chi}}\mathbf{V^I}\boldsymbol{\chi} && (6)\\ &= \boldsymbol{\chi^0} + \boldsymbol{\chi^0}\mathbf{V^I}\boldsymbol{\chi} + \boldsymbol{\chi^0}\tilde{\mathbf{V}}(\tilde{\boldsymbol{\chi}} + \tilde{\boldsymbol{\chi}}\mathbf{V^I}\boldsymbol{\chi}) && (7)\\ &= \boldsymbol{\chi^0} + \boldsymbol{\chi^0}\mathbf{V^I}\boldsymbol{\chi} + \boldsymbol{\chi^0}\tilde{\mathbf{V}}\boldsymbol{\chi} && (8)\\ &= \boldsymbol{\chi^0} + \boldsymbol{\chi^0}(\tilde{\mathbf{V}} + \mathbf{V^I})\boldsymbol{\chi}, && (9)\end{aligned}$$

which is the original Dyson equation.

At this point no approximations, except for the RPA, have been introduced. In particular, $\boldsymbol{\chi^0}$ in Eq. 4 is the non-interacting response function of the full vdWH. To make progress we make the assumption that the overlap/hybridization between wave functions (not to be confused with the basis functions) on neighbouring layers can be neglected. This allows us to replace χ^0 of the heterostructure by the sum of χ^0_i for the individual isolated layers. In practice this means that Eq. 4 can be solved for each layer separately.

We calculate χ^0 for the isolated layers within the RPA using single-particle wave functions and energies from density functional theory (DFT) as described in Ref.[1]. The interacting density response function, $\tilde{\chi}$, for the monolayer is obtained by solving the Dyson equation in a plane-wave basis with a 2D truncated Coulomb Kernel, $\tilde{V}^{2D}_{\mathbf{G}}$:

$$\tilde{V}^{2D}_{\mathbf{G},G_z} = \frac{4\pi}{G^2}\big[1-\cos(G_z L/2)\big]. \tag{10}$$

The use of a truncated Coulomb interaction is essential to avoid interaction between periodically repeated layers[2]. The truncation length is set to half the unit cell height, L. In the plane wave basis, the Dyson equation for the density response function, $\tilde{\chi}$, is then written:

$$\tilde{\chi}_{\mathbf{G},\mathbf{G}'}(\mathbf{q}_\parallel,\omega) = \chi^0_{\mathbf{G},\mathbf{G}'}(\mathbf{q}_\parallel,\omega) + \sum_{\mathbf{G}_1}\chi^0_{\mathbf{G},\mathbf{G}_1}(\mathbf{q}_\parallel,\omega)\tilde{V}^{2D}_{\mathbf{G}_1}(\mathbf{q}_\parallel)\tilde{\chi}_{\mathbf{G}_1,\mathbf{G}'}(\mathbf{q}_\parallel,\omega), \tag{11}$$

where $\mathbf{q}_\parallel$ belongs to the 2D Brillouin zone.

II. QEH MODEL

A. The dielectric building blocks

We start by defining the density response function for the individual layers, where the macroscopic average is

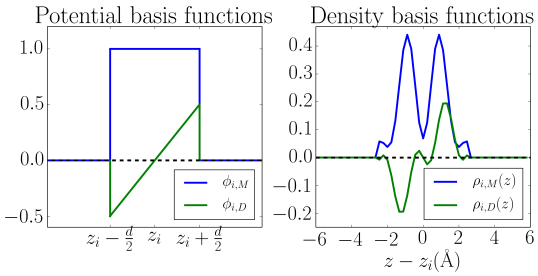

FIG. 1: Basis functions used to represent potentials (left) and induced densities (right) in the QEH model. The example is for graphene at $\mathrm{q}_\parallel = 0.029\text{Å}^{-1}$.

taken in the parallel directions. The response function is then expressed in terms of the perpendicular coordinates z and z', and the magnitude of the momentum transfer parallel to the layer, $q_\parallel$ (we assume isotropic materials, where the response does not depend on the direction of $q_\parallel$, but the method can be straightforwardly generalized to non-isotropic 2D materials):

$$\tilde{\chi}(z,z',q_\parallel,\omega) = \frac{1}{A}\int_A\int_A d\mathbf{r}_\parallel d\mathbf{r}'_\parallel \tilde{\chi}(\mathbf{r},\mathbf{r}',q_\parallel,\omega)$$
$$= \frac{1}{L}\sum_{\mathbf{G}_z,\mathbf{G}'_z} e^{i\mathbf{G}_z z}\tilde{\chi}_{\mathbf{G}_z,\mathbf{G}'_z}(q_\parallel,\omega)e^{-i\mathbf{G}'_z z'}, \quad (12)$$

where the integration is over the in-plane coordinates, A is the in-plane area of the supercell, and L is the height of the supercell perpendicular to the layer. Integrating over the in-plane coordinates corresponds to taking the zero components $\mathbf{G}_\parallel = \mathbf{G}'_\parallel = 0$ in the plane-wave representation of $\tilde{\chi}_{\mathbf{G},\mathbf{G}'}(\mathbf{q},\omega)$. Working with $\tilde{\chi}$ instead of $\tilde{\chi}^0$ ensures that local field effects within the isolated layer are exactly taken into account.

For an efficient representation of the response functions and solution of the Dyson equation we need a small yet accurate basis set to represent the induced densities in the layers and the potentials created by these induced densities. To represent potentials we simply use a constant and linear potential corresponding to a first order expansion of the induced potentials, see Fig 1(left). We refer to these as monopole (M) and dipole (D) potentials. The potential basis functions of layer i at position z_i are thus

$$\phi_{i,M}(z) = 1_{[z_i-d/2,z_i+d/2]} \quad (13)$$
$$\phi_{i,D}(z) = (z-z_i)\,1_{[z_i-d/2,z_i+d/2]} \quad (14)$$
$$1_C = \begin{cases} 1 & \text{if } z \in C \\ 0 & \text{if } z \notin C \end{cases} \quad (15)$$

where d is a localisation parameter that is set equal to the interplane distance. Since the density response is already confined to the layer, the precise value of d is not essential and in calculating the matrix elements of the intralayer response function we integrate over all space:

$$\tilde{\chi}_{i\alpha}(q_\parallel,\omega) = \int\int dz dz' \phi_{i,\alpha}(z)\tilde{\chi}(z,z',q_\parallel,\omega)\phi_{i,\alpha}(z') \quad (16)$$
$$\approx \int\int dz dz' (z-z_i)^\alpha \tilde{\chi}_i(z,z',q_\parallel,\omega)(z'-z_i)^\alpha, \quad (17)$$

where $\alpha = \{M,D\}$ or equivalently $\alpha = \{0,1\}$.

The basis functions can be interpreted as potentials that act on χ. In order to represent the induced densities produced by these potentials, we introduce two density basis functions defined as

$$\rho_{i,\alpha}(z,q_\parallel) = \frac{\int dz'\tilde{\chi}(z,z',q_\parallel,\omega=0)\,\phi_{i,\alpha}(z')}{\tilde{\chi}_{i,\alpha}(q_\parallel,\omega=0)}. \quad (18)$$

As an example, the monopole and dipole density basis functions for monolayer graphene are shown in Fig. 1(right). We have found that the frequency dependence of the basis functions can in general be omitted, while the $q_\parallel$-dependence is not always negligible. Dividing by $\tilde{\chi}_{i,\alpha}(q_\parallel,\omega=0)$ in Eq. 18 ensures that the density basis function is normalized such that the overlap with the potential basis is unity: $\langle\phi_{i,\alpha}|\rho_{i,\alpha}(q_\parallel)\rangle = 1$, where integration over z is implied. To ease the derivation of the Dyson equation in the monopole/dipole basis, we make the approximation that the potential and density basis functions form a dual basis, i.e.

$$\langle\phi_{i,\alpha}|\rho_{j,\beta}(q_\parallel)\rangle = \delta_{\alpha\beta}\delta_{ij}, \quad (19)$$

where $\alpha,\beta = \{M,D\}$, and i,j are layer indices. This implies that, within the subspace spanned by the basis functions, we have the completeness relation

$$\mathrm{P} = \sum_{i,\alpha}|\rho_{i,\alpha}\rangle\langle\phi_{i,\alpha}| = \hat{1}. \quad (20)$$

We note that Eq. 19 is not exact because of the small but finite overlap between potential and density basis functions on neighbouring layers. However, taking this into account gives very small modifications to the resulting vdWH dielectric properties. Finally, we note that working with a dual basis is natural as, in general, the spectral representation of the dielectric function is written in a dual basis of potential and density eigenfunctions[3].

B. Electrostatic Dyson equation

The Dyson equation (5) for the heterostructure density response function $\chi(z,z',q_\parallel,\omega)$ is now written in the potential basis of dimension $2N\times 2N$, where N is the number of layers. In the following the $(q_\parallel,\omega)$ variables are omitted from the expressions for simplicity. Response functions $\tilde{\chi}$, χ and Coulomb kernel V are regarded as operators and integration over $\mathbf{r},\mathbf{r}'$ is implied in the inner

products. The matrix elements of χ are written in the potential basis:

$$\langle\phi_{i,\alpha}|\chi|\phi_{j,\beta}\rangle = \langle\phi_{i,\alpha}|\tilde{\chi}|\phi_{j,\beta}\rangle + \langle\phi_{i,\alpha}|\tilde{\chi}\, V^I\, \chi|\phi_{j,\beta}\rangle. \quad (21)$$

The first term on the right hand side is simply the response function of the isolated layers for which we have $\langle\phi_{i,\alpha}|\tilde{\chi}|\phi_{j,\beta}\rangle = \tilde{\chi}_{i,\alpha}\delta_{i\alpha,j\beta}$. In the second term, applying $\langle\phi_{i,\alpha}|$ to $\tilde{\chi}$ returns $\tilde{\chi}_{i,\alpha}\langle\rho_{i,\alpha}|$ (this follows from Eq. 18 and the symmetry of $\tilde{\chi}(z,z')$). Now the completeness relation (20) is inserted between V^I and χ, leading to

$$\langle\phi_{i,\alpha}|\chi|\phi_{j,\beta}\rangle = \tilde{\chi}_{i,\alpha}\delta_{i\alpha,j\beta} \; + \\ \tilde{\chi}_{i,\alpha}\sum_{k,\alpha'}\langle\rho_{i,\alpha}|V^I|\rho_{k,\alpha'}\rangle\langle\phi_{k,\alpha'}|\chi|\phi_{j,\beta}\rangle$$

This leads to the final Dyson equation for the heterostructure:

$$\chi_{i\alpha,j\beta}(q_\parallel,\omega) = \tilde{\chi}_{i,\alpha}(q_\parallel,\omega)\delta_{i\alpha,j\beta} + \\ \tilde{\chi}_{i,\alpha}(q_\parallel,\omega)\sum_{k\neq i,\gamma} V_{i\alpha,k\gamma}(q_\parallel)\,\chi_{k\gamma,j\beta}(q_\parallel,\omega). \quad (22)$$

The Coulomb kernel is here defined in the density basis as: $V_{i\alpha,k\alpha'} = \langle\rho_{i,\alpha}|V|\rho_{k,\alpha'}\rangle$. The term $V|\rho_{k,\alpha'}\rangle$ is the potential at z from the density basis function in layer k, which is found by solving Poisson's equation for $|\rho_{k,\alpha'}\rangle$ on a real space grid. Since the density parallel to the layer just shows periodic oscillations with wave vector $q_\parallel$, Poisson's equation reduces to a 1D differential equation:

$$\frac{\partial^2}{\partial z^2}\Phi_{k\alpha'}(z) - q_\parallel^2\Phi_{k\alpha'}(z) = -4\pi\rho_{k\alpha'}(z). \quad (23)$$

The elements of the V matrix are then: $V_{i\alpha,k\alpha'} = \langle\rho_{i,\alpha}|\Phi_{k,\alpha'}\rangle$.

C. The dielectric matrix

The inverse dielectric function is related to χ through: $\epsilon^{-1} = \mathrm{I} - V\chi$. Due to the non-symmetric nature (in $\mathbf{r}$ and $\mathbf{r}'$) of the dielectric function, the elements of ϵ^{-1} are naturally written using a mixed density/potential basis:

$$\langle\rho_{i,\alpha}|\epsilon^{-1}|\phi_{j,\alpha}\rangle = \delta_{i\alpha,j\beta} + \langle\rho_{i,\alpha}|V\,\chi|\phi_{j,\beta}\rangle. \quad (24)$$

Upon insertion of the completeness relation (20) this gives

$$\epsilon^{-1}_{i\alpha,j\beta}(q_\parallel,\omega) = \delta_{i\alpha,j\beta} + \sum_{k,\gamma} V_{i\alpha,k\gamma}(q_\parallel)\chi_{k\gamma,j\beta}(q_\parallel,\omega). \quad (25)$$

III. PLASMONS EIGENMODES

By following a previously developed method for identifying plasmon eigenmodes in nanostructures from ab initio[3], the dielectric matrix for the heterostructure, Eq. 25, is diagonalized to solve the eigenvalue equation:

$$\sum_{j\beta}\epsilon_{i\alpha,j\beta}(q_\parallel,\omega)f_{n,j\beta}(q_\parallel,\omega) = \epsilon_n(q_\parallel,\omega)f_{n,i\alpha}(q_\parallel,\omega), \quad (26)$$

which returns the eigenvalues, $\epsilon_n(q_\parallel,\omega)$, and eigenvectors, $f_{n,i\alpha}(q_\parallel,\omega)$ of the dielectric matrix in the monopole/dipole basis. A plasmon eigenmode fullfills that:

$$\mathrm{Re}\sum_{j\beta}\epsilon_{i\alpha,j\beta}(q_\parallel,\omega)f_{n,j\beta}(q_\parallel,\omega) = 0, \quad (27)$$

corresponding to $\mathrm{Re}\epsilon_n(q_\parallel,\omega) = 0$. In practice, the plasmon energies are identified from the peaks in the eigenvalue loss-spectrum $-\mathrm{Im}\epsilon_n(q_\parallel,\omega)$ since this includes the finite imaginary part which can shift the plasmon energy. The right eigenfunctions $f_{n,i\alpha}$ give the induced potential of the plasmon in the basis of $\phi_{i,M/D}$. The left eigenfunctions, $f^n_{i\alpha}$, correspond to the induced density of the plasmon in the basis of $\rho_{i,M/D}$[3]. The induced density is thus given by

$$\rho_n(z,q_\parallel) = \sum_{i\alpha} f^n_{i\alpha}\rho_{i\alpha}(z,q_\parallel) \quad (28)$$

with the corresponding induced potential

$$\phi_n(z,q_\parallel) = \sum_{i\alpha} f^n_{i\alpha}\Phi_{i\alpha}(z,q_\parallel) \quad (29)$$

IV. EXCITONS

The Mott-Wannier model, widely used to model excitons in bulk semiconductors, can be straightforwardly generalised to 2D semiconductors. This leads to a 2D hydrogenic Hamiltonian of the form

$$\left[-\frac{\nabla^2_{2D}}{2\mu_{ex}} + W(\mathbf{r})\right]F(\mathbf{r}) = E_b F(\mathbf{r}), \quad (30)$$

where $F(\mathbf{r})$ is the exciton wave-function, μ_{ex} the exciton effective mass and $W(\mathbf{r}_\parallel)$ is the screened Coulomb potential which includes the screening coming from the 2D material itself and the environment, e.g. a substrate.

Now, consider electron and hole charge distributions given by (the in-plane variation is a plane wave of wave vector $q_\parallel$)

$$\rho^{e/h}(z,q_\parallel) = \sum_{i\alpha}\rho^{e/h}_{i\alpha}(q_\parallel)\rho_{i\alpha}(z,q_\parallel). \quad (31)$$

We can then calculate the screened interaction between the electron and hole charge distributions according to

$$W(q_\parallel) = \sum_{k\alpha,i\beta,j\gamma}\rho^e_{k\alpha}(q_\parallel)\epsilon^{-1}_{k\alpha,i\beta}(q_\parallel)V_{i\beta,j\gamma}(q_\parallel)\rho^h_{j\gamma}(q_\parallel). \quad (32)$$

In the case of excitons located in the layer 1 we can approximate $\rho^{e/h}(z, q_\parallel) = \rho_{1M}(z, q_\parallel)(z)$ and we recover the expression in the Methods section. We can describe a general charge distribution, e.g. using conduction/valence band charge distributions $\rho^{e/h}(z, q_\parallel) = |\psi_{c/v}(z, q_\parallel)|^2$, by a simple redefinition of the Coulomb matrix elements in Eq. 32.

Performing a 2D Fourier transform of $W(q_\parallel)$ yields the screened potential in real space:

$$W(\mathbf{r}_\parallel) = -\frac{1}{2\pi}\int_0^\infty dq_\parallel q_\parallel J_0(q_\parallel \mathbf{r}_\parallel) W(q_\parallel), \qquad (33)$$

where $J_n(x)$ is the Bessel function of the first kind. The exciton mass can be obtained e.g. from an ab-initio band structure calculation. We solve Eq. 30 using polar coordinates and a logarithmic radial grid.

V. SCREENING OF PERPENDICULAR FIELDS

In the manuscript we show the results for the dielectric function of multilayer MoS_2 for wavevectors in the plane of the layers (see Fig 3 in the main manuscript), and considered the spatial form of the response due to a constant perturbation (along z). However, the model can also be used to calculate the response to fields with a linear variation in the $z-$direction (perpendicular to the layers) and can thus be used to calculate the $z-$component of the dielectric function, ϵ_{zz}. This can be calculated in the optical limit, $q_z \to 0$, with the expression:

$$\epsilon^{-1}_{zz} = \frac{12}{L^3}\int_{-L/2}^{L/2}\int_{-\infty}^{\infty} z\,\epsilon^{-1}(z, z'\omega = 0)\, z'\, dz' dz, \qquad (34)$$

where L is the width of the structure. In the QEH model, this corresponds to taking the matrix product of $\epsilon^{-1}_{i\alpha,j\beta}(q_\parallel, \omega)$ with a vector, v, with the elements: $v_{j\beta} = \delta_{\beta,D}$, where only the dipole elements are non-zero: $v = \{0, 1, 0, 1, ...\}$. The expression becomes:

$$\epsilon^{-1}_{zz} = \frac{1}{L}\sum_{i,j} d_i\, v_{i,D}\, \epsilon^{-1}_{iD,jD}(q_\parallel = 0, \omega = 0)\, v_{j,D}, \qquad (35)$$

where d_i is the width of the individual layers and $L = \sum_i d_i$.

In Fig. 2 the induced potential of a N=4 layer MoS_2 slab due to an external potential with a linear form along z, $V_{\text{ext}}(z) \propto z$, is shown together with the ab initio result. The potential is clearly screened by the material, where the induced potential has opposite sign that the external potential. The ab initio result is in this case obtained by applying a weak electric field (within the linear response regime) in the z-direction on the ground-state DFT level. This calculation was performed on a real-space grid representation of the electronic wavefunctions, with a grid-spacing of $h = 0.18$ Å, and $(12, 12)$ k-points,

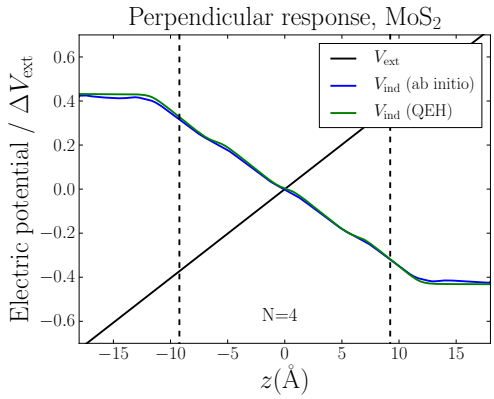

FIG. 2: Induced potential of a N=4 layer MoS_2 slab, due to an external perturbation with a constant slope across the structure. The potentials are normalized with respect to the potential drop across the structure, ΔV_{ext}, the width of the structure here defined as $L = 4d_{MoS_2} = 24.6$Å. The dashed lines indicate the center of the outermost layers.

which were sufficient to converge the ground-state electronic density that determines the total potential. The induced potential is then obtained as $V_{\text{ind}} = V_{\text{tot}} - V_{\text{ext}}$.

As seen in Fig. 2, the QEH model captures the response to perpendicular fields quite well, with a tendency to overestimate the drop in induced potential across the structure and therefore overestimate the dielectric function. This leads to a value of $\epsilon_{zz}(\text{QEH}) = 7.71$ compared to an ab initio value of $\epsilon_{zz}(\text{ab initio}) = 6.81$ for the $N = 4$ MoS_2 slab. In case of bulk MoS_2 we obtain $\epsilon_{zz}(\text{bulk, ab initio}) = 6.03$ compared to $\epsilon_{zz}(\text{N} = 100, \text{QEH}) = 7.83$, which means that the bulk limit is less well-described. However, this is to be expected since the model cannot account for the bulk limit as $q_\parallel \to 0$, since the dielectric function $\epsilon(q_\parallel \to 0) = 1$ for finite slab widths in the model, while for a 3D system the dielectric function tends to a finite value.

VI. COMPUTATIONAL DETAILS

A. Multilayer MoS_2

Ab initio calculations were performed for monolayer MoS_2 to obtain the monolayer density response functions and induced densities used as input for the QEH model. The single-particle energies and wave functions were calculated with the PBE exchange correlation functional, with a plane-wave basis set with an energy cutoff of 400 eV. A dense k-point sampling of $(128, 128)$ in the 2D Brillouin zone was used in order to calculate the response at low momentum transfers. In the linear re-

sponse RPA calculation we used an energy cutoff of 50 eV for the reciprocal lattice vectors. We used a nonlinear frequency grid from 0 to 35 eV, with an initial grid spacing of 0.02 eV and a broadening of 0.04 eV. Corresponding ab initio calculations were performed for bulk and bilayer MoS_2, but with a k-point sampling of $(64, 64, 1)$ for the bilayer and $(64, 64, 8)$ for bulk. For the monolayer and bilayer calculations the truncated Coulomb kernel, see Eq. 10, was used while the full, i.e. non-truncated kernel, was used for the bulk calculation. We used an in-plane lattice constants of 3.18 Å, and A-B stacking with 6.15 Å separation between layers. For the monolayer and bilayer calculation the unit cells contained 20 Å of vacuum to separate the periodic images in the z-direction. For the heterostructure calculation we used the same separation between the layers as for the ab initio calculations ($d = 6.15$ Å). We note that the effect of stacking arrangement (A-A or A-B) cannot be accounted for within the model.

B. Graphene/hBN heterostructures

Ab initio calculations were performed to obtain the dielectric building blocks of monolayer doped graphene and hBN. Also, full ab initio calculations were done for entire heterostructures, including up to three layers of hBN, or the equivalent amount of vacuum, separating the doped graphene layers. An in plane lattice-constant of 2.5 Å was used for both graphene and hBN, so that the heterostructure could be represented a 1×1 unit cell. The layers were stacked in A-B configuration, with 3.326 Å separation (c-lattice constant of 6.653). We used PBE exchange-correlation, a 340 eV energy cutoff for the plane waves in the ground state calculations, and (100,100) k-point sampling in the 2D Brillouin zone. In the response calculation doped structures were obtained by shifting the Fermi-level 1 eV upwards. An energy cutoff of 70 eV was used for the reciprocal lattice vectors, and unoccupied bands were included up to 35 eV above the Fermi level. All the calculations employed the truncated Coulomb interaction and 20 Å vacuum to separate the repeated structures. A non-linear frequency-grid with an initial grid spacing of 0.02 eV and a broadening of 0.05 eV was used to represent the dynamic response function. Plasmon eigenmodes were obtained by diagonalizing the dielectric matrix in Bloch representation as described in ref.[3].

C. Excitons in supported WS_2

The dielectric building blocks of the WS_2, hBN, and MoS_2 monolayers were calculated as follows. Single-particle energies and wave functions were calculated using LDA, a plane wave cut-off of 500 eV, and $(45, 45)$ k-points. The density response function was calculated within RPA using an energy cut-off of 300 eV and including empty states up to 50 eV above the Fermi level. The truncated Coulomb kernel was employed and 20 Å vacuum was included in the supercell to separate repeated layers. In setting up the heterostructure we used a separation of 3.22 Å between the 100 layers of h-BN and 5.08 Å between WS_2 and h-BN. For WS_2 on 50 layers of MoS_2 we used a uniform separation of 6.3 Å between all layers. We then calculated the screened interaction from Eq. 32 for $q_\parallel$ up to (and including) the second Brillouin zone. For calculating the exciton Rydberg series we solved Eq. 30 for spherical states on a radial logarithmic grid and verified that the exciton energies were converged to within 0.01 eV.

D. 2D Database

The dielectric building blocks were calculated for 51 transition metal dichalcogenides and oxides, hBN, and graphene at 10 different doping levels from 0.1 to 1 eV. For the single particle wave functions and energies obtained from DFT, we used PBE exchange-correlation and a plane-wave basis with a energy cutoff equal to 500 eV. The 2D Brillouin zone was sampled by (200,200) k-points for graphene, and for the remaining materials we used a k-point density corresponding to (100,100) k-points.

For the density response functions we used a cutoff of 100 eV for the transition metal dichalcogenides and oxides and 150 eV for graphene and hBN. The truncated Coulomb kernel was employed and 20 Å vacuum was included in the supercell to separate the repeated layers. All materials were represented on the same frequency grid from 0 to 35 eV, with an initial spacing of 0.01 eV and a broadening of 0.05 eV. The response functions were calculated for a range of in-plane momentum transfers, $q_\parallel$, within the first Brillouin zone of graphene up to a maximum value of $q_\parallel = 2.89$ Å^{-1}. At small $q_\parallel$ below 0.3 Å^{-1} we use a denser sampling with a grid spacing of 0.015 Å^{-1} in order to capture the strong $q_\parallel$-dependence of the plasmon energies and the dielectric function in this region. After this limit the grid spacing is increased to 0.029 Å^{-1}. In order to obtain all response functions on the same $q_\parallel$-grid, the data for the remaining materials was interpolated to the grid for graphene using conventional 2D spline interpolation.

* Electronic address: kiran@fysik.dtu.dk

† Electronic address: thygesen@fysik.dtu.dk

References

[1] Yan, J.; Mortensen, J. J.; Jacobsen, K. W.; Thygesen, K. S. *Phys. Rev. B* **2011**, *83*, 245122

[2] Rozzi, C.; Varsano, D.; Marini,A. ; Gross, E.; Rubio, A. *Phys. Rev. B* **2006**, *73*, 205119

[3] Andersen, K.; Jacobsen, K. W.; Thygesen, K. S. *Phys. Rev. B***2012**, *86*, 245129

Paper II

Excitons in van der Waals heterostructures: The important role of dielectric screening
Simone Latini, Thomas Olsen and Kristian S. Thygesen, *PRB*, **92**, pp 245123 (2015).
Editor's suggestion.

PHYSICAL REVIEW B **92**, 245123 (2015)

Excitons in van der Waals heterostructures: The important role of dielectric screening

S. Latini,* T. Olsen, and K. S. Thygesen
Center for Nanostructured Graphene (CNG) and Center for Atomic-scale Materials Design (CAMD), Department of Physics, Technical University of Denmark, 2800 Kongens Lyngby, Denmark
(Received 26 September 2015; revised manuscript received 16 November 2015; published 17 December 2015)

The existence of strongly bound excitons is one of the hallmarks of the newly discovered atomically thin semiconductors. While it is understood that the large binding energy is mainly due to the weak dielectric screening in two dimensions, a systematic investigation of the role of screening on two-dimensional (2D) excitons is still lacking. Here we provide a critical assessment of a widely used 2D hydrogenic exciton model, which assumes a dielectric function of the form $\epsilon(q) = 1 + 2\pi\alpha q$, and we develop a quasi-2D model with a much broader applicability. Within the quasi-2D picture, electrons and holes are described as in-plane point charges with a finite extension in the perpendicular direction, and their interaction is screened by a dielectric function with a nonlinear q dependence which is computed *ab initio*. The screened interaction is used in a generalized Mott-Wannier model to calculate exciton binding energies in both isolated and supported 2D materials. For isolated 2D materials, the quasi-2D treatment yields results almost identical to those of the strict 2D model, and both are in good agreement with *ab initio* many-body calculations. On the other hand, for more complex structures such as supported layers or layers embedded in a van der Waals heterostructure, the size of the exciton in reciprocal space extends well beyond the linear regime of the dielectric function, and a quasi-2D description has to replace the 2D one. Our methodology has the merit of providing a seamless connection between the strict 2D limit of isolated monolayer materials and the more bulk-like screening characteristics of supported 2D materials or van der Waals heterostructures.

DOI: 10.1103/PhysRevB.92.245123 PACS number(s): 71.35.Cc, 71.20.Nr, 78.67.Wj

I. INTRODUCTION

Atomically thin semiconductors [1] such as graphene, hexagonal boron-nitride (hBN), and MoS_2 are presently being intensely studied due to their extraordinary optoelectronic properties. It is characteristic for these two-dimensional (2D) semiconductors that excitonic effects play a fundamental role, substantially modifying the optical spectrum by introducing states within the band gap that couple strongly to light and shift the onset of optical transitions to lower energies [2–7]. Knowledge of the nature of the excitonic states is thus essential for device engineering [8–12]. The well known Mott-Wannier model [13], which schematizes the exciton as a bound electron-hole pair interacting via a statically screened Coulomb interaction, is widely used to estimate exciton binding energies and radii in bulk materials. The main approximations behind the Mott-Wannier model are essentially three: (i) The real band structure is replaced by two parabolic bands. (ii) The microscopic shape of the conduction and valence band wave functions is neglected. (iii) The dielectric function is assumed to be local in real space, i.e., q independent in reciprocal space. For 2D materials, the performance of the Mott-Wannier model and the validity of the underlying approximations have still not been systematically investigated. The present work focuses on (iii), which is the only approximation where the role of the reduced dimensionality represents a qualitative difference from the 3D case.

For bulk semiconductors the macroscopic dielectric constant is defined as the limiting value of $\epsilon(q)$ as $q \to 0$. For a 2D semiconductor this definition cannot be straightforwardly adopted since $\epsilon(q = 0) = 1$. In fact, for 2D systems the dielectric function is strongly q dependent, and a more elaborate treatment of the screening is required [14–16]. This issue has been treated by several authors [14,15,17,18], who envisioned the 2D material as a strict 2D system, i.e., mathematically 2D, with a dielectric function of the form

$$\epsilon_{2D}(\mathbf{q}) = 1 + 2\pi\alpha q, \tag{1}$$

where α is the 2D polarizability of the layer, which can be computed *ab initio*. The screened electron-hole interaction energy then follows

$$W_{2D}(\mathbf{q}) = -\frac{2\pi}{q}\epsilon_{2D}^{-1}(q), \tag{2}$$

where $2\pi/q$ is the 2D Fourier transform of $1/r$. This form of interaction has the merit of leading to an analytical expression in real space, and it has been successfully used to describe exciton binding energies and radii of several 2D systems [15,17,18]. We note that the form $1/q$ for the interaction and Eq. (1) for the dielectric function are consistent approximations which both become exact in the limit of vanishing thickness of the material, i.e., the strict 2D limit. However, to the best of our knowledge the validity range and limitations of these approximations have not previously been systematically explored.

In this paper we relax the assumptions behind the 2D model, adopting a microscopic approach that accounts for both the finite thickness of the layer and the full wave-vector dependence of the dielectric function. In the case of isolated monolayers, ours quasi-2D (Q2D) description agrees well with the established strict 2D model, providing a justification for the latter. However, in the case of 2D layers supported by semi-infinite substrates or for thicker, i.e., few-layer, 2D materials, we find it important to account for the finite thickness and include the full nonlinear q dependence of the dielectric function. In a recent paper we introduced a method for calculating the dielectric function of general

*Corresponding author: simola@fysik.dtu.dk

layered materials (so-called van der Waals heterostructures [19–21]) where the dielectric functions of the individual layers are computed *ab initio* and subsequently coupled together electrostatically [22]. In the present work we use this method to compute the screened electron-hole interaction and solve the resulting quasi-2D Mott-Wannier model for various types of heterostructures. We show that the exciton binding energy and radius can be effectively tuned by controlling the screening via the heterostructure environment. Surprisingly we find that the transition from a strongly bound exciton in monolayer MoS_2 (binding energy of 0.6 eV) to a weakly bound exciton in bulk MoS_2 (binding energy of 0.15 eV) can be seamlessly described by the quasi-2D Mott-Wannier model, accounting only for the change in the screening.

II. THE QUASI-2D PICTURE

Even though atomically thin semiconductors are referred to as 2D materials, they obviously do have a finite thickness. In this section, we show how the finite thickness can be accounted for within a 2D description. We shall refer to this description as the quasi-2D picture. To illustrate the concept, we consider the interaction energy between two arbitrary charge distributions,

$$V_{12} = \int d\mathbf{r}\, d\mathbf{r}' \frac{\rho_1(\mathbf{r})\rho_2(\mathbf{r}')}{|\mathbf{r}-\mathbf{r}'|}. \tag{3}$$

In the case of two point charges confined to a 2D plane [see Fig. 1(a)], each charge distribution is given by a delta function, i.e., $\rho_i(\mathbf{r}_\parallel) = q_i\delta(\mathbf{r}_\parallel - \mathbf{r}_{i,\parallel})$, leading to an interaction in reciprocal space:

$$V_{2D}(\mathbf{q}_\parallel) = q_1 q_2 \frac{2\pi}{|\mathbf{q}_\parallel|}. \tag{4}$$

Now we consider two charge distributions confined in a slab with finite thickness. We want to treat the real system, which is actually 3D, using an effective 2D description. We do this by depicting the charge distributions as lines of charge [Fig. 1(b)]. In other words, we assume that the charge densities are delta functions in-plane and have a certain distribution out-of-plane. The simplest approximation for the out-of-plane distribution is a step function of thickness d. This translates to $\rho_i(\mathbf{r}_\parallel, z) = \frac{q_i\delta(\mathbf{r}_\parallel - \mathbf{r}_{i,\parallel})}{d}\theta(\frac{d}{2} - |z - z_0|)$, with z_0 the center of the material in the perpendicular direction, which leads to an

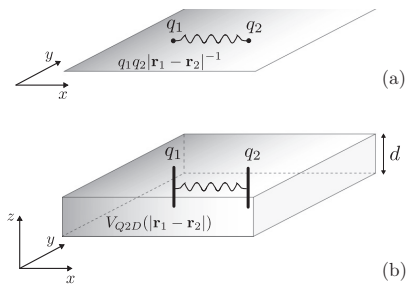

FIG. 1. Sketch of the (a) pure 2D and (b) quasi-2D Coulomb interaction. In the latter case the point charges can be thought of as lines of charge extending along the thickness of the material.

interaction energy of the form (see Appendix B)

$$V_{Q2D}(\mathbf{q}_\parallel) = \frac{4\pi q_1 q_2}{d|\mathbf{q}_\parallel|^2}\left[1 - \frac{2}{|\mathbf{q}_\parallel| d}\, e^{-|\mathbf{q}_\parallel| d/2} \sinh\left(\frac{|\mathbf{q}_\parallel| d}{2}\right)\right]. \tag{5}$$

It is instructive to note that in the limit of $q_\parallel d \ll 1$ we recover the 2D potential energy, while for $q_\parallel d \gg 1$ we get the 3D one (calculated in-plane):

$$V_{Q2D}(\mathbf{q}_\parallel) = \begin{cases} \frac{2\pi q_1 q_2}{|\mathbf{q}_\parallel|}, & q_\parallel d \ll 1, \\ \frac{4\pi q_1 q_2}{|\mathbf{q}_\parallel|^2}, & q_\parallel d \gg 1. \end{cases} \tag{6}$$

III. SCREENED INTERACTION

The (inverse) microscopic dielectric function gives the total potential to first order in the applied external potential,

$$V_{\text{tot}}(\mathbf{r}) = \int d\mathbf{r}' \epsilon^{-1}(\mathbf{r},\mathbf{r}') V_{\text{ext}}(\mathbf{r}'). \tag{7}$$

Notice that, since we are interested in static screening properties, we only considered a time-independent external perturbation. In standard *ab initio* calculations for 3D periodic systems, the dielectric matrix is calculated within the random phase approximation (RPA), which in plane-wave representation takes the form

$$\epsilon_{\mathbf{G}\mathbf{G}'}(\mathbf{q}) = \delta_{\mathbf{G}\mathbf{G}'} - v(\mathbf{q}+\mathbf{G})\chi^0_{\mathbf{G}\mathbf{G}'}(\mathbf{q}), \tag{8}$$

with $v(\mathbf{q}+\mathbf{G})$ the Fourier transform of the Coulomb potential and χ^0 the noninteracting response function. For a 3D periodic system, the total potential resulting from a plane-wave external potential $V_0 e^{i\mathbf{q}\cdot\mathbf{r}}$ has the form

$$V_{\text{tot}}(\mathbf{r}) = \tilde{V}_{\mathbf{q}}(\mathbf{r}) e^{i\mathbf{q}\cdot\mathbf{r}}, \tag{9}$$

where $\tilde{V}_{\mathbf{q}}(\mathbf{r})$ is a lattice periodic function. Since usually we are interested in macroscopic fields, we define the 3D macroscopic dielectric function as

$$\frac{1}{\epsilon_M(\mathbf{q})} \equiv \frac{\langle \tilde{V}_{\mathbf{q}}(\mathbf{r})\rangle_\Omega}{V_0} = \epsilon^{-1}_{00}(\mathbf{q}), \tag{10}$$

where $\langle\cdots\rangle_\Omega$ denotes a spatial average over a unit cell. Note that in general $\epsilon_M(\mathbf{q}) \neq \epsilon_{00}(\mathbf{q})$ due to local field effects [23].

A. Macroscopic dielectric function for 2D semiconductors

When Eq. (10) is applied to an *ab initio* calculation describing a 2D material as an infinite set of parallel sheets separated by a vacuum region of thickness L, $\epsilon_M(\mathbf{q}) = 1 + \mathcal{O}(1/L)$ [16]. This is a consequence of an averaging region much larger than the effective extension of the electron density around the material. The standard definition in Eq. (10) becomes meaningless in this case, which is the reason why relatively different values for ϵ_M have been reported for monolayer MoS_2 in the recent literature [4,24,25]. Therefore the definition of the macroscopic dielectric function has to be revised, accounting for the finite thickness. From the first equality in Eq. (10), it is natural to substitute an average along the entire unit cell in the out-of-plane direction with an average over a confined region describing the actual extension of the electronic density. In practice, we average the in-plane coordinates ($\mathbf{r}_\parallel$) over the unit cell area A and the out-of-plane coordinate from $z_0 - d/2$ to

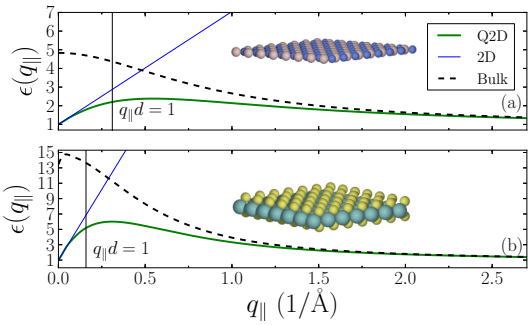

FIG. 2. (Color online) Macroscopic dielectric functions for (a) hBN and (b) MoS_2. The bulk(black), along with the Q2D (green) and 2D (blue) static dielectric functions are illustrated, the latter corresponding to the linear fits in the small $q_\parallel$ region. For these calculations the $q_\parallel$ values are taken along the $\Gamma - K$ direction, but the homogeneity of the materials has been numerically verified. The parameters used in the linear response ab initio calculation are discussed in Sec. V.

$z_0 + d/2$, where z_0 denotes the center of the material and d its width. The macroscopic dielectric function then becomes

$$\frac{1}{\epsilon_{\mathrm{Q2D}}(\mathbf{q}_\parallel)} \equiv \frac{\langle \tilde{V}_{\mathbf{q}}(\mathbf{r})\rangle_{A,d}}{V_0} = \frac{2}{d}\sum_{G_\perp} e^{iG_\perp z_0}\frac{\sin(G_\perp d/2)}{G_\perp}\epsilon^{-1}_{G_\perp 0}(\mathbf{q}_\parallel), \qquad (11)$$

with $\epsilon^{-1}_{\mathbf{GG}'}(\mathbf{q}_\parallel)$ calculated from $\chi^0_{\mathbf{GG}'}(\mathbf{q}_\parallel)$ according to the RPA expression in Eq. (8). We stress that it is essential to use a truncated Coulomb potential in Eq. (8) in order to decouple the layers in neighboring supercells [16]. Note that we used the label Q2D since this definition of macroscopic dielectric function is consistent with the Q2D picture, as we show later on. As a rule of thumb we choose d to be the distance between the layers in the bulk form, but the results for excitons are not very sensitive to this choice, as we show in the next session.

The q dependence of the static dielectric function is illustrated in Fig. 2 for the case of monolayer hBN and MoS_2. Without loss of generality, the $q_\parallel$ values reported in the plot are chosen to be along the Γ-K direction. Indeed, further numerical tests show that the dielectric function is isotropic, i.e., it is not significantly affected by different direction choices. In the low-$q_\parallel$ regime the dielectric function approaches 1, as expected for 2D materials [16]. We mention in passing that the dielectric functions of a large collection of 2D materials are available in the Computational Materials Repository [26]; see Refs. [27] and [22].

In the plots we also show the linear fit relevant for small $q_\parallel$ as well as the bulk dielectric function. We see that for $q_\parallel d \ll 1$ a linear ϵ is a viable approximation and we are in a 2D regime. In particular the 2D linear polarizability α can be calculated from the slope of the linear fit. On the other hand, when $q_\parallel d \gg 1$, the bulk behavior of the dielectric function is recovered.

B. Screened Interaction in reciprocal space

To account for the screening in the charge-charge interaction we modify Eq. (3), introducing the dielectric function

$$W_{12} = \int_V d\mathbf{r}\, d\mathbf{r}' d\mathbf{r}'' \frac{\rho_1(\mathbf{r})\epsilon^{-1}(\mathbf{r},\mathbf{r}'')\rho_2(\mathbf{r}')}{|\mathbf{r}'' - \mathbf{r}'|}. \qquad (12)$$

In the following, we specialize to the case of electron-hole interaction. Assuming an in-plane delta function distribution and an unspecified z dependence for the charge densities we can easily work out an expression for the screened interaction energy in reciprocal space:

$$W(\mathbf{q}_\parallel) = \int_{-\infty}^{\infty} dz\, dz' \rho_e(z,\mathbf{q}_\parallel)\epsilon^{-1}_{00}(z,z',\mathbf{q}_\parallel)\phi_h(z',\mathbf{q}_\parallel). \qquad (13)$$

Here $\rho_e(z,\mathbf{q}_\parallel)$ is the out-of-plane density distribution for the electron and $\phi_h(z,\mathbf{q}_\parallel)$ is the out-of-plane potential generated by the hole. For details on how this potential is calculated, see Appendix A. To study excitons in hBN and MoS_2, we take the out-of-plane electron and hole distributions to be $\rho_{e,h}(z) = \mp\int_A d\mathbf{r}_\parallel |\psi_{c,vK}(\mathbf{r}_\parallel,z)|^2$, with c and v the conduction and valence band indices respectively and K the high symmetry point of the first Brillouin zone, since for both materials that is where the lowest bound exciton is localized [1,28]. Furthermore, in Eq. (13) we have introduced a mixed representation for the dielectric function, specifically

$$\epsilon^{-1}_{00}(z,z',\mathbf{q}_\parallel) = \frac{1}{L}\sum_{G_\perp G'_\perp} e^{iG_\perp z}\epsilon^{-1}_{0G_\perp 0G'_\perp}(\mathbf{q}_\parallel)e^{-iG'_\perp z'}. \qquad (14)$$

Note that taking $G_\parallel = G'_\parallel = 0$ corresponds to an in-plane macroscopic dielectric function, which also accounts for local field effects.

To illustrate the effect of screening, Fig. 3 shows how a potential generated by either the step function density distribution or the actual hole density distribution is screened by hBN and MoS_2. In all cases the density distribution is normalized to 1. The possibility of using either the actual electron/hole out-of-plane density distribution (Fig. 4) or simply a step-function gives us two different approximations to calculate the screened interaction within the Q2D picture.

In the case of step-function density distributions, we can find an analytic expression for the screened potential in Eq. (13), if we make a further approximation. Indeed, if instead of considering the full z dependence of $\phi_h(z,\mathbf{q}_\parallel)$ we take its average value within a region of thickness d around the layer, and then screen the resulting constant potential by the full z-dependent dielectric function, the general expression Eq. (13) reduces to (see Appendix C)

$$W_{\mathrm{Q2D}}(\mathbf{q}_\parallel) = -\frac{4\pi}{d|\mathbf{q}_\parallel|^2}\epsilon^{-1}_{\mathrm{Q2D}}(\mathbf{q}_\parallel) \times\left[1 - \frac{2}{|\mathbf{q}_\parallel|d}e^{-|\mathbf{q}_\parallel|d/2}\sinh\left(\frac{|\mathbf{q}_\parallel|d}{2}\right)\right] = \epsilon^{-1}_{\mathrm{Q2D}}(\mathbf{q}_\parallel)V_{\mathrm{Q2D}}(\mathbf{q}_\parallel), \qquad (15)$$

where $\epsilon^{-1}_{\mathrm{Q2D}}(\mathbf{q}_\parallel)$ is the macroscopic dielectric function defined in Eq. (11). We thus see that ϵ_{Q2D} is the natural dielectric function to be used in the quasi-2D picture.

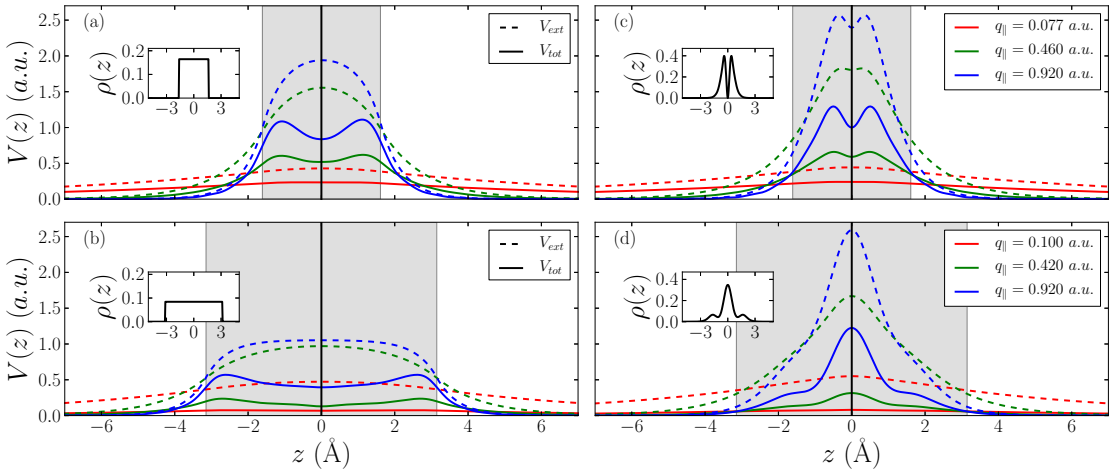

FIG. 3. (Color online) z dependence of the total potentials (solid lines) coming from external perturbations (dashed lines) at different in-plane wave vectors in the case of hBN [(a) and (c)] and MoS_2 [(b) and (d)]. Left panels: The external perturbation is generated by a step function density distribution (insets). Right panels: The external perturbation is generated by the actual hole out-of-plane density distribution (insets), which is calculated as $\rho_h(z) = \int_A d\mathbf{r}_\parallel |\psi_{vK}(\mathbf{r}_\parallel, z)|^2$, with v indicating the valence band and K the high symmetry point of the first Brillouin zone. In all cases the density distributions are normalized to 1.

For each of the two different Q2D models for the screened electron-hole interaction, we can associate a Q2D dielectric function, defined as the ratio between the bare and the screened potential:

$$\epsilon^{\gamma}_{\mathrm{Q2D}}(\boldsymbol{q}_\parallel) = \frac{\langle \rho^{\gamma}_e(\mathbf{q}_\parallel) | \phi^{\gamma}_h(\mathbf{q}_\parallel) \rangle}{\langle \rho^{\gamma}_e(\mathbf{q}_\parallel) | \epsilon^{-1}_{00}(\hat{z}, \hat{z}', \mathbf{q}_\parallel) | \phi^{\gamma}_h(\mathbf{q}_\parallel) \rangle}, \tag{16}$$

where for simplicity we have used a bracket notation for the integration over z and $\gamma = $ steps,wfs indicates whether the potentials are calculated from step functions or actual electron and hole density distributions. Figure 5 shows a comparison of the two dielectric functions thus obtained together with ϵ_{Q2D} from Eq. (11) for hBN and MoS_2. Clearly the curves perfectly agree in the low-$q_\parallel$ regime, while deviations appear for higher values. This observation is consistent with the fact that for small wave vectors the total potentials are flat and therefore well approximated by the Q2D average value (see Fig. 3). As we show later, the relevant $q_\parallel$ region for the screening is the one below the the black vertical line representing the inverse exciton radius, calculated from the *ab initio* Bethe-Salpeter equation (BSE) (see Sec. V). Therefore the three different Q2D approaches can be considered equivalent when dealing with excitons in these monolayer materials.

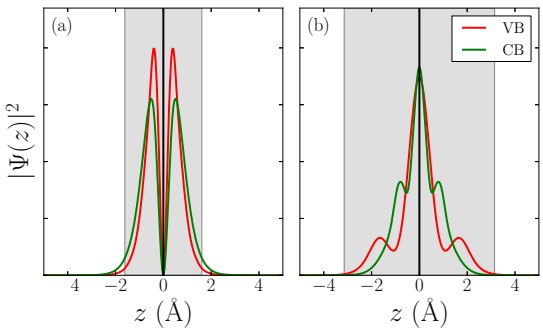

FIG. 4. (Color online) Valence (red) and conduction (green) band densities for (a) hBN and (b) MoS_2 calculated at the K point.

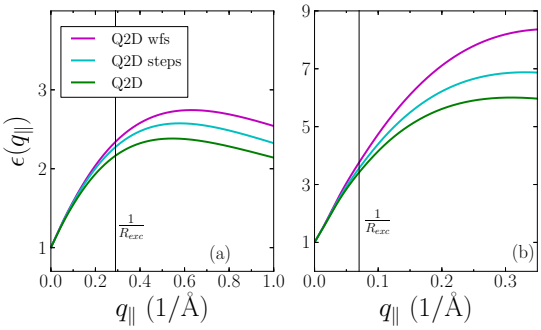

FIG. 5. (Color online) Macroscopic dielectric functions for (a) hBN and (b) MoS_2. The different dielectric functions are calculated with the three different approaches explained in the text: dielectric function from actual electron and hole distributions (magenta), dielectric function from step function distributions (cyan), and Q2D dielectric function (green). The vertical line represent the radius of the exciton in reciprocal space.

C. Screened interaction in real space

To obtain the form of the screened interaction energy in real space we Fourier transform Eq. (13):

$$W_{\mathrm{Q2D}}(\mathbf{r}_\parallel) = -\frac{2}{d}\int_0^\infty dq\,\frac{J_0(q|\mathbf{r}_\parallel|)}{q}\epsilon^{-1}_{\mathrm{Q2D}}(q) \times\left[1-\frac{2}{qd}e^{-qd/2}\sinh\left(\frac{qd}{2}\right)\right], \quad (17)$$

where $J_0(x)$ is the zeroth-order Bessel function and where we used the fact that the dielectric function is isotropic. This is the quasi-2D interaction which can be compared to its strict 2D counterpart defined in Eq. (2) [15]:

$$W_{\mathrm{2D}}(\mathbf{r}_\parallel) = \frac{1}{4\alpha}[H_0(x) - N_0(x)]_{x=r/2\pi\alpha}, \quad (18)$$

where $H_0(x)$ and $N_0(x)$ are the Struve and Neumann functions respectively. We stress here that the parameter α can be estimated from the slope of the fit in Fig. 2. We note that, while this procedure of calculating the 2D polarizability differs from the standard one, it is equivalent. In the case of MoS_2, for example, we obtain a value of 5.9 Å which agrees well with the value of 6.6 Å obtained in the literature [18].

In Fig. 6 we report the numerical results for different interaction energies: the bare Q2D (black) obtained from Eq. (17) setting ϵ_{Q2D} to 1, the screened Q2D (green) obtained from the same equation but including the screening as ϵ_{Q2D} and the screened 2D (blue) calculated from Eq. (18). The results are shown for both hBN and MoS_2.

We note that the bare Q2D interaction agrees with $-1/r$ beyond a distance given by the layer thickness d. Furthermore we see that increasing the layer thickness (going from hBN to MoS_2) reduces the bare Q2D interaction strength as expected from Eq. (17). Including the screening reduces the interaction strength even further. The reduction is most significant when using the linear dielectric function (strict 2D screening) as expected from Fig. 2, which shows that $\epsilon_{\mathrm{2D}}(q) > \epsilon_{\mathrm{Q2D}}(q)$ for all q. We see that, apart from a significant deviation for electron-hole separation smaller than roughly 1 Å, the 2D and Q2D screened interactions agree and both show a logarithmic

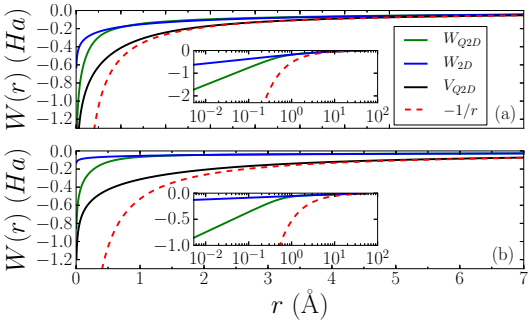

FIG. 6. (Color online) Screened Q2D and 2D interaction energies for (a) hBN and (b) MoS_2. The interactions are calculated numerically starting from the macroscopic dielectric functions in Fig. 2 and using Eqs. (17) and (18) respectively. The bare Q2D curves are calculated using the first equation but neglecting the screening.

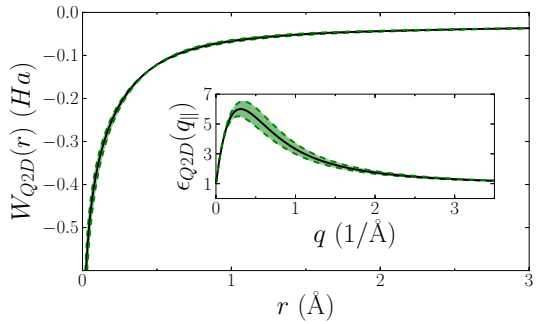

FIG. 7. (Color online) Variation of the macroscopic dielectric function and effective interaction energy in MoS_2 due to the change in the thickness d of the averaging region in the Q2D model. The continuous black lines are relative to $d = 6.29$ Å (the interlayer distance in the bulk), while the dashed lines delimiting the shaded region are calculated with a variation of $\pm 10\%$ in d.

dependence for $r \to 0$. It is not surprising that the behavior at short electron-hole separation is the same since both $W_{\mathrm{2D}}(q)$ and $W_{\mathrm{Q2D}}(q)$ go as $1/q^2$ for large wave vectors. In particular the logarithmic divergence can be understood directly as the two-dimensional anti-Fourier transform of $1/q^2$. For distances larger than the layer thickness, all the interactions (screened and bare) approach the same value $(-1/r)$, meaning that screening is completely absent in the asymptotic limit.

D. Importance of the thickness parameter

We now return to the problem of choosing the external parameter d entering the Q2D dielectric function. In Fig. 7 we show the Q2D dielectric function and the corresponding interaction when d is varied by $\pm 10\%$ around the interlayer distance in bulk MoS_2. To the left of the maximum, ϵ_{Q2D} is insensitive to d since the induced potential is constant over the averaging region. Also in the high $q_\parallel$ limit, ϵ_{Q2D} is not affected. This is because for these wave vectors the induced potential is in practice negligible. In general, increasing (decreasing) d decreases (increases) ϵ_{Q2D} in the large wave-vector region. Despite the fact that the variation in the dielectric function is fairly visible for intermediate q values, the screened interaction is barely modified. This is because the bare Q2D one shows an opposite dependence on d, such that the product $W_{\mathrm{Q2D}}(q) = \epsilon^{-1}_{\mathrm{Q2D}}(q)V_{\mathrm{Q2D}}(q)$ stays essentially unchanged. In terms of exciton binding energies we have found that a $\pm 10\%$ variation in d leads to a correction of less than 0.01 eV.

IV. GENERALIZED MOTT-WANNIER MODEL

An accurate description of excitonic effects requires the solution of a computationally demanding many-body problem, namely the Bethe-Salpeter equation (BSE) [29,30]. However, it is well known for 3D systems that a satisfying qualitative description can be obtained modeling the exciton as a hydrogenic atom constituted by an excited electron-hole pair interacting via a statically screened Coulomb interaction. In this section we generalize such a model to the Q2D case.

The Bethe-Salpeter two particle Hamiltonian for a 2D periodic system is given by

$$H^{2P}_{\substack{n_1n_2\mathbf{k}_1\\ n_3n_4\mathbf{k}_2}}(\mathbf{q}_\parallel) = \left(\epsilon_{n_2\mathbf{k}_1+\mathbf{q}_\parallel} - \epsilon_{n_1\mathbf{k}_1}\right)\delta_{n_1n_3}\delta_{n_2n_4}\delta_{\mathbf{k}_1\mathbf{k}_2} + \left(f_{n_1\mathbf{k}_1} - f_{n_2\mathbf{k}_1+\mathbf{q}_\parallel}\right)K_{\substack{n_1n_2\mathbf{k}_1\\ n_3n_4\mathbf{k}_2}}(\mathbf{q}_\parallel), \quad (19)$$

where n_i are band indices, $\mathbf{k}_i$ are vectors in the first 2D Brillouin zone, and $\mathbf{q}_\parallel$ is the in-plane momentum transfer, or exciton center-of-mass momentum. In the following we specialise to the case of vertical transitions, i.e., $\mathbf{q}_\parallel = 0$. K is the kernel containing the exchange and the screened direct Coulomb interaction. This Hamiltonian describes scattering processes between two electron-hole pairs excited by an external perturbation. In general these processes should involve all the occupied and unoccupied states in the spectrum; however, when the conduction and valence bands are well separated from the remaining bands, it is often a good approximation to include only the valence and conduction band states. Together with the Tanm-Dancoff approximation, this assumption allows us to express the resonant part of the two-particle Hamiltonian as

$$H^{2P(\mathrm{res})}_{\substack{vc\mathbf{k}\\ vc\mathbf{k}'}} = (\epsilon_{c\mathbf{k}'} - \epsilon_{v\mathbf{k}})\delta_{\mathbf{k}\mathbf{k}'} + K_{\substack{vc\mathbf{k}\\ vc\mathbf{k}'}}. \quad (20)$$

The kernel is given by

$$K_{\substack{vc\mathbf{k}\\ vc\mathbf{k}'}} = -\int_V d\mathbf{r}\,d\mathbf{r}'\psi_{v\mathbf{k}}(\mathbf{r})\psi^*_{c\mathbf{k}}(\mathbf{r}')W(\mathbf{r},\mathbf{r}')\psi^*_{v\mathbf{k}'}(\mathbf{r})\psi_{c\mathbf{k}'}(\mathbf{r}') + 2\int_V d\mathbf{r}\,d\mathbf{r}'\psi_{v\mathbf{k}}(\mathbf{r})\psi^*_{c\mathbf{k}}(\mathbf{r})v(\mathbf{r},\mathbf{r}')\psi^*_{v\mathbf{k}'}(\mathbf{r}')\psi_{c\mathbf{k}'}(\mathbf{r}'), \quad (21)$$

where $|\psi_{\alpha\mathbf{k}}\rangle$, with $\alpha = (v,c)$, represents single-particle Bloch states for the valence and conduction band, $W(\mathbf{r},\mathbf{r}') = \int d\mathbf{r}''\frac{\epsilon^{-1}(\mathbf{r},\mathbf{r}'')}{|\mathbf{r}''-\mathbf{r}'|}$ is the screened interaction potential, and $v(\mathbf{r},\mathbf{r}') = \frac{1}{|\mathbf{r}-\mathbf{r}'|}$ is the bare Coulomb potential. The first term on the right-hand side of Eq. (21) is the direct screened electron-hole potential while the second is the Coulomb exchange. Our full *ab initio* solution of the BSE shows that the exchange term only slightly decreases the exciton binding energy by 0.08 eV and 0.02 eV for hBN and MoS_2, respectively. This amounts to less than 5% of the total binding energy, and we therefore neglect the exchange contribution in the rest of the paper.

Throughout the BZ we consider the valence and conduction band wave functions to be plane waves in the in-plane direction and in the out-of-plane direction equal to $\psi_\perp(z) = \left(\int_A d\mathbf{r}_\parallel|\psi_{\alpha K}(\mathbf{r}_\parallel,z)|^2\right)^{1/2}$ up to a normalization factor and with $\alpha = v,c$. With this approximation and proceeding as for Eq. (13), the kernel becomes

$$K_{\substack{vc\mathbf{k}\\ vc\mathbf{k}'}} = \frac{1}{A}W(|\mathbf{k}-\mathbf{k}'|), \quad (22)$$

where $W(|\mathbf{k}|)$ is the screened interaction in Eq. (13), which can be evaluated in the various ways described in the previous section, depending on the level of approximation.

Completely analogous to the 3D case, we can introduce the envelope function $F(\mathbf{r}_\parallel)$, defined as $F(\mathbf{r}_\parallel) = \sum_k e^{-i\mathbf{k}\mathbf{r}_\parallel}A(\mathbf{k})$, with $A(\mathbf{k})$ excitonic weights in reciprocal space, and arrive at an eigenvalue problem of a 2D hydrogenic atom:

$$\left[-\frac{\nabla^2_{2D}}{2\mu_{ex}} + W(\mathbf{r}_\parallel)\right]F(\mathbf{r}_\parallel) = E_bF(\mathbf{r}_\parallel), \quad (23)$$

where μ_{ex} is the exciton effective mass, calculated from the hole and electron masses according to $\mu^{-1}_{ex} = m^{-1}_e + m^{-1}_h$.

TABLE I. Geometry and effective masses.

Material	a (Å)	L (Å)	d (Å)	μ^{ex} (a.u.)
MoS_2	3.20	23.0	6.29	0.27
hBN	2.50	23.0	3.22	0.37

V. EXCITON BINDING ENERGIES OF ISOLATED MONOLAYERS

In this section we investigate the performance of the Mott-Wannier model in Eq. (23) for the calculation of binding energies of the lowest bound exciton in hBN and MoS_2.

A. *Ab initio* calculation details

In order to solve Eq. (23) with either the Q2D or 2D potential energies, we need to calculate the dielectric matrix. We describe the two materials with a supercell technique and we optimize the structure using the local density approximation (LDA) exchange-correlation potential; geometrical details are provided in Table I. To calculate the noninteracting response function we use 150 eV cutoff energy for the reciprocal lattice vectors $\mathbf{G}$ and $\mathbf{G}'$ in order to account for local field effects. We construct χ^0 from LDA wave functions and energies, and we then get the dielectric matrix using a truncated Coulomb potential in order to avoid interaction between supercells [31]. The dielectric matrix is calculated on a 60×60 k-points grid. Since it turns out that the exciton binding energy is sensitive to the low wave-vector behavior of the screening, we use an expansion of the density response function χ^0 around $q_\parallel = 0$ in order to calculate the dielectric matrix in the small-$q_\parallel$ limit. All calculations are performed with the GPAW code [32,33], which is based on the projector augmented wave method. Details on the implementation of the linear response code can be found in Ref. [34]. We mention that the dielectric functions of more than fifty 2D materials calculated in this fashion are available in the Computational Materials Repository [26]. The exciton masses as computed from the LDA band structure are given in Table I.

To obtain the lowest bound exciton we numerically solve the Mott-Wannier equation on a logarithmic grid. With this method we are able to converge the lowest eigenvalue with a precision of 0.002 eV. For a benchmark, we perform BSE calculations using the GPAW code. For the screening of the electron-hole interaction we use the static dielectric function evaluated with the same parameters employed in the linear response calculation. The particle-hole states of the BSE Hamiltonian are constructed from a single LDA valence and conduction band. To compare directly to our model, all the BSE calculations are performed neglecting the exchange part of the kernel. We stress that the binding energy of the first

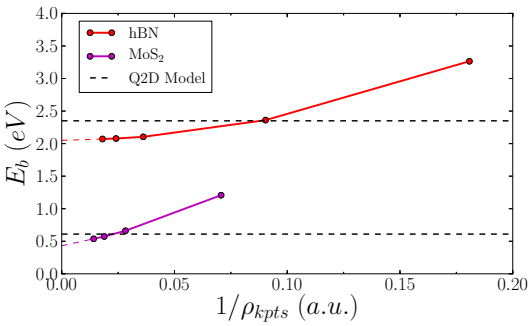

FIG. 8. (Color online) Convergence plot for the binding energy obtained from the BSE solution against the inverse of the k-points density. Extrapolation to infinite k-point sampling is shown. In the BSE the exchange contribution is left out. The horizontal dashed lines show the results given by the Q2D model.

exciton changes by less than 0.01 eV if the BSE Hamiltonian is constructed from the four highest and four lowest conduction bands. As reported previously [5,16], BSE binding energies in 2D materials are extremely sensitive to the k-point grid. We therefore perform BSE calculations with up to $60\times60\,k$ points, for which we get binding energies of 2.07 eV and 0.54 eV for hBN and MoS_2 respectively. Furthermore, assuming a linear dependence of the binding energy with respect to $1/\rho_{kpts}$, we extrapolate the results to infinite k-points sampling (see Fig. 8).

B. Results

The values for binding energy of the lowest bound exciton obtained with the different models for the screened electron-hole interaction along with the extrapolation from the BSE are reported in Table II. We first observe that there is practically no difference in the binding energies obtained from the Mott-Wannier model using either the Q2D or 2D screened interaction. Moreover, the result from the Mott-Wannier model(s) are within 0.3 eV and 0.18 eV of the BSE result for hBN and MoS_2, respectively. We consider this a reasonable agreement given the simplicity of the model.

TABLE II. Numerical values for energy (in eV) of the lowest bound excitonic state at the direct gap. Both the BSE and the models are based on LDA *ab initio* calculations. The exchange contribution is not included.

	E_b^{BSE}	E_b^{Q2D}	E_b^{2D}	E_b^{steps}	E_b^{wfs}
hBN	2.05	2.35	2.34	2.23	2.29
MoS_2	0.43	0.61	0.60	0.57	0.59

In Table II we also report the binding energies obtained when the electron-hole interaction is calculated numerically from Eq. (13) using step functions and actual electron and hole density distributions. As pointed out in the discussion of Fig. 5, we expect these two other approaches to give the same description of excitons. Indeed, the binding energies we obtained are in perfect agreement with the Q2D and 2D model results.

The agreement between the Q2D and 2D descriptions can be understood by looking at the q-space extension of the lowest bound exciton wave function shown in Fig. 9. We see that for both hBN and MoS_2 the exciton is confined to a rather narrow region around the K point. A localization of the exciton in q-space means that the relevant contribution to the electron-hole interaction comes from the low wave-vector regime. From the calculated excitonic wave functions in real space we obtain inverse exciton radii of 0.29 Å^{-1} for hBN and 0.07 Å^{-1} for MoS_2. Both of these values are comparable to $1/d$ (0.31 Å^{-1} and 0.16 Å^{-1}, respectively). As we have seen previously, in this limit the Q2D screened interaction reduces to the strict 2D

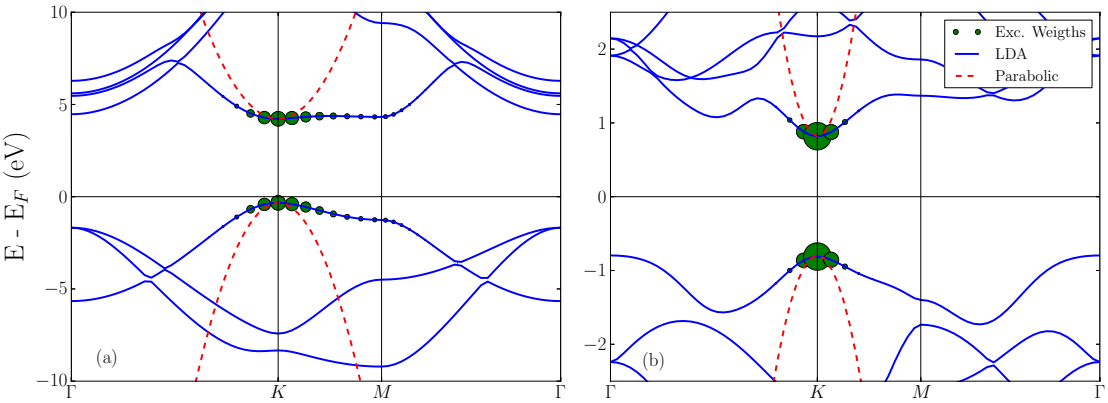

FIG. 9. (Color online) LDA band structure and exciton weights for (a) hBN and (b) MoS_2. In both materials the exciton is well localized at the K point. The excitonic weights are calculated as the absolute value squared of the eigenvector of the two-particle BSE Hamiltonian associated with the lowest bound exciton. In red the parabolic bands used in the Mott-Wannier model. The values for the electron and hole masses are 0.93 a.u. and 0.62 a.u. for hBN and 0.61 a.u. and 0.49 a.u. for MoS_2.

one, explaining the similarity of the binding energies obtained with the two descriptions.

To conclude this section, we notice that in the evaluation of the screened electron-hole interaction, we neglected the in-plane spatial variation of the conduction and valence band wave functions. The validity of this approximation can be checked by performing a BSE calculation where the screened interaction potential is evaluated using a dielectric matrix $\epsilon^{-1}_{\mathbf{G}\mathbf{G}'}$ where all matrix elements except for those where $\mathbf{G}_\parallel = \mathbf{G}'_\parallel = 0$ are set to zero. In other words, we neglect all the in-plane high frequency spatial variations of the wave functions. With this constriction we obtain a binding energy of 2.21 eV for hBN and 0.44 for MoS_2. The neglect of in-plane variations of the wave functions is thus responsible for 0.15 eV (hBN) and 0.01 eV (MoS_2) of the observed discrepancy between the Mott-Wannier model and the full BSE calculation.

VI. EXCITONS IN LAYERED STRUCTURES

In this section, we show that a linear approximation for the dielectric function breaks down when applied to excitons in multilayered structures. While it is possible to include the nonlinear q dependence of the dielectric function within a strict 2D model, the Q2D description turns out to be necessary to quantitatively capture screening effects.

A. The quantum electrostatic heterostructure (QEH) model

In order to calculate exciton binding energies in a layered structure we first need the dielectric function. This can be obtained using the quantum-electrostatic heterostructure (QEH) model that we introduced recently [22]. In brief, the underlying procedure in the calculation of the dielectric function can be divided in two parts. In the first part the full density response function of each isolated layer, calculated from first principles, is used to obtain the monopole/dipole components of the density response function as well as the spatial profile of the electron densities in the z direction induced by a monopole/dipole field. We refer to these data sets as the dielectric building block of the individual layer. In the second part, the dielectric building blocks are coupled together via the Coulomb interaction to give the dielectric matrix for the full structure. The dielectric matrix obtained from the QEH model can be used to obtain the electron-hole interaction according to

$$W(q_\parallel) = \underline{\rho}_e^{\intercal}(q_\parallel)\underline{\underline{\epsilon}}^{-1}(q_\parallel)\underline{\phi}_h(q_\parallel), \tag{24}$$

where $\underline{\rho}_e$ ($\underline{\phi}_h$) is the electron density (hole induced potential) vector expressed in a basis set of monopole/dipole densities (potentials). The basis set of induced densities and potentials is also used as (left and right) basis functions for representing $\underline{\underline{\epsilon}}^{-1}$. To be more explicit an arbitrary density vector $\underline{\rho}$ can be represented as $\underline{\rho}^{\intercal} = [\rho_{1M}, \rho_{1D}, \rho_{2M}, \rho_{2D}, \ldots, \rho_{nM}, \rho_{nD}]$ where $\rho_{i\alpha}$, with $\alpha = M, D$, is the induced monopole/dipole density at the layer i. A completely equivalent expression can be formulated for the induced potentials.

It is clear that the equation above is just a simple rewriting of Eq. (13) in terms of a minimal monopole/dipole basis. We point out that this formalism takes the finite extension of the layers in the out-of-plane direction into account, and is therefore consistent with the Q2D picture described in the previous sections. In Ref. [22] we showed, based on the comparison with full *ab initio* calculations, that the monopole/dipole basis is sufficient to obtain an accurate description of the dielectric and plasmonic properties of different layered heterostructures. We mention that in literature [35,36] the effect of environmental screening has been already investigated using a classical approach, proposed by Keldysh [37], based on the formation of image charges. To the best of our knowledge, this approach has only been applied to systems with a 2D layer embedded in two semi-infinite dielectric media. Furthermore, within this classical treatment, the intrinsic nonlocalities in the dielectric properties of the media and 2D layer are completely disregarded. Our method, instead, provides a quantum mechanical description of the nonlocal screening and can be applied to heterostructures of arbitrary thickness.

B. Breakdown of the linear screening model

As an example we consider two different types of heterostructures. The first, which we refer to as "on-top," consists of MoS_2 on top of n layers of hBN. The second, which we refer to as "sandwich," consists of an MoS_2 layer encapsulated in n layers of hBN; see Figs. 10(a) and 10(c). The interlayer distance between MoS_2 and hBN is set to 5.1 Å. In Figs. 10(b) and 10(d) we show the dielectric function of the MoS_2 layer as well as the linear approximation as a function of the in-plane wave vector for different number of hBN layers. The effective dielectric function of MoS_2 in the heterostructure is defined along the lines of Eq. (16):

$$\epsilon(q_\parallel) = \frac{\underline{\rho}_e^{\intercal}(q_\parallel)\underline{\phi}_h(q_\parallel)}{\underline{\rho}_e^{\intercal}(q_\parallel)\underline{\underline{\epsilon}}^{-1}(q_\parallel)\underline{\phi}_h(q_\parallel)}, \tag{25}$$

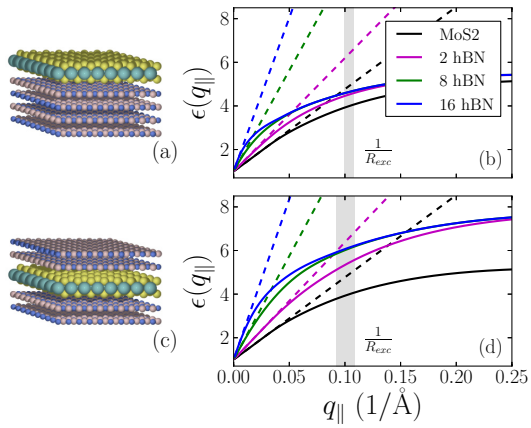

FIG. 10. (Color online) Left panels: The on-top (a) and sandwich (c) arrangements of the MoS_2/hBN heterostructures. Right panels: Effective dielectric function (full line) for the on-top (b) and sandwich (d) configurations. The linear approximations to the dielectric function is shown by dashed lines. The shaded regions in (b) and (d) represent the range of inverse exciton radii found for the considered structures. The q values below these regions are relevant for screening the electron-hole interaction, and for the thicker structures this region extends beyond the linear regime of $\epsilon(q)$.

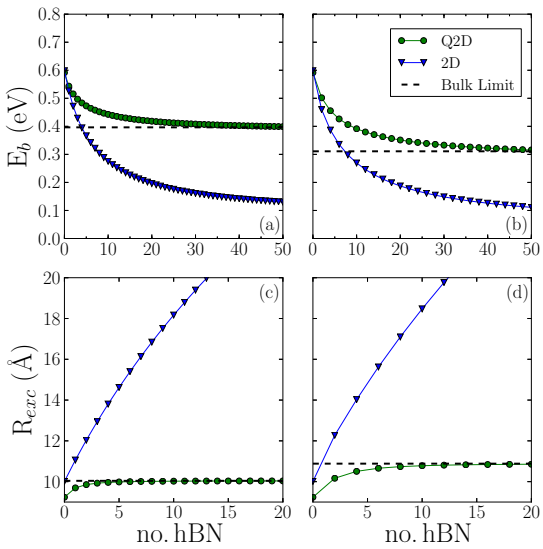

FIG. 11. (Color online) Energy and radius of the lowest bound exciton for the [(a) and (c)] on-top and [(b) and (d)] sandwich configuration as function of the number of hBN layers obtained from the Q2D (green) and 2D (blue) approaches.

which gives the ratio of the bare to the screened interaction between an electron and a hole in the MoS_2 layer.

From Fig. 10, we notice that adding hBN layers to MoS_2 changes the shape of the dielectric function, introducing a pronounced feature that shifts towards low $q_\parallel$ as the number of hBN layers is increased. This shoulder-like feature can be explained as an interplay between the 3D and 2D screening characters. When more hBN layers are added to the heterostructure, the system tends toward a bulk limit, where the dielectric function is larger than 1 for $q_\parallel = 0$. However, the heterostructure has a finite thickness d and, as required by the 2D limit, when $q_\parallel \ll 1/d$ the dielectric function is 2D-like and becomes 1 for $q_\parallel = 0$. This leads to a sharp drop in the dielectric function, which becomes steeper as the thickness of the heterostructure is increased, explaining the appearance of the shoulder-like feature. It is clear, from Fig. 10, that the main change in the dielectric function is caused by the nearest layers of hBN. Adding more layers only causes a slight variation. Obviously, this is due to the fact that hBN is less effective at screening the electron-hole interaction as the distance from MoS_2 is increased. For the same reason, the screening is more pronounced in the sandwich configuration than in the on-top configuration.

We then proceed to calculate the binding energy of the lowest bound exciton in the MoS_2 layer for the two different configurations, using both the full wave vector dependent dielectric function (quasi-2D) and its linear approximation (strict 2D). The results are shown in Figs. 11(a) and 11(b). When the full dielectric function is used, the binding energy converges towards 0.40 eV and 0.31 eV for the on-top and sandwich configurations, respectively. These values represent the bulk limits, i.e., MoS_2 on a hBN substrate and MoS_2 encapsulated by two semi-infinite stacks of hBN. The reduction in binding energy of 0.2 eV for the on-top configuration is in good agreement with the experimentally determined change in exciton energy of WS_2 when adsorbed on SiO_2 [38] (the bulk dielectric constants of SiO_2 and hBN are similar). In contrast, the assumption of linear dielectric screening completely fails in estimating the exciton binding energies. Indeed, it quickly diverges from the Q2D results, yielding much too small binding energies. This behavior results from the continuously increasing slope of the dielectric function, eventually arriving at a condition of perfect screening (infinite slope).

Figures 11(c) and 11(d) show the exciton radii obtained from the Q2D and 2D models. Interestingly, for the Q2D model the increase in the exciton radius due to the screening from the hBN is only 10% and 30% for the on-top and sandwich configurations, respectively. The range of the inverse exciton radius is indicated by a shaded region in Figs. 10(c) and 10(d). As we demonstrated in the previous section, the relevant $q_\parallel$ for the screening lie mainly below the inverse exciton radius. Inspection of Fig. 10 clearly indicates that in this regime the linear approximation overshoots the full wave-vector dependent dielectric function, and it gets worse as the number of layers is increased.

C. Limitations of the 2D picture in layered structures

In the previous paragraph we showed that the assumption of linear screening, i.e., Eq. (1), breaks down when the screening from the environment is included. It is, of course, possible within the 2D picture to couple a stack of 2D materials, each described by a linear dielectric function, using the QEH model. In this section we explore the validity of such an approach using the Q2D results obtained in the previous section as a reference.

We model the layered structure as infinitesimally thin planes described by 2D building blocks, as opposed to the Q2D ones used previously, and couple them electrostatically via the QEH. While it is straightforward to define multipole response function and induced density components when a finite thickness is considered, in 2D only the monopole components have an obvious definition. Within the 2D picture, the monopole induced density is described by a delta function centered at the layer position z_i. The component of the 2D response function of the (isolated) layer may be obtained from the corresponding 2D dielectric function in Eq. (1):

$$\tilde{\chi}^{M}_{2D}(q_\parallel) = \frac{q_\parallel}{2\pi}\left[\epsilon^{-1}_{2D}(q_\parallel) - 1\right] = -\frac{\alpha q_\parallel^2}{1 + 2\pi\alpha q_\parallel}. \quad (26)$$

For strict 2D layers, the Coulomb interaction between monopole charge densities in layers at z_i and z_k takes the form

$$V_{iM,kM}(q_\parallel) = \frac{2\pi e^{-q_\parallel |z_i - z_k|}}{q_\parallel}, \quad (27)$$

which reduces to the standard 2D Coulomb interaction in reciprocal space for coupling within the layer.

To test the QEH with 2D building blocks, we consider the "on-top" structure of the previous paragraph and in Fig. 12 we report the effective dielectric function and energy of the lowest bound exciton as a function of the number of hBN layers. It

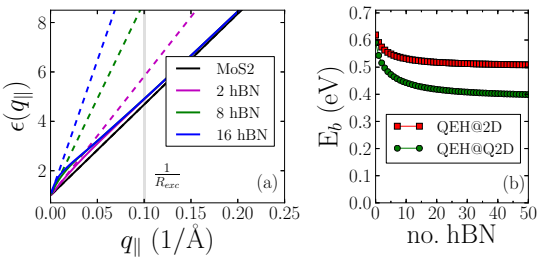

FIG. 12. (Color online) (a) Effective dielectric function (full line) and (b) energy of the lowest bound exciton for the on-top MoS_2-hBN configuration, calculated with the QEH model based on a 2D description of the layers. The linear approximations to the dielectric function is shown by dashed lines in panel (a), along with the range of inverse exciton radii found for the considered structures represented by the shaded region.

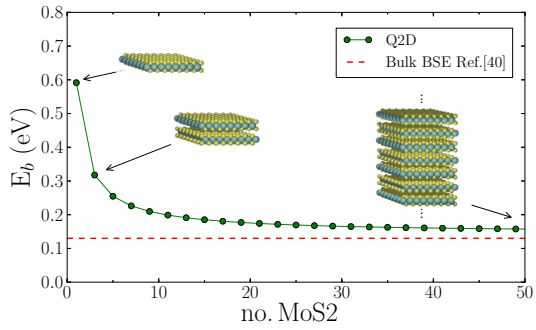

FIG. 13. (Color online) Energy of the lowest bound exciton for MoS_2 incapsulated in MoS_2 layers as function of the total number of MoS_2 layers obtained from the Q2D (green) and 2D (blue) approaches. With the Q2D approach we can clearly see the transition from the monolayer exciton to the bulk one.

is clear that the 2D dielectric function of the supported MoS_2 deviates significantly from the Q2D result [see Fig. 10(b)] for larger $q_\parallel$. However, for smaller $q_\parallel$ the 2D function actually reproduces qualitatively the nonlinear structure of the Q2D result. In terms of exciton binding energy, we observe a convergence to a finite value when the number of layers of hBN is increased, but the reduction in binding energy compared to the free-standing layer is 50% smaller than the reduction obtained with the Q2D approach. The underestimation of the screening can be ascribed essentially to two reasons. First, the potential generated by a 2D induced density decays faster than the actual one, making the neighboring layers less effective at screening the electron-hole interaction. Second, the dipole response of the layers, which would increase the screening even more, is not included. In particular we mention that, within the Q2D approach, removing the dipole contribution increases the converged value of the binding energy by 0.07 eV. To conclude, we have shown that, even though the 2D model does capture the essential nonlinear shape of $\epsilon(q_\parallel)$ in the small $q_\parallel$ regime, it underestimates the effect of environmental screening and consequently predicts too small changes in exciton binding energies due to substrate effects.

D. Transition from 2D to 3D excitons in MoS_2

As a final example, we study the 2D to 3D transition of the exciton in MoS_2. In layered bulk materials, the Mott-Wannier equation can be written as follows:

$$\left[-\frac{\nabla_\parallel^2}{2\mu_\parallel^{ex}} - \frac{\nabla_\perp^2}{2\mu_\perp^{ex}} + W(\mathbf{r})\right] F(\mathbf{r}) = E_b F(\mathbf{r}), \qquad (28)$$

where typically the exciton mass in the out-of-plane direction is much higher than that in the in-plane directions ($\mu_\perp^{ex} \gg \mu_\parallel^{ex}$). Consequently, we can neglect the out-of-plane component of the kinetic energy and be left with the 2D Mott-Wannier model. Additionally, the in-plane effective mass does not vary considerably going from monolayer to bulk MoS_2 as shown in Ref. [39]. Therefore, the main difference between the physics of excitons in monolayer and layered bulk is contained in the screened potential rather than the geometric confinement. Based on this, it is tempting to model the bulk exciton as an electron-hole pair confined to a single layer but with an interaction screened by the bulk environment. To test this we consider a multilayer MoS_2 structure and calculate the binding energy of an exciton localized in the central MoS_2 layer using the Q2D Mott-Wannier model with screened potential calculated from the QEH model. The results for the binding energy as a function of the number of MoS_2 layers are plotted in Fig. 13. As expected, the reduction of the exciton binding energy is larger when the monolayer is embedded in MoS_2 than in the case of hBN [Fig. 11(b)]. Amazingly, the binding energy converges towards a value of 0.16 eV, only 0.03 eV higher than the previously reported *ab initio* value for bulk MoS_2 [40]. This shows that the different nature of excitons in 2D and layered 3D materials is mainly caused by the screening, while quantum confinement plays a minor role.

VII. CONCLUSIONS

In this work we have presented a systematic study of the screening properties of two-dimensional semiconductors and layered structures. Taking into account the finite extension of the 2D material in the out-of-plane direction, we have proposed a general quasi-2D picture to describe the screened electron-hole interaction in the context of excitons. We have shown that, in the case of isolated layers, the excitons are typically large enough that the screening can be described by a linear dielectric function consistent with a strict 2D picture. On the other hand, for multilayer structures where the screening properties are intermediate between the 2D and 3D regimes, it is essential to include the nonlinear q dependence of the dielectric function. If this is done and a quasi-2D description is employed, very satisfactory results are obtained for both monolayer and multilayer structures using the same theoretical framework. In combination with a recently introduced scheme for computing dielectric functions of layered materials [22], this makes it possible to model exciton physics in general van der Waals heterostructures at very low computational cost.

ACKNOWLEDGMENTS

The authors acknowledge support from the Center for Nanostructured Graphene (CNG), sponsored by the Danish National Research Foundation, Project DNRF58.

APPENDIX A: POISSON'S EQUATION FOR LINES OF CHARGE

Charges in 2D materials can be depicted as lines extending over the thickness of the layer. The potential generated by a line of charge can be calculated from the Poisson equation,

$$\nabla^2\varphi(\mathbf{r}) = -4\pi\rho(\mathbf{r}). \tag{A1}$$

Because of the cylindrical symmetry of the line of charge, it is convenient to Fourier transform in the in-plane direction and rewrite Eq. (A1) as

$$\left[-|\mathbf{q}_\parallel|^2 - \frac{\partial^2}{\partial z^2}\right]\varphi(\mathbf{q}_\parallel,z) = -4\pi\rho(\mathbf{q}_\parallel,z). \tag{A2}$$

For a line of charge, the density distribution can be separated as an in-plane delta function and an out-of-plane function $\rho(z)$, and therefore its in-plane Fourier transform would read $\rho(\mathbf{q}_\parallel,z) = e^{-i\mathbf{q}_\parallel\cdot\mathbf{r}_\parallel}\rho(z)$. From the structure of Eq. (A2) and the form of the Fourier transformed density, it is convenient to write the potential as $\varphi(\mathbf{q}_\parallel,z) = \frac{e^{-i\mathbf{q}_\parallel\cdot\mathbf{r}_\parallel}}{|\mathbf{q}_\parallel|^2}\xi(z,\mathbf{q}_\parallel)$. Note that $\frac{e^{-i\mathbf{q}_\parallel\cdot\mathbf{r}_\parallel}}{|\mathbf{q}_\parallel|^2}$ is the Fourier transformed solution for the Poisson equation for a point charge in a 2D plane, therefore we can consider $\xi(z,\mathbf{q}_\parallel)$ as the out-of-plane component of the potential. Plugging $\varphi(z,\mathbf{q}_\parallel)$ and $\rho(\mathbf{q}_\parallel,z)$ in Eq. (A2), we finally obtain the Poisson equation for the out-of-plane potential generated by a line of charge:

$$\frac{\partial^2}{\partial z^2}\xi(z,\mathbf{q}_\parallel) - |\mathbf{q}_\parallel|^2\xi(z,\mathbf{q}_\parallel) = -4\pi|\mathbf{q}_\parallel|^2\rho(z). \tag{A3}$$

To make the notation more intuitive, in the text we redefine the out-of-plane potential generated by a line of charge as $\phi(z,\mathbf{q}_\parallel) = \frac{1}{|\mathbf{q}_\parallel|^2}\xi(z,\mathbf{q}_\parallel)$.

APPENDIX B: UNSCREENED Q2D INTERACTION

In this Appendix we derive the expression for the Q2D unscreened charge-charge interaction energy in Eq. (5). According to our Q2D picture and assuming a charge distribution $\rho_{1,2}(\mathbf{r}_\parallel,z) = \frac{q_i\delta(\mathbf{r}_\parallel-\mathbf{r}_{1,2,\parallel})}{d}\theta(\frac{d}{2}-|z-z_0|)$, the unscreened charge-charge interaction in reciprocal space can be written as

$$V_{\mathrm{Q2D}}(\mathbf{q}_\parallel) = \frac{q_1q_2}{A}\int_V d\mathbf{r}\frac{\theta\left(\frac{d}{2}-|z-z_0|\right)e^{i\mathbf{q}_\parallel\cdot\mathbf{r}_\parallel}}{d} \times \int_V d\mathbf{r}'\frac{1}{|\mathbf{r}-\mathbf{r}'|}\frac{\theta\left(\frac{d}{2}-|z'-z_0|\right)e^{-i\mathbf{q}_\parallel\cdot\mathbf{r}'_\parallel}}{d}, \tag{B1}$$

where $\mathbf{q}_\parallel$ is the reciprocal space vector corresponding to the separation vector $\mathbf{r}_{1,\parallel} - \mathbf{r}_{2,\parallel}$. To proceed, we notice that the integral in the second line can be interpreted as the potential generated by an in-plane Fourier transformed charge distribution $\rho(\mathbf{q}_\parallel,z') = \frac{\theta(\frac{d}{2}-|z'-z_0|)}{d}e^{-i\mathbf{q}_\parallel\cdot\mathbf{r}_\parallel}$, and its analytic form can be obtained solving Eq. (A2) as illustrated in Appendix A:

$$\varphi(\mathbf{q}_\parallel,z') = \frac{4\pi e^{-i\mathbf{q}_\parallel\cdot\mathbf{r}_\parallel}}{d|\mathbf{q}_\parallel|^2} \times \begin{cases} 1 - e^{-|\mathbf{q}_\parallel|d/2}\cosh(|\mathbf{q}_\parallel||z'-z_0|), & |z'-z_0| < \frac{d}{2}, \\ e^{-|\mathbf{q}_\parallel||z'-z_0|}\sinh(|\mathbf{q}_\parallel|d/2), & |z'-z_0| > \frac{d}{2}. \end{cases} \tag{B2}$$

Plugging this result in Eq. (B1) and integrating in-plane and along z separately, we recover the expression Eq. (5)

APPENDIX C: SCREENED Q2D INTERACTION

In the following we show how to derive the expression for the Q2D screened electron-hole interaction energy reported in Eq. (15). For charge distributions of the kind $\rho_i(\mathbf{r}_\parallel,z) = \frac{\delta(\mathbf{r}_\parallel-\mathbf{r}_{i,\parallel})}{d}\theta(\frac{d}{2}-|z-z_0|)$, the screened interaction reads

$$W_{\mathrm{Q2D}}(\mathbf{q}_\parallel) = -\int_V d\mathbf{r}d\mathbf{r}'\frac{\theta\left(\frac{d}{2}-|z-z_0|\right)e^{i\mathbf{q}_\parallel\cdot\mathbf{r}_\parallel}}{d}\epsilon^{-1}(\mathbf{r},\mathbf{r}') \times \int_V d\mathbf{r}''\frac{1}{|\mathbf{r}'-\mathbf{r}''|}\frac{\theta\left(\frac{d}{2}-|z''-z_0|\right)e^{-i\mathbf{q}_\parallel\cdot\mathbf{r}''_\parallel}}{d}. \tag{C1}$$

As done in Appendix B, we can interpret the integral in the second line as the potential in Eq. (B2). In order to keep the calculation analytic, we approximate $\varphi(\mathbf{q}_\parallel,z)$ with its average inside the slab in the out-of-plane direction as

$$\begin{aligned}\varphi(\mathbf{q}_\parallel,z) &\simeq \frac{1}{d}\int_{z_0-d/2}^{z_0+d/2} dz\,\varphi(\mathbf{q}_\parallel,z) \\ &= -\frac{4\pi e^{-i\mathbf{q}_\parallel\cdot\mathbf{r}_\parallel}}{d^2|\mathbf{q}_\parallel|^2}\left(1 - \frac{2}{|\mathbf{q}_\parallel|d}e^{-|\mathbf{q}_\parallel|d/2}\sinh(\mathbf{q}_\parallel d/2)\right) \\ &= \frac{e^{-i\mathbf{q}_\parallel\cdot\mathbf{r}_\parallel}}{d}V_{\mathrm{Q2D}}(\mathbf{q}_\parallel).\end{aligned} \tag{C2}$$

Inserting the last expression in Eq. (C2) and integrating in-plane, we get

$$\begin{aligned}W_{\mathrm{Q2D}}(\mathbf{q}_\parallel) &= V_{\mathrm{Q2D}}(\mathbf{q}_\parallel)\frac{1}{d}\int_{z_0-d/2}^{z_0+d/2} dz\int_{z_0-L/2}^{z_0+L/2}\epsilon_{00}^{-1}(z,z') \\ &= V_{\mathrm{Q2D}}(\mathbf{q}_\parallel)\epsilon_{\mathrm{Q2D}}^{-1}(\mathbf{q}_\parallel).\end{aligned} \tag{C3}$$

[1] Q. H. Wang, K. Kalantar-Zadeh, A. Kis, J. N. Coleman, and M. S. Strano, Electronics and optoelectronics of two-dimensional transition metal dichalcogenides, Nat. Nanotechnol. **7**, 699 (2012).

[2] K. F. Mak, C. Lee, J. Hone, J. Shan, and T. F. Heinz, Atomically Thin MoS_2: A New Direct-Gap Semiconductor, Phys. Rev. Lett. **105**, 136805 (2010).

[3] A. Splendiani, L. Sun, Y. Zhang, T. Li, J. Kim, C.-Y. Chim, G. Galli, and F. Wang, Emerging photoluminescence in monolayer MoS_2, Nano Lett. **10**, 1271 (2010).

[4] A. Ramasubramaniam, Large excitonic effects in monolayers of molybdenum and tungsten dichalcogenides, Phys. Rev. B **86**, 115409 (2012).

[5] D. Y. Qiu, F. H. da Jornada, and S. G. Louie, Optical Spectrum of MoS_2: Many-Body Effects and Diversity of Exciton States, Phys. Rev. Lett. **111**, 216805 (2013).

[6] M. M. Ugeda, A. J. Bradley, S.-F. Shi, H. Felipe, Y. Zhang, D. Y. Qiu, W. Ruan, S.-K. Mo, Z. Hussain, Z.-X. Shen *et al.*, Giant bandgap renormalization and excitonic effects in a monolayer transition metal dichalcogenide semiconductor, Nat. Mater. **13**, 1091 (2014).

[7] K. He, N. Kumar, L. Zhao, Z. Wang, K. F. Mak, H. Zhao, and J. Shan, Tightly Bound Excitons in Monolayer WSe_2, Phys. Rev. Lett. **113**, 026803 (2014).

[8] D. Jariwala, V. K. Sangwan, L. J. Lauhon, T. J. Marks, and M. C. Hersam, Emerging device applications for semiconducting two-dimensional transition metal dichalcogenides, ACS Nano **8**, 1102 (2014).

[9] M. Bernardi, M. Palummo, and J. C. Grossman, Extraordinary sunlight absorption and one nanometer thick photovoltaics using two-dimensional monolayer materials, Nano Lett. **13**, 3664 (2013).

[10] O. Lopez-Sanchez, D. Lembke, M. Kayci, A. Radenovic, and A. Kis, Ultrasensitive photodetectors based on monolayer MoS_2, Nat. Nanotechnol. **8**, 497 (2013).

[11] J. S. Ross, P. Klement, A. M. Jones, N. J. Ghimire, J. Yan, D.G. Mandrus, T. Taniguchi, K. Watanabe, K. Kitamura, W. Yao *et al.*, Electrically tunable excitonic light-emitting diodes based on monolayer WSe_2 pn junctions, Nat. Nanotechnol. **9**, 268 (2014).

[12] A. Pospischil, M. M. Furchi, and T. Mueller, Solar-energy conversion and light emission in an atomic monolayer pn diode, Nat. Nanotechnol. **9**, 257 (2014).

[13] G. Grosso and G. P. Parravicini, *Solid State Physics* (Elsevier Science, Amsterdam, 2000).

[14] P. Cudazzo, C. Attacalite, I. V. Tokatly, and A. Rubio, Strong Charge-Transfer Excitonic Effects and the Bose-Einstein Exciton Condensate in Graphane, Phys. Rev. Lett. **104**, 226804 (2010).

[15] P. Cudazzo, I. V. Tokatly, and A. Rubio, Dielectric screening in two-dimensional insulators: Implications for excitonic and impurity states in graphane, Phys. Rev. B **84**, 085406 (2011).

[16] F. Hüser, T. Olsen, and K. S. Thygesen, How dielectric screening in two-dimensional crystals affects the convergence of excited-state calculations: Monolayer MoS_2, Phys. Rev. B **88**, 245309 (2013).

[17] O. Pulci, P. Gori, M. Marsili, V. Garbuio, R. Del Sole, and F. Bechstedt, Strong excitons in novel two-dimensional crystals: Silicane and germanane, Europhys. Lett. **98**, 37004 (2012).

[18] T. C. Berkelbach, M. S. Hybertsen, and D. R. Reichman, Theory of neutral and charged excitons in monolayer transition metal dichalcogenides, Phys. Rev. B **88**, 045318 (2013).

[19] H. Terrones, F. López-Urías, and M. Terrones, Novel hetero-layered materials with tunable direct band gaps by sandwiching different metal disulfides and diselenides, Sci. Rep. **3**, 1549 (2013).

[20] L. Britnell, R. M. Ribeiro, A. Eckmann, R. Jalil, B. D. Belle, A. Mishchenko, Y.-J. Kim, R. V. Gorbachev, T. Georgiou, S. V. Morozov *et al.*, Strong light-matter interactions in heterostructures of atomically thin films, Science **340**, 1311 (2013).

[21] A. K. Geim and I. V. Grigorieva, Van der Waals heterostructures, Nature (London) **499**, 419 (2013).

[22] K. Andersen, S. Latini, and K. S. Thygesen, Dielectric genome of van der Waals heterostructures, Nano Lett. **15**, 4616 (2015).

[23] S. L. Adler, Quantum theory of the dielectric constant in real solids, Phys. Rev. **126**, 413 (1962).

[24] T. Cheiwchanchamnangij and W. R. L. Lambrecht, Quasiparticle band structure calculation of monolayer, bilayer, and bulk MoS_2, Phys. Rev. B **85**, 205302 (2012).

[25] A. Molina-Sánchez, D. Sangalli, K. Hummer, A. Marini, and L. Wirtz, Effect of spin-orbit interaction on the optical spectra of single-layer, double-layer, and bulk MoS_2, Phys. Rev. B **88**, 045412 (2013).

[26] The dielectric building blocks and the QEH software can be downloaded from https://cmr.fysik.dtu.dk/vdwh/vdwh.html, accessed 2015-08-18.

[27] F. A. Rasmussen and K. S. Thygesen, Computational 2D materials database: Electronic structure of transition-metal dichalcogenides and oxides, J. Phys. Chem. C **119**, 13169 (2015).

[28] F. Hüser, T. Olsen, and K. S. Thygesen, Quasiparticle GW calculations for solids, molecules, and two-dimensional materials, Phys. Rev. B **87**, 235132 (2013).

[29] G. Strinati, Effects of dynamical screening on resonances at inner-shell thresholds in semiconductors, Phys. Rev. B **29**, 5718 (1984).

[30] G. Onida, L. Reining, and A. Rubio, Electronic excitations: Density-functional versus many-body Green's-function approaches, Rev. Mod. Phys. **74**, 601 (2002).

[31] C. A. Rozzi, D. Varsano, A. Marini, E. K. U. Gross, and A. Rubio, Exact Coulomb cutoff technique for supercell calculations, Phys. Rev. B **73**, 205119 (2006).

[32] J. Enkovaara, C. Rostgaard, J. Jørgen Mortensen, J. Chen, M. Dułak, L. Ferrighi, J. Gavnholt, C. Glinsvad, V. Haikola, H. A. Hansen *et al.*, Electronic structure calculations with GPAW: A real-space implementation of the projector augmented-wave method, J. Phys.: Condens. Matter **22**, 253202 (2010).

[33] The GPAW code is available as part of the CAMPOS software, https://wiki.fysik.dtu.dk/gpaw/, accessed 2010-09-30.

[34] J. Yan, K. W. Jacobsen, and K. S. Thygesen, Optical properties of bulk semiconductors and graphene/boron nitride: The Bethe-Salpeter equation with derivative discontinuity-corrected density functional energies, Phys. Rev. B **86**, 045208 (2012).

[35] C. Zhang, H. Wang, W. Chan, C. Manolatou, and F. Rana, Absorption of light by excitons and trions in monolayers of metal dichalcogenide MoS_2: Experiments and theory, Phys. Rev. B **89**, 205436 (2014).

[36] A. Steinhoff, J.-H. Kim, F. Jahnke, M. Rosner, D.-S. Kim, Ch. Lee, G. H. Han, M. S. Jeong, T. O. Wehling, and C. Gies, Efficient excitonic photoluminescence in direct and indirect band gap monolayer MoS_2, Nano Lett. **15**, 6841 (2015).

[37] L. V. Keldysh, Pis'ma Zh. Eksp. Teor. Fiz. **29**, 176 (1979) [JETP Lett. **29**, 658 (1979)].

[38] A. Chernikov, T. C. Berkelbach, H. M. Hill, A. Rigosi, Y. Li, O. B. Aslan, D. R. Reichman, M. S. Hybertsen, and T. F. Heinz, Exciton Binding Energy and Nonhydrogenic Rydberg Series in Monolayer WS_2, Phys. Rev. Lett. **113**, 076802 (2014).

[39] H. Peelaers and C. G. Van de Walle, Effects of strain on band structure and effective masses in MoS_2, Phys. Rev. B **86**, 241401 (2012).

[40] H.-P. Komsa and A. V. Krasheninnikov, Effects of confinement and environment on the electronic structure and exciton binding energy of MoS_2 from first principles, Phys. Rev. B **86**, 241201 (2012).

Paper III

Simple Screened Hydrogen Model of Excitons in Two-Dimensional Materials

Thomas Olsen, Simone Latini, Filip A. Rasmussen and Kristian S. Thygesen, *PRL*, **116**, pp 056401 (2016).

Simple Screened Hydrogen Model of Excitons in Two-Dimensional Materials

Thomas Olsen,* Simone Latini, Filip Rasmussen, and Kristian S. Thygesen
Center for Atomic-Scale Materials Design and Center for Nanostructured Graphene (CNG), Department of Physics, Technical University of Denmark, 2800 Kgs. Lyngby, Denmark
(Received 22 October 2015; published 2 February 2016)

We present a generalized hydrogen model for the binding energies (E_B) and radii of excitons in two-dimensional (2D) materials that sheds light on the fundamental differences between excitons in two and three dimensions. In contrast to the well-known hydrogen model of three-dimensional (3D) excitons, the description of 2D excitons is complicated by the fact that the screening cannot be assumed to be local. We show that one can consistently define an effective 2D dielectric constant by averaging the screening over the extend of the exciton. For an ideal 2D semiconductor this leads to a simple expression for E_B that only depends on the excitonic mass and the 2D polarizability α. The model is shown to produce accurate results for 51 transition metal dichalcogenides. Remarkably, over a wide range of polarizabilities the binding energy becomes independent of the mass and we obtain $E_B^{2D} \approx 3/(4\pi\alpha)$, which explains the recently observed linear scaling of exciton binding energies with band gap. It is also shown that the model accurately reproduces the nonhydrogenic Rydberg series in WS_2 and can account for screening from the environment.

DOI: 10.1103/PhysRevLett.116.056401

A striking property of two-dimensional semiconductors is the ability to host strongly bound excitons. This was initially predicted theoretically for hexagonal boron nitride (hBN) [1], graphane [2], and various transition metal dichalcogenides [3–5], and has subsequently been confirmed experimentally [6–8]. The quantum confinement of excitons in two dimensions comprises a tempting and intuitively appealing explanation for the large binding energies in these materials [9]. However, it has become clear that it is the reduced dielectric screening in two dimensions that is the main origin of the large binding energy [3,10]. The 2D electronic system is rather poor at screening interactions and the effective Coulomb interaction between an electron and a hole is simply much stronger in two dimensions than in three dimensions.

A rigorous treatment of excitons requires advanced computational methodology such as the Bethe-Salpeter equation [11,12]. This approach has been applied to obtain absorption spectra for numerous insulators and usually yields very good agreement with experiments [13]. However, only systems of modest size can be treated by such methods and simplified models of excitons will be an inevitable ingredient in calculations of realistic systems. For example, if the effect of substrates or the dielectric environment is to be included in the calculation of excitons in 2D systems [14], the computations become intractable with a standard Bethe-Salpeter approach. For 3D materials the Mott-Wannier model comprises a strong conceptual and intuitive picture that provides a simple framework for calculating exciton binding energies [15]. In the center-of-mass frame, an excited electron-hole pair can be shown to satisfy a hydrogenic Schrödinger equation, where band structure effects are included through an excitonic effective mass μ and the dielectric screening from the environment is included through the static dielectric constant ϵ_0. The exciton binding energy in atomic units is then written as

$$E_B^{3D} = \frac{\mu}{2\epsilon_0^2}. \tag{1}$$

Thus, the daunting task of solving the Bethe-Salpeter equation, has been reduced to the calculation of just two parameters: the effective mass and the static dielectric constant, both of which are easily obtained with any standard electronic structure software package. This approximation is well justified whenever the screening is local, such that its Fourier transform can be approximated by a constant in the vicinity of the origin. However, in highly anisotropic structures such as layered materials this assumption is expected to break down.

In 2D dielectrics, it is well known that the screening takes the form $\epsilon(\mathbf{q}) = 1 + 2\pi\alpha q$ [2], where α is the 2D polarizability. The screening is thus inherently nonlocal in real space, and it is not obvious if it is possible to arrive at a hydrogenic model like Eq. (1). Instead, one can calculate the 2D screened potential and solve the Schrödinger equation for the electron-hole wave function

$$\left[-\frac{\nabla^2}{2\mu} + W(\mathbf{r})\right]\psi(\mathbf{r}) = E_n\psi(\mathbf{r}), \tag{2}$$

where $W(\mathbf{r})$ is the 2D convolution of the Coulomb interaction and $\epsilon^{-1}(\mathbf{r}-\mathbf{r}')$. This approach has previously been shown to provide good agreement with the Bethe-Salpeter equation [14,16]. In the Supplemental Material

[17] we assess that the binding energies of 7 transition metal dichalcogenides obtained with the Bethe-Salpeter equation agree well with results obtained from Eq. (2). However, in general the solution of Eq. (2) is a tedious task and it would be highly desirable to have an expression like Eq. (1) from which the exciton binding energy in a given material can be easily estimated and understood. To accomplish this, we calculate the average screening felt by the exciton. To this end, we consider the expression

$$\epsilon_{\text{eff}} = \frac{a_{\text{eff}}^2}{\pi}\int_0^{2\pi} d\theta \int_0^{1/a_{\text{eff}}} dq q \epsilon(\mathbf{q}), \tag{3}$$

where a_{eff} is the effective Bohr radius. For the 2D hydrogen atom the Bohr radius is given by $a = \epsilon/(2\mu)$ and Eq. (4) has to be solved self-consistently for ϵ_{eff} given an expression for $\epsilon(\mathbf{q})$. In a strictly 2D system, the screening is linear in q and Eq. (3) can be solved to yield

$$\epsilon_{\text{eff}} = \frac{1}{2}(1 + \sqrt{1 + 32\pi\alpha\mu/3}). \tag{4}$$

Using that the hydrogenic binding energy in two dimensions is a factor of four larger than in three dimensions [9], we obtain

$$E_B^{\text{2D}} = \frac{8\mu}{(1 + \sqrt{1 + 32\pi\alpha\mu/3})^2}. \tag{5}$$

This is the main result of the present Letter and comprises a long-sought-for 2D analog of Eq. (1).

A remarkable property of the expression (5) is the fact that it becomes independent of the effective mass if the polarizability is large. More precisely,

$$E_B^{\text{2D}} \approx \frac{3}{4\pi\alpha}, \qquad 32\pi\alpha\mu/3 \gg 1. \tag{6}$$

It may come as a surprise that the binding energy becomes independent of mass, since a large mass gives rise to a localized exciton and the binding energy typically increases with localization. This is reflected in Eq. (1), where the binding energy is seen to be proportional to the mass. However, in two dimensions, short range interactions are screened more effectively than long range interactions. Thus, there are two opposing effects of the exciton mass and for large polarizabilities the binding energy becomes independent of mass. In order to assert the applicability of the expressions (5)–(6), we have calculated the effective masses and static polarizabilities (in the random phase approximation) of 51 semiconducting monolayers of transition metal dichalcogenides. For indirect band gap materials we use the effective mass at the indirect gap. The calculations were performed with the electronic structure code GPAW [18,19], and we refer to the Supplemental Material [17] and Ref. [20] for details on the calculations.

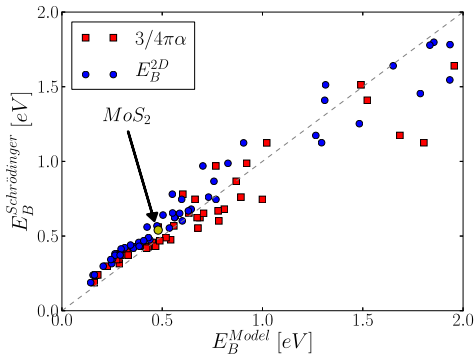

FIG. 1. Exciton binding energies of 51 transition metal dichalcogenides calculated as the lowest eigenvalue of Eq. (2) (vertical axis) and the model result Eq. (5) (horizontal axis). We have indicated the well-known example of MoS_2.

In Fig. 1 we compare the model binding energies with the full solution of Eq. (2). Using the expression (5), the agreement is seen to be on the order of 10%. With the approximated expression (6), we obtain excellent agreement for binding energies up to ~0.5 eV, whereas the binding energies are underestimated for strongly bound excitons.

Recently, first-principles calculations have indicated that exciton binding energies in different 2D materials scale linearly with the band gaps [21]. In the present model, this behavior comes out naturally since (without local field effects) the in-plane components of the polarizability in the random phase approximation are given by

$$\alpha = \sum_{m,n}\int_{BZ}\frac{d\mathbf{k}}{(2\pi)^2}(f_{n\mathbf{k}} - f_{m\mathbf{k}})\frac{|\langle u_{m\mathbf{k}}|\hat{r}_\parallel|u_{n\mathbf{k}}\rangle|^2}{\varepsilon_{n\mathbf{k}} - \varepsilon_{m\mathbf{k}}}, \tag{7}$$

and we expect that α will be roughly inversely proportional to the band gap. This is illustrated in Fig. 2 for the 51

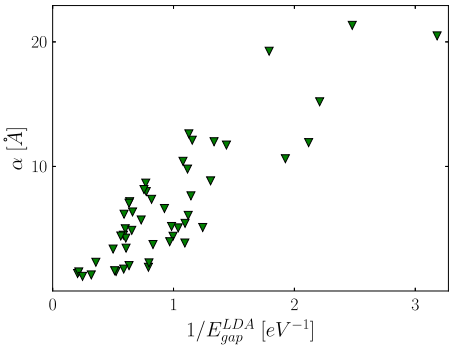

FIG. 2. The 2D polarizability of 51 transition metal dichalcogenides shown as a function of LDA band gaps.

transition metal dichalcogenides. Combining this with Eq. (6) thus gives $E_B^{2D} \propto E_{gap}$. However, in the present model the scaling originates solely from the screening and not the effective mass as previously proposed [21]. For the present set of materials, we do not observe any correlation between binding energies and effective mass. We use the LDA band gaps and not the quasiparticle gaps, which could be obtained from, for example, *GW* calculations [20], since LDA typically gives a better estimate of the two-particle excitation energies that enters the expression for α. In contrast, the use of *GW* gaps would underestimate the screening due to the lack of electron-hole interactions.

To validate the general applicability of the effective screening model, we now show that it can also be used to account for the entire exciton spectrum in 2D materials. In Ref. [22], the exciton spectra of graphene derivatives was predicted to deviate from the 2D Rydberg series and in Ref. [23], the exciton spectrum of WS_2 was measured and shown to deviate significantly from the Rydberg series of a 2D hydrogen model scaled by an overall screening factor. The reason is simply that the effective screening depends on the n quantum number due to the increasing spatial extent of higher lying Rydberg states. The authors used the results to define n-dependent effective screenings ϵ_n, which were then determined by fitting each term in the Rydberg series to a 2D hydrogen model. The Rydberg series is thus written as

$$E_n^{2D} = -\frac{\mu}{2(n-\frac{1}{2})^2\epsilon_n^2}. \tag{8}$$

Two of the present authors have recently shown that the Rydberg series can accurately be reproduced by solving Eq. (2) with a screened 2D potential calculated from first principles [14], and we will assume that approach to be an accurate reference. Here we calculate the n-dependent effective screening from first principles by replacing a_{eff} in Eq. (3) by an n-dependent characteristic extension of the state. To this end, we note that for $l = 0$, the first moment of a state with principal quantum number n in a 2D hydrogen atom with Coulomb interaction scaled by $1/\epsilon$ is [9]

$$a_n \equiv \langle n|\hat{r}|n\rangle = \epsilon[3n(n-1)+1]/(2\mu), \tag{9}$$

where $\hat{r} = \sqrt{\hat{x}^2 + \hat{y}^2}$. In terms of this, the a_{eff} defined previously is given by a_1 and E_B^{2D} is $-E_1^{2D}$. Within the linear model the effective screening for state n then becomes

$$\epsilon_n = \frac{1}{2}\left(1 + \sqrt{1 + \frac{32\pi\alpha\mu}{9n(n-1)+3}}\right). \tag{10}$$

It is straightforward to generalize these expressions to $l \neq 0$ [9], which results in a larger value of the effective radius a_{nl} and thus $\epsilon_{n,l>0} < \epsilon_{n,l=0}$. The energy is still given by Eq. (8) and at a given n, the higher angular momentum excitons will therefore have a larger binding energy, which has been observed in the case of $2H$-WS_2 monolayers [6]. As a case study we consider this material and apply the linear screening model. We obtain a first-principles 2D polarizability of $\alpha = 5.25$ Å and $\mu = 0.19$. In Fig. 3 we show the Rydberg series calculated with the generalized hydrogen model, which agrees very well with a full solution of Eq. (2). In contrast, the pure 2D hydrogen model with an overall effective screening is seen to significantly underestimate the binding energies at higher lying states, since the decreased screening of extended states is not taken into account. We also note that the model binding energies of the $n = 1$ state agree very well with a full solution of the Bethe-Salpeter equation, which yields an exciton binding energy of 0.54 eV [24].

We now proceed to show how the effect of screening by the environment can naturally be taken into account in the present framework. It should be noted, however, that the linear model for the screening is expected to break down for systems where the vertical extent of a substrate becomes comparable to the Bohr radius of the exciton. For example, if we consider a stack of N monolayers, α will diverge in the limit of large N, since the bulk system will have $\epsilon(\mathbf{q} = \mathbf{0}) \neq 1$ [14,25]. The linear regime will therefore only be valid for $q \ll 1/Nd$, where d is the interlayer distance. As an example where we expect the linear model to be applicable, we consider a monolayer $2H$-MoS_2 and compare the isolated layer with the two cases where it is in the vicinity of another layer of $2H$-MoS_2 and in the vicinity of a metallic layer of $1T$-MoS_2. In Fig. 4, we show the absorption spectrum calculated from the Bethe-Salpeter equation based on Kohn-Sham eigenvalues. The BSE calculations were performed in a plane wave basis with a 2D Coulomb truncation scheme [26,27] using a 60×60 k-point mesh. It is well known that the low energy absorption spectrum of this system exhibits a double

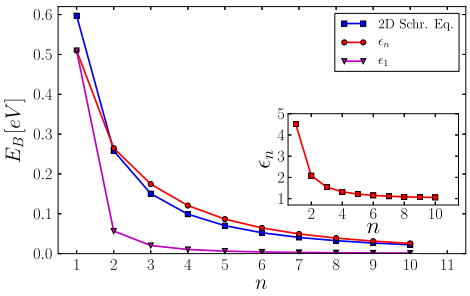

FIG. 3. Rydberg series of a monolayer of $2H$-WS_2 calculated with the generalized hydrogen model with linear screening [Eqs. (8) and (10)] and from the solution of the 2D screened Schrödinger equation (2). The results are compared with the bare hydrogen model where the effective screening obtained from the ground states is used for all states.

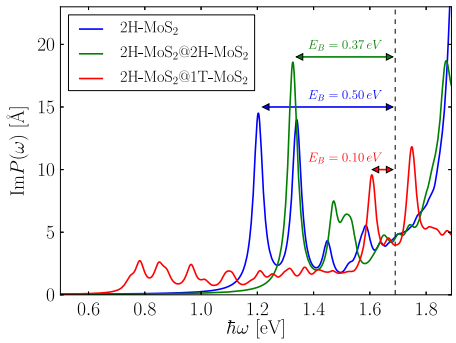

FIG. 4. Dynamic 2D polarizability of $2H$-MoS_2 in different environments calculated from the Bethe-Salpeter equation based on Kohn-Sham eigenvalues. The vertical lines at 1.7 eV marks the Kohn-Sham band gaps, which are nearly identical in the three cases.

excitonic peak due a spin-orbit split valence band [28,29]. This facilitates the identification of the excitons in the $2H$-MoS_2 layer in the vicinity of a metallic substrate with low lying excitations. We have not performed the full spinorial BSE calculations, but simply included spin-orbit effects in the band structure in order to identify the excitons. In the following we consider the binding energies of the lowest exciton. The isolated layer exhibits an exciton bound by 0.50 eV. In the vicinity of another $2H$-MoS_2 layer, the binding energy is decreased to 0.37 eV and the metallic $1T$-MoS_2 decreases the binding energy to 0.10 eV. We note that the quasiparticle band structure corrections are expected to be much smaller for the case of $2H$-MoS_2@$1T$-MoS_2 such that the actual positions of the excitons would be similar for the three cases in an optical absorption experiment. However, we have chosen to leave out the quasiparticle corrections in order to illustrate the difference in binding energies more clearly.

To apply the model we wish to calculate $\epsilon(\mathbf{q})$ for the $2H$-MoS_2 layer when it is in the vicinity of a screening environment. For small q, we may still write it as $\epsilon(\mathbf{q}) = 1 + 2\pi\tilde{\alpha}q$ and we would like to extract $\tilde{\alpha}$, which is the relevant quantity for the screened hydrogen model. We calculate it by the finite difference

$$2\pi\tilde{\alpha} = \epsilon(\mathbf{q}_1) - 1, \tag{11}$$

where $\mathbf{q}_1$ is a small finite value of q. In the present case we take $\mathbf{q}_1$ as the smallest q vector in the direction of K obtained from a 60×60 k-point grid. The 2D dielectric function is obtained from

$$\frac{1}{\epsilon(\mathbf{q})} = \frac{\langle V_{\mathrm{tot}}(r_\parallel, z_0) e^{-i\mathbf{q}\cdot\mathbf{r}} \rangle_A}{V_{\mathbf{q}}}, \tag{12}$$

where $V_{\mathrm{tot}}(\mathbf{r})$ is the total potential resulting from an external perturbation $V_{\mathrm{ext}}(\mathbf{r}) = V_{\mathbf{q}} e^{i\mathbf{q}\cdot\mathbf{r}}$ and $\langle \ldots \rangle_A$ denotes the average over the 2D unit cell of area A. It is straightforward to relate this expression to an average over the microscopic dielectric function $\epsilon^{-1}(\mathbf{r}, \mathbf{r}')$, which can be calculated in the random phase approximation by most electronic structure codes. We take z_0 to be at the center of the $2H$-MoS_2 layer, but we note that $\tilde{\alpha}$ is approximately independent of the value of z_0 when z_0 is chosen in any part of the central 3.0 Å of the layer. In Table I, we display the calculated values of $\tilde{\alpha}$ along with the exciton binding energies obtained from the model (5), the 2D Schrödinger equation (2), and the BSE calculations. As expected, the environment strongly affects the value of $\tilde{\alpha}$. In particular, the metallic $1T$-MoS_2 layer significantly increases the screening, whereas the presence of another $2H$-MoS_2 layer results in a less pronounced effect. We find good agreement between the simple model, the 2D Schrödinger equation, and the BSE calculations. We should note that the convergence of the exciton binding energies in the presence of the metallic $1T$-MoS_2 layer is very slow with respect to k-point sampling and the converged result is expected to exhibit a lower binding energy than the one obtained here. Furthermore, we have not included the intraband contribution (Drude response) to the static screening, which is expected to scale as $\sim 1/q$ in 2D metals. On the other hand, the $1T$ structure is known to distort into the so-called $1T'$ structure, which is a topological insulator with a gap on the order 50 meV [30], and in that case the Drude response will not be present. In any case, the screening is treated at the same footing in the BSE and the model calculations since the values of $\tilde{\alpha}$ were obtained by a finite difference calculation on the same k-point grid that was used in the

TABLE I. Exciton binding energies for $2H$-MoS_2 in different environments calculated from the Bethe-Salpeter equation (BSE), the 2D Schrödinger equation, and the generalized screened hydrogen model. We also display the values of $\tilde{\alpha}$, which is the polarizability of the single $2H$-MoS_2 layer used in the calculations. For all calculations we used an effective exciton mass of 0.276, which was obtained from the *ab initio* band structure.

	$2H$-MoS_2	$2H$-MoS_2@$2H$-MoS_2	$2H$-MoS_2@$1T$-MoS_2
E_B^{BSE} [eV]	0.50	0.37	0.10
$E_B^{\mathrm{Schr.}}$ [eV]	0.54	0.40	0.17
E_B^{Model} [eV]	0.48	0.30	0.10
$\tilde{\alpha}$ [Å]	5.83	10.0	30.1

BSE calculations. The exact conditions under which the linear model is applicable will depend on the thickness of the substrate as well as the screening properties of the substrate. For extended substrates, the present approach may be generalized by calculating the full $\epsilon(\mathbf{q})$ and solving Eq. (3) numerically, but it is not clear that the analytical results derived from the 2D hydrogen model (8) are able to produce reliable results in this case. Alternatively, one may solve a quasi-2D Schrödinger equation that incorporates the finite extent of the slab [25]. We note that the present method can be viewed as a generalized hydrogen model analogue of the approach taken by Ugeda *et al.* [7], where the full substrate screening was taken into account when solving the Bethe-Salpeter equation for the layer.

To conclude, we have presented an analytical expression for the exciton binding energies in 2D semiconductors that only depends on the static 2D polarizability and the effective mass, and produces good agreement with the solution of the full screened 2D Schrödinger equation. It has also been shown that for large polarizabilities, the result becomes independent of mass and yields a linear relation between exciton binding energies and band gaps. It has previously been anticipated that the nonhydrogenic Rydberg series could be attributed to an n-dependent value of the effective screening [23]. Here we have obtained an explicit expression for ϵ_n that provides an accurate account of the full exciton spectrum. It has also been shown that the model can be generalized to incorporate the effect of a simple screening environment. We do not claim that the presented expression for the effective screening (3) in the linear model is unique. In fact, it is based on an unweighted average of a linear model for the nonlocal 2D screening over the extent of the exciton and it is easy to imagine more elaborate averaging schemes. However, we believe that the simplicity is the main merit of this procedure and the resulting analytical expressions are very easy to apply to a given 2D material. In particular, for complicated structures it may not be possible to treat the electron-hole interaction by a first-principles approach and our model results could be a crucial ingredient in understanding the excitonic structure in such materials.

The Center for Nanostructured Graphene (CNG) is sponsored by the Danish National Research Foundation, Project No. DNRF58.

*tolsen@fysik.dtu.dk

[1] L. Wirtz, A. Marini, and A. Rubio, Phys. Rev. Lett. **96**, 126104 (2006).
[2] P. Cudazzo, C. Attaccalite, I. V. Tokatly, and A. Rubio, Phys. Rev. Lett. **104**, 226804 (2010).
[3] F. Hüser, T. Olsen, and K. S. Thygesen, Phys. Rev. B **88**, 245309 (2013).
[4] H. P. Komsa and A. V. Krasheninnikov, Phys. Rev. B **86**, 241201 (2012).
[5] D. Y. Qiu, F. H. da Jornada, and S. G. Louie, Phys. Rev. Lett. **111**, 216805 (2013).
[6] Z. Ye, T. Cao, K. OBrien, H. Zhu, X. Yin, Y. Wang, S. G. Louie, and X. Zhang, Nature (London) **513**, 214 (2014).
[7] M. M. Ugeda, A. J. Bradley, S.-F. Shi, F. H. da Jornada, Y. Zhang, D. Y. Qiu, W. Ruan, S.-K. Mo, Z. Hussain, Z.-X. Shen, F. Wang, S. G. Louie, and M. F. Crommie, Nat. Mater. **13**, 1091 (2014).
[8] A. Hanbicki, M. Currie, G. Kioseoglou, A. Friedman, and B. Jonker, Solid State Commun. **203**, 16 (2015).
[9] X. L. Yang, S. H. Guo, F. T. Chan, K. W. Wong, and W. Y. Ching, Phys. Rev. A **43**, 1186 (1991).
[10] P. Cudazzo, I. V. Tokatly, and A. Rubio, Phys. Rev. B **84**, 085406 (2011).
[11] S. Albrecht, L. Reining, R. Del Sole, and G. Onida, Phys. Rev. Lett. **80**, 4510 (1998).
[12] M. Rohlfing and S. G. Louie, Phys. Rev. Lett. **81**, 2312 (1998).
[13] G. Onida, L. Reining, and A. Rubio, Rev. Mod. Phys. **74**, 601 (2002).
[14] K. Andersen, S. Latini, and K. S. Thygesen, Nano Lett. **15** 4616 (2015).
[15] G. H. Wannier, Phys. Rev. **52**, 191 (1937).
[16] T. C. Berkelbach, M. S. Hybertsen, and D. R. Reichman, Phys. Rev. B **88**, 045318 (2013).
[17] See Supplemental Material at http://link.aps.org/supplemental/10.1103/PhysRevLett.116.056401 for computational details and a comparison of the 2D Scrödinger equation with BSE calculations for 7 TMDs.
[18] J. Enkovaara *et al.*, J. Phys. Condens. Matter **22**, 253202 (2010).
[19] J. Yan, J. J. Mortensen, K. W. Jacobsen, and K. S. Thygesen, Phys. Rev. B **83**, 245122 (2011).
[20] F. A. Rasmussen and K. S. Thygesen, J. Phys. Chem. C **119**, 13169 (2015).
[21] J.-H. Choi, P. Cui, H. Lan, and Z. Zhang, Phys. Rev. Lett. **115**, 066403 (2015).
[22] S. Huang, Y. Liang, and L. Yang, Phys. Rev. B **88**, 075441 (2013).
[23] A. Chernikov, T. C. Berkelbach, H. M. Hill, A. Rigosi, Y. Li, O. B. Aslan, D. R. Reichman, M. S. Hybertsen, and T. F. Heinz, Phys. Rev. Lett. **113**, 076802 (2014).
[24] H. Shi, H. Pan, Y.-W. Zhang, and B. I. Yakobson, Phys. Rev. B **87**, 155304 (2013).
[25] S. Latini, T. Olsen, and K. S. Thygesen, Phys. Rev. B **92**, 245123 (2015).
[26] C. A. Rozzi, D. Varsano, A. Marini, E. K. U. Gross, and A. Rubio, Phys. Rev. B **73**, 205119 (2006).
[27] F. Hüser, T. Olsen, and K. S. Thygesen, Phys. Rev. B **87**, 235132 (2013).
[28] K. F. Mak, C. Lee, J. Hone, J. Shan, and T. F. Heinz, Phys. Rev. Lett. **105**, 136805 (2010).
[29] A. Molina-Sánchez, D. Sangalli, K. Hummer, A. Marini, and L. Wirtz, Phys. Rev. B **88**, 045412 (2013).
[30] X. Qian, J. Liu, L. Fu, and J. Li, Science **346**, 1344 (2014).

Paper IV

Interlayer excitons and Band Alignment in MoS_2/hBN/WSe_2 van der Waals Heterostructures

Simone Latini, Kirsten T. Winther, Thomas Olsen and Kristian S. Thygesen, to be submitted.

Interlayer excitons and Band Alignment in MoS_2/hBN/WSe_2 van der Waals Heterostructures

Simone Latini,*,†,‡ Kirsten T. Winther,† Thomas Olsen,† and Kristian S. Thygesen*,†,‡

†*Center for Atomic-scale Materials Design, Department of Physics, Technical University of Denmark, DK - 2800 Kgs. Lyngby, Denmark*

‡*Center for Nanostructured Graphene, Technical University of Denmark, DK - 2800 Kgs. Lyngby, Denmark*

E-mail: simola@fysik.dtu.dk; thygesen@fysik.dtu.dk

Abstract

Van der Waals heterostructures (vdWH) provide an ideal playground for exploring light-matter interactions at the atomic scale. In particular, structures with a type-II band alignment can yield detailed insight into free carrier-to-photon conversion processes, which are central to e.g. solar cells and light emitting diodes. An important first step in describing such processes is to obtain the energies of the interlayer exciton states existing at the interface. Here we present a general first-principles method to compute the electronic quasi-particle (QP) band structure and excitonic binding energies of incommensurate vdWHs. The method combines our quantum electrostatic heterostructure (QEH) model for obtaining the dielectric function with the many-body GW approximation and a generalized 2D Mott-Wannier exciton model. We calculate

the level alignment together with intra and interlayer exciton binding energies of bilayer MoS_2/WSe_2 with and without intercalated hBN layers, finding excellent agreement with experimental photoluminescence spectra. Comparison to density functional theory calculations demonstrate the crucial role of self-energy and electron-hole interaction effects.

Keywords

van der Waals heterostructures, interlayer Excitons, band alignment, G_0W_0, Mott-Wannier model.

The use of two-dimensional (2D) transition metal dichalcogenides[1–4] as fundamental building blocks in (opto)electronics has proved highly promising for the construction of ultrathin high performance devices.[5–10] By reassembling different 2D crystals into van der Waals heterostructures, designer materials with new and tailored properties can be made.[10–17] As for 2D monolayers,[18–23] the optical properties of few-layer van der Waals heterostructures are strongly influenced by excitonic effects[10,15,16] as a consequence of the weak screening of the electron-hole interaction.[24] In addition to the intralayer excitons localized in the constituent monolayers, vdWHs can host more complex types of excitons with electrons and holes residing in distinct layers, so-called (spatially) indirect excitons or interlayer excitons. Because of the spatial charge separation, interlayer excitons posses longer electron-hole recombination lifetimes[25,26] than intralayer excitons, which make them ideal candidates for realization of bosonic many-particle states like Bose-Einstein condensates.[27] Moreover, interlayer excitons are believed to play a central role in the charge separation process following photoabsorption in solar cells or photodetectors.[28,29] Of key importance to this process is the exciton binding energy which quantifies the strength with which the electron and hole are bound together. Due to the larger electron-hole separation, interlayer excitons are expected to have lower

binding energies than intralayer excitons. However, a detailed understanding of interlayer excitons in vdWHs is still lacking mainly because of the highly non-local nature of the dielectric function of 2D materials which makes screening less effective at larger distances. This is in fact the origin of the non-hydrogenic Rydberg series in 2D semiconductors and the non-degeneracy of 2D excitons with different angular momentum quantum numbers.[30] The understanding of excitonic effects alone, however, is not sufficient for device engineering, where the knowledge of the alignment of the electronic bands of the vdWH is also crucial. Several experimental investigations have shown, for example, that an underlying type-II band alignment is required for the formation of interlayer excitons.[31–33] However, experimental data has not been supported by consistent theoretical studies yet. It is well known that density functional theory (DFT) calculations are problematic when it comes to prediction of band gaps and band alignment at interfaces and do not take excitonic effects into account. An important deficit of the DFT approach, in addition to its general tendency to underestimate band gaps, is its failure to describe image charge renormalization effects that shift the energy levels of a 2D semiconductor[34] or molecule[35,36] when adsorbed on a polarizable substrates. Ideally, one should employ many-body perturbation theory like the GW approximation to obtain reliable band energies or the Bethe Salpeter Equation (BSE) for exciton binding energies. However, the computational cost of such methods make them unfeasible for vdWHs containing more than a few lattice matched 2D crystals.

Here, we show how to overcome these limitations, by means of our recently developed quantum electrostatic heterostructure (QEH) approach[37] and accurately calculate interlayer exciton binding energies and electronic bands of vdWHs. For the excitons, the QEH allows us to calculate the the screened electron-hole interaction to be used in a generalized 2D Mott-Wannier model.[24] For the band energies we use the QEH to modify isolated layer G_0W_0 calculations by including the effect of interlayer screening on the electronic levels. Remarkably we are able to predict band positioning in a vdWH at the cost of, at most, N-G_0W_0 monolayer calculations, with N the number of layers in the stack.

In this letter we apply our method to the case of MoS_2-WSe_2 bilayers intercalated with a varying number of h-BN layers. The MoS2/hBN/WSe2 represents a prototypical type-II heterostructure. Its well defined atomic structure and the possibility of varying the thickness of the hBN spacer and the relative orientation of the photoactive layers, makes it an ideal platform for studying light-matter processes on atomic length scales. At the same time, the incommensurate nature of the van der Waals interfaces presents a great challenge for ab-initio calculations. Nevetheless, we show that our QEH-based methodology allows us to efficiently simulate the electronic structure of MoS_2/hBN/WSe_2, including excitonic and self-energy effects, and accurately reproduce experimental photoluminescence spectra.

The main requirement for the existence of interlayer exciton is that the bottom of the conduction band and the top of the valence band in a van der Waals stack are located in two different layers. As shown in the following, this is the case of MoS_2-WSe_2 based heterostructures. Because of lattice mismatch (see table 1), MoS_2 and WSe_2 form incommensurable heterostructures and therefore realistic band structure calculations require the use of relatively large in-plane supercells as illustrated in panel (b) of fig. 1. By rotating the layers with respect to each other, not only can the dimension of the supercell be reduced, but we can also mimic more closely the experimental situation where the alignment angle between the layers is not controlled. Following the procedure described by Komsa et al,[38] we set up the MoS_2-WSe_2 bilayer for two different alignment angles, specifically $\sim 16.1^\circ$ and $\sim 34.4^\circ$, so that each layer is strained by less than 1%. To be able to compare the band structure of the bilayer with the ones of the constituent isolated monolayers, we unfold the electronic bands of the supercell to the ones of the primitive MoS_2 and WSe_2 cells. This is done by following the method described in Ref. 39. We stress that, because of the lattice mismatch and a non-zero alignment angle, the first Brillouin zones (BZ) of the two materials are different in size and rotated with respect to each other as shown in panel (c) and (e) of fig. 1. This implies that the unfolding of the bands has to be performed accordingly.

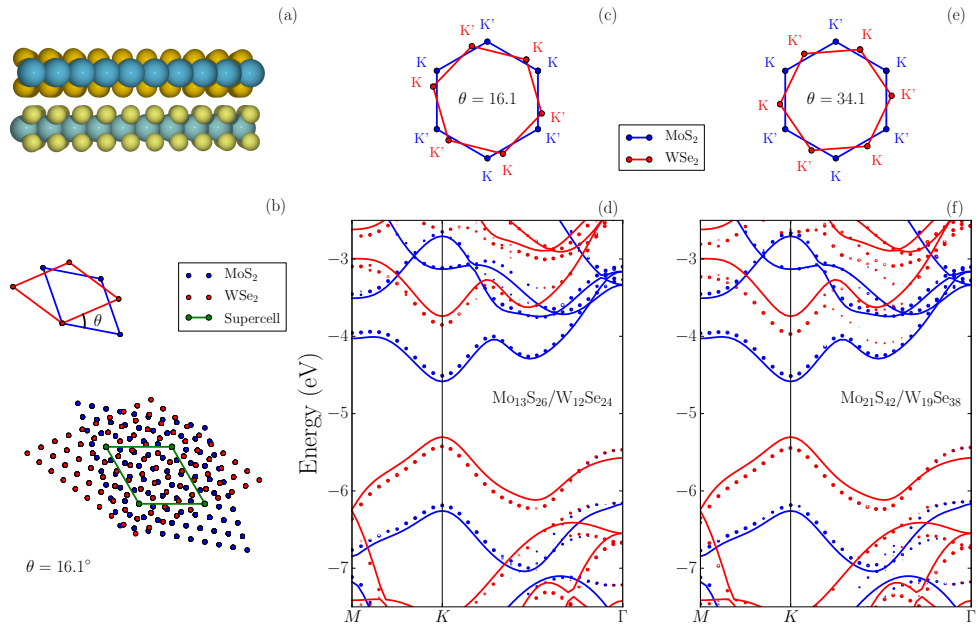

Figure 1: Panel (a) cartoon of the MoS_2-WSe_2 bilayer system. Panel (b) Representation of real space primitive and super-cell for $\theta = 16.1°$. Panels (c) and (e) illustrate how the BZs are twisted and differ in size for the two different alignment angles θ, 16.1° (a) and 34.4° respectively. The unfolded LDA band structure with respect to vacuum for MoS_2-WSe_2 bilayers with for $\theta = 16.1°$ and $\theta = 34.4°$ are plotted in panel (d) and (f) respectively. Circles are used for the unfolded bilayer bands, while continuous lines are used for the isolated layers. The bands are colored in blue or red based on the character of the band, i.e. if they either belong to the MoS_2 or WSe_2 layers and the size. For comparison the isolated layers LDA bands are shown with continuous lines. For simplicity no spin-orbit coupling is included in the electronic bands.

The unfolded band structures, aligned with respect to vacuum level, for the two different bilayers are shown as circles in fig. 1 panel (d) and (f) and compared to the isolated monolayers bands in continuous lines. The band structures have been calculated using the local density approximation (LDA) as described in the Methods section and for simplicity the effect of spin-orbit coupling is not included here. We can clearly confirm that MoS_2 and WSe_2 form a type II heterostructure, where the top of the valence band is localized on the WSe_2 layer, while the bottom of the conduction band belongs to MoS_2. This implies that MoS_2/WSe_2 can host interlayer excitons as sketched in fig. 5 (a). Furthermore, no signif-

icant difference in the band structure emerges for the two different alignment angles and thus we can conclude that the band structure of the bilayer is independent of the alignment angle. When comparing to the bands of the isolated monolayer, we can distinguish two main effects, as thoroughly shown in the Supporting Information: the effect of interlayer hybridization, only around the Γ point, and a layer-dependent shift in energy throughout the Brillouin zone. For the latter, we observe the MoS_2 bands to be shifted up in energy while the WSe_2 bands are shifted down, with a consequent increase in indirect gap of 0.21 eV relative to the vacuum level-aligned isolated layers. Such an asymmetric shift is a clear signature of the formation of a dipole at the interface of the two layers as a consequence of charge rearrangement induced by the misalignment between the band gap center of the two materials. To summarize, since hybrization is minimal around the K-point, which is where the relevant band edges reside, and the charge transfer effect, if needed, can be accounted for just by adding a constant shift, we learn that the bands of the bilayer can be directly obtained as a superposition of the constituent isolated monolayers bands.

While in terms of computational cost it would be advantageous to utilize LDA band structures for quantitative description of bands in vdWHs, their use is largely questionable when accuracy on band alignment and on band gaps is required. To illustrate the LDA failure, we compare the LDA and G_0W_0 electronic bands for the isolated MoS_2 and WSe_2 monolayers in panel (a) of fig. 2. In both approaches we include the effect of spin-orbit coupling at a non-self-consistent level. While the qualitative picture of a type II band alignment is preserved within the G_0W_0 approximation, the band alignment and band gaps predicted by LDA are wrong. This is even more evident in panel (b) of fig. 2, where we directly show the band edges for the isolated MoS_2 and WSe_2 layers. One could possibly argue that the inaccuracy is due to the LDA exchange correlation functional rather than the DFT approach itself. For this reason we also calculated band edges using the HSE06 hybrid functional, which is known to perform well for band structures. However, as shown in panel (b), HSE is better than LDA but still not as accurate as G_0W_0. We thus conclude that the G_0W_0

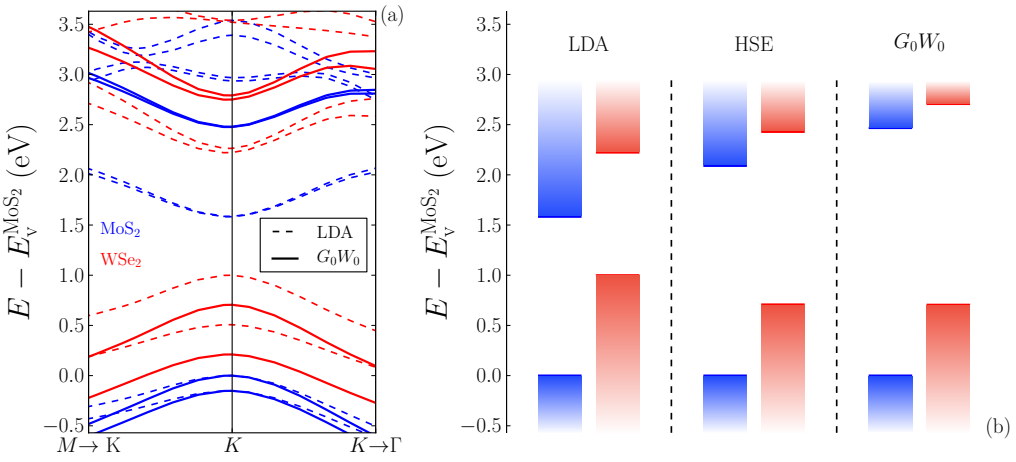

Figure 2: Panel (a) LDA and G_0W_0 band structures for the isolated layers. The panel illustrates a restricted part of the BZ around the K-point. The color code is the same as for fig. 1, i.e. blue for MoS_2 and red for WSe_2. Panel (b) band edges within different approximations. Because of the uncertainty of the G_0W_0 vacuum levels, all the bands are aligned with respect to the top of the valence band in MoS_2. For the HSE calculations the HSE06 hybrid functional is used. Spin-Orbit Effects are included.

approximation is essential to obtain a quantitatively correct description of the band gaps and band alignment. Importantly, we notice that while DFT predicts a rather large difference in band gap centers of around $1eV$, G_0W_0 gives a much smaller difference of around 0.3 eV. This, together with the increased band gaps predicted by G_0W_0, strongly indicates that the charge transfer and associated dipole shift of the bands, could be significantly overestimated by DFT-LDA. We thus conclude that the band structure of the heterobilayer around the K-point can be obtained by combining the G_0W_0 band structures of the isolated layers aligned with respect to a common vacuum level and corrected for image charge screening effects (see later).

The state of the art for describing excitonic effects from first principles is the many-body

Bethe-Salpeter Equation (BSE).[40–42] The solution of the BSE is, however, computationally demanding already at the monolayer level and practically impossible for incommensurate van der Waals heterostructures. However, it is well-known that, under well defined assumptions the excitonic many-body problem can be rephrased in terms of an effective hydrogenic Hamiltonian, the Mott-Wannier Hamiltonian,[43] which gives a satisfactory description of several excitonic properties[24,44–46]. In the case of excitons in vdWHs, the motion of the electron and the hole is restricted to the in-plane direction. This is a direct consequence of the anisotropy of layered structures, which entails that the effective masses at the K-point in out-of-plane direction are much higher than the in-plane direction. With this consideration the hydrogenic Hamiltonian reduces to a 2D problem:

$$\left[-\frac{\nabla^2_{2D}}{2\mu_{\mathrm{ex}}} + W(\mathbf{r}_\parallel)\right] F(\mathbf{r}_\parallel) = E_{\mathrm{b}} F(\mathbf{r}_\parallel), \tag{1}$$

where μ_{ex} is the exciton effective mass and $W(\mathbf{r}_\parallel)$ is the electron-hole interaction energy. The exciton effective mass is evaluated as $\mu_{\mathrm{ex}}^{-1} = m_{\mathrm{e}}^{-1} + m_{\mathrm{h}}^{-1}$, where the hole and electron masses are calculated ab-initio and reported in table 1.

In the case of interlayer excitons eq. (1) is still valid. Indeed even if the electron and the hole are separated in the out-of-plane direction, their motion is still confined in their respective layers. On the other hand, this spatial separation affects the screened electron-hole interaction energy, as shown below. In the specific case of MoS_2/WSe_2 heterostructures, the electron and hole effective masses have to be estimated from the WSe_2 and MoS_2 valence and conduction bands respectively. We found an interlayer exciton effective mass of 0.244 a.u.

Table 1: Lattice parameters and effective masses. The latter are calculated at the point K of the BZ.

Material	a_{MM} (Å)	a_{XX} (Å)	m_{h}	m_{e}	μ_{intra}
MoS_2	3.18	3.13	0.56	0.55	0.27
WSe_2	3.30	3.31	0.48	0.44	0.23

The Coulomb interaction between the electron and the hole in an exciton is highly sensitive to the dielectric properties of the material.[47] As we showed in our recent work,[24] the dielectric screening of finite thickness vdWHs is strongly non local. Using our recently developed quantum-electrostatic heterostructure (QEH) model, we can determine the dielectric properties of these complex structures from first principles.[37] Briefly, we first condense the dielectric response of each single layer into a "dielectric building block" consisting of the monopole and dipole components of the density response function of the isolated layer.[48] Second, the dielectric building blocks are coupled together electrostatically by solving a Dyson-like equation in the discrete monopole/dipole basis in order to obtain the density response function for the whole structure. The underlying assumption of the QEH is that hybridization is weak enough that is does not affect the dielectric properties of the heterostructure. We have found that this approximation is surprisingly good.

A collection of more than 50 dielectric building blocks together with the software for the electrostatic coupling can be found in Ref. 49

From the response function, the dielectric function of the heterostructure is determined and it can be used to obtain the screened electron-hole interaction energy:

$$W(q_\parallel) = \underline{\rho}_{\mathrm{e}}^{\intercal}(q_\parallel)\ \underline{\underline{\epsilon}}^{-1}(q_\parallel)\ \underline{\phi}_{\mathrm{h}}(q_\parallel), \tag{2}$$

where $\underline{\rho}_{\mathrm{e}}$ ($\underline{\phi}_{\mathrm{h}}$) is the electron density (hole induced potential) vector expressed in a basis set of monopole/dipole densities (potentials). The basis set of induced densities and potentials is also used as (left and right) basis functions for representing $\underline{\underline{\epsilon}}^{-1}$ (see Ref. 37). The underlying structure of a vector in the multipole basis can be readily understood. An arbitrary density vector $\underline{\rho}$ is represented as $\underline{\rho}^{\intercal} = [\rho_{1\mathrm{M}}, \rho_{1\mathrm{D}}, \rho_{2\mathrm{M}}, \rho_{2\mathrm{D}}, \cdots, \rho_{\mathrm{nM}}, \rho_{\mathrm{nD}}]$ where $\rho_{i\alpha}$, with $\alpha = \mathrm{M,D}$, is the induced monopole/dipole density at the layer i. A completely equivalent representation can be used for the potential. Now, for the specific case of an interlayer exciton in the MoS_2/WSe_2 bilayer, the electron density vector takes the form $\underline{\rho_{\mathrm{e}}}^{\intercal} = [\rho_{1\mathrm{M}}, \rho_{1\mathrm{D}}, 0, 0]$, while

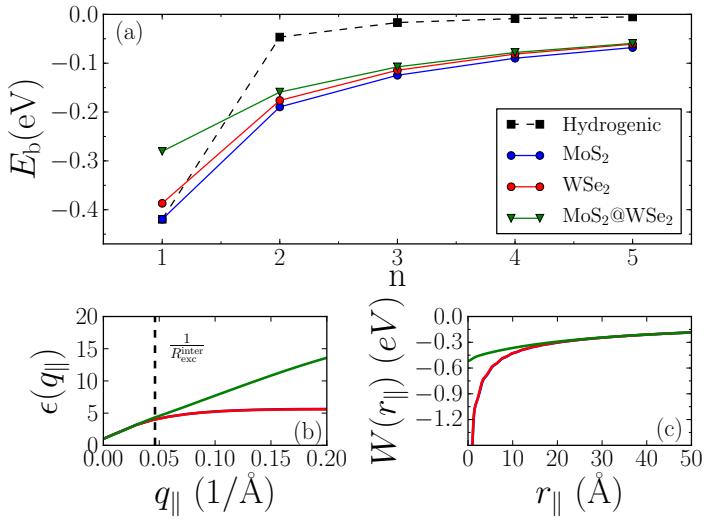

Figure 3: Panel (a) Rydberg series for intra and interlayer excitons. The hydrogenic series is obtained from the standard expression for the energy of a 2D hydrogen atom, i.e. $E_b = \frac{\mu_{ex}}{2(n-1/2)^2\epsilon^2}$ and by fitting ϵ to the lowest lying excitonic state in MoS_2. Panel (b) effective dielectric function and panel (c) Screened electron-hole interaction for intra and interlayer excitons in bilayer MoS_2-WSe_2.

the potential induced by the hole is $\underline{\phi}_h^\intercal = [0, 0, \phi_{2M}, \phi_{2D}]$. Because the electron and hole distribution do not have dipole components, we set $\rho_{1M} = 1$, $\rho_{1D} = 0$ and $\phi_{2M} = 0$, $\phi_{2D} = 0$.

It is useful to define an effective dielectric function for the electron-hole interaction as the unscreened Coulomb interaction over the screened one:

$$\epsilon(q_\parallel) = \frac{\underline{\rho}_e^\intercal(q_\parallel)\ \underline{\phi}_h(q_\parallel)}{\underline{\rho}_e^\intercal(q_\parallel)\ \underline{\underline{\epsilon}}^{-1}(q_\parallel)\ \underline{\phi}_h(q_\parallel)}, \tag{3}$$

A typical signature of excitons in two-dimensional materials is the non-hydrogenic Rydberg series.[50] The Rydberg series along with the full wave-vector dependent effective dielectric screening and electron-hole interaction for the intra and inter-layer excitons in the MoS_2/WSe_2 bilayer are shown in fig. 3 panel (a), (b) and (c) respectively. The non-hydrogenic nature of the Rydberg series should be clear from the comparison with the dashed line in panel (a) which represents the Rydberg series obtained from an hydrogenic equation

where the electron-hole interaction is screened by a constant dielectric function. The first interesting characteristic to notice is that the intra and interlayer Rydberg series converge towards each others for higher excited excitonic states. This is not surprising considering that higher lying states are more delocalized and once their radius is much greater than the heterostructure thickness intra and interlayer excitons are practically indistinguishible, provided that the screening of the electron-hole interaction is comparable. As shown in panel (b), the effective dielectric function is indeed the same for inter and intra-layer excitons within the region of relevant wavevectors values, i.e. values of $q_{\parallel}$ smaller than the reciprocal of the exciton radius (indicated with a vertical line in panel (b) for the lowest lying exciton). However, it is clear from panel (c) that the screened interaction for the interlayer exciton is lower than for the intralayer ones, and it does not diverge for $r_{\parallel} \to 0$. This is a simple consequence of the finite electron-hole spatial separation, which guarantees that the electron and the hole are separated even for $r_{\parallel} = 0$.

To explore the effect of spatial separation even further, we study the case of MoS_2-WSe_2 heterostructures intercalated with h-BN. To isolate the effect of screening, we perform the same calculations with h-BN is substituted by vacuum. The results for the lowest intra and inter-layer exciton binding energies are shown in panel (a) and (b) of fig. 4. Clearly the behavior of the interlayer exciton is quite similar in the two cases, meaning that the main effect of inserting hBN layers is to increase the electron-hole separation. In contrast, the binding energy of the intralayer excitons increases in the case of increasing vacuum while it remains constant when more hBN layers are inserted. This is because moving MoS_2 and WSe_2 apart decreases the screening whereas inserting more hBN layers increases it, leading to an overall compensation.

When stacking 2D layers together, the exciton binding energy is not the only quantity that is affected. Indeed, also the band gap of each of the layers in the stack is reduced due to the increased dielectric screening. The state of the art method for properly including the

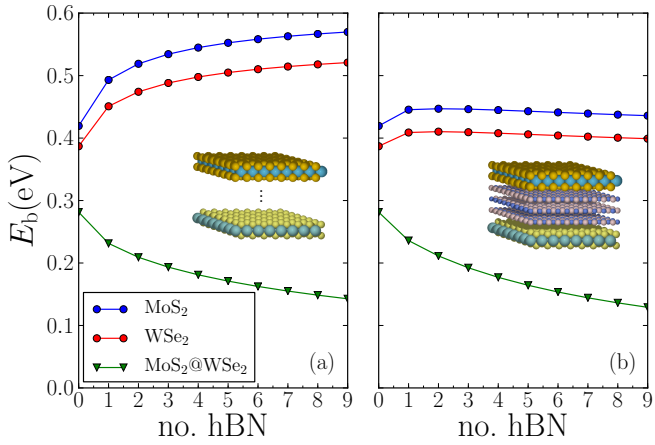

Figure 4: Intra and Interlayer exciton binding energy as a function of number of intercalating vacuum (a) and h-BN (b) layers.

effect of dielectric screening in band structures is the G_0W_0 method.[34,51–53] In this many-body theory based approach, the information of electronic screening is contained in the dynamical screened Coulomb potential:

$$\bar{W}_{\mathbf{GG'}}(\mathbf{q},\omega) = \left[\epsilon^{-1}_{\mathbf{GG'}}(\mathbf{q},\omega) - \delta_{\mathbf{GG'}}\right] \frac{4\pi}{|\mathbf{G}+\mathbf{q}|^2}. \tag{4}$$

Computing $\bar{W}_{\mathbf{GG'}}(\mathbf{q},\omega)$ is a demanding task even for simple materials and it is practically impossible for multi-layer vdWHs. Fortunately, as described elsewhere,[54] the effect of screening on the band structure of a given layer in a van der Waals stack, can be accounted for by combining the QEH model with a standard G_0W_0 method at the computational cost of a monolayer calculation. The main idea is to correct $\bar{W}_{\mathbf{GG'}}(\mathbf{q},\omega)$ for a given layer in the following manner:

$$\bar{W}^{\mathrm{vdWH}}_{\mathbf{GG'}}(\mathbf{q},\omega) = \bar{W}^{\mathrm{monolayer}}_{\mathbf{GG'}}(\mathbf{q},\omega) + \delta W(\mathbf{q},\omega)\delta_{\mathbf{G}0}\delta_{\mathbf{G'}0} \tag{5}$$

where $\delta W(\mathbf{q},\omega)$ is the correction to the head of the matrix $\bar{W}_{\mathbf{GG'}}$ that includes the extra screening coming from the neighboring layers. For a given layer, such a correction is efficiently

calculated within the QEH model. Indeed, by using an expression equivalent to eq. (2), the electron-electron interaction is calculated for the isolated layer and the layer in the vdWH, then $\delta W(\mathbf{q}, \omega)$ is obtained as the difference between the two interactions. Once corrected, the screened potential can be used directly in a standard monolayer G_0W_0 calculation. With this approach, which we refer to as G_0W_0-QEH, we are able to efficiently calculate the band positions of any vdWHs and, specifically for this work, the position of the valence band maximum and conduction band minimum of MoS_2 and $WSe2_2$ for a varying number of hBN layers. A verification of the G_0W_0-QEH approach for the specific MoS_2/WSe_2 system is provided in the supporting information.

The level alignment for a bilayer MoS_2-WSe_2 obtained from the G_0W_0-QEH and including spin-orbit coupling effects is shown in fig. 5 panel (a), whereas the difference in intra and interlayer gaps with respect to the isolated layers are reported in panel (b). Although the band gap renormalization is noticeable when going from monolayers to bilayer, the intercalation of h-BN does not have a considerable effect. Comparing to the variation in exciton binding energy in panel (c), we observe a similar trend for the intralayer cases whereas for the interlayer case the trend is different. This is reasonable since, differently from the interlayer exciton, there is not explicit dependence of the interlayer gap on MoS_2-WSe_2 separation.

With the knowledge of band edges position and exciton binding energies we are now ready to calculate the position of the excitonic photoluminescence (PL) peaks in MoS_2/WSe_2 based heterostructures.

The photoluminescence signal is generated by radiative electron-hole pairs recombination. Considering that typical radiative recombination times in TMDCs are much longer than electron and hole thermalization times, we expect the exciton recombination to happen from the K-point of the conduction band in MoS_2 and the K-point of the valence band in WSe_2. We note that, the lattice mismatch and a non-zero alignment angle between the two layers implies a mismatch of the first BZ of the two materials, as shown in fig. 1.

This means that for a radiative transition to happen the momentum mismatch has to be compensated by some other physical mechanism. Mechanisms of this kind could include phonon assisted transition, electron-electron interaction, defect scattering or breaking of momentum conservation induced by the exterior potential field generated by the neighboring layers.[55] Here we focus on the energetics of the process, which should not be effected by the particular recombination mechanism. Taking into account the type-II band alignment, the position of the pholuminescence peak of the lowest bound exciton is given by:

$$E_{\mathrm{PL}} = E_{\mathrm{IG}} - E_{\mathrm{b}}^{\mathrm{Inter}} \tag{6}$$

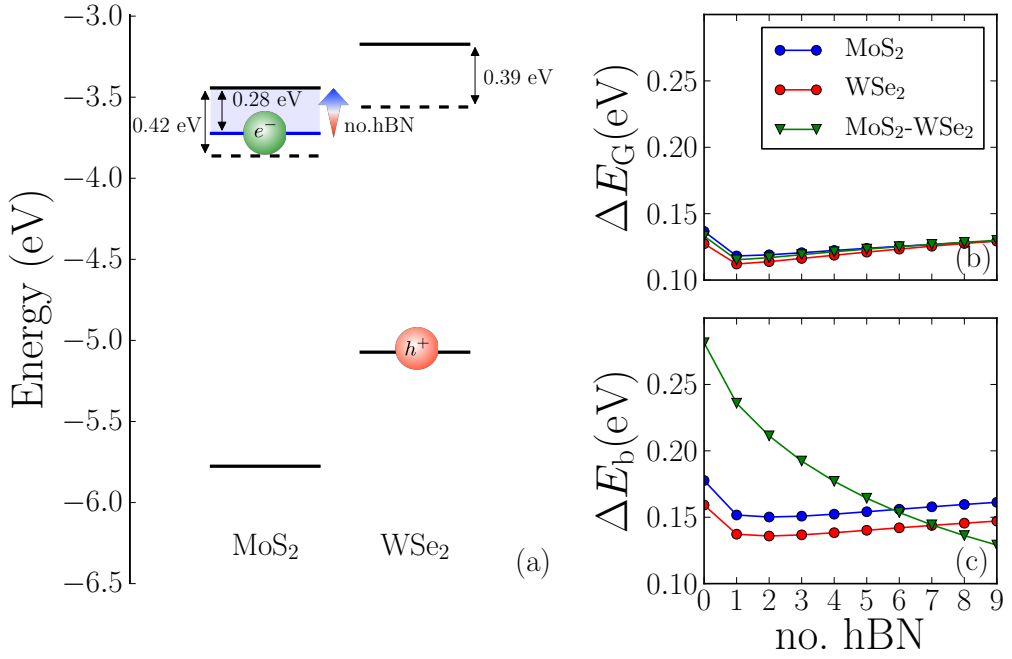

Figure 5: (a) Band alignment diagram for bilayer MoS_2/WSe_2 calculated within the G_0W_0-QEH approximation (see text for details), along with lowest intra and inter-layer excitonic levels for bilayer MoS_2/WSe_2. The shaded region and the arrow shows that the interlayer exciton binding energy decreases with an increasing number of intercalating h-BN. Variation in intra and interlayer gaps (b) and exciton binding energies (c) as a function of intercalated BN layers.

where E_{IG} is the interlayer electronic gap and $E_{\mathrm{b}}^{\mathrm{Inter}}$ the interlayer exciton binding energy. The positions of the lowest energy photoluminescence peak for isolated layers, as well as for MoS_2-WSe_2 based heterostructures with a varying number of intercalating hBN layers are plotted in fig. 6 for the free standing and supported case. Experimental photoluminescence spectra from Ref. 31 are also reported in the same figure. For the supported case we use 30 layers of hBN to simulate the effect of a substrate. The choice of hBN as a substrate is enforced by the QEH approach which applies only to layered materials, but it is justified by the fact that hBN has a bulk dielectric constant similar to SiO_2, which is the substrate used in the experiment. The agreement with the photoluminescence peaks for MoS_2 it is good but for WSe_2 it is underestimated by around 0.15 eV. Roughly the same constant shift is seen for the heterostructures. This indicates that the deviation is due to a too high positioning of the WSe_2 valence band by the G_0W_0-QEH. However, the agreement is still highly satisfactory.

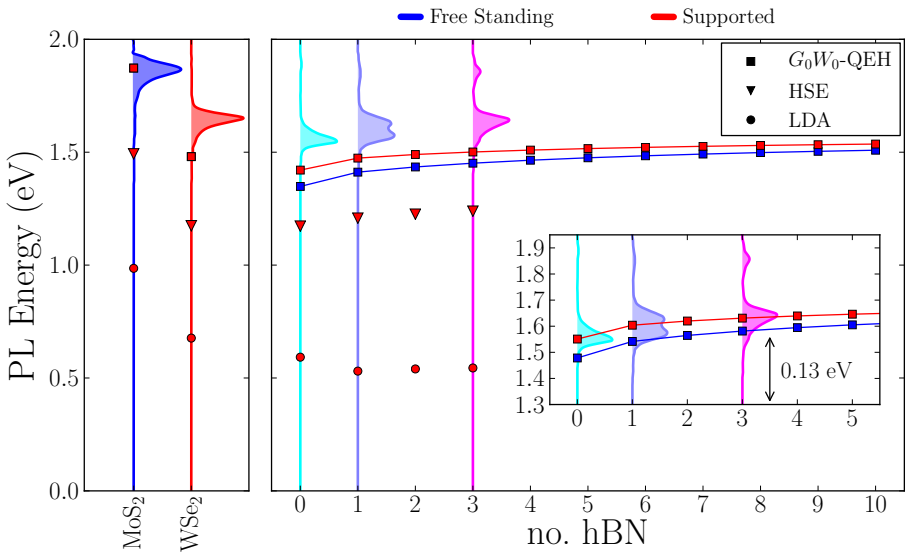

Figure 6: Comparison of the calculate position of the excitonic photoluminescence peaks with experimental data for isolated layers (left panel) and MoS_2-WSe_2 based heterostructures (right panel). The experimental data[31] is reported as shaded colored curves. Inset: same as in the main figure, but with a shift of $0.25eV$, to highlight that we can well reproduce the trend.

Indeed shifting our values by $0.13eV$ we can well reproduce the data for increasing number of intercalating layers as shown in the inset. This indicates that it is the estimated indirect bandgap to be slightly off, but a difference of just $0.13eV$ is still quite accurate for our multi-step approach. According to the experimental interpretation in Ref. 31, while the PL peak for the bilayer without hBN shows a clear interlayer exciton peak, with the intercalation of hBN the interlayer exciton signal is reduced and eventually covered by the WSe_2 intralayer exciton PL peak for three h-BN layers. If this is the case, it is not possible to completely validate the trend of our ab-initio PL peaks values through the actual experimental data. Anyways to demonstrate that using G_0W_0 for monolayer bands is strictly necessary, fig. 6 shows the photoluminescence peaks obtained using a band alignment from LDA and HSE calculations. It is evident that the LDA dramatically underestimates the position of the photoluminescence peaks for both the isolated layer and the bilayer case. The HSE improves the band alignment significantly, but is still around 0.3 eV below the experimental values. Furthermore even the trend of the indirect exciton peak as a function of hBN layers is reversed by LDA. This is a consequence of the strong charge transfer predicted by LDA as discussed earlier. Indeed, charge transfer tends to open the indirect band gap and therefore shift the PL peaks up in energy, with a shift that decreases with increasing number of hBN layers. This shift in energy is larger and opposite to the optical band gap reduction due to interlayer excitons, which explains why the position of the LDA PL peaks descrease in energy in contrast with the G_0W_0 results.

In conclusion, we presented a general approach to calculate band alignment and interlayer excitons in incommensurate van der Waals heterostructures. For the MoS_2/WSe_2 heterostructure, we found that interlayer hybridization is important only around the Gamma-point of the BZ and therefore does not influence the opto-electronic properties that are governed by states around the K-point. This implies that an accurate description of the band edge positions can be obtained from the isolated monolayer band structures aligned relative to a common vacuum level and renormalized by the polarization effect from neighboring

layers. We find interlayer excitons to have significant binding energies of up to 0.3 eV and showing monotonic decrease with the layer separation. Comparison with experimental photoluminescence spectra revealed a constant redshift of the calculated lowest optical transition of around 0.15 eV, which we ascribe to a slight overestimation of the WSe_2 valence band edge by G_0W_0. Our calculations show that it is possible to obtain quantitatively accurate band- and exciton energies for rather complex vdWHs when employing proper methods, and highlight the deficiencies of standard density functional theory for band alignment problems.

Methods

All the ab-initio calculation in this work are performed with GPAW.[56,57] The band structures of the twisted bilayers were calculated at the DFT level with an LDA exchange correlation functional and double-zeta polarized atomic orbitals as a basis set. The HSE06 and LDA calculations for the monolayers were performed using a plane wave basis set with a cut off energy of 500 eV and 18×18 k-point grids. For lattice matched heterostructures modeled in a minimal unit cell, it was checked that the atomic orbital basis yields the same band structure as well converged plane wave calculations. For the calculation of dielectric properties of van der Waals heterostructures we utilized dielectric building blocks available in Ref. 49. Specifically the response function of each building block was calculated on a plane-waves basis with 100 eV cut-off energy and 100×100 k-point mesh. In order to avoid spurious interaction from artificial replica in the out-of-plane direction, a truncated Coulomb interaction with 20 Å of vacuum is used. The interlayer distance between the layers are taken as average of the interlayer distance in their respective bulk form, specifically $d_{MoS_2/WSe_2} = 6.51$Å, $d_{MoS_2/hBN} = 5.08$ Å , $d_{hBN/hBN} = 3.2$ Å and $d_{WSe_2/hBN} = 5.28$ Å. The monolayer G_0W_0 calculations have been performed employing a new efficient technique[58] that overcomes the problem of slow convergence of the band structures with k-point grid and yields well converged band gaps with 18×18 k-points (rather than 40×40 using standard approaches). We used an energy

cut-off of 150 eV for the dielectric function and sum over empty states. The G_0W_0 band energies were extrapolated as $1/N_G$ to the infinite plane wave limit.

The Mott-Wannier equation in eq. (1) was solved on a radial logarithmic grid ensuring numerical convergence of exciton energies up to 0.002 eV.

Acknowledgement

The authors acknowledge support the Center for Nanostructured Graphene (CNG), which is sponsored by the Danish National Research Foundation, Project DNRF58.

Supporting Information Available

Additional details are reported in the supplemental material. This material is available free of charge via the Internet at http://pubs.acs.org/.

References

(1) Wang, Q. H.; Kalantar-Zadeh, K.; Kis, A.; Coleman, J. N.; Strano, M. S. *Nature nanotechnology* **2012**, *7*, 699–712.

(2) Mak, K. F.; Lee, C.; Hone, J.; Shan, J.; Heinz, T. F. *Phys. Rev. Lett.* **2010**, *105*, 136805.

(3) Splendiani, A.; Sun, L.; Zhang, Y.; Li, T.; Kim, J.; Chim, C.-Y.; Galli, G.; Wang, F. *Nano letters* **2010**, *10*, 1271–1275.

(4) Ramasubramaniam, A. *Phys. Rev. B* **2012**, *86*, 115409.

(5) Jariwala, D.; Sangwan, V. K.; Lauhon, L. J.; Marks, T. J.; Hersam, M. C. *ACS nano* **2014**, *8*, 1102–1120.

(6) Lopez-Sanchez, O.; Lembke, D.; Kayci, M.; Radenovic, A.; Kis, A. *Nature nanotechnology* **2013**, *8*, 497–501.

(7) Ross, J. S.; Klement, P.; Jones, A. M.; Ghimire, N. J.; Yan, J.; Mandrus, D.; Taniguchi, T.; Watanabe, K.; Kitamura, K.; Yao, W. *Nature nanotechnology* **2014**, *9*, 268–272.

(8) Pospischil, A.; Furchi, M. M.; Mueller, T. *Nature nanotechnology* **2014**, *9*, 257–261.

(9) Steinhoff, A.; Kim, J.-H.; Jahnke, F.; Rosner, M.; Kim, D.-S.; Lee, C.; Han, G. H.; Jeong, M. S.; Wehling, T. O.; Gies, C. *Nano letters* **2015**, *15*, 6841–6847.

(10) Massicotte, M.; Schmidt, P.; Vialla, F.; Schädler, K.; Reserbat-Plantey, A.; Watanabe, K.; Taniguchi, T.; Tielrooij, K.; Koppens, F. *Nature nanotechnology* **2016**, *11*, 42–46.

(11) Geim, A.; Grigorieva, I. *Nature* **2013**, *499*, 419–425.

(12) Terrones, H.; López-Urías, F.; Terrones, M. *Scientific reports* **2013**, *3*.

(13) Britnell, L.; Ribeiro, R.; Eckmann, A.; Jalil, R.; Belle, B.; Mishchenko, A.; Kim, Y.-J.; Gorbachev, R.; Georgiou, T.; Morozov, S. *Science* **2013**, *340*, 1311–1314.

(14) Withers, F.; Del Pozo-Zamudio, O.; Mishchenko, A.; Rooney, A. P.; Gholinia, A.; Watanabe, K.; Taniguchi, T.; Haigh, S. J.; Geim, A. K.; Tartakovskii, A. I.; Novoselov, K. S. *Nat. Mater.* **2015**, *14*, 301–306.

(15) Bernardi, M.; Palummo, M.; Grossman, J. C. *Nano letters* **2013**, *13*, 3664–3670.

(16) Ma, Q.; Andersen, T. I.; Nair, N. L.; Gabor, N. M.; Massicotte, M.; Lui, C. H.; Young, A. F.; Fang, W.; Watanabe, K.; Taniguchi, T. *Nature Physics* **2016**, *12*, 455–459.

(17) Hong, X.; Kim, J.; Shi, S.-F.; Zhang, Y.; Jin, C.; Sun, Y.; Tongay, S.; Wu, J.; Zhang, Y.; Wang, F. *Nature nanotechnology* **2014**, *9*, 682–686.

(18) Qiu, D. Y.; da Jornada, F. H.; Louie, S. G. *Phys. Rev. Lett.* **2013**, *111*, 216805.

(19) Ugeda, M. M.; Bradley, A. J.; Shi, S.-F.; Felipe, H.; Zhang, Y.; Qiu, D. Y.; Ruan, W.; Mo, S.-K.; Hussain, Z.; Shen, Z.-X. *Nature materials* **2014**, *13*, 1091–1095.

(20) He, K.; Kumar, N.; Zhao, L.; Wang, Z.; Mak, K. F.; Zhao, H.; Shan, J. *Phys. Rev. Lett.* **2014**, *113*, 026803.

(21) Zhang, C.; Wang, H.; Chan, W.; Manolatou, C.; Rana, F. *Physical Review B* **2014**, *89*, 205436.

(22) Berkelbach, T. C.; Hybertsen, M. S.; Reichman, D. R. *Phys. Rev. B* **2013**, *88*, 045318.

(23) Molina-Sánchez, A.; Palummo, M.; Marini, A.; Wirtz, L. *Physical Review B* **2016**, *93*, 155435.

(24) Latini, S.; Olsen, T.; Thygesen, K. S. *Physical Review B* **2015**, *92*, 245123.

(25) Rivera, P.; Schaibley, J. R.; Jones, A. M.; Ross, J. S.; Wu, S.; Aivazian, G.; Klement, P.; Seyler, K.; Clark, G.; Ghimire, N. J. *Nature communications* **2015**, *6*.

(26) Palummo, M.; Bernardi, M.; Grossman, J. C. *Nano letters* **2015**, *15*, 2794–2800.

(27) Fogler, M.; Butov, L.; Novoselov, K. *Nature communications* **2014**, *5*.

(28) Lee, C.-H.; Lee, G.-H.; Van Der Zande, A. M.; Chen, W.; Li, Y.; Han, M.; Cui, X.; Arefe, G.; Nuckolls, C.; Heinz, T. F. *Nature nanotechnology* **2014**, *9*, 676–681.

(29) Skinner, B. *Physical Review B* **2016**, *93*, 235110.

(30) Olsen, T.; Latini, S.; Rasmussen, F.; Thygesen, K. S. *Physical review letters* **2016**, *116*, 056401.

(31) Fang, H.; Battaglia, C.; Carraro, C.; Nemsak, S.; Ozdol, B.; Kang, J. S.; Bechtel, H. A.; Desai, S. B.; Kronast, F.; Unal, A. A. *Proceedings of the National Academy of Sciences* **2014**, *111*, 6198–6202.

(32) Rivera, P.; Seyler, K. L.; Yu, H.; Schaibley, J. R.; Yan, J.; Mandrus, D. G.; Yao, W.; Xu, X. *Science* **2016**, *351*, 688–691.

(33) Heo, H.; Sung, J. H.; Cha, S.; Jang, B.-G.; Kim, J.-Y.; Jin, G.; Lee, D.; Ahn, J.-H.; Lee, M.-J.; Shim, J. H. *Nature communications* **2015**, *6*.

(34) Hüser, F.; Olsen, T.; Thygesen, K. S. *Phys. Rev. B* **2013**, *87*, 235132.

(35) Garcia-Lastra, J. M.; Rostgaard, C.; Rubio, A.; Thygesen, K. S. *Physical Review B* **2009**, *80*, 245427.

(36) Neaton, J. B.; Hybertsen, M. S.; Louie, S. G. *Physical review letters* **2006**, *97*, 216405.

(37) Andersen, K.; Latini, S.; Thygesen, K. S. *Nano letters* **2015**, *15*, 4616–4621.

(38) Komsa, H.-P.; Krasheninnikov, A. V. *Physical Review B* **2013**, *88*, 085318.

(39) Popescu, V.; Zunger, A. *Physical Review B* **2012**, *85*, 085201.

(40) Salpeter, E. E.; Bethe, H. A. *Physical Review* **1951**, *84*, 1232.

(41) Strinati, G. *Phys. Rev. B* **1984**, *29*, 5718–5726.

(42) Onida, G.; Reining, L.; Rubio, A. *Rev. Mod. Phys.* **2002**, *74*, 601–659.

(43) Grosso, G.; Parravicini, G. *Solid State Physics*; Elsevier Science, 2000.

(44) Cudazzo, P.; Attaccalite, C.; Tokatly, I. V.; Rubio, A. *Phys. Rev. Lett.* **2010**, *104*, 226804.

(45) Cudazzo, P.; Tokatly, I. V.; Rubio, A. *Phys. Rev. B* **2011**, *84*, 085406.

(46) Pulci, O.; Gori, P.; Marsili, M.; Garbuio, V.; Del Sole, R.; Bechstedt, F. *EPL (Europhysics Letters)* **2012**, *98*, 37004.

(47) Komsa, H.-P.; Krasheninnikov, A. V. *Phys. Rev. B* **2012**, *86*, 241201.

(48) Yan, J.; Jacobsen, K. W.; Thygesen, K. S. *Phys. Rev. B* **2012**, *86*, 045208.

(49) The dielectric building blocks and the QEH software can be downloaded from:. https://cmr.fysik.dtu.dk/vdwh/vdwh.html, Accessed: 2015-08-18.

(50) Chernikov, A.; Berkelbach, T. C.; Hill, H. M.; Rigosi, A.; Li, Y.; Aslan, O. B.; Reichman, D. R.; Hybertsen, M. S.; Heinz, T. F. *Phys. Rev. Lett.* **2014**, *113*, 076802.

(51) Cheiwchanchamnangij, T.; Lambrecht, W. R. L. *Phys. Rev. B* **2012**, *85*, 205302.

(52) Hüser, F.; Olsen, T.; Thygesen, K. S. *Phys. Rev. B* **2013**, *88*, 245309.

(53) Rasmussen, F. A.; Thygesen, K. S. *The Journal of Physical Chemistry C* **2015**, *119*, 13169–13183.

(54) Winther, K. T.; Thygesen, K. S. *to be submitted*

(55) Yu, H.; Wang, Y.; Tong, Q.; Xu, X.; Yao, W. *Physical review letters* **2015**, *115*, 187002.

(56) Enkovaara, J.; Rostgaard, C.; Mortensen, J. J.; Chen, J.; Dułak, M.; Ferrighi, L.; Gavnholt, J.; Glinsvad, C.; Haikola, V.; Hansen, H. *Journal of Physics: Condensed Matter* **2010**, *22*, 253202.

(57) The **gpaw** code is available as part of the CAMPOS software:. https://wiki.fysik.dtu.dk/gpaw/, Accessed: 2010-09-30.

(58) Rasmussen, F. A.; Schmidt, P. S.; Winther, K. T.; Thygesen, K. S. *arXiv preprint arXiv:1511.00129* **2016**,

Supporting Information

Simone Latini,*,†,‡ Kirsten T. Winther,† Thomas Olsen,† and Kristian S. Thygesen*,†,‡

†*Center for Atomic-scale Materials Design, Department of Physics, Technical University of Denmark, DK - 2800 Kgs. Lyngby, Denmark*

‡*Center for Nanostructured Graphene, Technical University of Denmark, DK - 2800 Kgs. Lyngby, Denmark*

E-mail: simola@fysik.dtu.dk; thygesen@fysik.dtu.dk

Effect of Hybridization and Charge-Transfer

In the main text we argued that the use of supercells is essential for a good description of the band structure of mismatched bilayers and the main differences between the bands of the isolated layers and the bilayers are consequence of charge transfer and hybrization separately. In this section of the supporting information we prove these arguments for the case of MoS_2/WSe_2 based structures.

We start out by demonstrating that using a supercell is unavoidable if an accurate band structure of the MoS_2/WSe_2 is needed. This is shown in fig. 1, where we plot the band structure of the strained bilayer and isolated monolayers in panel (a) and the corresponding unstrained structures in panel (b). In both panels, the bands belonging to the isolated layers are drawn with continuous lines while the ones for the bilayers are drawn with circles. The unstrained bilayer is constructed using a supercell and an alignment angle of ~ 16.1 as described in the main text, whereas for the strained bilayer we use a unit cell with the

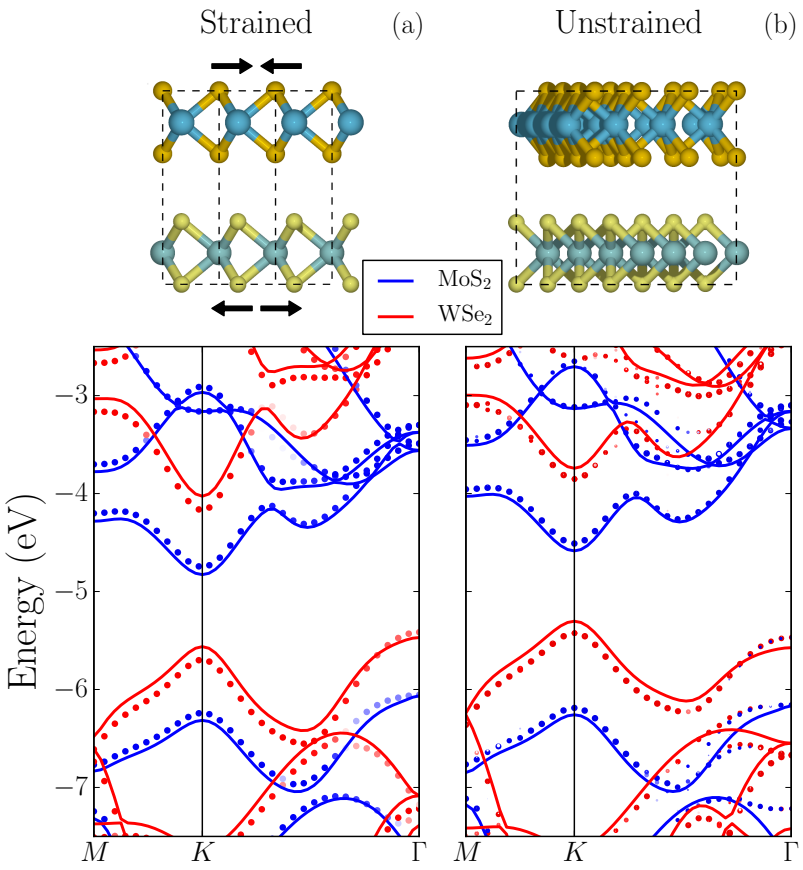

Figure 1: Panel (a) electronic bands for strained bilayer MoS_2/WSe_2 (circles) and isolated monolayers (continuous line). Panel (b) the same as in (a) but for the unstrained structures. For the unstrained bilayer an alignment angle of $\sim 16.1^\circ$ is used. In the strained structures the lattice parameter is the average of the lattice parameter of isolated MoS_2 and WSe_2. The figure shows that the effect of charge transfer can be inferred from a simpler strained calculation.

lattice parameter equal to the average of the lattice parameter of the isolated monolayers. From the figure it is evident that straining the layers has a considerable effect both on the curvature of the bands and on their positioning with respect to vacuum. We thus conclude that accurate band structures cannot be obtained without employing supercells. However, it is still possible to extract information about charge transfer and hybridization from the

strained calculations. Indeed, we can see from fig. 1 that the relative difference between isolated layers and bilayer, in both panels, are practically the same.

Based on this consideration we proceed the analysis of charge transfer and hybridization using the strained calculations, which are computationally more feasible. As explained in the main text, we observe a constant shift in energy, upwards for MoS_2 and downwards for WSe_2, and a wavevector dependent variation around Γ when comparing the isolated layers to the bilayer. While the effect of hybridization is a direct consequence of the mixing among wavefunctions of the two layers, charge transfer results from the rearrangement of the electrons at the bilayer interface due to the difference in band gap centers of the two materials. From a DFT calculation point of view, it is the self-consistent procedure, in particular the change in the Hartree potential in each loop, that allows the rearrangement of the electrons once the two materials are put together. This means that performing a

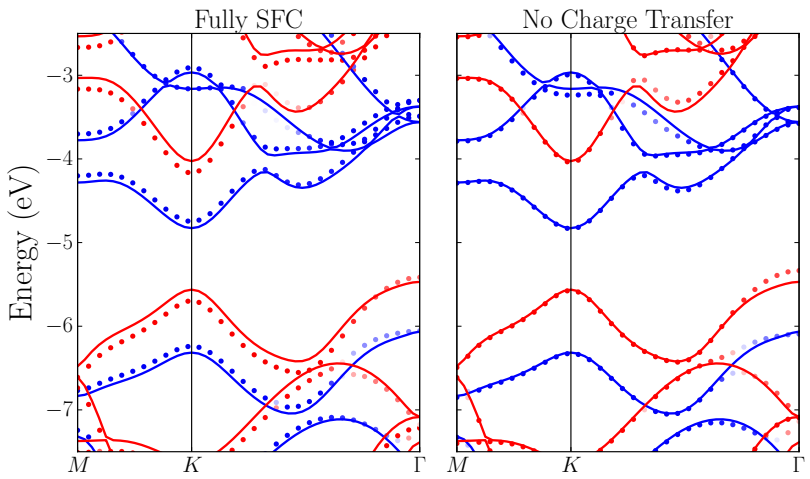

Figure 2: Left panel: bands for strained MoS_2/WSe_2 bilayer (circles) and constituent monolayers (continuous lines). Here the charge transfer effect manifests as constant shift in opposite direction for MoS_2 (in blue) and WSe_2 (in red). Right panel bands for the same systems but for the bilayer the Hartree potential is not updated self-consistently. Keeping the Hartree potential fixed to the one of the isolated layers prevent charge transfer and therefore bilayer and monolayers bands coincide as long as hybrization is negligible. Hybridization is present around Γ.

non-self-consistent DFT calculation starting from the self-consistent ground state density of the isolated layers, would not allow for the update of the Hartree potential and consequent electrons rearrangement. The fully self-consistent band structures (reported for comparison from fig. 1 (a)) and the non self-consistent ones are shown in fig. 2, left and right panel respectively. In panel (b), the isolated layers bands are now exactly on top of the bilayer ones throughout most of the Brillouin zone and therefore it should be now clear that the rigid shift of the bands was a signature of charge transfer. Furthermore the alteration of the bands around the Γ point has not disappeared. This is exactly what we expected considering that hybrization is a result of the overlap of the wavefunctions which is accounted for in the non-self-consistent calculation.

Validity of the QEH correction on G_0W_0 band structure

To check the validity of our G_0W_0-QEH approach we perform G_0W_0 calculations for strained MoS_2 and WSe_2 isolated layers and MoS_2/WSe_2 bilayers. The choice of strained structure is obviously imposed by the feasibility of a G_0W_0 calculation for the bilayers. For the following calculation plane-wave mode has been used. In the left panel of fig. 3 we report the bands for the strained MoS_2/WSe_2 bilayer from a G_0W_0 calculation (continuous black line) and the G_0W_0-QEH approach. The G_0W_0 bands for the isolated layers are also shown as reference. As expected from the extra screening that each layer provides to the other, the intra and inter layer gaps are reduced compared to the isolated layer ones and such an effect is grasped both from the full G_0W_0 calculation and the G_0W_0-QEH method. However, the agreement between G_0W_0 and G_0W_0-QEH is not striking. This is because the effect of charge transfer is still present at the G_0W_0 level, since the Hartree potential generated by the charge rearrangement at the interface is the same as the DFT one. Only self-consistency, indeed, could relieve this problem. To prove that charge transfer is still there and that it is an effect inherited from the starting LDA calculation, we evaluate the layer dependent energy shift at

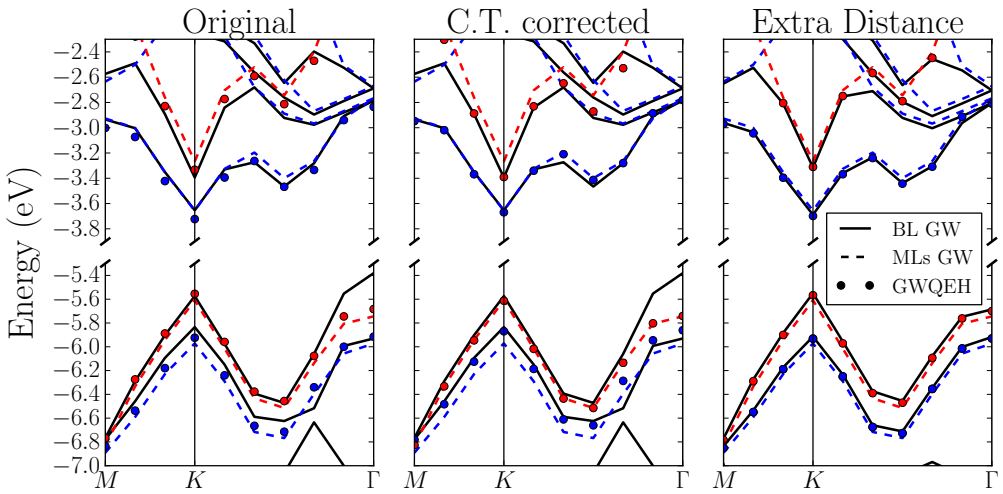

Figure 3: Comparison of the GWQEH method to G_0W_0 calculation for the lattice-matched bilayer. Left panel: reference calculation. Central panel: GWQEH bands are shifted upwards for MoS_2 and downwards for WSe_2 to account for the charge transfer. The values of the shifts are extracted from the comparison between the isolated layers and bilayer LDA calculations. Right panel: the layer separation is artificially increased by 3Å. With the extra distance we expect the effect of charge transfer and hybridization to be completely negligible.The isolated layer bands are reported in all the panels as reference. As usual blue is used for MoS_2 and red for WSe_2.

the K-point by comparing isolated layers and bilayers bands at the LDA level and then add these shifts to the G_0W_0-QEH bands. The results are shown in the central panel of fig. 3. The agreement is nearly perfect and it supports our argument on the importance of charge transfer. As a side note, we mention that the effect of charge transfer using plane-wave mode, as opposed to LCAO, is a bit lower, namely we get an increase in interlayer gap of 0.11 eV compared to the 0.21 eV reported in the main text.

As a further proof of the validity of the G_0W_0-QEH method we repeat the G_0W_0 for the bilayer adding 3 Å to interlayer distance between MoS_2 and WSe_2. This guarantees that charge transfer and hybridization effects are negligible. Screening effects, on the other hand, are still appreciable being the Coulomb coupling between the layers long range. The bands for such a system are shown in the right panel of fig. 3 and it is clear that the G_0W_0-QEH

does a good job.

Paper V

Stark shift and electric-field-induced dissociation of excitons in monolayer MoS_2 and hBN/MoS_2 heterostructures

Sten Haastrup, Simone Latini, Kirill Bolotin and Kristian S. Thygesen, *PRB*, **94**, pp 041401(R) (2016). Rapid Communication

PHYSICAL REVIEW B **94**, 041401(R) (2016)

Stark shift and electric-field-induced dissociation of excitons in monolayer MoS_2 and hBN/MoS_2 heterostructures

Sten Haastrup,[1] Simone Latini,[2,1] Kirill Bolotin,[3,4] and Kristian S. Thygesen[2,1]
[1]*Department of Physics, Center for Atomic-Scale Materials Design (CAMD), Technical University of Denmark, 2800 Kgs. Lyngby, Denmark*
[2]*Department of Physics, Center for Nanostructured Graphene (CNG), Technical University of Denmark, 2800 Kgs. Lyngby, Denmark*
[3]*Department of Physics, Vanderbilt University, Nashville Tennessee 37240, USA*
[4]*Department of Physics, Freie University, 14195 Berlin, Germany*
(Received 11 February 2016; published 1 July 2016)

Efficient conversion of photons into electrical current in two-dimensional semiconductors requires, as a first step, the dissociation of the strongly bound excitons into free electrons and holes. Here we calculate the dissociation rates and energy shift of excitons in monolayer MoS_2 as a function of an applied in-plane electric field. The dissociation rates are obtained as the inverse lifetime of the resonant states of a two-dimensional hydrogenic Hamiltonian which describes the exciton within the Mott-Wannier model. The resonances are computed using complex scaling, and the effective masses and screened electron-hole interaction defining the hydrogenic Hamiltonian are computed from first principles. For field strengths above 0.1 V/nm the dissociation lifetime is shorter than 1 ps, which is below the lifetime associated with competing decay mechanisms. Interestingly, encapsulation of the MoS_2 layer in just two layers of hexagonal boron nitride (hBN), enhances the dissociation rate by around one order of magnitude due to the increased screening. This shows that dielectric engineering is an effective way to control exciton lifetimes in two-dimensional materials.

DOI: 10.1103/PhysRevB.94.041401

Two-dimensional (2D) semiconductors, such as single- and few-layer transition-metal dichalcogenides, are presently being intensively researched due to their extraordinary electronic and optical properties which include strong light-matter interactions, spin-valley coupling, and easily tunable electronic states [1–14]. One of the hallmarks of the 2D semiconductors is the presence of strongly bound excitons with binding energies reaching up to 30% of the band gap. These large binding energies are mainly a result of the reduced dielectric screening in two dimensions [15–19]. Although such strongly bound excitons are highly interesting from a fundamental point of view (for example, in the context of Bose-Einstein condensates [20]) they are problematic for many of the envisioned applications of 2D materials, such as photodetectors and solar cells which rely on efficient conversion of photons into electrical currents. This is because the strong attraction between the electron and the hole makes it difficult to dissociate the excitons into free carriers.

Photocurrent measurements on suspended MoS_2 samples have found that the photocurrent produced by below-band-gap photons is strongly dependent on the applied voltage indicating that the electric field plays an important role in the generation of free carriers [21]. One way to increase the photoresponse could be to embed the active 2D material into a van der Waals heterostructure [22–24]. This embedding would enhance the screening of the electron-hole interaction without altering the overall shape of the band structure of the material. The effects of this increased screening on the exciton dissociation are studied in this Rapid Communication.

In general, rigorous calculations of exciton binding energies require a many-body approach, such as the Bethe-Salpeter equation (BSE) which directly finds the (real) poles of the interacting response function, corresponding to the neutral excitation energies of the system [25,26]. Such calculations are computationally demanding and typically only used to study excitations from the ground state, i.e., not in the presence of external fields. We mention, however, that the BSE has been used to study field-induced exciton dissociation in carbon nanotubes by fitting the BSE absorption spectrum to the Fano line shape [27]. In this Rapid Communication we take a different approach using that, under certain simplifying circumstances, the calculation of the many-body excitonic state can be reformulated as an effective hydrogenic Hamiltonian whose eigenvalues and eigenstates represent the exciton binding energies and the envelope wave function describing the relative electron-hole motion. This is the so-called Mott-Wannier model which has been instrumental in the description of excitons in inorganic bulk semiconductors. A 2D version of the Mott-Wannier model has recently been shown to yield exciton binding energies in good agreement with BSE calculations and experiments for both freestanding [15,16,18,19,28] and supported [15,28,29] transition-metal dichalcogenide layers. The dissociation rate of the exciton is then obtained by complex scaling, which is a formally exact technique to compute resonance energies and lifetimes. By employing a recently developed quantum-classical method for calculating the dielectric function of general van der Waals heterostructures, we predict the effect of embedding the MoS_2 in hBN on the screened electron-hole interaction and exciton dissociation rate.

When an in-plane constant electric field is applied to an exciton, it will eventually decay into a free electron and hole. This effect belongs to a class first studied by Keldysh [30] and Franz [31], who examined how the optical properties of semiconductors change in the presence of a static electric field. The application of a constant electric field changes the exciton from a bound state to a resonance with a finite lifetime equal to the inverse dissociation rate.

The literature on resonances in quantum physics is vast, and we will not go into the topic here but simply mention a few important facts. First, it should be understood that even the definition of a resonance is nontrivial. The reason for this can be understood from *Howland's razor* which states that no satisfactory definition of a resonance can depend only on the structure of a single operator on an abstract Hilbert space [32]. To illustrate the content of the statement consider the Stark effect in hydrogen: Let $\hat{H}(\epsilon) = -\frac{1}{2}\Delta - 1/r + \epsilon x$. It can be shown that $\hat{H}(\epsilon)$ is unitarily equivalent to $\hat{H}(\epsilon')$ for all nonzero ϵ and ϵ's. Since we expect the properties of the resonances and, in particular, their lifetimes to depend on field strength ϵ, this example shows that the resonance cannot be viewed only as a property of the operator $\hat{H}(\epsilon)$. Instead the notion of resonance is only meaningful when the real-space geometry of the given system and relevant boundary conditions on the wave functions are considered.

There are generally two approaches used to compute resonances. The so-called indirect methods identify resonances as the poles of the scattering amplitude analytically extended to the complex energy plane [33], whereas the direct methods obtain the resonance states directly as eigenstates of a complex scaled non-Hermitian Hamiltonian [34,35]. In this Rapid Communication we will use the latter approach.

To describe excitons in a 2D semiconductor we use a Mott-Wannier model of the form

$$\left[-\frac{\nabla_{\mathrm{2D}}^2}{2\mu_{\mathrm{ex}}} + W(\mathbf{r})\right]F(\mathbf{r}) = E_{\mathrm{b}}F(\mathbf{r}), \tag{1}$$

where μ_{ex} is the exciton effective mass $\mu_{\mathrm{ex}}^{-1} = m_{\mathrm{e}}^{-1} + m_{\mathrm{h}}^{-1}$, W is the screened electron-hole interaction, $\mathbf{r}$ is an in-plane position vector, and E_{b} denotes the exciton binding energy. In principle there should be an exchange term included here, but a full *ab initio* solution of the BSE has shown that the exchange term decreases the binding energy of the lowest exciton in MoS_2 by less than 4% [15], and the term can therefore be neglected.

The screened electron-hole interaction is obtained as the inverse Fourier transform of $[\epsilon_{\mathrm{2D}}(\mathbf{q})q]^{-1}$, where $\epsilon_{\mathrm{2D}}(\mathbf{q})$ is the static dielectric function of the 2D material and $1/q$ is the in-plane 2D Fourier transform of $1/r$. In the small-q limit, we can approximate ϵ as a linear function of q [16–19] so that

$$\epsilon_{\mathrm{2D}}(\mathbf{q}) = 1 + 2\pi\alpha q, \tag{2}$$

with α being the polarizability of the material. An analytic expression can then be obtained for the screened electron-hole interaction [17],

$$W(\mathbf{r}) = \frac{1}{4\alpha}[Y_0(x) - H_0(x)]_{x=r/2\pi\alpha}, \tag{3}$$

where Y_0 is a Bessel function of the second kind and H_0 is a Struve function. For later use we note that both of these functions are analytic on the entire complex plane away from $z = 0$.

The expression (3) for the screened interaction relies on a first-order expansion of $\epsilon_{\mathrm{2D}}(q)$ around $q = 0$; the validity of this approximation has been demonstrated for a number of freestanding 2D semiconductors [16,18,19] and recently for MoS_2 embedded in a few layers of *h*BN [15]. As a rule of thumb, the linear screening approximation [Eq. (2)] remains valid for intralayer excitons in van der Waals heterostructures as long as the in-plane exciton radius is large compared to the thickness of the heterostructure [15]. For thicker slabs, the linear approximation breaks down, and the fully q-dependent $\epsilon_{\mathrm{2D}}(\mathbf{q})$ must be used to obtain $W(r)$. We follow the common practice of using the static dielectric function for evaluating the screened interaction of the Mott-Wannier model. For details on how we calculate the dielectric functions of 2D layers and heterostructures we refer to Ref. [29]. Using these methods, the static dielectric function $\epsilon_{\mathrm{2D}}(q)$ can be calculated, and the slope at $q = 0$ can be determined.

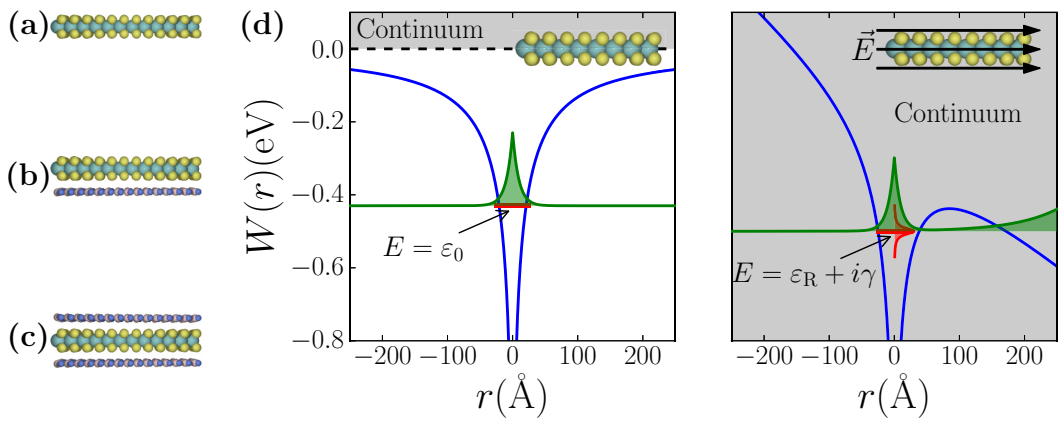

FIG. 1. (a)–(c) The three different structures considered in this Rapid Communication: isolated MoS_2, MoS_2 on a single layer of *h*BN, and MoS_2 sandwiched between two *h*BN layers. (d) Illustration of the Mott-Wannier model for monolayer MoS_2 in the absence (left) and presence (right) of an in-plane constant electric field. The exciton potential is shown in blue, the exciton wave function is sketched in green, and the energy is shown in red. When an electric field is applied, the energy of the exciton shifts down, and the sharp energy peak is broadened due to the coupling to the continuum of states.

Here we have considered a MoS_2 layer in three different configurations: isolated, placed on a single layer of *h*BN, and sandwiched between two *h*BN layers. The systems are sketched in Figs. 1(a)–1(c). The distance between the MoS_2 base plane and the *h*BN sheets was 5.1 Å and was chosen as the mean of the interlayer distance in pure MoS_2 and *h*BN. Sensitivity testing showed that varying this distance by 20% results in a variation in the slope of $\epsilon_{2D}(\mathbf{q})$ of less than 2%.

The lattices of MoS_2 and *h*BN are incommensurable, but the quantum-electrostatic heterostructure model introduced in Ref. [29] allows us to obtain the dielectric function of the heterostructure by electrostatic coupling of the response of the individual layers thus avoiding the issue of in-plane lattice mismatch. Table I shows the obtained polarizabilities and corresponding exciton binding energies. As expected, embedding the MoS_2 in *h*BN leads to an increase in screening and a reduction in the binding energy with the calculated results for the binding energy being in good agreement with *ab initio* calculations [15].

Once an in-plane constant electric field is applied to the system, the bound states of the Mott-Wannier Hamiltonian become metastable. The situation is illustrated in Fig. 1(d). In the model we have used, we assume that the band structure and, in particular, the effective mass of the exciton are not altered by the electric field.

Within the so-called direct methods, a resonance is defined as an eigenstate of the Hamiltonian under the boundary condition that only outgoing waves exist outside the scattering region. Such an eigenstate must necessarily have a complex eigenvalue $E = \epsilon_0 - i\gamma$ and a wave function that adopts the asymptotic form $e^{\pm iKx}$ for $x \to \pm\infty$ (focusing on the one-dimensional case for simplicity) where $K = k - i\kappa$ with $k > 0$ (an outgoing wave) and $\kappa > 0$. The latter condition implies that the wave function increases exponentially away from the scattering region. The decay rate of the resonance state, evaluated as the rate of decay of the probability for finding the particle in any finite region of space, is given by $\gamma = k\kappa$. It can be shown that the resonance eigenvalue E is a pole of the analytically continued scattering matrix [36].

To compute the resonance, one could in principle solve the Schrödinger equation with the appropriate boundary conditions. In practice, however, it is more convenient to perform a "complex scaling" of the Hamiltonian, whereby the coordinate $r \to e^{i\theta}r$ and $\nabla \to e^{-i\theta}\nabla$, and then solve for the eigenstates of the resulting (non-Hermitian) operator $\hat{H}_\theta$ with the more standard zero boundary conditions. For $\theta > \tan^{-1}(\gamma/k)$, the complex scaled resonance wave function (that is the wave function evaluated on the line $re^{i\theta}$ after analytic continuation) is an eigenstate of $\hat{H}_\theta$ with eigenvalue E but now decaying exponentially as $r \to \pm\infty$. The resonances thus appear as isolated complex eigenvalues of $\hat{H}_\theta$ with energy independent of θ and a square integrable wave function [37]. The complex scaled wave function of the bound states remain exponentially decaying eigenstates of $\hat{H}_\theta$ with real eigenvalues [34].

The unbound continuum states have a different behavior: If the potentials involved are localized, the asymptotic form of these states as $r \to \infty$ is e^{ikr} with $k, r \in \mathbb{R}$. They are thus finite at infinity but non-normalizable. If this is to remain true after the complex scaling is performed, the transformation $r \to re^{i\theta}$ must be accompanied by the transformation $k \to ke^{-i\theta}$. As the energy of a plane wave is proportional to k^2, the complex scaling operation results in the energy of the continuum states rotating into the complex plane at an angle of 2θ.

We mention that the complex scaling procedure cannot be applied to any potential $V(\mathbf{r})$ [35], but the class of potentials for which the procedure works is large enough to include the bare and the screened Coulomb potential [38] as well as a constant electric field [39].

In Fig. 2 we show an example of the spectrum of the complex-scaled exciton Hamiltonian for isolated MoS_2 in zero field for different values of the scaling parameter θ. The two classes of states, bound and unbound, can clearly be distinguished; for zero field there are no resonances.

For the systems shown in Figs. 2(a)– 2(c) we compute the screened interaction between charges located in the MoS_2 layer using the random phase approximation (RPA) and the local density approximation (LDA) as implemented in the GPAW code [40,41]. The response calculations were done with a 60×60 k-point grid and a 150-eV energy cutoff for $\mathbf{G}$ and $\mathbf{G}'$. The bandstructure obtained from the LDA calculations gives an effective exciton mass for MoS_2 of $0.27m_e$. Once α and μ_{ex} are known, the 2D eigenvalue problem for the complex-scaled Hamiltonian is solved on a real-space grid using radial coordinates. In order to converge the exciton energies, a large simulation cell is needed—significantly larger than the exciton radius, which is around 10 Å for all of the systems considered.

TABLE I. Calculated values for the polarizability (α) and exciton binding energy (E_b) for single-layer MoS_2 in the three configurations shown in Figs. 2(a)–2(c).

Material	α (a.u.)	E_b (eV)
MoS_2	11.1	0.62
MoS_2-*h*BN	13.0	0.55
*h*BN-MoS_2-*h*BN	16.1	0.47

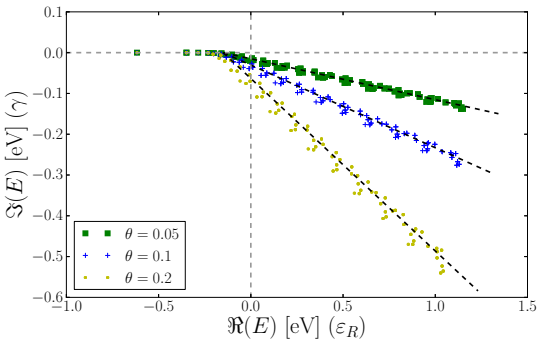

FIG. 2. The different behaviors of bound and continuum states under the complex scaling operation for the potential corresponding to isolated MoS_2. The black dashed lines start at −0.15 eV and have been rotated into the complex plane by -2θ for each of the complex scaling angles. Note that the continuum starts at −0.15 eV and not 0 because of the finite size of the simulation box.

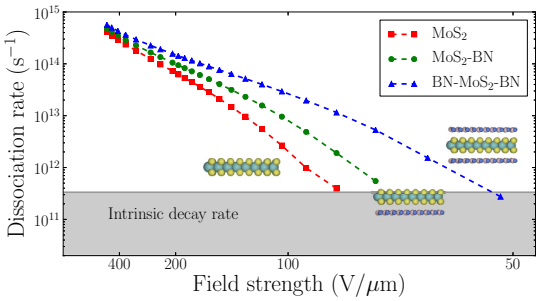

FIG. 3. The dissociation rate of an exciton in the MoS_2 layer as a function of in-plane field strength for the three different structures. The intrinsic decay rate spans between the defect-assisted fast decay of the excitons of 2–5 ps (upper limit) and the much slower radiative recombination of the excitons at room temperature (lower limit).

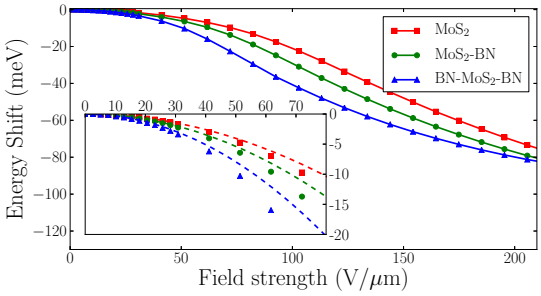

FIG. 4. The Stark shift in the MoS_2 heterostructures. The inset shows the shift for small fields, along with the shift predicted for a 2D hydrogen atom with an effective dielectric constant ϵ_{eff}; see Eq. (4).

As the screened potential has a logarithmic singularity at $r = 0$ while being virtually flat at the edge of the simulation cell, a nonlinear grid is used, which allows us to perform simulations in a disk of radius 250 Å. The Laplacian is represented by a finite-difference stencil. In order to avoid diagonalization of the full Hamiltonian, we used the iterative eigensolver ARPACK.

Figure 3 shows the MoS_2 exciton dissociation rate as a function of in-plane field strength for three different structures. As expected, larger fields lead to shorter lifetimes, and the rate is seen to depend roughly exponentially on $1/E$ for the considered field strengths. It can also be seen that the dissociation rate can be tuned to a high degree by changing the environment of the MoS_2. When MoS_2 is placed on a single layer of boron nitride, the extra screening greatly increases the dissociation rate, and similarly, when the MoS_2 is sandwiched between two layers of BN, the rate is even larger. This is as expected since larger screening results in more weakly bound excitons, which should in turn dissociate more readily. Adding more *h*BN layers on either side is expected to further enhance the screening and hence the dissociation rates, but this has not been pursued here as the linear screening model breaks down in this regime [15].

Along with information about the lifetime of the resonant states, the complex eigenvalue can provide information on the Stark shift of the resonance energy, an effect which is directly observable in optical absorption measurements. Figure 4 shows how the real part of the eigenvalue varies with field strength, and as expected, for small fields we observe a parabolic shift. The breakdown of this parabolic behavior occurs at smallest fields for the most screened excitons.

Recently, it has been shown that excitons in 2D materials can be described by a 2D hydrogen model with an effective dielectric constant [28], which for the linear screening described by Eq. (2) is given by $\epsilon_{\text{eff}} = \frac{1}{2} + \frac{1}{2}\sqrt{1 + 32\pi\alpha\mu/3}$. Based on this model and second-order perturbation theory, the shift can be predicted to be

$$\Delta E = -\frac{21}{64}\frac{\epsilon_{\text{eff}}^4}{\mu^3}E^2. \tag{4}$$

Figure 4 shows that this prediction fits well with our calculations for small fields.

In a real device, the field-induced dissociation of excitons described here is in competition with other decay mechanisms, such as direct radiative recombination [42], defect-assisted recombination [43], and exciton-exciton annihilation [44]. The relative importance of these effects is highly dependent on the temperature of the MoS_2, the presence and concentration of defects, and the exciton density.

At very low temperatures, the direct radiative decay of zero momentum excitons dominates with a characteristic lifetime of ∼200 fs [42,45,46]. At room temperature, most of the excitons have nonvanishing momenta, and the radiative recombination lifetime is ∼1 ns [42,43]. For these systems, defect-assisted recombination therefore becomes an important mechanism with a characteristic lifetime of 2–5 ps [43,47,48]. Exciton-exciton annihilations become important only when the density of excitons in a sample is large; equivalently when the average distance between excitons is small. At a density of 1×10^{12} cm^{-2}, the effective lifetime from annihilation is on the order of 10 ps [44].

The calculations performed here indicate that for field strengths larger than 0.1 V/nm, the dissociation lifetime is shorter than 1 ps in all the systems considered. A potential gradient of this size (0.1 V/nm) over the extent of the exciton (around 2 nm) is realistic to achieve close to the metal-MoS_2 contact region where charge transfer and interface dipole formation driven by Fermi-level mismatch can lead to significant variation of the potential and band energies even in the absence of an applied bias voltage. Under such conditions, the field-induced dissociation is faster than any other decay channel and should therefore dominate as indicated by the fact that in Fig. 3, the data points all lie above the shaded region.

To summarize we have used complex scaling to compute the lifetime of excitons in two-dimensional MoS_2 and MoS_2/hBN structures under an applied static electric field. The exciton was simulated using a 2D Mott-Wannier model which has previously been found to yield a reliable description of the lowest-lying excitonic states in transition-metal dichalcogenides. We found that for field strengths around 0.1 V/nm, the exciton dissociation is larger than the intrinsic exciton decay rate in MoS_2. Moreover, encapsulation in a few layers of *h*BN was found to increase the dissociation rate by an order of magnitude for fixed field strength due to the increased screening provided by the electrons in the *h*BN.

The authors gratefully acknowledge financial support from the Center for Nanostructured Graphene (Project No. DNRF103) financed by the Danish National Research Foundation.

[1] Q. H. Wang, K. Kalantar-Zadeh, A. Kis, J. N. Coleman, and M. S. Strano, Nat. Nanotechnol. **7**, 699 (2012).
[2] K. F. Mak, C. Lee, J. Hone, J. Shan, and T. F. Heinz, Phys. Rev. Lett. **105**, 136805 (2010).
[3] A. Splendiani, L. Sun, Y. Zhang, T. Li, J. Kim, C.-Y. Chim, G. Galli, and F. Wang, Nano Lett. **10**, 1271 (2010).
[4] A. Ramasubramaniam, Phys. Rev. B **86**, 115409 (2012).
[5] D. Y. Qiu, F. H. da Jornada, and S. G. Louie, Phys. Rev. Lett. **111**, 216805 (2013).
[6] M. M. Ugeda, A. J. Bradley, S.-F. Shi, H. Felipe, Y. Zhang, D. Y. Qiu, W. Ruan, S.-K. Mo, Z. Hussain, Z.-X. Shen *et al.*, Nat. Mater. **13** 1091 (2014).
[7] K. He, N. Kumar, L. Zhao, Z. Wang, K. F. Mak, H. Zhao, and J. Shan, Phys. Rev. Lett. **113**, 026803 (2014).
[8] D. Jariwala, V. K. Sangwan, L. J. Lauhon, T. J. Marks, and M. C. Hersam, ACS Nano **8**, 1102 (2014).
[9] M. Bernardi, M. Palummo, and J. C. Grossman, Nano Lett. **13**, 3664 (2013).
[10] O. Lopez-Sanchez, D. Lembke, M. Kayci, A. Radenovic, and A. Kis, Nat. Nanotechnol. **8**, 497 (2013).
[11] J. S. Ross, P. Klement, A. M. Jones, N. J. Ghimire, J. Yan, D. Mandrus, T. Taniguchi, K. Watanabe, K. Kitamura, W. Yao *et al.*, Nat. Nanotechnol. **9**, 268 (2014).
[12] A. Pospischil, M. M. Furchi, and T. Mueller, Nat. Nanotechnol, **9**, 257 (2014).
[13] K. F. Mak, K. He, C. Lee, G. H. Lee, J. Hone, T. F. Heinz, and J. Shan, Nature Mater. **12**, 207 (2013).
[14] A. Chernikov, T. C. Berkelbach, H. M. Hill, A. Rigosi, Y. Li, O. B. Aslan, D. R. Reichman, M. S. Hybertsen, and T. F. Heinz, Phys. Rev. Lett. **113**, 076802 (2014).
[15] S. Latini, T. Olsen, and K. S. Thygesen, Phys. Rev. B **92**, 245123 (2015).
[16] T. C. Berkelbach, M. S. Hybertsen, and D. R. Reichman, Phys. Rev. B **88**, 045318 (2013).
[17] P. Cudazzo, C. Attaccalite, I. V. Tokatly, and A. Rubio, Phys. Rev. Lett. **104**, 226804 (2010).
[18] P. Cudazzo, I. V. Tokatly, and A. Rubio, Phys. Rev. B **84**, 085406 (2011).
[19] O. Pulci, P. Gori, M. Marsili, V. Garbuio, R. Del Sole, and F. Bechstedt, Europhys. Lett. **98**, 37004 (2012).
[20] M. M. Fogler, L. V. Butov, and K. S. Novoselov, Nat. Commun. **5**, 4555 (2014).
[21] A. R. Klots, A. K. M. Newaz, B. Wang, D. Prasai, H. Krzyzanowska, J. Lin, D. Caudel, N. J. Ghimire, J. Yan, B. L. Ivanov, K. A. Velizhanin, A. Burger, D. G. Mandrus, N. H. Tolk, S. T. Pantelides, and K. I. Bolotin, Sci. Rep. **4** 6608 (2014).
[22] H. Terrones, F. López-Urías, and M. Terrones, Sci. Rep. **3** 1549 (2013).
[23] L. Britnell, R. Ribeiro, A. Eckmann, R. Jalil, B. Belle, A. Mishchenko, Y.-J. Kim, R. Gorbachev, T. Georgiou, S. Morozov *et al.*, Science **340**, 1311 (2013).
[24] A. Geim and I. Grigorieva, Nature (London) **499**, 419 (2013).
[25] G. Strinati, Phys. Rev. B **29**, 5718 (1984).
[26] G. Onida, L. Reining, and A. Rubio, Rev. Mod. Phys. **74**, 601 (2002).
[27] V. Perebeinos and P. Avouris, Nano Lett. **7**, 609 (2007).
[28] T. Olsen, S. Latini, F. Rasmussen, and K. S. Thygesen, Phys. Rev. Lett. **116**, 056401 (2016).
[29] K. Andersen, S. Latini, and K. S. Thygesen, Nano Lett. **15**, 4616 (2015).
[30] L. V. Keldysh, J. Exp. Theor. Phys. **33**, 994 (1957).
[31] W. Franz, Z. Naturforschung A **13a**, 484 (1958).
[32] B. Simon, Int. J. Quantum Chem. **14**, 529 (1978).
[33] J. Taylor, *Scattering Theory : The Quantum Theory on Nonrelativistic Collisions* (Wiley, New York, 1972), p. 477.
[34] E. Balslev and J. M. Combes, Commun. Math. Phys. **22**, 280 (1971).
[35] J. Aguilar and J. M. Combes, Commun. Math. Phys. **22**, 269 (1971).
[36] N. Hatano, K. Sasada, H. Nakamura, and T. Petrosky, Prog. Theor. Phys. **119**, 187 (2008).
[37] W. P. Reinhardt, Annu. Rev. Phys. Chem. **33**, 223 (1982).
[38] B. Simon, Ann. Math. **97**, 247 (1973).
[39] I. W. Herbst and B. Simon, Phys. Rev. Lett. **41**, 1759 (1978).
[40] J. J. Mortensen, L. B. Hansen, and K. W. Jacobsen, Phys. Rev. B **71**, 035109 (2005).
[41] J. Enkovaara, C. Rostgaard, J. J. Mortensen, J. Chen, M. Dulak, L. Ferrighi, J. Gavnholt, C. Glinsvad, V. Haikola, H. A. Hansen *et al.*, J. Phys.: Condens. Matter **22**, 253202 (2010).
[42] M. Palummo, M. Bernardi, and J. C. Grossman, Nano Lett. **15**, 2794 (2015).
[43] H. Shi, R. Yan, S. Bertolazzi, J. Brivio, B. Gao, A. Kis, D. Jena, H. G. Xing, and L. Huang, ACS Nano **7**, 1072 (2013).
[44] D. Sun, Y. Rao, G. A. Reider, G. Chen, Y. You, L. Brézin, A. R. Harutyunyan, and T. F. Heinz, Nano Lett. **14**, 5625 (2014).
[45] H. Wang, C. Zhang, W. Chan, C. Manolatou, S. Tiwari, and F. Rana, Phys. Rev. B **93**, 045407 (2016).
[46] C. Poellmann, P. Steinleitner, U. Leierseder, P. Nagler, G. Plechinger, M. Porer, R. Bratschitsch, C. Schueller, T. Korn, and R. Huber, Nature Mater. **14**, 889 (2015).
[47] T. Korn, S. Heydrich, M. Hirmer, J. Schmutzler, and C. Schüller, Appl. Phys. Lett. **99**, 102109 (2011).
[48] D. Lagarde, L. Bouet, X. Marie, C. R. Zhu, B. L. Liu, T. Amand, P. H. Tan, and B. Urbaszek, Phys. Rev. Lett. **112**, 047401 (2014).

Paper VI

Exciton ionization in multilayer transition-metal dichalcogenides
Thomas G. Pedersen, Simone Latini, Kristian S. Thygesen, Héctor Mera, Branislav K. Nikolić, *New Journal of Physics*, **18** (7), pp 073043 (2016).

New Journal of Physics
The open access journal at the forefront of physics

Deutsche Physikalische Gesellschaft DPG
IOP Institute of Physics

Published in partnership with: Deutsche Physikalische Gesellschaft and the Institute of Physics

PAPER

Exciton ionization in multilayer transition-metal dichalcogenides

Thomas Garm Pedersen[1], **Simone Latini**[2], **Kristian S Thygesen**[2], **Héctor Mera**[3] **and Branislav K Nikolić**[3]

[1] Center for Nanostructured Graphene (CNG) and Department of Physics and Nanotechnology, Aalborg University, DK-9220 Aalborg Øst, Denmark
[2] Center for Nanostructured Graphene (CNG) and Center for Atomic-scale Materials Design (CAMD), Department of Physics, Technical University of Denmark, DK-2800 Kongens Lyngby, Denmark
[3] Department of Physics and Astronomy, University of Delaware, Newark, DE 19716-2570, USA

E-mail: tgp@nano.aau.dk

Keywords: transition-metal dichalcogenides, exciton ionization, mott-wannier excitons

OPEN ACCESS

RECEIVED
22 April 2016

REVISED
30 June 2016

ACCEPTED FOR PUBLICATION
8 July 2016

PUBLISHED
25 July 2016

Abstract

Photodetectors and solar cells based on materials with strongly bound excitons rely crucially on field-assisted exciton ionization. We study the ionization process in multilayer transition-metal dichalcogenides (TMDs) within the Mott-Wannier model incorporating fully the pronounced anisotropy of these materials. Using complex scaling, we show that the field-dependence of the ionization process is strongly dependent on orientation. Also, we find that direct and indirect excitons behave qualitatively differently as a result of opposite effective anisotropy of these states. Based on first-principles material parameters, an analysis of several important TMDs reveals WSe_2 and $MoSe_2$ to be superior for applications relying on ionization of direct and indirect excitons, respectively.

1. Introduction

Transition-metal dichalcogenides (TMDs) including MoS_2, $MoSe_2$, WS_2, and WSe_2 are layered two-dimensional semiconductors with unique electronic and optical properties. They are highly promising for optoelectronic applications such as photodetectors [1–5], solar cells [6, 7], and light emitting diodes [8]. In their monolayer form, MoS_2, $MoSe_2$, WS_2, and WSe_2 are direct bandgap semiconductors. Importantly, the low dimensionality and reduced screening leads to highly prominent exciton effects with binding energies of several hundred meVs [9, 10]. Such excitons greatly modify both linear [11] and nonlinear [12] optical properties. Regarding applications, exciton binding energies significantly larger than the thermal energy at room temperature (~25 meV) increase radiative electron-hole recombination and are, therefore, beneficial for efficient light emission. In contrast, strongly bound excitons may reduce the efficiency of photodetectors and solar cells because these devices require exciton ionization in order to separate electrons and holes. The first monolayer TMD-based photodetectors showed relatively low efficiencies [1]. By improving material quality and thereby increasing carrier mobility, the responsivity was subsequently greatly improved [2, 4]. These devices all operated in the parallel collection mode, in which an in-plane bias between metal contacts drives the current along the monolayer. Recently, devices based on perpendicular collection, i.e. transport between layers, have emerged as promising alternatives. In particular, both efficient and ultrafast photoresponse has been demonstrated for MoS_2 [3] and WSe_2 [5] photodetectors. Importantly, this approach allows for devices based on stacking of appropriate two-dimensional materials. Thus, contacts for carrier collection can be fabricated by encapsulation of the photoactive semiconductor between conducting graphene sheets [3, 5].

The highly promising characteristics demonstrated in [3, 5] were obtained for multilayer samples having thicknesses of 50 nm [3] and between 2.2 and 40 nm [5], respectively. In such samples, electron and holes are delocalized across several layers and, moreover, screening is increased compared to monolayers. Hence, in slabs thicker than the bulk exciton Bohr radius, the exciton binding energy is significantly reduced. This is expected to contribute to the high sensitivity and response rate observed experimentally. The limiting factors for the rate are poorly understood, however. In [5], the response rate was shown to increase approximately linearly with bias voltage between the graphene contacts while an inverse quadratic dependence on sample thickness was found.

This suggests that out-of-plane drift is the limiting factor for the rate [5]. It is clear, however, that a full description of the response involves several physical mechanisms. In fact, the photoresponse itself is a combined process consisting of (i) exciton creation upon photon absorption, (ii) field-assisted ionization of the exciton, (iii) transport of dissociated carriers, and (iv) collection at the contacts. Hence, the applied bias performs a two-fold function of driving both exciton ionization and carrier transport.

The process of exciton ionization is a crucial step in the photoresponse. In materials with strongly bound excitons, such as TMDs, thermal ionization is inefficient and a strong external electric field is required for efficient carrier separation. As an estimate, the required field strength for efficient dissociation is given by the ratio between exciton binding energy and Bohr radius. A full description of the ionization process is needed, however, to model the dependence of the ionization rate on field strength. Moreover, in anisotropic materials, the ionization rate will depend on the direction of the applied field. In the present paper, we study the exciton ionization process in anisotropic TMDs using a modified Mott-Wannier [13] approach incorporating the material anisotropy. In this approach, bulk dielectric constants and effective masses lead to an exciton eigenvalue problem that is mathematically identical to that of a hydrogen atom embedded in an anisotropic material. The material constants are calculated from first-principles density-functional theory. To describe field-assisted ionization, an electric field is added to the Mott-Wannier equation. We apply the complex scaling technique [14] and hypergeometric resummation [15, 16] to compute ionization rates and Stark shifts of excitons in typical TMDs. These are highly non-perturbative phenomena. In particular, the ionization rate cannot be described using a finite-order perturbation expansion [14]. Our work is related to a recent work [17], in which the second-order Stark shift in phosphorene was studied. This two-dimensional material has strong in-plane anisotropy. Also, in TMDs, the optical Stark effect, i.e. non-perturbative effects of strong laser excitation, has been demonstrated [18, 19]. In addition, a recent study by some of the present authors has described exciton dissociation in monolayer MoS_2, demonstrating a pronounced dependence on screening by the surroundings [20]. Very recently [21], experimental Stark shifts due to static perpendicular fields in MoS_2 multilayers with thicknesses between one and five layers were reported. The weak thickness dependence of the observed shift clearly indicates that exciton effects are important. So far, however, exciton ionization due to static fields in multilayer TMDs has not been discussed in any quantitative theoretical work.

2. Anisotropic exciton model

In a truly two-dimensional material, the nonlocal wave vector dependence of the dielectric constant is important for a correct description of screening [10]. In a three-dimensional material, however, dispersion is much less pronounced and the dielectric constant can be assumed independent of wave vector, i.e. approximated by the long-range limit $\varepsilon(\vec{q} \to 0)$ [22]. In uniaxially anisotropic three-dimensional materials such as multilayer TMDs, the dielectric constant is then given by a constant tensor $\overleftrightarrow{\varepsilon} = \mathrm{diag}(\varepsilon_x, \varepsilon_x, \varepsilon_z)$ with separate elements for the out-of-plane (z-axis) and in-plane (x-axis) values. Similarly, the effective masses for these directions differ. For direct excitons, electrons and holes are located at the K point. For indirect excitons, holes reside at the Γ point whereas electrons are located at the conduction band minimum Σ roughly midway between Γ and K. In fact, the in-plane effective mass depends on rotation angle in the (x, y) plane. This relatively weak in-plane dependence will be ignored, however. Thus, below we take the effective hole masses computed for the $K \to M$ and $\Gamma \to M$ directions for direct and indirect excitons, respectively. For electrons, the corresponding directions are $K \to M$ and $\Sigma \to M$, respectively. The out-of-plane effective masses are determined from the dispersion along the perpendicular lines passing through the band extrema. For the conduction band, the electron (e) effective mass tensor in then of the diagonal form $\overleftrightarrow{m}^{(e)} = \mathrm{diag}(m_x^{(e)}, m_x^{(e)}, m_z^{(e)})$, and similarly for holes (h) in the valence band. Moreover, the reduced mass tensor for the electron-hole pair is $\overleftrightarrow{m} = \mathrm{diag}(m_x, m_x, m_z)$ with $m_i = m_i^{(e)} m_i^{(h)} / (m_i^{(e)} + m_i^{(h)})$. Introducing the relative-motion coordinate $\vec{r}_{eh} = \vec{r}_e - \vec{r}_h$ of the electron hole pair, the Mott-Wannier problem for excitons in the presence of an electric field $\vec{F}$ is of the form

$$\left\{ -\frac{\hbar^2}{2m_x}\left(\frac{\mathrm{d}^2}{\mathrm{d}x_{eh}^2} + \frac{\mathrm{d}^2}{\mathrm{d}y_{eh}^2}\right) - \frac{\hbar^2}{2m_z}\frac{\mathrm{d}^2}{\mathrm{d}z_{eh}^2} - V(\vec{r}_{eh}) + e\vec{F}\cdot\vec{r}_{eh} \right\}\psi = E_{eh}\psi, \tag{1}$$

with the anisotropically screened electron-hole attraction [23, 24]

$$V(\vec{r}_{eh}) = \frac{e^2}{4\pi\varepsilon_0\sqrt{\varepsilon_x\varepsilon_z}\,(x_{eh}^2 + y_{eh}^2 + (\varepsilon_x/\varepsilon_z)z_{eh}^2)^{1/2}}. \tag{2}$$

It is convenient to scale distances according to anisotropic Bohr radii $a_x^* = (m_0/m_x)\sqrt{\varepsilon_x\varepsilon_z}\,a_0$ and $a_z^* = (m_0/\sqrt{m_x m_z})\sqrt{\varepsilon_x\varepsilon_z}\,a_0$ for the x- and z-directions, respectively, with m_0 the free electron mass and $a_0 = 4\pi\varepsilon_0\hbar^2/(m_0 e^2)$ the hydrogen Bohr radius. Similarly, we introduce the effective exciton Hartree energy

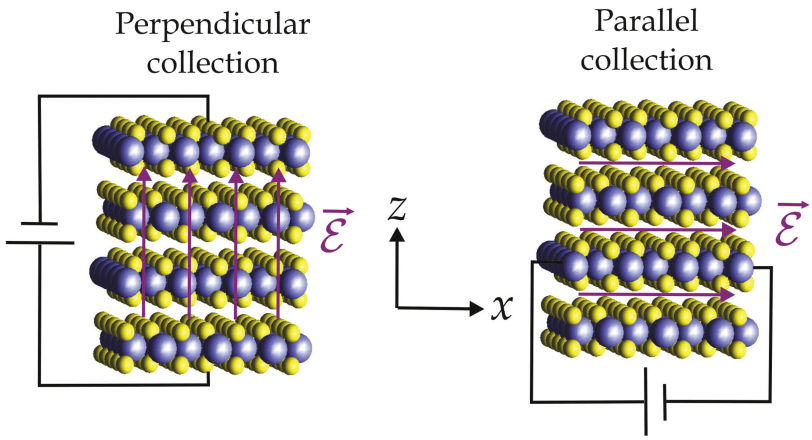

Figure 1. Schematic illustration of the collection modes for different field orientations.

Ha*=$m_x/(m_0\varepsilon_x\varepsilon_z)$Ha with Ha $=\hbar^2/(m_0a_0^2)$ the atomic Hartree. In these units, i.e. writing $\vec{r}_{eh}=(a_x^*x,\ a_x^*y,\ a_z^*z)$ and $E_{eh}=$ Ha*E, equation (1) becomes

$$\left\{-\frac{1}{2}\nabla^2-\frac{1}{(r^2-\kappa z^2)^{1/2}}+\vec{\mathcal{E}}\cdot\vec{r}\right\}\psi=E\psi \tag{3}$$

with the anisotropy parameter $\kappa=1-\varepsilon_x m_x/\varepsilon_z m_z$. We note that the electric field $\vec{\mathcal{E}}$ is now given in effective units so that $\vec{F}=\mathcal{E}_0(\mathcal{F}_x\mathcal{E}_x,\ \mathcal{F}_x\mathcal{E}_y,\ \mathcal{F}_z\mathcal{E}_z)$ with $\mathcal{E}_0=\mathrm{Ha}/ea_0=5.14\cdot10^{11}$ V m^{-1} the characteristic field strength in atomic units and the anisotropic field scaling factors given by

$$\mathcal{F}_z=\frac{m_x^{3/2}m_z^{1/2}}{m_0^2(\varepsilon_x\varepsilon_z)^{3/2}},\qquad \mathcal{F}_x=\frac{m_x^2}{m_0^2(\varepsilon_x\varepsilon_z)^{3/2}}. \tag{4}$$

As illustrated in figure 1, these scaling factors are the appropriate ones for the cases of perpendicular collection ($\vec{\mathcal{E}}$ along z) and parallel collection ($\vec{\mathcal{E}}$ along x), respectively.

In the effective exciton units, the consequences of anisotropy are entirely governed by the single parameter κ. Hence, if $\kappa=0$, the material is effectively isotropic. In contrast, $\kappa>0$ means that, in scaled coordinates, the Coulomb attraction is less sensitive to the z coordinate. In fact, as κ approaches unity, the z-dependence of the interaction vanishes. Hence, for $\kappa>0$ excitons will tend to delocalize perpendicular to the layers. If $\kappa<0$, delocalization within individual layers is enhanced. These trends are illustrated by the schematic insets in figure 2. We stress that this picture is only valid in scaled coordinates. As shown below, the sign of κ differs for direct and indirect excitons. Hence, the large effective masses for the z-direction for direct excitons mean that $\kappa>0$ for these states in TMDs. In contrast, indirect excitons have nearly isotropic effective masses and it is mainly the dielectric constants that lead to anisotropy. The fact that $\varepsilon_x>\varepsilon_z$ consequently means that $\kappa<0$ for indirect excitons.

To solve the eigenvalue problem, we introduce cylindrical polar coordinates $\{\rho,\ \theta,\ z\}$ and expand in a Laguerre-type basis

$$\psi(\rho,\ \theta,\ z)=\sum_{m=0}^{M}\sum_{n=0}^{N}\sum_{l=0}^{L}R_{ml}(\rho)\cos l\theta\,\{c_{mnl}^{(s)}\varphi_{ns}(z)+c_{mnl}^{(p)}\varphi_{np}(z)\} \tag{5}$$

with $\varphi_{ns}(z)=L_n(k\,|z|)\mathrm{e}^{-k|z|/2}$, $\varphi_{np}(z)=zL_n^1(k\,|z|)\mathrm{e}^{-k|z|/2}$, and $R_{ml}(\rho)=\rho^l\mathrm{e}^{-q\rho/2}L_m^{2l}(q\rho)$. The parameters k and q can be optimized to minimize the exciton ground state energy. We find however, that $k=q=2$ is very nearly the optimal choice in all cases. For $\vec{\mathcal{E}}=\mathcal{E}\hat{z}$, cylindrical symmetry is preserved around the z-direction and for the exciton ground state $L=0$ is sufficient in the expansion above. On the other hand, for $\vec{\mathcal{E}}=\mathcal{E}\hat{x}$, the symmetry is broken and we use an expansion limited by $L=5$. In this case, however, inversion symmetry *along* z is maintained and $c_{mnl}^{(p)}=0$. In the former case, we include 30 basis states for both ρ and z dependencies, i.e. $M=N=29$. Similarly, for $\vec{\mathcal{E}}=\mathcal{E}\hat{x}$, we take $M=N=19$. Hence, the size of the basis is 1800 and 2400 for the two cases, respectively.

In the limits $\kappa=0$ and $\kappa=1$, the Wannier equation describes three-dimensional and two-dimensional excitons, respectively. We note, however, that for $\kappa=1$ the exciton state is actually completely delocalized along

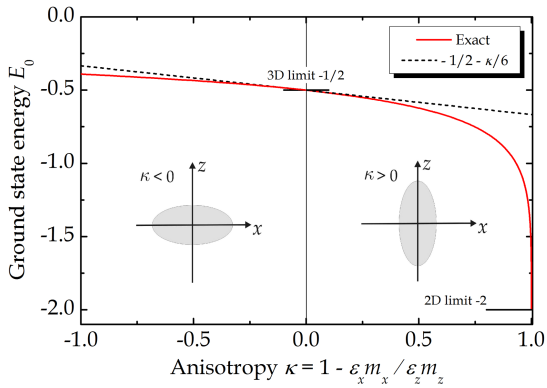

Figure 2. Exciton ground state energy versus anisotropy. The horizontal black lines indicate the limiting values and the dashed line is the first order perturbation result. The insets illustrate exciton delocalization for different signs of the effective anisotropy.

the z-direction and the 2D behavior pertains to the in-plane character only. This follows from the behavior of the potential $(r^2 - \kappa z^2)^{-1/2} \to (x^2 + y^2)^{-1/2}$ as the limit $\kappa = 1$ is approached. Hence, the in-plane and out-of-plane motions decouple completely leading to delocalization along z. The 2D character of the exciton in this limit is, however, rather different from excitons in monolayer TMDs because of differences in screening, which has a pronounced nonlocal wave vector dependence for monolayers, as discussed above. In figure 2, we show the binding energy E_0 of the ground state as a function of the anisotropy. As expected, the limits for $\kappa = 0$ and $\kappa = 1$ are $E_0 = -1/2$ and $E_0 = -2$, respectively. Importantly, though, for $\kappa = 1$ the ground state is, in fact, the lower limit of a continuum reflecting the delocalized z-dependence. In contrast, the state is fully localized for $\kappa = 0$. In figure 2, we also include the perturbation result valid for small κ, i.e. for materials that are only weakly anisotropic, see appendix and [25].

3. Exciton ionization

As mentioned above, field-ionization is a non-perturbative phenomenon that is not captured in any finite-order perturbation expansion in field strength. In the presence of the field, the bound state energies turn into complex resonances. Writing $E(\mathcal{E}) = \Delta - \mathrm{i}\Gamma/2$ we may decompose such complex eigenvalues into their real and imaginary parts. The interpretation is then that the real part Δ represents the Stark energy whereas the imaginary part provides the ionization rate Γ. This rate can be understood as the rate of tunneling from the bound state into the dissociated state. There are two commonly sought routes to obtaining Γ, both of which we will pursue below. The first is the purely numerical approach of complex scaling [14, 20] that immediately provides both real and imaginary parts of the resonance. Alternatively, a semi-analytical result can be obtained through analytical continuation and resummation of a low-order perturbation series [15, 16, 26].

In a direct bandgap material, the excitation and ionization processes are conceptually simple. Hence, for excitation by photon energies close to the fundamental exciton, the initial excitation quickly relaxes to the lowest direct exciton. From here, the state then either recombines (radiatively or non-radiatively) or becomes ionized. In contrast, an indirect bandgap material is more complicated. Assuming again excitation by low energy photons and ignoring phonon-assisted processes, the initial excitation is the direct exciton as the transition to the indirect one is optically forbidden by momentum conservation. Hence, if ionization happens sufficiently rapidly, the dissociating species is still the direct exciton. Conversely, ionization after thermal relaxation to the indirect exciton means that this species is the relevant one. It follows that a rapid ionization rate, i.e. ionization in a strong field, pertains to the direct exciton. Slow ionization in weak fields, on the other hand, will predominantly happen from the indirect exciton. In the present work, we will study ionization of both species. As our focus is on strong field ionization, however, we will mainly illustrate results relevant for direct excitons, i.e. the $\kappa > 0$ regime.

If a weak electric field is applied, the resonance is approximately $E_{x,z}(\mathcal{E}) \approx E_0 + E^{(2)}_{x,z}\mathcal{E}^2$, where subscripts x and z indicate parallel and perpendicular collection, respectively. The coefficient of the second order term determines the exciton polarizability $\alpha_{x,z}$ through $E^{(2)}_{x,z} = -\frac{1}{2}\alpha_{x,z}$. More generally, if a perturbation expansion in the electric field is applied, the ground state energy is written $E_{x,z}(\mathcal{E}) = \sum_{n=0}^{\infty} E^{(2n)}_{x,z}\mathcal{E}^{2n}$. Only even powers of the electric field appear due to inversion symmetry of the unperturbed system in the Mott-Wannier model. The zeroth order term $E^{(0)}_{x,z} = E_0$ is the unperturbed ground state energy and obviously independent of field

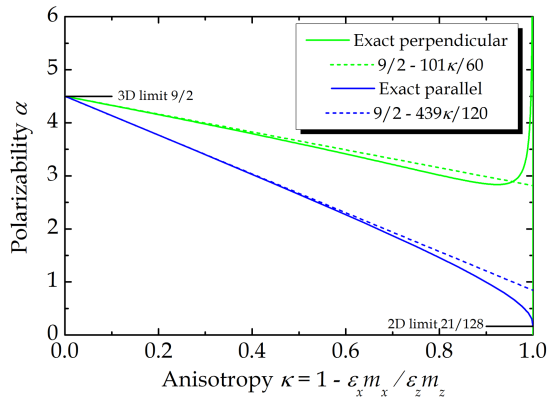

Figure 3. Exact numerical polarizabilities (solid lines) and linearized approximations (dashed lines) for perpendicular (green) and parallel (blue) collection modes.

direction. Using a finite-field approach, we solve the Wannier equation equation (3) in the presence of a small electric field of magnitude $\mathcal{E} = 10^{-3}$ applying the localized bases introduced above. By subtracting the field-free ground state energy, we obtain the direct exciton ($\kappa > 0$) polarizabilities shown in figure 3. As shown in the figure, the behavior for highly anisotropic materials is strongly dependent on the direction of the applied field. The two curves start from a common value of $9/2$ in agreement with the exact value for the hydrogen atom [27, 28]. For values of κ approaching unity, however, their behaviors are markedly different. Thus, in the perpendicular case, the polarizability diverges reflecting the completely delocalized state along the z-direction. In contrast, in the parallel case, the polarizability remains finite and eventually reaches a value of $21/128 \approx 0.1641$ in the 2D limit [29]. Again, in the plot, we include the approximate results found by linearizing in κ as derived in the appendix, i.e. $\alpha_x \approx 9/2 - 439\kappa/120$ and $\alpha_z \approx 9/2 - 101\kappa/60$. It is seen that these describe the exact behavior surprisingly well even for anisotropies as large as $\kappa \sim 0.8$. By solving for several distinct (small) field strengths, the finite-field approach can be extended to provide higher order terms in the field expansion. In this way it can be shown that linearization in κ remains reasonably accurate for higher order terms as well.

In fact, the full asymptotic series $\sum_{n=0}^{\infty} E_{x,z}^{(2n)} \mathcal{E}^{2n}$ is highly divergent for all finite values of the field strength. However, by appropriate resummation of a finite series, physically meaningful quantities can be obtained from it. Traditionally, Padé approximants have been applied to this end [26]. These typically require partial expansions of high order to be successful. We have recently shown [15, 16] that hypergeometric resummation provides a very efficient alternative. Here, only the first five non-vanishing terms $0 \leqslant n \leqslant 4$ of the expansion are needed to find a highly accurate result. We have previously applied this result to the three-dimensional [15] and low-dimensional [16] hydrogen problems, which are mathematically very similar to the Wannier problem considered here. In the appendix, the required series are provided for both collection modes and below we demonstrate how these may be used to accurately describe both Stark energy and exciton ionization.

The complex scaling method [14] is based on a coordinate scaling $\vec{r} \rightarrow \vec{r}\mathrm{e}^{\varphi}$. By analytically continuing into the complex plane, the parameter φ can be taken purely imaginary, i.e. $\varphi = \mathrm{i}\theta$ with θ real. In turn, the complex scaled Wannier equation reads as

$$\left\{-\frac{\mathrm{e}^{-2\mathrm{i}\theta}}{2}\nabla^2 - \frac{\mathrm{e}^{-\mathrm{i}\theta}}{(r^2 - \kappa z^2)^{1/2}} + \mathrm{e}^{\mathrm{i}\theta}\vec{\mathcal{E}} \cdot \vec{r}\right\}\psi = E\psi. \tag{6}$$

For finite field and rotation angle θ, the eigenstates are square integrable and the eigenvalues complex, as explained above. In fact [14], the eigenvalue is independent of the value of θ as long as a finite value is adopted. In practise, a small θ-dependence is observed whenever expansion in a finite basis is applied. We have found, however, that this dependence is negligible if bases of the sizes discussed above are used. Below, all results will be for $\theta = 0.4$.

In figure 4, the solid lines show the complex scaling results for four values of the anisotropy ranging from none ($\kappa = 0$) to substantial ($\kappa = -1.0$ and $\kappa = 0.8$). Moreover, both collection modes are analyzed. At vanishing field strength, the Stark energy, i.e. the real part of the resonance, agrees with the results in figure 2. As the field is increased, the energy initially decreases quadratically with a prefactor given by the polarizability in figure 3. However, beyond a field strength of approximately $\mathcal{E} \sim 0.1$, a significantly softer behavior is found. At a

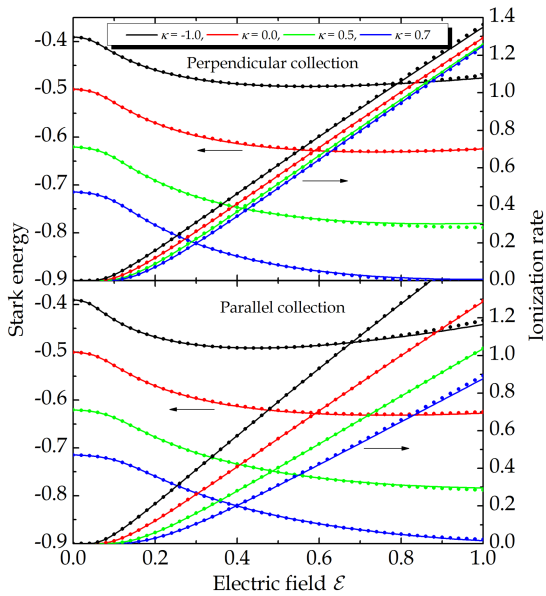

Figure 4. Exciton Stark energy (left axes) and ionization rate (right axes) for two orientations of the electric field. Both complex scaling (solid lines) and hypergeometric resummation results (dots) are shown.

similar field strength, the ionization rate increases dramatically before becoming approximately linear in the field. In weak fields, the ionization rate is dominated by an exponential $\Gamma \sim \exp(-c/\mathcal{E})$ behavior. All of these features agree with the analogous findings for atomic hydrogen [15]. It is observed that increased anisotropy leads to reduced ionization, mainly as a result of the increased exciton binding energy. Moreover, in the perpendicular collection mode, the ionization rate in relatively large fields is only weakly sensitive to the anisotropy, i.e. all curves share roughly the same slope. In contrast, for the parallel case, the slope decreases markedly as κ is increased. This difference relates to the delocalization behavior of the states as shown in the insets of figure 2. Thus, as κ increases, the states become increasingly delocalized in the perpendicular direction. This, taken by itself, increases ionization in a perpendicular field but not in a parallel one. Hence, delocalization partially counteracts the increased exciton binding for the perpendicular collection mode.

The complex scaling results are based on diagonalization of relatively large matrices on a fine grid of electric field strengths. Such a fine grid is required in order to track the evolution of a particular state as the field is increased. This approach is therefore computationally demanding and it is of interest to compare with the much simpler hypergeometric resummation approach. As explained above, the method takes the first five terms in the asymptotic expansion of the field dependence as input. In the appendix, the required expansions are provided. We apply these within the hypergeometric resummation approach used in [16] and thereby obtain Stark energies and ionization rates at practically no computational cost. These are shown by the dots in figure 4. For vanishing anisotropy, the agreement is essentially perfect, as expected [15, 16]. Remarkably, however, the agreement is excellent even for large values of $|\kappa|$. This demonstrates the power of the hypergeometric resummation approach. We stress that, using the series provided in the appendix, accurate calculation of resonances for any given material (within the class studied here) can be made at a fraction of the computational cost compared to the full complex scaling.

4. Application to TMDs

To convert any result of the Wannier approach to physical quantities we require specific values of the anisotropic dielectric constants and effective masses. To this end, we have performed first-principles calculations for the important TMDs MoS_2, $MoSe_2$, WS_2, and WSe_2 using the Random Phase Approximation and including spin–orbit interaction. All calculations were performed with the projector augmented wave electronic structure code GPAW [30, 31] and include local-field effects in the dielectric response. Full details on the calculations can be found in [32]. The first-principles results for direct and indirect excitons are listed in table 1 and 2, respectively.

Table 1. Material parameters for direct excitons in TMDs.

Mat.	m_x/m_0	m_z/m_0	ε_x	ε_z	κ	Ha*	E_0	$\mathcal{F}_x$	$\mathcal{F}_z$
MoS_2	0.293	3.096	13.24	5.61	0.777	107 meV	−83 meV	$1.3\,10^{-4}$	$4.4\,10^{-4}$
WS_2	0.184	1.997	12.49	5.87	0.804	68 meV	−54 meV	$5.4\,10^{-5}$	$1.8\,10^{-4}$
$MoSe_2$	0.333	1.573	15.06	7.62	0.582	79 meV	−52 meV	$9.0\,10^{-5}$	$2.0\,10^{-4}$
WSe_2	0.198	1.198	13.80	7.07	0.677	55 meV	−39 meV	$4.1\,10^{-5}$	$1.0\,10^{-4}$

Table 2. Material parameters for indirect excitons in TMDs.

Mat.	m_x/m_0	m_z/m_0	ε_x	ε_z	κ	Ha*	E_0	$\mathcal{F}_x$	$\mathcal{F}_z$
MoS_2	0.355	0.364	13.24	5.61	−1.302	130 meV	−48 meV	$2.0\,10^{-4}$	$2.0\,10^{-4}$
WS_2	0.295	0.340	12.49	5.87	−0.827	108 meV	−44 meV	$1.4\,10^{-4}$	$1.5\,10^{-4}$
$MoSe_2$	0.404	0.394	15.06	7.62	−1.027	96 meV	−37 meV	$1.3\,10^{-4}$	$1.3\,10^{-4}$
WSe_2	0.387	0.373	13.80	7.07	−1.025	108 meV	−42 meV	$1.6\,10^{-4}$	$1.5\,10^{-4}$

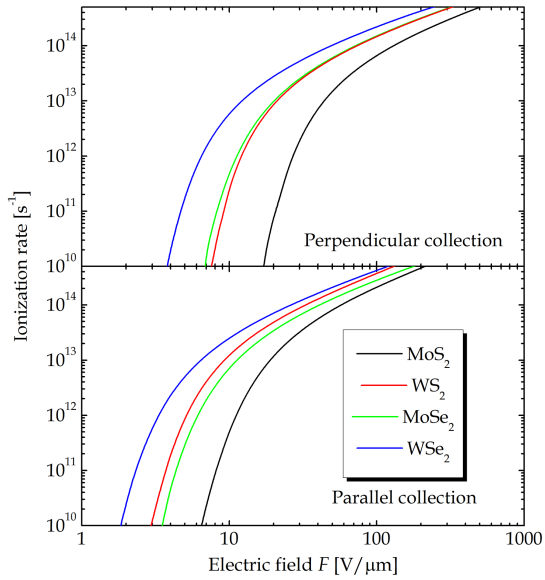

Figure 5. Direct exciton ionization rates converted into physical units for different TMDs. The upper and lower panels are for perpendicular and parallel collection, respectively.

For direct excitons, the anisotropy manifests itself in highly different out-of-plane and in-plane effective masses. As seen in table 1, these masses differ by nearly an order on magnitude. Similarly, the out-of-plane dielectric constants are less than half the in-plane values. For both sulphides MoS_2 and WS_2, these values translate into an anisotropy of $\kappa \approx 0.8$. Thus, even if the two materials are obviously dissimilar, their effective anisotropy is essentially the same. The dissimilarity reveals itself in the field scaling factors, however, which are about twice as large in MoS_2 as in WS_2 as a result of the much larger effective masses of the former. This means that any normalized field strength in figure 4 translates into a much smaller physical field in WS_2 relative to MoS_2. An approximately similar ratio is found for the field scaling of $MoSe_2$ relative to WSe_2. To complete the conversion and translate the ionization rate Γ into physical units, the frequency scale $\mathrm{Ha}^*/\hbar$ is applied. The converted results for direct and indirect excitons obtained from this procedure are shown in figures 5 and 6, respectively.

In the effective exciton units, a field of unity magnitude corresponds to a physical field of $F_{x,z} = \mathcal{F}_{x,z}\mathcal{E}_0 = \mathrm{Ha}^*/a^*_{x,z}$, i.e. the ratio between effective Hartree and Bohr radius for the particular field direction. From tables 1 and 2 it is seen that the direct and indirect exciton binding energies constitute about 75% and 40% of Ha*, respectively. Hence, estimating the field strength required for efficient ionization as $|E_0|/a^*_{x,z}$ is equivalent to unity field strength $\mathcal{E} \sim 1$ in exciton units within a factor of approximately two. From

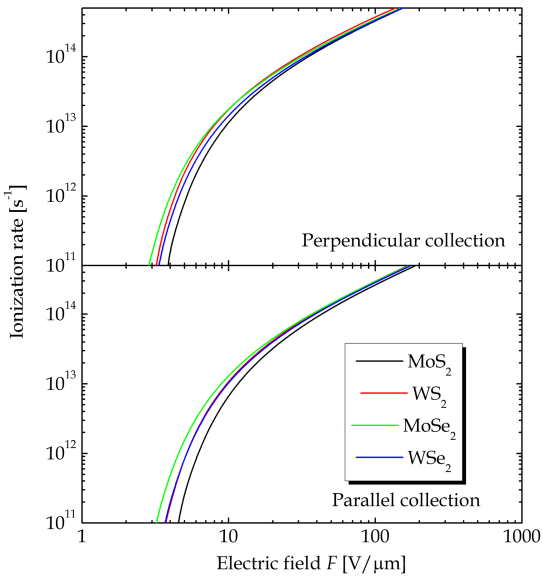

Figure 6. Same as figure 5 but for indirect exciton ionization. Note that WS_2 and WSe_2 results nearly coincide.

figure 4 it is seen that at such a field strength, ionization is well into the linear regime. Hence, using $|E_0|/a^*_{x,z}$ as an estimate for the ionization threshold is partly supported by our results. In fact, the transition from exponential to linear field-dependence in figure 4 occurs around $\mathcal{E} \sim 0.1$, which may be considered a better measure for the threshold.

For both direct and indirect excitons, the magnitude of the ionization rate reflects the exciton binding energy. Hence, there is a simple correlation between the binding energies in tables 1 and 2, on the one hand, and the ordering of the curves in figures 5 and 6 on the other, with strongly bound excitons leading to suppressed ionization. The larger differences for the direct exciton binding energies lead to more spread-out curves as compared to the indirect ones. Overall, the best candidates for efficient ionization of direct and indirect excitons are WSe_2 and $MoSe_2$, respectively. For the direct excitons (figure 5) the WSe_2 rate is significantly higher than the second best material, i.e. $MoSe_2$ and WS_2 for perpendicular and parallel collection, respectively. In comparison, the differences for indirect excitons are modest.

We end this section with a brief comparison to the experimental photoresponse rate observed in [5]. In that work, the photoresponse rate was determined using two-pulse excitation with an adjustable delay. Hence, the extraction time of the photogenerated carriers produced by the first pulse is probed by the second pulse. The extraction time itself is a measure of at least three processes occurring in series: (i) exciton ionization, (ii) drift to the TMD/graphene interface, and (iii) transfer across the interface. Hence, importantly, the measurement is dominated by the slowest among these processes and the experimental rate cannot necessarily be identified with the actual ionization rate. The fastest response $\sim 2 \cdot 10^{11} \mathrm{s}^{-1}$ was seen for a WSe_2 device having a slab thickness of 2.2 nm. This thickness is larger than the perpendicular exciton Bohr radius (1.1 and 1.4 nm for direct and indirect excitons, respectively) and we therefore expect the bulk picture in the present work to be applicable. Bias voltages up to 1.2 V were applied in the measurement and the response rate typically increased with applied bias. The precise value of the internal electric field is subject to some uncertainty and depends on the geometrical capacitance and interface charges (see [5], supplementary information). It is clear, however, that the theoretical ionization rates computed above exceed the measured rate by a significant factor. In fact, for field strengths of 100 V $\mu\mathrm{m}^{-1}$ and above, the converted results in figures 5 and 6 for perpendicular collection are found to be at least $2.2 \cdot 10^{14}$ s^{-1} and $3.3 \cdot 10^{14}$ s^{-1} for direct and indirect excitons, respectively. This is obviously significantly larger than the experimental response rate. Hence, in agreement with [5], we conclude that exciton ionization is not the limiting process in the observed photoresponse at this field strength. Rather, drift of the carriers to the contacts after ionization is the probable cause of the reduction. Generally, carrier drift in the perpendicular direction is much slower than in-plane drift. For instance, the ratio between parallel and perpendicular carrier mobility for the related material $MoSe_2$ can be as large as 10^3 [33]. The limiting role of carrier drift is further evidenced by the inverse square dependence of the rate on sample thickness [5]. Finally, a transfer time of 1 ps

across the interface between graphene and WS_2 was recently reported [34]. Assuming a similar rate for WSe_2, this implies an upper limit of $\sim 10^{12}$ s^{-1} for the measured photoresponse rate.

5. Summary

In summary, we have considered the process of field-assisted exciton ionization in multilayer TMDs. By solving an anisotropic Mott-Wannier equation we are able to extract exciton binding energies. Combined with complex scaling and resummation techniques, we subsequently find exciton Stark shifts and ionization rates as a function of external field strength. When applied to sulphides (MoS_2 and WS_2) and selenides ($MoSe_2$ and WSe_2), our results show that, in scaled exciton units, all of these materials behave similarly. However, after conversion into physical units, significant differences emerge. Thus, direct excitons in the tungsten compound WSe_2 are found to ionize in substantially smaller fields as a result of the smaller exciton binding energy. Similarly, for the indirect exciton, the ionization rate of $MoSe_2$ is the highest among the compounds considered.

Acknowledgments

This work is financially supported by the Center for Nanostructured Graphene (CNG) and the QUSCOPE center. CNG is sponsored by the Danish National Research Foundation, project DNRF103 and QUSCOPE is sponsored by the Villum foundation. HM and BKN are supported by NSF under Grant No. ECCS 1509094.

Appendix. Perturbation series

For materials that are only weakly anisotropic so that $|\kappa| \ll 1$, the Wannier equation equation (3) may be approximated by the linearized problem

$$\left\{-\frac{1}{2}\nabla^2 - \frac{1}{r} - \frac{\kappa}{2}\frac{z^2}{r^3} + \vec{\mathcal{E}}\cdot\vec{r}\right\}\psi = E\psi. \tag{A1}$$

We wish to find the perturbation series for the energy as an asymptotic series in the electric field $E_{x,z}(\mathcal{E}) = \sum_{n=0}^{\infty} E_{x,z}^{(2n)}\mathcal{E}^{2n}$. In the isotropic case $\kappa = 0$, well-known results for the 3D hydrogen problem [16, 27] readily provide the 8th order expansion

$$E_{\kappa=0}(\mathcal{E}) = -\left\{\frac{1}{2} + \frac{9}{4}\mathcal{E}^2 + \frac{3555}{64}\mathcal{E}^4 + \frac{25\,127\,79}{512}\mathcal{E}^6 + \frac{13\,012\,777\,803}{16\,384}\mathcal{E}^8 + O(\mathcal{E}^{10})\right\}. \tag{A2}$$

To include a finite but small anisotropy, we now calculate the first order correction in κ to the eigenvalue in equation (A1) using linear perturbation theory. To this end, the wave function $\psi_{\kappa=0}(\mathcal{E})$, correct to 8th order in the field $\mathcal{E}$, is required. Fortunately, the separation in parabolic coordinates applied in [16] immediately provides this function. If the field is along z such that both perturbations in equation (A1) preserve the rotational symmetry around the z-axis, the analysis is straightforward and for the total energy $E_z(\mathcal{E}) \approx E_{\kappa=0}(\mathcal{E}) + \Delta E_z(\mathcal{E})$ one finds the correction

$$\Delta E_z(\mathcal{E}) = \kappa\left\{-\frac{1}{6} + \frac{101}{120}\mathcal{E}^2 + \frac{842\,137}{13\,440}\mathcal{E}^4 + \frac{10\,128\,18\,143}{107\,520}\mathcal{E}^6 + \frac{82\,343\,723\,712\,163}{37\,847\,040}\mathcal{E}^8 + O(\mathcal{E}^{10})\right\}. \tag{A3}$$

On the other hand, if the field is in-plane $\vec{\mathcal{E}} = \mathcal{E}\hat{x}$, equation (A1) is conveniently symmetrized over directions perpendicular to the field and reformulated as

$$\left\{-\frac{1}{2}\nabla^2 - \frac{1+\frac{\kappa}{4}}{r} + \frac{\kappa}{4}\frac{x^2}{r^3} + \mathcal{E}x\right\}\psi = E\psi. \tag{A4}$$

Hence, the isotropic Coulomb term is renormalized by a factor of $1 + \frac{\kappa}{4}$. A simple scaling calculation shows that the $2n'$th order field correction for the isotropic case equation (A2) acquires a factor $(1-3n)\frac{\kappa}{2}$ as a consequence. The second κ -dependent term in equation (A4) is the same as for the perpendicular case except for a factor $-1/2$. Adding the two contributions, it follows that for the parallel case

$$\Delta E_x(\mathcal{E}) = \kappa\left\{-\frac{1}{6} + \frac{439}{240}\mathcal{E}^2 + \frac{28\,906\,13}{26\,880}\mathcal{E}^4 + \frac{32\,086\,505\,77}{21\,5040}\mathcal{E}^6 + \frac{24\,831\,096\,026\,2067}{75\,694\,080}\mathcal{E}^8 + O(\mathcal{E}^{10})\right\}. \quad \text{(A5)}$$

The linearization in κ means that the above results cannot be immediately applied in the experimentally relevant range for TMDs $|\kappa| \geqslant 0.5$. We therefore fit the full κ -dependence to a polynomial using (i) the exact known limits for $\kappa = 0$ and $\kappa = 1$ [16], (2) the exact linear behavior equations (A3) and (A5), and (3) numerical Stark energies for intermediate values. The results for $\kappa \geqslant 0$ for the two orientations are

$$\begin{aligned} E_x^{(2)} &= -2.25 + 1.6802\kappa + 1.0397\kappa^2 - 2.3298\kappa^3 + 1.7779\kappa^4 \\ E_x^{(4)} &= -55.547 + 102.93\kappa - 38.103\kappa^2 - 24.578\kappa^3 + 15.27\kappa^4 \\ E_x^{(6)} &= -4907.8 + 14\,153\kappa - 12\,874\kappa^2 + 2431.9\kappa^3 + 1196.3\kappa^4 \\ E_x^{(8)} &= -79\,4240 + 31\,040\,00\kappa - 44\,720\,00\kappa^2 + 27\,616\,00\kappa^3 - 599450\kappa^4, \end{aligned} \quad \text{(A6)}$$

and

$$\begin{aligned} E_z^{(2)} &= -2.25 + 0.841\,97\kappa - 0.304\,37\kappa^2 + 1.2014\kappa^3 - 0.917\,73\kappa^4 \\ E_z^{(4)} &= -55.547 + 62.705\kappa - 46.093\kappa^2 + 107.7\kappa^3 - 92.28\kappa^4 \\ E_z^{(6)} &= -4907.8 + 9432.1\kappa - 12\,285\kappa^2 + 22\,899\kappa^3 - 18\,157\kappa^4 \\ E_z^{(8)} &= -794\,240 + 21\,796\,00\kappa - 38\,894\,00\kappa^2 + 65\,712\,00\kappa^3 - 47\,654\,00\kappa^4. \end{aligned} \quad \text{(A7)}$$

We do not attempt to incorporate negative κ -value into the fit but provide here the relevant expressions for the characteristic case of $\kappa = -1$

$$\begin{aligned} E_{x,\kappa=-1}(\mathcal{E}) &\approx -0.3909 - 4.098\mathcal{E}^2 - 236.0\mathcal{E}^4 - 49\,290\mathcal{E}^6 - 19.00\cdot 10^6\mathcal{E}^8 + O(\mathcal{E}^{10}) \\ E_{z,\kappa=-1}(\mathcal{E}) &\approx -0.3909 - 3.016\mathcal{E}^2 - 130.9\mathcal{E}^4 - 20\,690\mathcal{E}^6 - 6.033\cdot 10^6\mathcal{E}^8 + O(\mathcal{E}^{10}). \end{aligned} \quad \text{(A8)}$$

References

[1] Yin Z, Li H, Li H, Jiang L, Shi Y, Sun Y, Lu G, Zhang Q, Chen X and Zhang H 2012 *ACS Nano* **6** 74–80
[2] Lopez-Sanchez O, Lembke D, Kayci M, Radenovic A and Kis A 2013 *Nat. Nanotechnol.* **8** 497–501
[3] Yu W J, Liu Y, Zhou H, Yin A, Li Z, Huang Y and Duan X 2013 *Nat. Nanotechnol.* **8** 952–8
[4] Wang H, Zhang C, Chan W, Tiwari S and Rana F 2015 *Nat. Commun.* **6** 8831
[5] Massicotte M, Schmidt P, Vialla F, Schädler K G, Reserbat-Plantey A, Watanabe K, Taniguchi T, Tielrooij K J and Koppens F H L 2016 *Nat. Nanotechnol.* **11** 42–6
[6] Bernardi M, Palummo M and Grossman J C 2013 *Nano Lett.* **13** 3664–70
[7] Lopez-Sanchez O, Llado E A, Koman V, Morral A F, Radenovic A and Kis A 2014 *ACS Nano* **8** 3042–8
[8] Withers F *et al* 2014 *Nat. Mater.* **14** 301–6
[9] Ramasubramaniam A 2012 *Phys. Rev.* B **86** 115409
[10] Olsen T, Latini S, Rasmussen F and Thygesen K S 2016 *Phys. Rev. Lett.* **116** 056401
[11] Qiu D Y, da Jornada F H and Louie S G 2013 *Phys. Rev. Lett.* **111** 216805
[12] Trolle M L, Seifert G and Pedersen T G 2014 *Phys. Rev.* B **89** 235410
[13] Wannier G H 1937 *Phys. Rev.* **52** 191–7
[14] Herbst I W and Simon B 1978 *Phys. Rev. Lett.* **41** 67–9
[15] Mera H, Pedersen T G and Nikolić B K 2015 *Phys. Rev. Lett.* **115** 143001
[16] Pedersen T G, Mera H and Nikolić B K 2016 *Phys. Rev.* A. **93** 013409
[17] Chaves A, Low T, Avouris P, Çakır D and Peeters F M 2015 *Phys. Rev.* B **91** 155311
[18] Kim J, Hong X, Jin C, Shi S-F, Chang C-Y S, Chiu M-H, Li L-J and Wang F 2014 *Science* **346** 1205–8
[19] Sie E J, McIver J W, Lee Y-H, Fu L, Kong J and Gedik N 2015 *Nat. Mater.* **14** 290–4
[20] Haastrup S, Latini S, Thygesen K S and Bolotin K *Phys. Rev.* B **94** 041401
[21] Klein J, Wierzbowski J, Regler A, Becker J, Heimbach F, Müller K, Kaniber M and Finley J J 2016 *Nano Lett.* **16** 1554–9
[22] Latini S, Olsen T and Thygesen K S 2015 *Phys. Rev.* B **92** 245123
[23] Landau L D and Lifshitz E M 1969 *Electrodynamics of Continuous Media* (Oxford: Pergamon)
[24] Pedersen T G and Lynge T B 2002 *Phys. Rev.* B **65** 085201
[25] Wheeler R G and Dimmock J O 1962 *Phys. Rev.* **125** 1805–15
[26] Jentschura U D 2001 *Phys. Rev.* A **64** 013403
[27] Hasse H R 1930 *Proc. Cambridge Phil. Soc.* **26** 542–55
[28] Sewell G L 1949 *Proc. Cambridge Phil. Soc.* **45** 678–9
[29] Pedersen T G 2007 *Solid State Commun.* **141** 569–72
[30] Enkovaara J *et al* 2010 *J. Phys. Condens. Matter* **22** 253202
[31] Yan J, Mortensen J J, Jacobsen K W and Thygesen K S 2011 *Phys. Rev.* B **83** 245122
[32] Rasmussen F A and Thygesen K S 2015 *J. Phys. Chem.* C **119** 13169–83
[33] Kautek W 1982 *J. Phys. C: Solid State Phys* **15** L519–25
[34] He J, Kumar N, Bellus M Z, Chiu H-Y, He D, Wang Y and Zhao H 2014 *Nat. Commun.* **5** 5622

{2.7182818284}ϑφερτυθιοπσδφγηξκλ